ARCHITECTURAL ELEMENTS OF BURIED VOLCANIC SYSTEMS AND THEIR IMPACT ON GEOENERGY RESOURCES

by

ALAN PATRICK BISCHOFF

A dissertation submitted in partial fulfilment of the requirements for the Degree of

DOCTOR OF PHILOSOPHY IN GEOLOGY

January, 2019

Abstract

This PhD investigates the architecture of volcanic systems buried in New Zealand sedimentary basins. These “fossil” volcanoes occur in great numbers around the globe, typically comprising complex magmatic-sedimentary systems that produce large impacts in the evolution of the host sedimentary basin. The interaction between magmatism and sedimentation creates a range of geological conditions that can favour the occurrence of geoenergy resources, such as hydrocarbons and geothermal energy. Interpretation of volcanoes in the subsurface requires a multidisciplinary approach that combines insights from complementary disciplines, such as sedimentology, stratigraphy, and volcanology into a unified model. Over the last two decades, knowledge of volcanic systems in sedimentary basins has increased significantly, largely due to improvements in the quality and availability of seismic reflection data. This PhD research uses data from 2D and 3D seismic reflection surveys to characterise the spatio-temporal distribution of the fundamental building blocks (i.e. architectural elements) of buried volcanic systems, aiming to provide insights for exploration of geoenergy resources. Here, we divide the stratigraphic record of these “volcanic basins” into three first-order magmatic sequences (i.e. pre-, syn- and post-magmatic), which can be sub-divided into second-order magmatic stages related to the emplacement, construction, degradation and burial of the volcanoes.

Two case-study areas have been utilised to determine how the architectural elements vary systematically in buried monogenetic and polygenetic volcanic systems. These study areas are the Kora Volcanic System (KVS) and Maahunui Volcanic System (MVS), located in the Taranaki and Canterbury basins respectively. Both volcanic systems formed in marine environments during the Miocene, and show systematic spatio-temporal distributions of architectural elements. In both cases, each one of the magmatic sequences and stages are characterised by a network of genetically related architectural elements, formed by interactions between intrusions, eruptions and sedimentation. Syn-intrusive architectural elements are formed by magma emplaced into the host basin strata (emplacement stage), and include hypabyssal intrusions such as sills, dikes and small plutonic bodies, together with associated deformed strata. Syn-eruptive and inter-eruptive architectural elements are formed during the constructional stage, and include all primary eruptive, epiclastic, and associated sedimentary deposits formed during active and quiescent volcanism. Post-magmatic architectural elements are formed during the passive degradational and burial stages of volcanism, comprising sedimentary deposits impacted by the presence of volcanic structures, which can influence sedimentation millions of years after complete burial of volcanic edifices.

In detail, the architectural elements of each volcanic system also display differences. Dikes and sills of the KVS plumbing system typically formed along, or branching from, simultaneous Miocene rift faults. Explosive submarine volcanism in Kora formed a large-volume (ca 95 km^3) basaltic-andesitic compound volcano erupted from a fixed central conduit, which dominated seafloor topography and created localized debris deposits that interfinger with hemipalagic sediments and deep-water channel deposits. In contrast, the monogenetic MVS plumbing system distributed magma to dispersed eruptive centres, which formed small-volume (< 6 km^3) basaltic submarine volcanoes equivalent of maar-diatreme and tuff cones erupted at ca 1000 m depth. Degradation of volcanoes in the MVS was differential, with strong erosion on the top of shallower and higher edifices that were emergent above sea-level during a late Miocene base-level fall, while volcanoes that remain below the sea-level were not subject to significant degradation and are now well preserved beneath bathyal sediments.

Analysis of the architectural elements of the KVS and MVS provide insights into the exploration of geoenergy resources in buried and active volcanic systems elsewhere. Intrusions and magmatic deformation, including large saucer-sills and intrusion swarms, have the potential to produce four-way closures and reservoirs that can host significant oil and gas accumulations. These intrusions can also produce high-temperature intrusion-related geothermal systems. Both petroleum and geothermal systems can be enriched in CO_2, CH_4, and H_2S if the intrusions were emplaced in carbonate or organic-rich host rocks. Eruptive and sedimentary architectural elements can form substantial hydrocarbon fields with reservoirs in paleogeomorphic structures formed by changes in lithologies and by the presence of stratigraphic discontinuities between the volcano and enclosing sedimentary strata. Syn-eruptive reservoirs can be sealed, if volcanic structures are buried by fine-grained marine sediments or evaporitic rocks. Progressive burial of the volcanoes can create ideal conditions for deposition of high-quality carbonate reservoirs located on topographic seabed highs above buried volcanic structures. Due to differential compaction between the volcanoes and enclosing sedimentary rocks, these carbonate reservoirs can be entrapped in large four-way closures, with potential to host world-class hydrocarbon fields. Therefore, analysis of volcano-stratigraphic architecture of buried volcanoes can be used to build models for the exploration of geoenergy resources such as hydrocarbons and geothermal electricity.

Dedication

For my beloveds, Mirve Törmä and the little one that she is carrying in her womb. I am blessed for having you in my life. You girls rock!

Acknowledgments

I would like to thanks my supervisors Andy Nicol, Mac Beggs, Darren Gravley and Ben Kennedy for the support and guidance during this PhD research. Thanks for Mark Webster for reviewing the thesis, and for Paul Ashwell, Carlos Kazianis, Jarg Pettinga, Alex Nichols, Kari Basset, Michael MacMaster, Karoly Németh, Priscila Smith, David Clague, Jim Cole, Elisabeth Bertolett, Josh Borella, Jonathan Davidson, Marlene Villeneuve, Catherine Reid, Gabor Kereszturi, and Samuel Hampton for providing support for my geological interpretations. Thanks for the technical support from Matt Cockcroft, Sacha Baldwin, Rebekah Hunt, Jane Newman, Janet Warburton, Lizzy McKinnon, Te Maire Tau, Rob Spiers, Rachel Musgrave, Abbey Douglas, John Southward, and Chris Grimshaw. Without your help, this work will not be possible. Thanks for the Electron Microscopic Center and Geology laboratory of the University of Canterbury for providing access and material for this thesis. Thanks for Sylvia dos Anjos, Sverre Plank, Leonardo Oliveira, Maria José Oliveira, Anna Kwasniewski, Webster Mohriak, Pujon Wang, Ari Roisenberg, Evandro de Lima, Claiton Scherer and Luis Fernando de Ross for the constructive interaction with our research group during these years. Thanks for Sverre Plank, Christopher Jackson and Simon Holford for reviewing Chapter 3 priority to publication in the AAPG Interpretation Journal in 2017, and for Simon Holford and Adrian Pittari for examining the thesis. Thanks for Andrew Miall, despite we haven't met, your work has inspired this PhD thesis. Special thanks for my workmates Andrea Barrier, Hanfei Wang and Marcos Rossetti for sharing their time and efforts to study "fossil" volcanoes. I would like to acknowledge the funding support from the University of Canterbury Doctoral Scholarship, Masson Trust, GNS, Department of Geological Sciences of the University of Canterbury, Frontiers Abroad, and New Zealand Ministry of Business, Innovation and Employment, and to IHS Markit for providing academic licence to use the Kingdom software. Thanks for the New Zealand Petroleum and Minerals for providing the datasets and access to well samples of exploration drillholes in Canterbury and Taranaki basins used in this research. Thank you my partner Mirve Törmä for all support during this time.

Contents

1 Introduction 24

1.1 Research Rationale 24

1.2 Research Hypothesis 25

1.3 Research Objectives 25

1.4 Studied Areas 26

1.5 Thesis Structure 27

1.6 References 30

2 Concepts and Techniques 33

2.1 Fundamental Concepts of Seismic Reflection Interpretation 34

2.2 Seismic Imaging of Igneous Rocks in Sedimentary Basins 36

2.3 Seismic Attributes 37

2.4 Seismic Stratigraphy 39

2.5 Seismic Volcano-Stratigraphy 40

2.6 Sequence Stratigraphy 41

2.7 Sequence Volcano-Stratigraphy 43

2.8 Seismic Geomorphology 43

2.9 Stratigraphic Record of Volcanism 45

2.10 Sedimentary and Volcanic Architectural Elements 45

2.11 Architectural Elements Analysis Applied in Geoenergy Exploration 48

2.12 Conclusion 49

2.13 References 49

3 Stratigraphy of Architectural Elements in a Buried Polygenetic Volcanic System and Implications for Hydrocarbon Exploration 56

3.1 Abstract 56

3.2 Introduction 57
3.3 Kora Volcano Geologic Setting and Exploration 58
3.4 Data and Methods 61
3.5 Stratigraphy of Architectural Elements of Kora Volcanic System 62
3.5.1 Syn-Magmatic Sequence 62
3.5.2 Post-Magmatic Sequence 72
3.6 Economic Potential and Petroleum Plays 80
3.6.1 Syn-Magmatic Traps and Reservoirs 81
3.6.2 Post-Magmatic Traps and Reservoirs 82
3.7 Conclusions 83
3.8 References 84
4 Seismic Reflection and Petrographic Characterisation of a Buried Monogenetic Volcanic Field 89
4.1 Abstract 89
4.2 Introduction 90
4.3 Geological Setting 93
4.4 Dataset, Methods and Limitations 96
4.4.1 Data Set 97
4.4.2 Petrography, RXF and SEM-EDS Methods and Limitations 97
4.4.3 Methods and Limitations to Reconstruct Buried Volcanoes from Seismic Data 99
4.4.4 Seismic Stratigraphy Methods 107
4.5 Geological Characterisation of Maahunui Volcanic Field 110
4.5.1 Results from Petrography, RXF and SEM-EDS Analysis 110
4.5.2 Age of the MVF and depth of the monzogabbro intrusion 126
4.5.3 Volcanic and Hypabyssal Seismic Facies 128
4.5.4 Volcano Morphology and Relationship with Intrusions and Diatremes 132

4.5.5 Paleo-Physiography and Paleo-Environmental Reconstruction 134
4.5.6 Vent Distribution and Eruptive Fingerprint 140
4.6 Controls on MVF Morphology 141
4.6.1 Eruptive Styles and Edifice Growth Mechanisms 142
4.6.2 Post-Eruptive Paleogeography 144
4.7 Conclusions 147
4.8 References 147
5 Stratigraphy of Architectural Elements in a Buried Monogenetic Volcanic System 156
5.1 Abstract 156
5.2 Introduction 157
5.3 Concepts, Methods and Terminology 160
5.4 Stratigraphy of Architectural Elements of Maahunui Volcanic System 165
5.4.1 Syn-Magmatic Sequence 165
5.4.2 Post-Magmatic Sequence 194
5.5 Conclusions 197
5.6 References 198
6 Models for Exploration of Geoenergy Resources in Monogenetic Volcanic Fields within Sedimentary Basins 205
6.1 Implications for Geoenergy Resources 205
6.2 Petroleum Plays in Buried Monogenetic Volcanic Fields 205
6.2.1 Petroleum Elements of the Emplacement Stage 207
6.2.2 Petroleum Elements of the Constructional Stage 208
6.2.3 Petroleum Elements of the Degradational Stage 209
6.2.4 Petroleum Elements of the Burial Stage 210
6.3 Intrusion-Related Hydrothermal Systems 211
6.4 Conclusions 214

6.5 References 214

7 Conclusions 218

8 Appendix 1: Complementary Information of the Methods Used to Calculate the Height and Volume of Buried Volcanoes from Seismic Reflection Data 223

List of Figures

Figure 1: Diagram showing the workflow adopted in this PhD research. Seismic reflection and well data were integrated with observations from outcropping analogue systems. 33

Figure 2: Fundamental concepts of seismic reflection acquisition and interpretation. Modified from Sheriff and Geldart (1995) and Wright (2013). Seismic line in A is from Canterbury Basin, New Zealand. Seismic image from Bischoff (unpublished data, 2015). 35

Figure 3: 2D profile of a seismic survey in Canterbury Basin, New Zealand. Figure A shows the vertical wiggle track at individual shot points. Strong impedance contrasts display positive amplitude peaks. These peaks can be laterally tracked (B) to display the subsurface characteristics of the area such as lithological contacts, geological units geometries and chronostratigraphic surfaces. Seismic images from Bischoff (unpublished data, 2015)..... 35

Figure 4: Saucer-shaped sills imaged in the Waka 3D seismic survey (e.g. Blanke, 2010) from offshore Canterbury Basin, New Zealand. The locations of the sills are highlighted by the blue ellipses. Image from Bischoff (unpublished data, 2015). 36

Figure 5: 2D seismic section (A) and 3D opacity rendering (B) of a potential sill-fed volcano in the Nimitz-3D seismic survey, Taranaki Basin, New Zealand. Note that the intrusive and extrusive parts of the volcano show high amplitude reflectors in contrast with basin sedimentary strata. Images from Bischoff (unpublished data, 2018)..... 37

Figure 6: 2D seismic profile (A) and time-slice view (B) of a saucer-shaped sill intruding into marine sedimentary strata, offshore Taranaki Basin in the Vulcan-3D seismic survey. Purple ellipses display the relevant information of the 3D survey for the analysed data. Top image shows a 2D section of a saucer-shaped sill evidenced by the attribute *envelope*. Bottom image show the same saucer-shaped sill in plan, evidenced by the attribute amplitude at a time-slice at 3.7 TWT sec. Yellow line in top image is the reference for the time slice in the bottom image. Seismic images from Bischoff (unpublished data, 2018). 38

Figure 7: (A) Common internal seismic reflection configurations, and (B) seismic reflection terminations observed in seismic data. Modified from Mitchum et al. (1977); Emery and Myers (1996); Catuneanu (2006), and Wright (2014). 39

Figure 8: Diagram showing the evolution of sequence stratigraphic approaches. From Catuneanu et al. (2010). 41

Figure 9: Allogenic controls on sedimentation, and their relationship to environmental energy flux, sediment supply, accommodation space, and depositional trends adapted for volcanic basins (modified from Catuneanu, 2006). 42

Figure 10: Model-independent workflow vs. model-dependent choice in sequence stratigraphy presented in Catuneanu et al. (2009) and Catuneanu et al. (2010). The model-independent workflow leads to the subdivision of the stratigraphy into a succession of genetic units separated by sequence stratigraphic surfaces. After this sequence stratigraphic framework is built, the geoscientist may make model-dependent choices with respect to the selection of surfaces that should be elevated to the status of sequence boundary. In this study, after following a model-independent approach for the recognition of the stratal pattern of the basins, we propose the use of *magmatic sequences and stages* to subdivide the stratigraphic record of volcanic basins. Abbreviations: forced regressive (FR), normal regressive (NR) and transgressive (T) surfaces. 42
Figure 11: A) Channelized lava flow erupted from Kilauea Volcano, Lower East Rift Zone, Hawaii. B and C) 3D and 2D seismic images of an analogue channelized lava flow in Vulcan-3D, offshore Taranaki, New Zealand). This 3D volume together with the nearby Romney-3D reveal several large late Cretaceous polygenetic volcanoes that formed in association with rifting and opening of the Tasman Sea. Figures B and C from Bischoff (unpublished data, 2018). 44
Figure 12: Seismic images showing the morphology of shallow intrusions that fed an extrusive flow at the early Paleocene paleosurface in Otway Basin, Southern Australia. (A) Arbitrary 2D seismic reflection profile. (B) 3D opacity-rendered view. From Holford et al. (2012). 44
Figure 13: Stratigraphic model showing the faciological distribution and architecture of a hypothetical volcanic system. Deposits show lateral variation with increasing distance from the eruptive centre. Vertical succession occurs by the alternation of syn-eruptive and inter-eruptive deposits, bounded by proxies of chronostratigraphic surfaces. Figure from Orton (1996). 45
Figure 14: 3D representation of the main deep-water architectural elements. From Haughton (2006). 46
Figure 15: Examples of volcanic architectural elements in Lyttelton Volcano, Banks Peninsula Volcanic Complex. Each one of these elements is a three-dimensional rock unit genetically related to a particular process or a suite of processes occurring within the volcano. These elements are separated from each other by internal facies (e.g. composition, fragmentation, grain size), and external bounding-surfaces (e.g. cross-cutting relationship, angular or sharp contacts, changes in paleo-flow directions). 47
Figure 16: An example of the hierarchy of volcanic architectural elements in Tongariro Volcanic Complex, New Zealand. In a large-scale, the Red Crater (A) is one of several vents that compose the Tongariro Volcanic Complex. Downscaling, the flanks of the Red Crater are mainly composed by bedded inclined pyroclastic air-fall deposits, minor lava flows, and cross-cutting feeder dikes (B). A detailed view of part of the Red Crater flanks (C) show a succession of individual coarse-grained air-fall deposits, formed by changes in the dynamics of a single eruption, or by accumulation of tephra due to multiple eruption-cycles. At each scale, these sets of individual rock units (i.e. architectural elements) are formed in response to co-genetic processes occurring over a particular time-scale, and are physically separated from each other by a hierarchy of internal and external bounding surfaces. 48
Figure 17: Location map of the study area and data set available. Kora is one of the volcanic complexes of the MVB, erupted from the Early Miocene to Late Pliocene in the Northern Taranaki graben. Detailed map modified from Giba et al. (2013). 58

Figure 18: Local chronostratigraphic chart showing the age and occurrence of the main lithostratigraphic units in the study area. Compiled from Bergman et al. (1992), King and Thrasher (1996), OMV (2011), and insights from this study. Stratigraphic ages modified from the International Chronostratigraphic Chart 2014 and New Zealand Geological Time Scale 2015. 59
Figure 19: Schematic representation of the stratigraphic sequences, magmatic sequences, stages, architectural elements, and predominant processes associated with the Kora volcanic system. Numbers in circles represent the location of the architectural elements indicated in the key. Numbers in squares indicate predominant processes in the key. The symbols in the bottom part of the architectural elements key illustrate the database used on the interpretations. The terms “observed in seismic” represent architectural elements find in seismic data, “drilled” represent architectural elements sampled by wells, and “analogues” represent architectural elements recognized in modern and ancient analogues. Conduit zones and dikes have lateral thickness exaggerated for visualization proposes. Abbreviations are SyInS (syn-intrusive surface), PrErS (Pre-eruptive surface), PoErS (post-eruptive surface), PoDgS (post-degradational surface) and PoBuS (post-burial surface). More details about these volcano-stratigraphic surfaces in chapter 5. 63
Figure 20: A 2D seismic section of the Kora volcano and a representation of the main stratigraphic sequences and processes. Note the progradation of clinoforms from the southeast to the northwest. 64
Figure 21: Seismic images of pre-magmatic strata deformed during magma emplacement. (a) Time slice in dip of maximum similarity seismic cube showing faults in radial pattern and the circular structure of the Kora volcano. The FFD is a forced-folded dome pushed up by underlying sills and dikes intrusions. (b) Inline and crossline sections of the Kora volcano combined with a volume rendering seismic envelope showing the pre-eruptive dome (evident in red, corresponding to the Tangaroa Formation). 65
Figure 22: Seismic images of syn-intrusive architectural elements. (a) High-amplitude geobody extraction revealing the 3D geometry of a saucer-shaped intrusion. (b and d) Detail of the intrusion showing a semi lobate body in plan view with magma-fingers structures at the terminations. (c) The 2D cross section of the amplitude anomaly. 66
Figure 23: Seismic images of syn-intrusive architectural elements. (A) Cross section applying the optical stacking technique. (B) Geobody extraction of high-amplitude anomalies (red) showing sill and dikes jacking-up the overlaying sedimentary strata. (C) Volume rendering envelope showing the distribution of high-amplitude geobodies. Note that the bodies are concentrated toward the southern and eastern part of the seismic cube, region where the Miocene rift faults are more frequent and present larger displacement. 67
Figure 24: Seismic images of syn-intrusive and syn-eruptive architectural elements. (A) Time slice through the dip of maximum similarity seismic cube at 1084 ms TWT. The darker blue colours represent the core of parasitic vents and cone sectors, whereas the lighter blue colours represent sedimentary strata that onlap these structures. Note the radial pattern of lineaments associated with the smaller parasitic and satellite vents circled in yellow and green. (B) The 2D cross section showing the relationship of parasitic vents and conduit zones. (C) A 2D cross section showing mount-like structures interpreted to be small parasitic vents. 68
Figure 25: Seismic images and outcrop analogues representing the syn and inter-eruptive architectural elements of Kora volcanic system. (A) Volume rendering envelope showing the northwest part of Kora volcano. Note that discontinuous high-amplitude reflectors diverge outward from the main vent complex (red). (B and D)

Geometry of eruptive (air fall, pyroclastic density currents, and lava flow deposits) and sedimentary deposits on Ngauruhoe volcano and Red Crater, Tongariro National Park, New Zealand. Note that on the flanks of the volcano, the deposits are amalgamated and discontinuous, and in the foothills, deposits form continuous and lobate bodies. (A and C) These geometric patterns are also recognized in seismic images of the Kora volcano. 69

Figure 26: A 2D seismic section showing the endogenous and exogenous part of the syn-magmatic sequence, overlaying strata from the pre-magmatic sequence and covered by strata from the post-magmatic sequence. The 3D seismic cube is tied with lithofacies and well logs drilled on the wells (e.g., Kora-1, red = gamma ray and green = density). 70

Figure 27: Well-core description and photographs of the main lithofacies recovered on the Kora-1A well. The green curve is the density log from Kora-1, located 50 m from Kora-1A. Numbers in blue are permeability measurements from Kora-1A cores. P1: Polymictic (more than three types of volcanic clasts) clast-supported, rounded volcanic conglomerate with sandy matrix; P2: well-sorted tuff; P3: polymictic clast-supported, well-rounded volcanic conglomerate; and P4: moderately sorted lapilli-tuff. 71

Figure 28: Seismic images of architectural elements formed during the degradational stage. (a) Composite cross section and volume rendering envelope showing the Kora volcano and the relationship with Late-Miocene to Pliocene deep-water channel systems. (b) Detailed 2D cross sections showing low sinuosity (1, 2) and high-sinuosity channels (3). 73

Figure 29: Seismic images of architectural elements formed during the degradational stage. (a) Composite cross section and volume rendering showing the Kora volcano and the relationship with deep-water channel systems. (b) Time-slice on the dip of the maximum similarity cube showing faults in the radial pattern (closer to the cone) interfering with the northeast faults from the Miocene rift. Note that some of the faults are compartmentalizing the high-sinuosity channel deposits. (c) Volume rendering envelope showing low and high deep-water channels and possible debris avalanche deposits. 75

Figure 30: Seismic images of architectural elements formed during the burial stage. (a) Composite cross section and volume rendering envelope showing the Kora volcano and the lobate sheet-like deposits. (b) Dip section showing the lobate sheet-like deposits in detail. Note the foreset indicating migration of clinoforms from the southeast to northwest at the burial interval. (c) Cross section showing the lobate sheet-like deposits perpendicular to the paleodepositional direction. Note that most of faults do not displace sediments deposited during the burial period. 76

Figure 31: Seismic images of the architectural elements formed during the burial period. Note the dome over the buried Kora volcano and the sedimentary systems that interact with the second seamount. The volcanic edifice was completely buried by approximately 4 Ma ago and still had a strong influence on the development of sedimentary systems until at least the Pleistocene. (a) Dip of maximum similarity cube showing the location of the buried Kora volcano and the development of fans, deltas, dendritic drainages, gullies, and canyons during the progradation of the slope (northwest) and establishment of a shelf (southeast) in the region. (b) A 2D cross section showing the seamount over the volcanic edifice. 77

Figure 32: Seismic images of architectural elements formed during the burial stage. Time slice through the dip of maximum similarity cube showing the relationship of the buried Kora volcano and the enclosing sedimentary architectural elements. The dashed line represents the position of the shelf break. 78
Figure 33: Overlap of the dip of the maximum similarity seismic cube and the amplitude volume rendering seismic cube showing the main geometrical shape of the seamount-edge fans and the relationship with the seamount produced due to the burial of Kora volcanic edifice. 79
Figure 34: A) Map showing the age and location of volcanic rocks onshore and offshore northern Canterbury Basin, together with the main seismic and well data used in this work. Red dots indicate the locations of volcanoes in the Maahunui Volcanic Field, which is the focus of this study (Chapters 4 & 5). Location of Paleogene to Cretaceous offshore volcanoes were mapped in association with Andrea Barrier (UC PhD candidate in structural geology). Onshore volcanoes are from GNS geologic map (Forsyth et al., 2008). B) New Zealand topographic and bathymetric map from the NZ Petroleum Exploration 2018 datapack. Black square in B) shows the location of the detailed map in A. 93
Figure 35: 2D regional strike/oblique seismic line showing the stratigraphic architecture, the main geotectonic events in the northern part of the Canterbury Basin, and the occurrence of the MVF (red). The Resolution-1 and Clipper-1 wells were used to tie the seismic data to chronostratigraphic surfaces that represent important changes during the basin evolution. Cretaceous-Paleogene surfaces and rift faults courtesy of Andrea Barrier, UC PhD candidate in structural geology. 94
Figure 36: Local chronostratigraphic chart of the study area. We subdivide Tokama Siltstone within the vicinity of MVF into 4 depositional units according to their depositional setting (in blue). Two main volcanic events within northern Canterbury basin during the Miocene emplaced MVF and Banks Peninsula. The main magmatic events are each represented by pre, syn and post-magmatic sequences, and are shown in the right part of the figure. Stratigraphic ages follow the International Chronostratigraphic Chart 2014 and New Zealand Geological Time Scale 2015 (Raine et al., 2015). 96
Figure 37: Seismic morphometric measurements and example of morphology classification of MVF volcanoes. A) Shows a positive symmetric cone (crater-type). B) Shows a compound morphology. Bottom part (nf01 in light red) has a negative funnel-like shape (crater-type) and its lateral association. Upper part (pc13 in light blue) shows a positive asymmetric cone shape (crater-type) and its lateral association. Note that pc13 have one of the flanks eroded by canyons. TWT in the seismic lines are convert to distance in metres using the method in section 4.4.3.1. 101
Figure 38: 2D dip section (line CB-82-06) showing evidence of differential degradation related with the late Miocene (lM) unconformity and of differential compaction (burial doming and “seagull wings”). PrErS is the pre-eruptive surface, while PoErS is the post-eruptive surface. PoDgS is the post-gradational surface. 105
Figure 39: A) Isochron map between pre-eruptive (PrErS) and post-eruptive surfaces (PoErS) of MVF showing the location of MVF cone-type volcanoes. Note that the surfaces thin and amalgamate with increasing distance from individual or clusters of volcanoes, defining the seismic detectable boundaries of MVF. B) Uninterpreted seismic section across volcano pc-14. C) Interpretation of seismic section in B) showing the PrErS and PoErS surfaces and the associated isochron. Diatremes were excluded during mapping of the PrErS

surface due to computer limitations, as they would have shown a false positive structure in the isochron map. 109
Figure 40: Macroscopic and microscopic photographs of the monzogabbro recovered from a depth of -1962.25 m in the Resolution-1 well. A) Photograph of a medium-grained leucocratic intrusive rock composed of plagioclase (pl) and pyroxene (aug). Zeolite analcite (zeo) occurs filling cavities. Chlorite (chl) occurs as an alteration of primary minerals. Thin-section photographs in plain (B and D) and cross-polarized light (C and E) showing ophitic texture of plagioclase (pl) and augite (aug), olivine (ol) crystals partially replaced by iddingsite (id), and clinopyroxenes (aug) replaced by biotite (bi) and chlorite (chl), which suggests magma crystallization at shallow depths and H_2O interaction. Accessory minerals are: opaques (op) and apatite (ap). Photographs and petrographic identifications were made in conjunction with Marcos Rossetti (UC PhD candidate in physical volcanology). 111
Figure 41: Macroscopic and microscopic photographs of the monzogabbro recovered at -1962.25 m in the well Resolution-1. Thin-section in cross-polarized light (A), plain light (B) and macroscopic polished section (C) showing augite (aug) and plagioclase (pl) with ophitic texture. Thin section in cross-polarized light (D) and natural light (E) showing zeolite (zeo) filling interstitial space and plagioclase altered to clays. Macroscopic photograph of Resolution-1 core at the depth of 1663 m (C) showing augite, plagioclase, acicular crystals of zeolite and miarolitic cavities (mia). Photographs and petrographic identifications were made in conjunction with Marcos Rossetti (UC PhD candidate in physical volcanology). 112
Figure 42: Composite well data of the Oligocene-Miocene interval of Resolution-1 well showing the lithologies, ages, paleo-environments, stratigraphy and wire-logs. Symbol bs@ is the given biostratigraphic age in Schiøler et al. (2011). Blue dashed lines show the bathymetry trend. Numbers in black ellipses are ages according to the 2015 NZ Geologic Time Scale (Raine et al., 2015). Numbers in red ellipses are estimated ages of the MVF based on the integration of these dataset. 114
Figure 43: A) Macroscopic photograph of an unwashed cuttings sample of a massive siltstone containing benthonic foraminifera recovered from the interval 1120 to 1130 m from the Resolution-1 well (middle Tokama). B) Microscope photograph in crossed-polarized light of unwashed cutting samples of volcanic clasts and a gastropod in a muddy matrix from the interval of 1130 to 1140 m in Resolution-1. 116
Figure 44: Macroscopic photographs of unwashed cutting samples from the interval of -1130 to -1140 m in Resolution-1. A) Volcanic fragments and bioclasts immersed in a muddy matrix. Black fragments are mainly altered pyroxenes (B). 118
Figure 45: Macroscopic photographs of plagioclase (pl) and pyroxene (py) phenocrysts in microporphyritic texture (A), and a broken plagioclase fragment (B). C to F show photographs in cross-polarized thin-section of rocks with microporphyritic and vitrophyric textures. Note that phenocrysts with broken angular borders (C and F) are associated with peloidal (pel) and palagonite (pal) clasts. 120
Figure 46: Macroscopic images of volcanic fragments submerged in water (A) during the washing process of samples from the interval of -1130 to -1140 m in Resolution-1. These rocks show altered microporphyritic texture with blocky equant and jigsaw-fit texture. Microscope (B and C) and SEM (D) images of spall shards with cuneiform (cun), and blocky (blo) shapes in jigsaw-fit (jig) texture. Microscope (E) and SEM (F) images of loose glassy shards with blocky and splintery (spl) shapes in vitriclastic and jigsaw-fit jig texture. 121

Figure 47: A and B) Macroscopic images of loose shards with cuspate, cuneiform, blocky (blo) and platy (pla) shapes, and common relic bubble walls (bw). C) Hypocrystalline fragment containing concentric spherules (sph) and vesicles (ves). D) Photograph of thin-sections in plain light showing palagonite (pal) and glassy shards with, cuspate (cus), platy (pla) and pumice (pum) shapes, and relics of bubble walls (bw). E) Macroscopic image of microcrystalline blocky equant fragment with some micro-vesicles. F) Macroscopic photograph of loose and poorly indurated spalls of shards with common vesicles. 122
Figure 48: A and B) Thin-sections in plain light showing fragments of very-fine grained rocks with a pervasive alteration to palagonite (pal), shards with cuspate (cus) and platy (pla) shapes, and fragments of broken crystals (bc). Macroscopic images of limestone (C) and sandstone lithics (D), which may correspond to rocks of Amuri and Omihi limestones, and Charteris Bay sandstone. 123
Figure 49: Thin-sections in plain (A and B) and cross-polarized (C) light showing spherules with and without an inner core enveloped in a palagonite (pal) film. Macroscopic (D) and SEM (E) examples of poorly indurated highly porous glassy aggregate are also displayed. 124
Figure 50: Macroscopic (A) and plain light microscopic (B) examples of well indurated aggregate of cored spherules (sph), associated with vesicles (ves) and intense palagonite alteration. Plain light (B), cross-polarized and SEM (E and F) images of spherule with a glassy devitrified (palagonite) inner core, enveloped in a single concentric outer rim associated with an array of acicular crystals in radial pattern and pseudo-perlitic (per) cracks. ... 125
Figure 51: Interpreted 2D dip seismic section at the Resolution-1 well (thick dashed line). Saucer-shaped sills (a) were intruded into Cretaceous sedimentary strata during the middle Miocene (ca 12.5 Ma K-Ar) and caused doming of the overlying strata. The doming consequentially changed the sea-floor topography and promoted deposition as channelized systems (c) next to the dome structures. The syn-eruptive interval (between PrErS and PoErS) is defined by the occurrence of volcanic material (b) interbedded with sedimentary rocks of the Tokama Siltstone of Waiauan age (ca 12.7 to 11 Ma) and seismic stratigraphic analysis. At the border of the domed strata, disrupted reflectors and faults suggest magma and hydrothermal fluid pathways that fed eruptions onto the middle Miocene paleo-seafloor. All seismic anomalies interpreted to correspond to buried volcanoes of the MVF occur between PrErS and PoErS surfaces, which merge to form a single reflector in all directions away from the MVF. Seismic anomalies interpreted to correspond to intrusions are located below PrErS. The available evidence together with geochemical and petrographic analysis demonstrate that the intrusive and extrusive rocks penetrated by the Resolution-1 well have a co-genetic relationship, which together with estimations of sedimentation rate in the area allow us to propose that the MVF was formed from ca 12.7 to 11.5 Ma. Cretaceous to Paleogene horizons courtesy of Andrea Barrier. 127
Figure 52: Igneous seismic facies in the study area. A) Regional 2D strike/oblique seismic section showing the lower (PrErS) and upper (PoErS) stratigraphic limits of the MVF (see chapter 4.5.5 for details). B and C show images interpreted as volcanoes erupted in the MVF, while figures D, E and F show images of interpreted intrusions. 131
Figure 53: Pie diagrams showing the qualitative-quantitative morphometric results from MVF volcanoes. See text for details. 133
Figure 54: Pie diagrams showing the depth of diatreme craters (A), and number of volcanoes interpreted to be underlain by large (> 2 km) and shallow (ca 1 km) intrusions (B). 134

Figure 55: Chronostratigraphic maps of the northern Canterbury Basin. The MVF erupted entirely in a lower bathyal setting (D and C), and was buried in a lower to uppermost bathyal setting (B) due to rapid SE progradation in the northern Canterbury Basin. During the Neogene, the physiography of the basin evolved from a ramp to a basin-slope morphology (C to A). Outcropping paleo-environments compiled from Field et al. (1989). During mapping of the PrErS chronostratigraphic horizon, we corrected the effects of local deformation underneath eruptive vents and near shallow intrusions. 135

Figure 56: Composite paleo-physiographic and paleo-environmental map of the study area from ca 12.7 to 11 Ma. Abbreviations are plotted at the position of MVF volcanoes and correspond to their morphology. Pc's are positive cones, pt's are positive trapezium, pm's are positive mounds, nf's are negative funnel-like structures and nb's are negative basin-like seismic anomalies. Red dashed lines show the approximate bathymetry at the onset of eruptions in the MVF. Blue dashed line shows the position of the shelf-break at 11 Ma. Note that all pm's and pt's are located within relatively shallow waters, proximal the 11 Ma shelf-break (except pm03 which was eroded by canyons). To construct this map, we combine information from the pre-, syn-, and post-eruptive stages of MVF in a single map. First, we produce an isochron map of the syn-eruptive stage of MVF (background rainbow colours), which is approximately equivalent to the interval (in TWT) between PrErS (12.7 Ma) and PoErS (11.5 Ma). This isochron map was produced by applying a mathematical algorithm embedded in the Kingdom Software, which subtracts the time of the PoErS from time of the PrErS (Figure 39). The isochron background map shows the location of each volcano in the MVF. We opt for the non-reconstructed forms of the volcanoes (PoErS using HaBs volcanic heights) for two reasons: first, computational limitation to map a theoretical reconstructed morphology in the software, which could create several interpolation errors and artefacts. Second, because the degraded morphology of the volcanoes is related to the position of the 11 Ma proto shelf-break, we decided to show the effects of erosion in the composite map. To estimate the 12.7 Ma (onset of volcanism) bathymetric contours of the study area, we first integrate biostratigraphic data at the location of the Resolution-1 well, with the local chronostratigraphic map of 12.5 Ma (Figure 55D). The distal contour in MVF is highlighted by the red dashed line on the right hand corner of the map, which corresponds to water depths ranging from 1000 to 1500 m. The proximal bathymetric contour (red dashed lines showing bathymetry ranging from 500 to 750 m deep) was estimated by calculating the slope angle (ca 1.5 degree) of the pre-eruptive regional ramp from seismic data, and in relation to the distance from neritic rocks of similar age outcropping in the Canterbury plains (Figure 55D), which was compiled from paleogeographic maps presented in Field et al. (1989). The position of the 11 Ma shelf-break (blue dashed line), was mapped from 2D seismic lines in the study area, and adjusted using the contours of the chronostratigraphic map of 11 Ma as required (Figure 55B). Note that volcanoes distal the 11 Ma proto-shelf break show a sharp increase in slope towards their summit, while volcanoes located proximal to this line show shallower slopes. Compare the contours that represent the morphology of pt03 vs. pc 17 in the right-hand corner of the map. 136

Figure 57: Isochron maps of the northern Canterbury Basin. By 11 Ma and younger, most volcanoes were buried by the slope progradation associated with increasing sediment supply from the NW (A), simultaneously with the installation of the Banks Peninsula. Note in (B) that a thicker pile of sediments were deposited at the location of the edifices of the MVF during their erosion and partial burial. 137

Figure 58: 2D regional seismic lines showing the location of the MVF in relation to the regional chronostratigraphic horizons mapped in the study area from the Cretaceous to Recent, and the main physiography of the basin. Neogene to Recent shelf-break migration is indicated by arrows that show the location of the shelf-break at each time, with the arrowhead pointing in the direction of migration. Cretaceous-Paleogene horizons were supplied by Andrea Barrier. 139
Figure 59: Morphometric analysis of MVF volcanoes relative to their post-eruptive paleo-environmental location. Blue bars show the height of volcanoes after burial (as they were measured in seismic lines). Orange bars show decompacted height values. Grey bars show reconstructed original height of the MVF volcanoes. Red dashed line shows the limit between preservation and degradation of the edifices. Compare pm03 vs. pc04 for example. Red arrow points to a volcano with evidence of canyon erosion. 141
Figure 60: Top images show 2D seismic sections of crater (left) and cone (right) type dominated volcanoes. In the seismic sections, crater-type is characterised by deep funnel and basin-like excavations into the PrErS horizon, while cone-type is characterised by upwards deflection of the PoErS above the PrErS and reflectors that pile-up above PrErS. Bottom images correspond to interpreted subaerial analogues. The crater-type is a classic maar-diatreme volcano (McDougal Crater, in USA), while the cone-type is a well-known scoria cone (SP Crater, USA). Despite morphometric differences, tuff cones and scoria cones share many morphologic similarities, such as the presence of a crater zone with layers inward dipping, and peripheral flanks with layers outward dipping. Note the geometric similarity between the volcanoes in seismic and analogue images. Complete interpretation of the different types of volcanoes is presented in Chapter 5. 143
Figure 61: A and B show attribute analysis of pt02 and pc06 volcanoes and their seismic morphology. The curvature (B) attribute suggests that the internal and external parts of the volcanoes (black) are composed by rocks with similar acoustic properties, which are interpreted to represent volcaniclastic rocks eroded from the pt02 and deposited next to its flanks. C shows the morphological contrast between pt03 and pc17. Note that in both cases, extinct volcanic edifices located at shallow water (pt02 and pt03) show flattened tops in relation to the position of the 11 Ma unconformity, while volcanoes located at deeper water (pc06 and pc17) do not show a morphological relationship with this unconformity. This suggests that distal volcanoes were below see-level and were well preserved. Blue dashed lines show the interpreted position of the sea-level at ca 11 Ma, based on the flattened top of proximal volcanoes. 145
Figure 62: Morphometric analysis of crater-type MVF volcanoes in relation to the lM unconformity. Data have been organised by the position of volcanoes relative to the 11 Ma shoreline (proximal and distal). They were then organized by the estimated degree of degradation from the highest to smallest values, and finally by oHm from smallest to highest values. The yellow fill represents volcanoes with a moderate to high degree of degradation. At the left-hand side of the graph, all volcanoes are pc's of < 200 m oHm and show little degradation. All pt's and pm's are located on the shelf at 11 Ma and have oHm > 200 m. We interpret that at ca 11 Ma, these volcanoes were volcanic islands and experienced wave erosion. All volcanoes located on the slope do not show significant evidence of degradation, with the exception of pm03 which was eroded by canyons. The H:W ratio was multiplied by 500 for visualisation proposes. Note that the estimated degradation (grey) and the H:W (yellow) curves are inversely proportional, which indicates that a higher

degree of degradation produced volcanoes with smaller H:W ratios, due to their loss in height (H) and gain in diameter (W). 146
Figure 63: Conceptual representation of the magmatic sequences and stages (left), predominant geological processes, stratigraphic surfaces (centre), and boundaries of MVF and MFS (right). 161
Figure 64: Methods used for the identification and interpretation of volcanic and sedimentary architectural elements in the MVS. The input 2D seismic reflection are described and compared with analogues. Elements sampled by drillholes can provide an accurate geological characterisation of the anomaly, while interpretation without physical confirmation remains only hypothetical. 164
Figure 65: Schematic representation of the stratigraphic sequences and surfaces, magmatic stages, architectural elements, and predominant processes associated with MVS. Numbers in circles represent the location of the architectural elements indicated in the key. Numbers in squares indicate the predominant processes in the key. The symbols in the right hand corner illustrate the database used for interpretations. Conduit zones and dikes have lateral thicknesses exaggerated for visualization proposes. In this framework, PoDgS and PoBuS are related to the volcano in the centre of the figure, and to the 11 Ma unconformity described in chapter 4. Lateral variation of the lithostratigraphic units are not shown in the image. The pre-eruptive dome is a regional feature shown in Figure 68. 166
Figure 66: Photographs of potential analogue dikes outcropping in the Canterbury Basin. Intrusions have different patterns and products according to their depth of emplacement. At deeper levels, dikes show sharp contacts and little branching into enclosing sediments (D), while at shallower levels, they show magma finger terminations and several thin apophysis with peperitic borders. Thirty meters above the shallower intrusions, calcite veins (C) suggest migration of fluids up-sequence. 169
Figure 67: 2D seismic images (A and B) of disrupted blocks, and a possible outcrop scale analogue of this architectural element in Banks Peninsula formed by host pyroclastic deposits cross-cut by multiple dike intrusions. 170
Figure 68: Top early Miocene isochron map of the northern part of Canterbury Basin. Red contours correspond to higher topography. The area inside the white dashed line shows semi-regional uplift with maximum vertical relief of ca 100 meters, coincident with the location of large sill and dike and sill swarms of the MVS plumbing system. This surface was chosen to demonstrate uplift of the sequence that predate the MVF, because in contrast to the PrErS, the top early Miocene surface is less disrupted by shallow intrusions, and reflectors can be tracked with more confidence at the sub-volcanic level. 171
Figure 69: 2D seismic reflection lines showing the locations and geometries of the five plumbing-types observed in the MVS. Images A, B and C for the same line ANZ-001 which display the seismic attributes pseudo-relief (A), amplitude (B) and envelope (C). Note the systematic vertical distribution from type-1 (deeper) to type-4 (shallower) and their relationship. Type-5 differs from the other types in that it represents a deep source-to-surface feeder systems. 173
Figure 70: 2D seismic reflection images and characterisation of the five plumbing-types from the MVS. Seismic attributes of the images are: Type-1= amplitude, Type-2= pseudo-relief, Type-3= envelope, Type-4= amplitude and Type-5= pseudo-relief. 174

Figure 71: Images on the left hand side show schematic cross-sections through a maar-diatreme and a tuff ring, and their typical volcano-sedimentary processes, deposits and morphology (from Kereszturi and Németh, 2013). On the right-hand side are shown interpreted 2D seismic lines of the MVS crater-type volcanoes, and their main large scale architecture. 177
Figure 72: Uninterpreted (above) and interpreted (below) 2D seismic line showing the main architectural elements related to crater-type volcanoes in the MVS. Numbers in red circles are syn-intrusive architectural elements, in green syn-eruptive, and in yellow post-magmatic architectural elements. We observe that crater-type volcanoes present two distinctive morphologies related to at least two different eruptive-styles: lower part (in red) shows funnel-like excavation into PrErS and lateral high amplitude parallel reflectors, which we interpret to represent a submarine equivalent of a maar-diatreme volcano, and may be related to large submarine phreatomagmatic eruptions. Upper part (in blue) shows cone-like morphology and lateral semi-continuous reflectors in wedge-shape, which we interpreted as intra-crater volcanoes formed by late eruptive events, and associated material that overspills from the rim of the underlying maar-diatreme structure. WD is the interpreted approximate water-depth at the time of the formation of the volcanos. .. 181
Figure 73: Three-dimensional representation of the main syn-eruptive architectural elements of crater-type volcanos of the MFV and their average size. Each of these large-scale elements can be composed by sets of smaller-scale elements formed by the interplay of volcanism, external environments, and concomitant sedimentation. 183
Figure 74: Images on the left-hand side show schematic cross-sections through tuff and scoria cones showing their typical volcano-sedimentary processes, deposits and morphology (from Kereszturi and Németh, 2013). Seismic images on the right-hand side show interpreted 2D lines of MVS crater-type volcanoes, and their large-scale architecture. The seismic section in the lower right-hand corner shows a buried submarine Eocene volcano 40 km offshore of Oamaru (Barrier et al., 2017), which we use as analogue for our interpretations..... 184
Figure 75: Uninterpreted (left) and interpreted (right) 2D seismic line showing the main architectural elements related to crater-type in the MVS. Numbers in red circles are syn-intrusive architectural elements, in green syn-eruptive, and in yellow post-magmatic architectural elements. We observe that crater-type volcanoes are mainly composed of a basal cone, a central crater, a tephra flank and a cone apron. These volcano-types produce upward convex morphologies between the PrErS and PoErS horizons, which we have interpreted to represent the submarine equivalents of tuff cones. Note that the central-crater show inward dipping reflectors while the tephra flank shows outward-dipping reflectors and minor excavation into the PrErS horizon..... 186
Figure 76: Photographs of potential analogue for MVS syn-eruptive architectural elements outcropping in Kakanui South Head submarine volcanic edifice, near Oamaru, South Island of New Zealand. A) Map showing the location of the vent and flanks of the cone. B) Massive, chaotic, to amalgamated intra-crater lapilli-tuff to tuff-breccia interpreted to be deposited by tephra jets, ballistic and debris flow of material remobilized into the central crater (Corcoran and Moore, 2009; Moorhouse; 2015). C) Angular contact between amalgamated beds inward dipping towards the central crater, and tabular layers of tephra outward-dipping towards the flanks of the edifice. D) Thin-bedded, tabular, semi-circular layers of lapilli-tuff formed by low-volume tephra

jetting and eruption-fed density currents deposited at the flanks of the volcanic edifice (Corcoran and Moore, 2009; Kaulfuss et al., 2012). 189
Figure 77: Three-dimensional representation of the main syn-eruptive architectural elements of crater-type volcanoes of the MFV and their average size. Each of these large scale elements can contain sets of smaller-scale architectural elements formed by the interplay of volcanism and concomitant sedimentation. 191
Figure 78: Uninterpreted (above) and interpreted (below) 2D seismic line showing the main architectural elements related to cone-type volcanoes in the MVS volcanos. Numbers in red dots are syn-intrusive architectural elements, in green syn-eruptive, and in yellow post-magmatic architectural elements. Based on seismic stratigraphic interpretation, the lower sequence of volcaniclastics recovered in Resolution-1 was probably sourced from volcanoes NW or W of the well (likely nf02 and nf03). Tuffs from -1103 to -1110 m depth were likely vented from pc-14. WD is the interpreted approximate water depth at the time of the formation of these volcanos. 194
Figure 79: Seismic attribute analysis of pt02 and pc06 volcanoes. Note that the attributes show similarity between the internal and external parts of pt02, which we interpreted as a plume of sediments deposited after erosion of extinct volcanic islands during the degradational stage. 196
Figure 80: Schematic representation of the possible petroleum plays associated with buried monogenetic volcanic systems, based on the observation of the MVS architectural elements. Distinctive sets of architectural elements can create prospective plays according to the magmatic stages of emplacement, construction, degradation, and burial of the volcanoes (following volcano-stratigraphic models proposed in Bischoff et al. (2017) and chapter 5 of this thesis). Sandstones below the PrErS (yellow) and limestones above the PoErS (blue) were added to this model to illustrate possible plays formed by the interaction of these lithologies with volcanism. 206
Figure 81: Schematic representation of the possible intrusion-related hydrothermal systems associated with buried monogenetic volcanic systems, based on the observation of MVS architectural elements. Distinctive sets of architectural elements can create prospective plays according to the magmatic stages of emplacement, construction, degradation and burial of the volcanoes. Sandstones below the PrErS (yellow) were added to this model to illustrate possible plays formed by the interaction of this lithology with volcanism. 212
Figure 82: Graphs showing the population of HaBm (Height after burial in meters) for MVF volcanoes using the Relative Impedance Index method (RII) to estimate the acoustic velocities of buried volcanoes. A) Black lines show expected bounds in HaBm calculated from maximum and minimum velocities of tuffaceous rocks compiled from laboratory and drill-hole measurements elsewhere. Blue lines define the bounds in HaBm using estimations of velocities from the RII method. Note that blue lines (RII approach) show a property of convergence between maximum and minimum ranges with increasing calculated height, while black lines show divergence. 223
Figure 83: Reconstructed morphology of volcanoes imaged by 2D seismic lines in Maah 225
Figure 84: Reconstructed morphology of volcanoes imaged by 2D seismic lines in Maahunui Volcanic Field and Kora Volcano. Seismic lines correspond to the height of the “summit” of the volcanoes. 225
Figure 84: Reconstructed morphology of volcanoes imaged by 2D seismic lines in Maahunui Volcanic Field and Kora Volcano. Seismic lines correspond to the height of the “summit” of the volcanoes. 226

List of Tables

Table 1: Areas studied during this PhD research project. 27
Table 2: Structure of this PhD thesis. 28
Table 3: Attributes and parameters used on the seismic morphological Characterisation and reconstruction of MVF volcanoes. 100
Table 4: Equations used to calculate seismic morphometric parameters of the MVF volcanoes. 107
Table 5: Main stratigraphic and paleo-environmental characteristics of the Tokama Siltstone depositional units. Highlighted middle Tokama unit (red) is interbedded with the volcaniclastic rocks described in the section 4.5.1.5. 117
Table 6: Main stratigraphic and paleo-environmental characteristics of the MVF area. Interval highlighted in red corresponds to the active eruptive time in the volcanic field. 140
Table 7: Main characteristics of the stratigraphic surfaces that bound distinctive magmatic sequences and stages in the MVS. 163
Table 8: Main characteristics of the syn-intrusive architectural elements in the MVS. 167
Table 9: Main characteristics of the architectural elements of the crater-type dominate volcanoes formed during the constructional magmatic stage in the MVS. 178
Table 10: Main characteristics of the architectural elements of the cone-type dominate volcanoes formed during the constructional magmatic stage in the MVS. 185

Chapter 1

Introduction

1 Introduction

1.1 Research Rationale

In a world with increasing demand for energy, this PhD research aims to provide insights for both petroleum and geothermal industries. This study characterises the architecture of volcanic systems buried in sedimentary basins, by identifying the geological situations that favour the occurrence of valuable geoenergy resources, such as hydrocarbons and geothermal energy. A vast range of petroleum plays can form in association with buried volcanic systems, with some examples of world-class hydrocarbon fields estimated to contain > 1Gbbl currently in production (e.g. Mohriak, 2008; Carlotto et al., 2017). Important energy resources can also occur in active volcanic systems emplaced in sedimentary basins, because, for example, the interaction of magma with the host sedimentary strata can form prolific intrusion-related hydrothermal systems (e.g. Stimac et al., 2015; Montanari et al., 2017). However, in certain conditions, volcanism can be detrimental for geoenergy exploitation by degrading the quality of reservoirs (e.g. Schutter, 2003), or producing large amounts of greenhouse gases such as CO_2, CH_4 and H_2S (e.g. Svensen et al., 2017). Today, it is widely accepted that the interaction between magmatism and sedimentation can have both positive and negative impacts on geoenergy resources (e.g. Wight and Hardian, 1982; Planke et al., 1999; Schutter, 2003; Rohrman, 2007; Holford et al., 2012; Rateau et al., 2013; Bischoff et al., 2017). Despite the increase in knowledge of these volcanic systems (and their associated geoenergy prospects) in the last few decades, the conditions that determine their success or failure as economic resources remains poorly understood.

In this PhD thesis, I aim to demonstrate that an understanding of the complete architecture of buried volcanic systems, from emplacement to burial, is necessary for de-risking the exploration of oil and gas in sedimentary basins affected by magmatism. Studies of these "fossil" volcanic systems can provide insights into the geothermal exploration and production of sedimentary basins that are experiencing active volcanism today. Oil and gas resources found in buried volcanic systems can add substantial capital and knowledge to promote a viable business transition to renewable sources or geoenergy. In the upcoming years, the crossover from oil and gas to geothermal energy may play an important role in the transition towards sustainable use of these subsurface geoenergy resources.

1.2 Research Hypothesis

Petroleum and geothermal systems share many similarities. Both systems rely on the presence of certain fundamental elements and processes to form prospects suitable for exploration and production of geoenergy. Since the 1990's, the concept of a *petroleum system* from Magoon and Dow (1994) make an important impact on the way that the industry explores and exploits oil and gas. The petroleum system is a unifying concept that evaluates the presence of fundamental elements (source, reservoir, seal, and trap) and essential processes (generation, migration, and accumulation) that are necessary for an oil and gas field to exist. Similarly, key elements and conditions are also necessary for the formation of hydrothermal systems including: a source of heat (typically magma or hot igneous rocks), a reservoir body (which can be fractured or porous), water (vapour or liquid), and a permeable network to transfer fluids and heat through the system (e.g. Goff and Janik, 1999; Stimac et al., 2015).

In sedimentary geology, the concept of *architectural elements* was introduced to describe the fundamental building blocks of sedimentary systems (Allen, 1983; Miall, 1985). After the development of this concept, architectural element analysis has been widely applied to further the understanding of the fundamental processes that control the formation of petroleum systems in sedimentary settings. I hypothesise that volcanic systems, such as *sensu stricto* sedimentary systems, are comprised of sets of igneous and sedimentary architectural elements with petrophysical characteristics that can provide storage, and can conduct, or can entrap fluids, such as water, oil, and gas.

This PhD thesis proposes that "volcanic" architectural elements occur in a predictable stratigraphic order, and that they are controlled by the interplay of igneous and sedimentary processes, such as magmatic intrusions, eruptions, degradation, and burial of the volcanic structures within the sedimentary strata. Here, I propose that the analysis of architectural elements can be applied to reduce exploratory risks, and increase the likelihood of finding geoenergy resources associated with buried and active volcanic systems.

1.3 Research Objectives

The main aim of this PhD thesis is to construct volcano-sedimentary frameworks that helps explain the complete architecture of volcanic systems buried in sedimentary basins. These frameworks will identify how the fundamental architectural elements vary in time and space

within the buried volcanic systems. The volcano-stratigraphic frameworks aim to illustrate possible combinations of architectural elements that can favour the formation of petroleum accumulations and geothermal fields, in association with monogenetic and polygenetic volcanism in sedimentary basins. In addition, this work aims to encourage an effective transfer of knowledge between the well-established oil and gas industry and the geothermal sector. The work programme includes development of techniques that can be applied to evaluate the risks and uncertainties of subsurface exploration and production of geoenergy in volcanic areas. However, a large number of variables control the fluid-flow properties of volcanic systems and the formation of petroleum occurrences, such as the diverse morphology of these systems (e.g. Silva and Lindsay, 2015), complex facies architecture (e.g. Pittari et al., 2008; Jerram et al., 2009) and rapid changes in petrophysical properties of volcanic rocks (e.g. Heap and Kennedy, 2016). Therefore, the application of concepts introduced in this thesis will likely need to be considered on a case-by-case basis. In this thesis, I briefly evaluate how the interaction of magmatism and sedimentation controls the architecture of buried volcanic systems and their potential to contain geoenergy resources. Further research will be required to understand these systems in suffice detail to document their full diversity.

1.4 Studied Areas

To select of suitable areas for this study, the following factors were considered: i) geological situation (i.e. volcanic systems buried in sedimentary basins), ii) data availability (i.e. seismic reflection, wells, outcrops), and iii) access to outcrops analogues for the buried systems. To observe the way the architectural elements vary systematically in monogenetic versus polygenetic buried volcanic systems, and to understand their impact on hydrocarbons and geothermal system, we combine information from two detailed case-study areas located in Taranaki and Canterbury sedimentary basins, New Zealand. These case-study areas were complemented with insights from another nine support areas located in onshore and offshore New Zealand sedimentary basins (Table 1), and with tens of worldwide analogues described in the literature.

Table 1: Areas studied during this PhD research project.

Status	Volcanic Reference	Location	Age	Volcanic System	Dataset used
Detailed case-study	Kora Volcano	Taranaki Basin	Miocene	Polygenetic submarine composite volcano	Wells, 2D and 3D seismic volumes
Detailed case-study	Maahunui Volcanic Field	Canterbury Basin	Middle Miocene	Monogenetic submarine volcanic field	Wells and 2D seismic
Support	Albacore volcano (informal name)	Taranaki Basin	Miocene	Polygenetic submarine composite volcano	Wells, 2D and 3D seismic
Support	Nimitz volcanoes (informal name)	Taranaki Basin	Miocene	Submarine polygenetic volcanic complex	Wells, 2D and 3D seismic
Support	Parihaka Volcano (informal name)	Taranaki Basin	Miocene	Polygenetic submarine composite volcano	Wells, 2D and 3D seismic
Support	Romney and Vulcan volcanoes (informal name)	Taranaki Basin	Late Cretaceous	Polygenetic subaerial/paralic volcanic complex	Wells, 2D and 3D seismic
Support	Barque volcanoes (informal name)	Canterbury Basin	Late Cretaceous/ Paleocene	Polygenetic subaerial/paralic volcanic complex	2D and 3D seismic
Support	Waiareka and Deborah Volcanic Field	Canterbury Basin	Eocene-Oligocene	Monogenetic submarine volcanic field	Outcrops, wells and 2D seismic
Support	Banks Peninsula Volcanic Complex	Canterbury Basin	Late Miocene	Polygenetic subaerial/paralic volcanic complex	Outcrops, wells and seismic
Support	Waka intrusions and vents (informal name)	Canterbury Basin	Miocene	Hypabyssal intrusions and hydrothermal vents	2D and 3D seismic
Support	Tongariro and Ruapehu volcanoes	Central North Island	Pleistocene to Recent	Polygenetic subaerial composite volcanoes	Outcrops

1.5 Thesis Structure

This PhD research is presented in seven chapters, four of which (chapters 3, 4, 5 and 6) have been, or will be, published as separate papers. The structure of the thesis is subdivided as presented in Table 2. Chapters 3, 4, 5 and 6 were prepared as manuscripts for journal publication, contain an abstract and introduction and, as such, are *stand alone* in the sense that each can be

read and understood independently, but follow a logical sequence of related themes. These chapters are preceded by an introduction to the overall topic and a brief literature review to explain the main concepts and techniques applied in this study. Preparing the chapters as a series of papers results in some duplication within the thesis, especially at the beginning of each chapter. I have reduced this repetition by incorporating the geological settings for the Kora and Maahunui volcanic systems in chapters 3 and 4, respectively. The research described in this thesis has been conducted by me (Alan Bischoff), however, many others have contributed to refining the ideas and their presentation. The chapters are all written in the first person plural ("we"), as is common practice for multi-authored publications. In particular, Andy Nicol and Mac Beggs contributed insights into the geological context and petroleum potential of Kora volcano (Chapter 3), and Ben Kennedy, Andrea Barrier, Darren Gravely, Marcos Rossetti and Hanfei Wang to the Maahunui studies presented in Chapters 4, 5. And 6. I am first author in the Kora publication (Bischoff et al., 2017) and anticipate also being first-author on all remaining two publications.

Table 2: Structure of this PhD thesis.

Chapter	Title	Comments
Chapter 1	Introduction	Thesis outline and contents
Chapter 2	Concept and Techniques	As used for the entire thesis
Chapter 3	Stratigraphy of Architectural Elements in a Buried Polygenetic Volcanic System and Implications for Hydrocarbon Exploration	Kora Volcanic System, Taranaki Basin
Chapter 4	Seismic Reflection and Petrographic Characterisation of a Buried Monogenetic Volcanic Field	Maahunui Volcanic System, Canterbury Basin
Chapter 5	Stratigraphy of Architectural Elements in a Buried Monogenetic Volcanic System	Maahunui Volcanic System, Canterbury Basin
Chapter 6	Models for Exploration of Geoenergy Resources in Monogenetic Volcanic Fields within Sedimentary Basins	Generic and based on Maahunui Volcanic System
Chapter 7	Conclusions and further work	Conclusions from this thesis and further work

Chapters 1 and 2 setup the thesis and provide the technical background necessary to analyse and interpret the main body of the research presented in chapters 3, 4, 5 and 6. As a product of this PhD research, we expect three publications in high impact scientific journals:

Publication 1 (Chapter 3): Stratigraphy of Architectural Elements in a Buried Volcanic System and Implications for Hydrocarbon Exploration

In this first paper we reveal the architecture of Kora Volcanic System (KVS), drawing insights for hydrocarbon exploration. The purpose of this paper is to show the complete architecture of a buried composite submarine volcanic system. Kora is a Miocene volcano active for ca 10 Ma and currently buried by more than 1000 m of sedimentary strata offshore Taranaki Basin, New Zealand. A sub-commercial hydrocarbon field was discovered within volcanogenic deposits on Kora Volcano in the 1980's. This manuscript was submitted to AAPG Interpretation Journal on the 3rd of November, 2016, was accepted on the 24th of March, 2017, and published in the special edition Subsurface Expression of Igneous Systems and Their Impacts on Petroleum Systems on the 19th of June, 2017. The full publication is available online on https://doi.org/10.1190/INT-2016-0201.1.

Publication 2 (Chapter 4): Seismic Reflection and Petrographic Characterisation of a Buried Monogenetic Volcanic Field

The second manuscript will present the analysis and conclusions from Maahunui Volcanic Field (MVF), a previously uncharacterised middle Miocene monogenetic volcanic field, currently buried by ca 1000 m of sedimentary strata in the offshore Canterbury Basin. In this manuscript, we will present morphological reconstruction of 31 submarine equivalents of maar-diatreme and tuff cone volcanoes using 2D seismic reflection data. In this paper we will show the lithological evidence that supports an igneous origin for the features recognized in seismic, and the interpretations about their eruptive-styles that had occurred in a bathyal setting, with water depths of ca 1000 m.

Publication 3 (Chapter 5 and 6)**:** Stratigraphy of Architectural Elements in a Buried Monogenetic Volcanic System and Implication on Geoenergy Exploration

In this manuscript we will present the complete architecture of Maahunui Volcanic System (MVS), together with a prediction of the geologic conditions that can favour the occurrence of geoenergy resources in monogenetic submarine volcanic fields. In this manuscript, we will show the distribution of igneous and sedimentary architectural elements that result from the

emplacement, submarine eruptions, and burial of a monogenetic volcanic field in a sedimentary basin. The two Maahunui papers are expected to be submitted and published in 2019.

1.6 References

Allen, J. R. L., 1983, Studies in Fluviatile Sedimentation: Bars, Bar-Complexes and Sandstone Sheets (Low-Sinuosity Braided Streams) in the Brownstones (L. Devonian), Welsh Borders: Sedimentary Geology, 33 (4): 237–93. doi:10.1016/0037-0738(83)90076-3.

Bischoff, A. P., A. Nicol, M. Beggs., 2017, Stratigraphy of architectural elements in a buried volcanic system and implications for hydrocarbon exploration: Interpretation, doi:10.1190/INT-2016-0201.1.

Carlotto, M. A., R. C. B. Silva., A. A. Yamato., W. L. Trindade., J. L. P. Moreira., R. A. R. Fernandes, O. J. S. Ribeiro., et al. 2017. Libra: A Newborn Giant in the Brazilian Presalt Province. In Gialnt Fields of the Decade 2000-2010. doi:10.1306/13572006M1133685.

Goff, F., Janik, C.J., 2000, Geothermal Systems, Encyclopedia of Volcanoes, Academic Press, Chapter-49, pp. 817 – 834.

Holford, S. P., N. Schofield, J. D. MacDonald, I. R. Duddy, P. F. Green., 2012, Seismic Analysis of Igneous Systems in Sedimentary Basins and Their Impacts on Hydrocarbon Prospectivity: Examples from the Southern Australian Margin. APPEA Journal, 52, 229–52.

Jerram, D. A., R. T. Single., R. W. Hobbs., C. E. Nelson., 2009, Understanding the offshore flood basalt sequence using onshore volcanic facies analogues: An example from the Faroe-Shetland basin: Geological Magazine, doi:10.1017/S0016756809005974.

Kereszturi, G., K. Németh., 2013, Monogenetic Basaltic Volcanoes: Genetic Classification, Growth, Geomorphology and Degradation: Updates in Volcanology - New Advances in Understanding Volcanic Systems, doi:http://dx.doi.org/10.5772/51387.

Magoon, L. B., and W. G. Dow, 1994, The Petroleum System: AAPG Memoir, doi:10.1126/science.51.1323.468.

Miall, A. D., 1985, Architectural-Element Analysis: A New Method of Facies Analysis Applied to Fluvial Deposits. Earth-Science Reviews Elsevier Science Publishers B.V 22: 261–308. doi:10.1016/0012-8252(85)90001-7.

Montanari, D., M. Bonini,, G. Corti,, A. Agostini,, C. Ventisette., 2017, Forced folding above shallow magma intrusions: Insights on supercritical fluid flow from analogue modelling: doi:10.1016/j.jvolgeores.2017.07.022.

Mohriak, W.U., M. Nemcok., G. Enciso., 2008. South Atlantic divergent margin evolution: rift-border uplift and salt tectonics in the basins of SE Brazil. In: Pankhurst, R.J., Trouw, R.A.J., Brito Neves, B.B. & de Wit, M.J. (eds.), West Gondwana pre-Cenozoic correlations across the South Atlantic region. Geological Society of London, Special Publication 294, p.365-398.

Pittari, A., Cas, R. A. F., Lefebvre, N., Robey, J., Kurszlaukis, S., Webb, K., 2008. Eruption processes and facies architecture of the Orion Central kimberlite volcanic complex, Fort à la Corne, Saskatchewan; kimberlite mass flow deposits in a sedimentary basin. Journal of Volcanology and Geothermal Research, 174(1), 152–170. https://doi.org/https://doi.org/10.1016/j.jvolgeores.2007.12.019

Planke, S., E. Alvestad, O. Eldholm., 1999, Seismic Characteristics of Basaltic Extrusive and Intrusive Rocks. The Leading Edge 18 (3): 342. doi:10.1190/1.1438289.

Rateau, R., N. Schofield, M. Smith., 2013, The Potential Role of Igneous Intrusions on Hydrocarbon Migration, West of Shetland. Petroleum Geoscience 19 (3): 259–72. doi:10.1144/petgeo2012-035.

Rohrman, M., 2007, Prospectivity of Volcanic Basins: Trap Delineation and Acreage de-Risking. AAPG Bulletin 91 (6): 915–39. doi:10.1306/12150606017.

Schutter, S. R., 2003, Hydrocarbon Occurrence and Exploration in and around Igneous Rocks. Geological Society, London, Special Publications 214 (1): 7–33. doi:10.1144/GSL.SP.2003.214.01.02.

Silva, S. D., J. M. Lindsay., 2015, Primary Volcanic Landforms. The Encyclopedia of Volcanoes. doi:10.1016/B978-0-12-385938-9.00015-8.

Stimac, J., F. Goff, and C. J. Goff., 2015, Intrusion-Related Geothermal Systems, in The Encyclopedia of Volcanoes: doi:10.1016/B978-0-12-385938-9.00046-8.

Svensen, H. H., T. H. Torsvik., S. Callegaro., L. Augland., T. H. Heimdal., D. A. Jerram., S. Planke., and E. Pereira., 2017, Gondwana Large Igneous Provinces: plate reconstructions, volcanic basins and sill volumes: Geological Society, London, Special Publications, doi:10.1144/SP463.7.

Wight, A.W.R., Hardian, D., 1982, Importance of diagenesis in carbonate exploration and production, Lower Batu Raja Carbonates, Krisna Field, Java Sea: Indonesian Petroleum Association, 11th Annual Convention, Proceedings, p. 211–236.

Chapter 2

Concepts and Techniques

2 Concepts and Techniques

This chapter aims to briefly introduce the main techniques and fundamental concepts applied in this thesis to characterise the architecture of buried volcanic systems using seismic reflection and borehole data (Figure 1). The structure of the thesis is designed to provide background information to support our interpretations in each independent chapter, in which we present more detailed discussions of the concepts and techniques applied in this study.

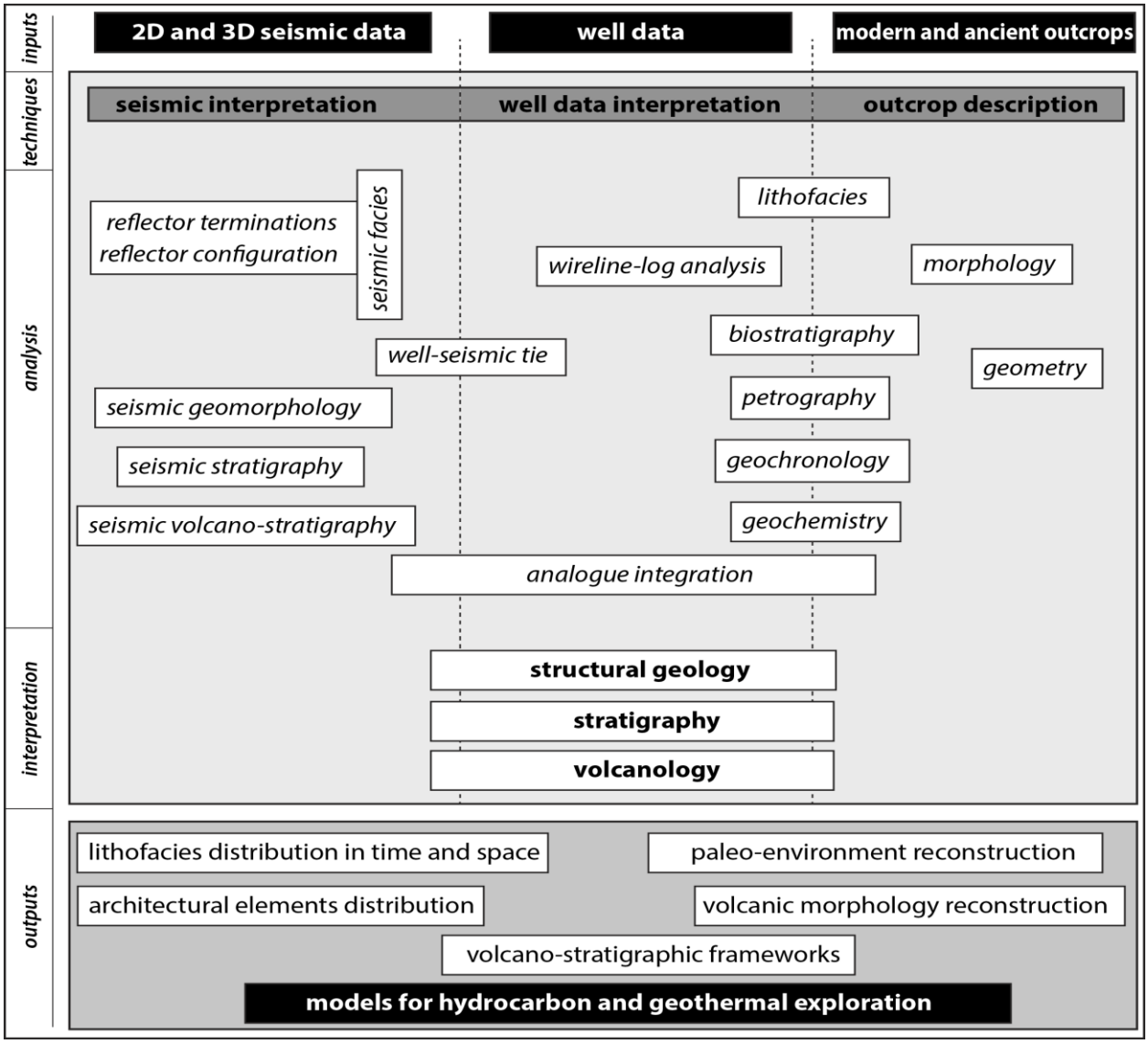

Figure 1: Diagram showing the workflow adopted in this PhD research. Seismic reflection and well data were integrated with observations from outcropping analogue systems.

In this study, large datasets of 2D and 3D seismic surveys were integrated with biostratigraphic, geochronological, geochemical, petrophysical and petrographic information from many wells of the Taranaki and Canterbury basins. Interpretation of these datasets were made using a multidisciplinary approach that integrates insights from disciplines such as structural geology,

stratigraphy and volcanology into a unified model to explain the geology of the studied areas. The integration of these disciplines enables us to understand the spatio-temporal distribution of facies and geobodies within the buried volcanoes, and to reconstruct the paleo-environmental scenarios in which volcanic events occurred during the evolution of the host sedimentary basins. This background information is the basis for construction of volcano-stratigraphic frameworks that represent the architecture of volcanic systems buried in sedimentary basins. These frameworks can be used to propose models for the exploration and development of geoenergy resources such as hydrocarbons and geothermal power (Figure 1).

2.1 Fundamental Concepts of Seismic Reflection Interpretation

In geophysical exploration the word *seismic* refers to the natural or artificial vibration of the ground in response to a stimulus (Sheriff and Geldart, 1995). During seismic events, waves travel through the geological strata, gathering with them information about the subsurface structure and composition of the Earth. Seismic reflection surveying is a geophysical technique developed to indirectly observe the subsurface of the Earth. In this method, artificial waves are generated at the Earth's surface. These waves are sourced with a certain energy, then they travel through the subsurface. The physical proprieties of the waves (e.g. velocity, energy, and reflectance) are affected by successive geologic layers. When the waves cross from one layer to another with different density, they reflect and refract at the contacts of the layers (Figure 2). The reflected waves are then captured by geophones back at the surface, and contain information about physical interfaces that represent subsurface lithological contacts, structural or stratigraphic boundaries, or the effects of interstitial fluids in the rock pore system. The seismic reflection concept is based on *Snell's Law of Reflection*, a geophysical principle that describes changes in the properties of seismic waves (such as reflectance, refractance and velocity) when they travel from one physical medium to another (e.g. Sheriff and Geldart, 1995; Yilmaz, 2001). The changes in wave velocities across medium boundaries with different density is called *acoustic impedance*, which is directly proportional to the contrast in density and velocity from one medium to another. Thus, stronger acoustic impedance interfaces appear as stronger reflectors in seismic reflection profiles (Figure 2; Figure 3). Three steps are required to use seismic reflection data in geological interpretation: a) data acquisition; b) data processing; c) data analysis. During the initial step of a seismic survey, the data are collected, usually along a regular grid, in which the distance between seismic lines define the horizontal resolution of the survey. The vertical

resolution depends on the parameters of acquisition such as frequency of the seismic waves and the time interval over which the data is record. Vertical resolution is strongly influenced by the characteristics of the seismic reflectors such as thickness, heterogeneity within the geological layers and presence of interstitial fluids. The raw seismic data are then processed to reduce seismic noise and errors encountered during the acquisition process (e.g. Sheriff and Geldart, 1995; Catuneanu, 2006; Abdelmalak et al., 2016; Marfurt, 2018). Finally, the information is displayed on 2D profiles showing the two-way travel time of the waves versus the horizontal distance of receptors (Figure 2; Figure 3; Figure 4) or on 3D seismic volumes (Figure 5).

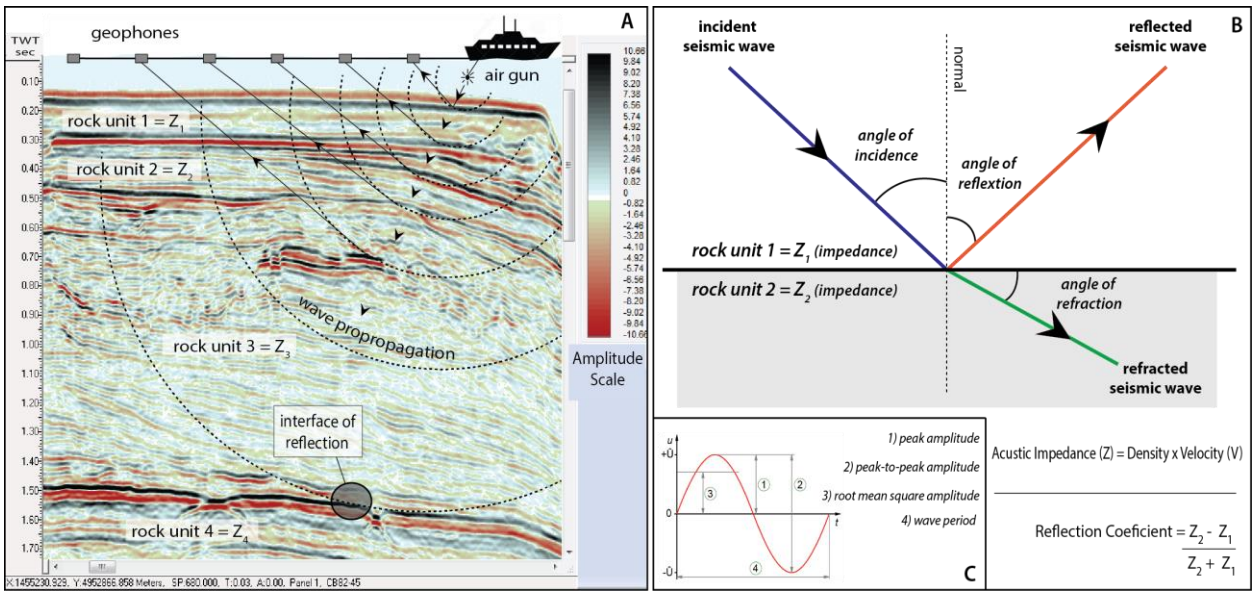

Figure 2: Fundamental concepts of seismic reflection acquisition and interpretation. Modified from Sheriff and Geldart (1995) and Wright (2013). Seismic line in A is from Canterbury Basin, New Zealand. Seismic image from Bischoff (unpublished data, 2015).

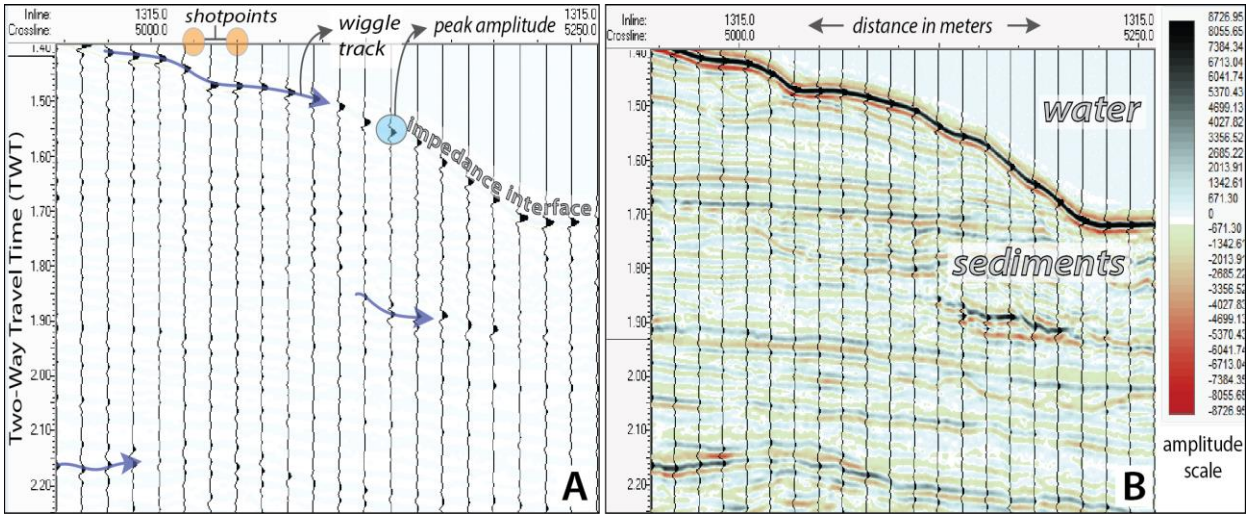

Figure 3: 2D profile of a seismic survey in Canterbury Basin, New Zealand. Figure A shows the vertical wiggle track at individual shot points. Strong impedance contrasts display positive amplitude peaks. These peaks can be laterally tracked (B) to display the subsurface characteristics of the area such as lithological contacts, geological units geometries and chronostratigraphic surfaces. Seismic images from Bischoff (unpublished data, 2015).

2.2 Seismic Imaging of Igneous Rocks in Sedimentary Basins

Igneous rocks in sedimentary basins are often identified in seismic reflection data by the presence of high amplitude reflectors within the seismic dataset (e.g. Holford et al., 2012; Rateau et al., 2013; Alves et al., 2015; Reynolds et al., 2017; Rabbel et al., 2018). These high amplitude reflectors result from the commonly strong impedance contrast between the igneous rock (i.e. denser, faster) and the host sedimentary strata (i.e. softer, slower). Characteristically, massive and unaltered basalts and diabase have seismic velocities > 5000 m/s, which contrasts strongly with typical sedimentary rocks such as sandstones and mudstones, which usually have acoustic velocities < 3000 m/s (e.g. Planke et al., 2000; Holford et al., 2012; Klarner and Klarner, 2012). An example of high amplitude reflectors interpreted as igneous intrusive in origin (e.g. Blanke, 2010) are shown in Figure 4. Despite the straight-forward concept underpinning the identification of igneous rocks in seismic data using their high impedance contrast, many complications can arise when distinguishing intrusive and extrusive bodies (e.g. Hansen and Cartwright, 2006; Holford et al., 2012; Bischoff, 2015; Schofield et al., 2016), steeply inclined geobodies (e.g. Magee et al., 2013; Infante-Paez and Marfurt, 2017), and igneous rocks with original physical characteristics that were altered by fracturing, metasomatism or weathering processes (e.g. Planke et al., 2000; Planke et al., 2005; Nara et al., 2011; Holford et al., 2012; Heap and Kennedy, 2016; Cant et al., 2017; Mordensky et al., 2018). These limitations are discussed in detail in chapters 3, 4 and 5.

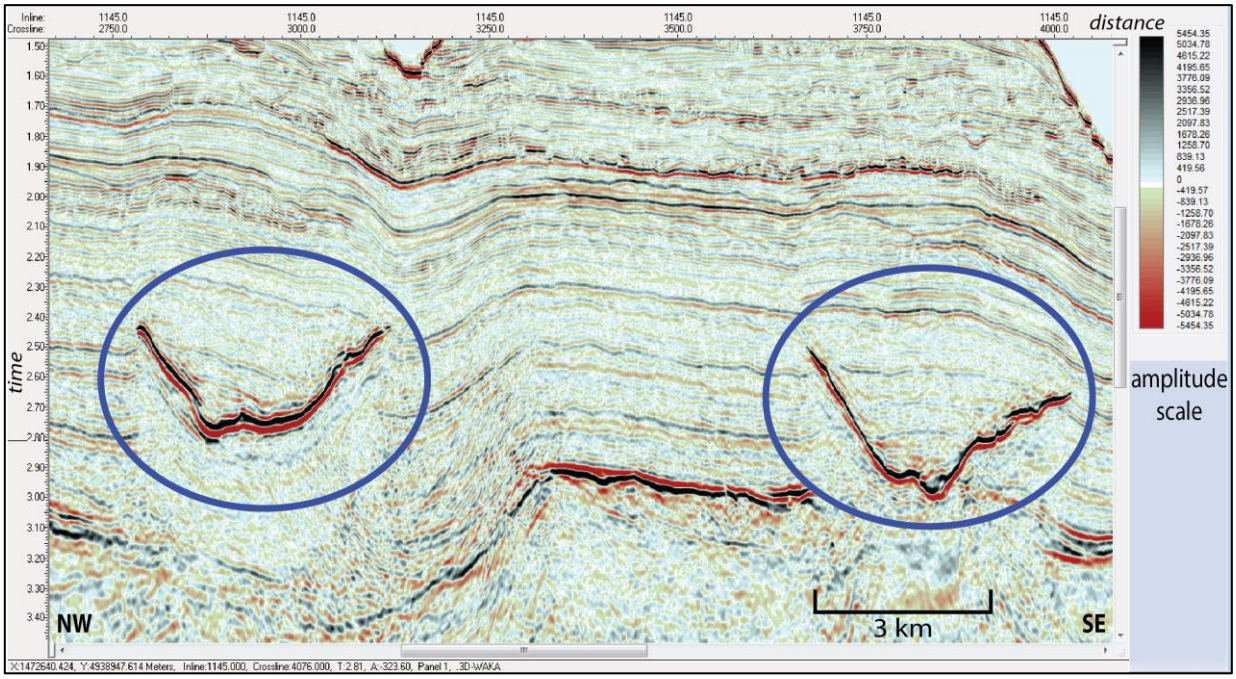

Figure 4: Saucer-shaped sills imaged in the Waka 3D seismic survey (e.g. Blanke, 2010) from offshore Canterbury Basin, New Zealand. The locations of the sills are highlighted by the blue ellipses. Image from Bischoff (unpublished data, 2015).

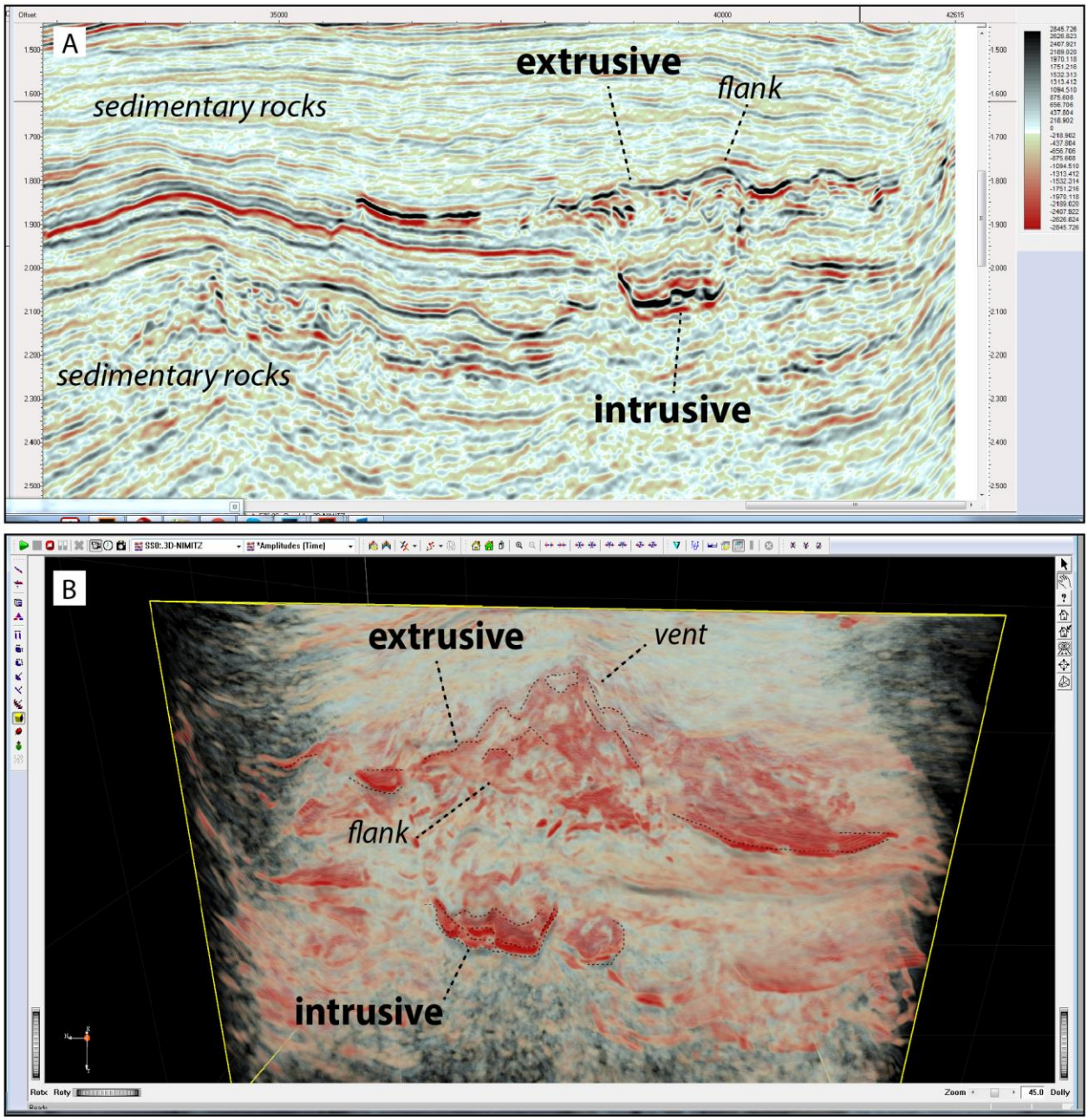

Figure 5: 2D seismic section (A) and 3D opacity rendering (B) of a potential sill-fed volcano in the Nimitz-3D seismic survey, Taranaki Basin, New Zealand. Note that the intrusive and extrusive parts of the volcano show high amplitude reflectors in contrast with basin sedimentary strata. Images from Bischoff (unpublished data, 2018).

2.3 Seismic Attributes

A seismic attribute is a quantitative measurement of a seismic characteristic of interest. These attributes are geophysical properties extracted or derived from the seismic reflection data. A vast range of attributes can be extracted from seismic data such as amplitude, coherence, instantaneous phase and envelope (e.g. Chopra and Marfurt, 2005; Abdelmalak et al., 2016; Marfurt, 2018). These attributes can be informative about characteristics of the subsurface rocks such as geometry, contact relationship, density of the rocks, and possible lithologies. The

amplitude of the acoustic waves is the most common attribute used to display seismic reflection data. When plotted in 2D profiles, the wave amplitude peaks in intensity at the points where the waves cross impedance interfaces (Figure 2; Figure 3). For comparison, Figure 6A shows an example of a sill intrusion analysed using the *envelope* attribute.

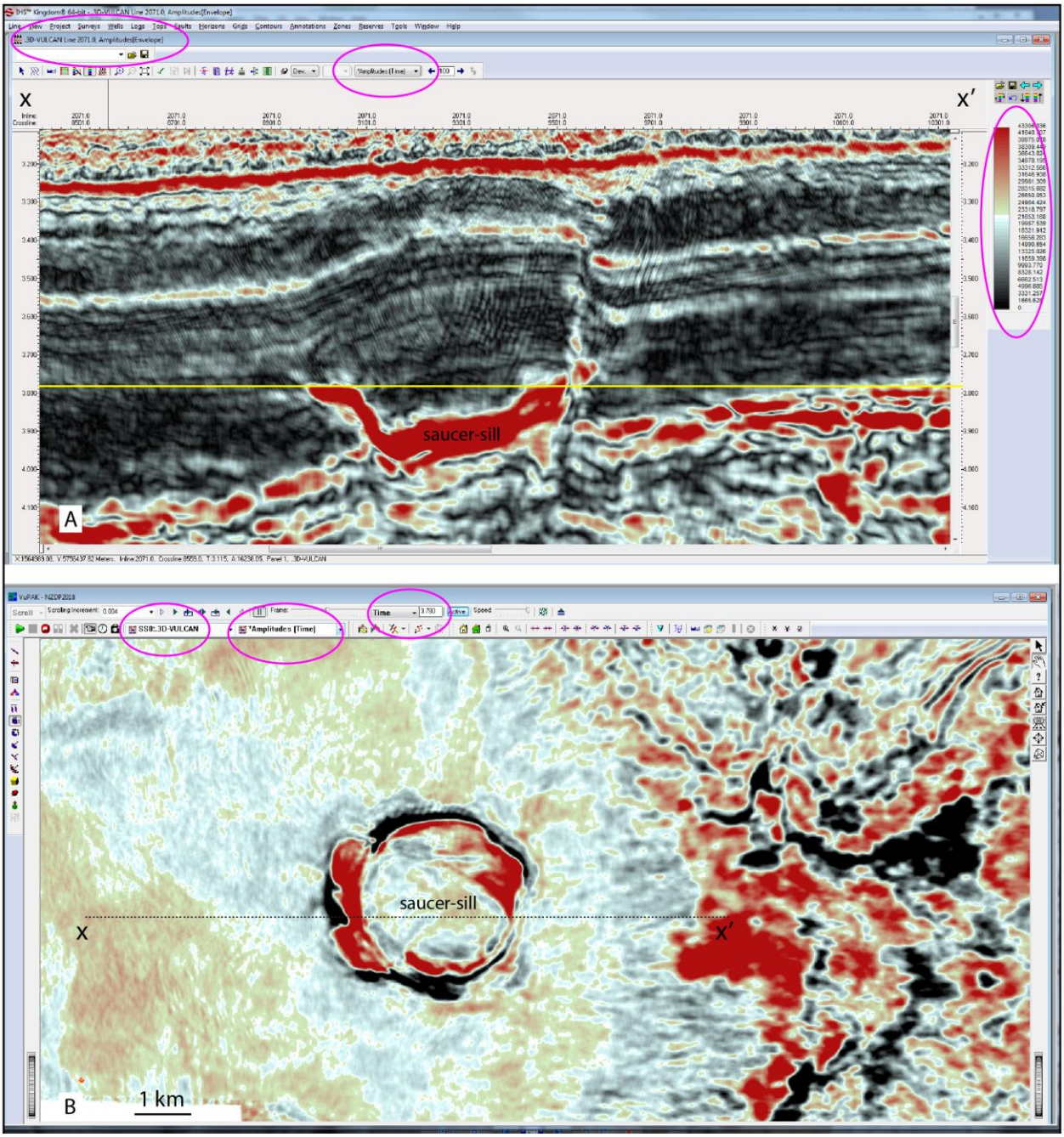

Figure 6: 2D seismic profile (A) and time-slice view (B) of a saucer-shaped sill intruding into marine sedimentary strata, offshore Taranaki Basin in the Vulcan-3D seismic survey. Purple ellipses display the relevant information of the 3D survey for the analysed data. Top image shows a 2D section of a saucer-shaped sill evidenced by the attribute *envelope*. Bottom image show the same saucer-shaped sill in plan, evidenced by the attribute amplitude at a time-slice at 3.7 TWT sec. Yellow line in top image is the reference for the time slice in the bottom image. Seismic images from Bischoff (unpublished data, 2018).

2.4 Seismic Stratigraphy

Seismic stratigraphy is a geological approach to stratigraphic interpretation using seismic reflection data. In this approach, two main aspects of the seismic reflectors are observed (Figure 7): i) the configuration of reflectors relative to each other (e.g. parallel, divergent, chaotic, etc.) and ii) the termination of reflectors (e.g., toplap and downlap; etc.). The relationship between the terminations of the reflectors can indicate original depositional limits and structural boundaries of distinctive geobodies, while the internal configuration of the reflectors can provide insights about depositional processes within the geobodies (e.g. Mitchum et al., 1977; Posamentier and Vail, 1988).

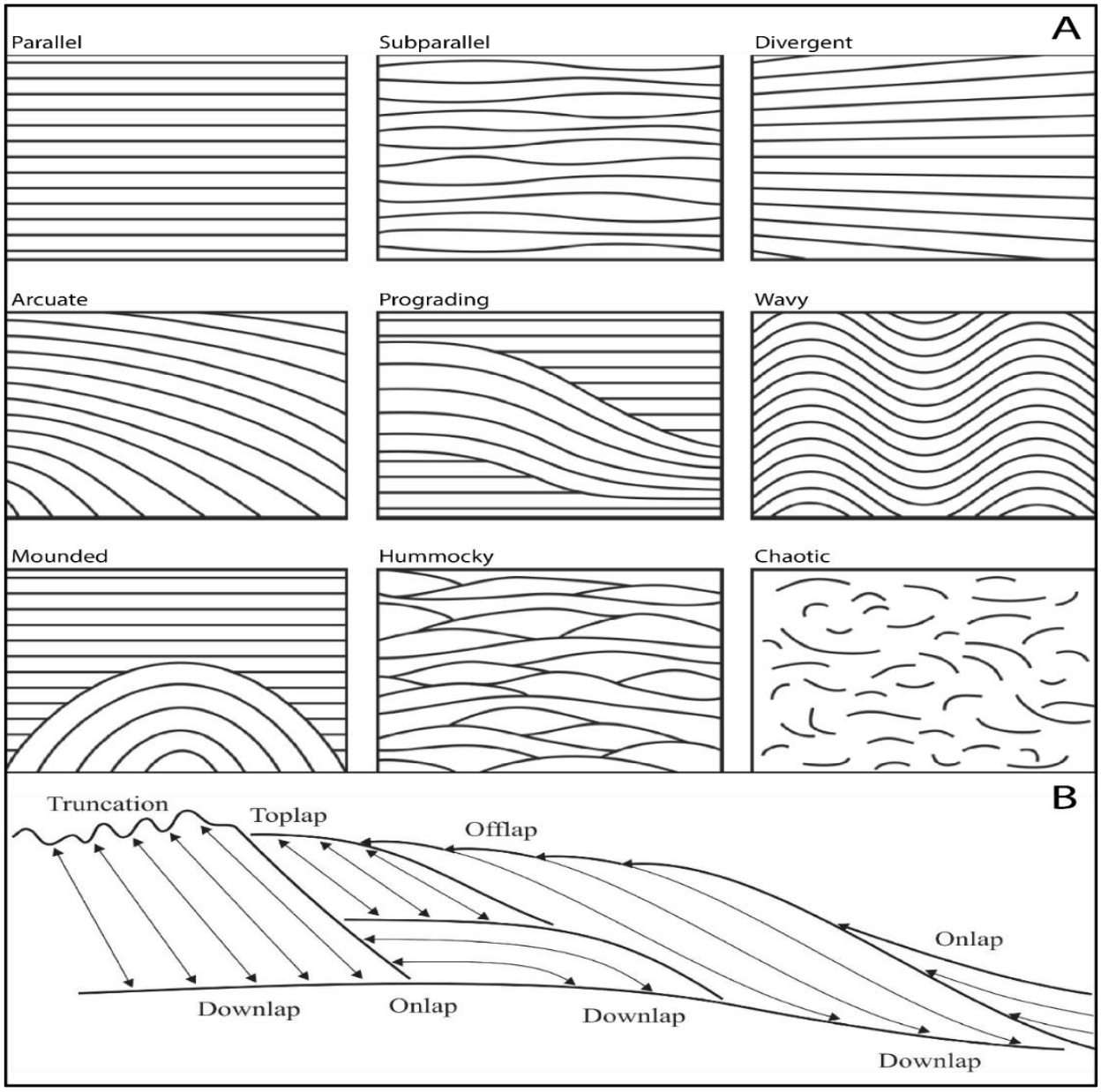

Figure 7: (A) Common internal seismic reflection configurations, and (B) seismic reflection terminations observed in seismic data. Modified from Mitchum et al. (1977); Emery and Myers (1996); Catuneanu (2006), and Wright (2014).

As the properties of seismic reflectors are controlled by the physical properties of the rock boundaries and stratal surfaces that correspond to velocity-density contrasts (Vail and Mitchum, 1977), seismic reflectors typically follow chronostratigraphic surfaces rather than lithostratigraphic units (Vail et al., 1977; Tipper, 1993) and allow for the direct application of stratigraphic concepts to the interpretation of the seismic data (i.e., Steno's Laws: original horizontality, superposition, lateral continuity, cross-cutting relationships and the principle of inclusion).

2.5 Seismic Volcano-Stratigraphy

Seismic volcano-stratigraphy is a subset of seismic stratigraphy developed to analyse the stratigraphic record of sedimentary basins that contain large volumes of magma using seismic reflection data. Planke and Alvestad (1999) defined seismic volcano-stratigraphy as "the study of the nature, geological history, and emplacement environment of extrusive volcanic rocks from seismic data". Seismic volcano-stratigraphy is based on seismic facies analysis and the concepts of seismic stratigraphy (Mitchum et al., 1977).

Planke and Alvestad (1999) suggest that buried volcanic complexes often show distinctive seismic facies, which result from the interaction of the volcanism with the concomitant external paleo-environments. Important volcanic-stratigraphic stratal changes are observed in relation to the location of the paleo-shoreline (e.g. Planke et al., 2000), but other factors such as volume and rate of effusions, magma viscosity, and distribution of eruptive vents may also contribute to the final stratal pattern of a basin that experienced volcanism (e.g. Cas and Wright., 1993; Single and Jerram, 2004; Planke et al., 2017). At rifted margins that contain large-volume basaltic provinces, Planke et al. (2000) recognize six characteristic volcanic seismic facies units which they refer to as: landward flows, lava delta, inner flows, inner seaward dipping reflectors, outer seaward dipping reflectors and outer high. Herzer (1995) described three main seismic facies (main body, sloping apron and wide almost flat ring plain) for a buried volcanic arc in the offshore Northland Peninsula, New Zealand.

Here, we applied the concepts of seismic volcano-stratigraphy to recognize the stratal pattern of sedimentary basins related to the emplacement, construction, degradation and burial of an individual polygenetic volcano (Kora volcanic system; chapter 3), and of a monogenetic volcanic field (Maahunui volcanic system; chapters 4 and 5).

2.6 Sequence Stratigraphy

Sequence stratigraphy is a method applied to analyse the stratigraphic record of sedimentary basins in a temporal and spatial framework. This method identifies changes in the stratal depositional trends of the basin to place stratigraphic surfaces that bound genetically related rock units of different scales (e.g. sequences, system tracts, parasequences). Such trends represent the dispersion of material in specific stacking patterns of progradation, retrogradation and aggradation (e.g. Van Wagoner et al., 1990), which reflect the balance between sedimentation rates, changes in accommodation rates, and energy flux of the environment (e.g. Catuneanu, 2006). Several models have been proposed (Figure 8) suggesting how the method of sequence stratigraphy should be applied.

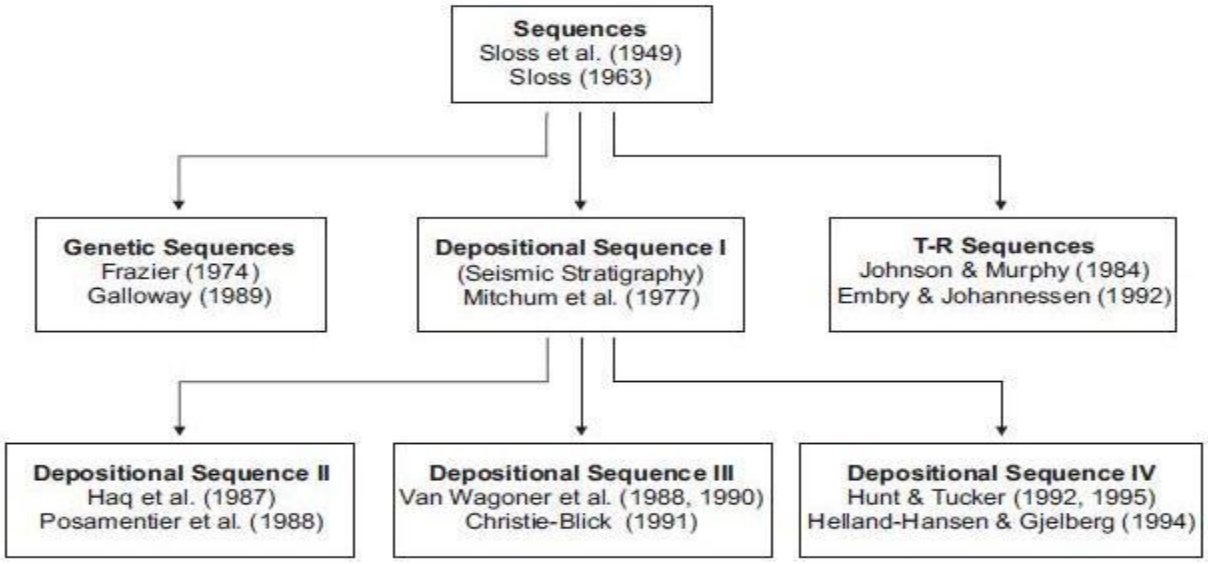

Figure 8: Diagram showing the evolution of sequence stratigraphic approaches. From Catuneanu et al. (2010).

The various approaches mainly differ in terms of nomenclature and the choice of which stratigraphic surfaces should be selected to limit sequence boundaries, but they agree that changes in depositional trends are controlled by the interplay of autogenic (i.e. from within the system) and allogenic (i.e. from outside of the system) mechanisms (Figure 9). Today, vast amount of literature explain how allogenic and autogenic mechanisms induce base-level changes and formation of recognizable stratigraphic sequences in sedimentary basins (e.g. Jervey, 1988; Walker, 1992; Miall, 2000; Miall and Miall, 2000; Catuneanu, 2006). In summary, tectonics, eustasy and climate are the main allogenic mechanisms that control variables such as sediment supply, accommodation space, and energy flux in sedimentary environments. Additional processes such as thermal subsidence, sediment compaction, and flexural loading also contribute

to the final architecture of the basins (e.g. Miall, 2000; Catuneanu, 2006). The depositional trends of sedimentary basins with large volumes of magma (i.e. volcanic basins; e.g. Planke et al., 2017; Svensen et al., 2017), are strongly impacted by igneous events (Planke et al., 2000). Figure 9 shows an adapted diagram that explains the allogenic and autogenic controls on depositional trends for volcanic basins.

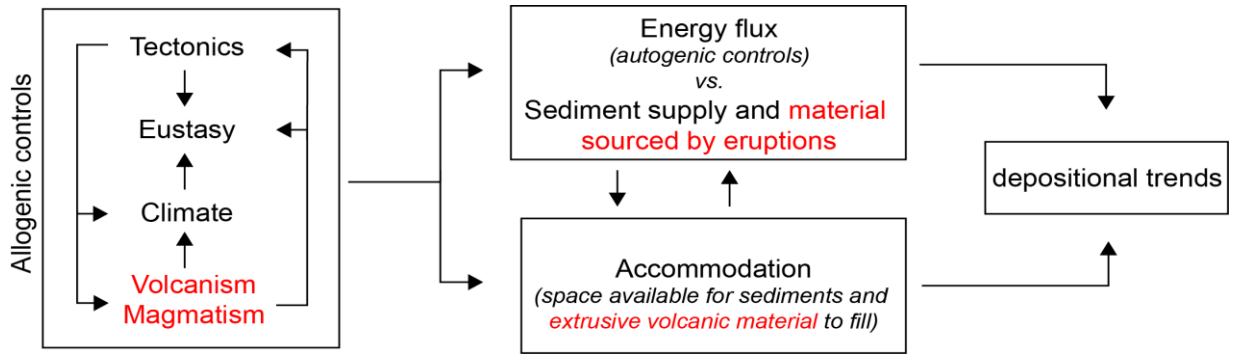

Figure 9: Allogenic controls on sedimentation, and their relationship to environmental energy flux, sediment supply, accommodation space, and depositional trends adapted for volcanic basins (modified from Catuneanu, 2006).

In this study, we follow a model-independent methodology (e.g. Catuneanu et al., 2009; Catuneanu et al., 2010) to identify the bounding surfaces that mark important shifts in basin stratal patterns (Figure 10). In volcanic basins, these changes are strictly controlled by expressive igneous events (e.g. Planke et al., 2000; Bischoff et al., 2016; Bischoff et al., 2017), which encourages us to propose a volcano-stratigraphic model based on sequences bounded by the beginning and end of distinct magmatic stages experienced during basin evolution. These volcano-stratigraphic frameworks are the topics of chapter 3, 4 and 5.

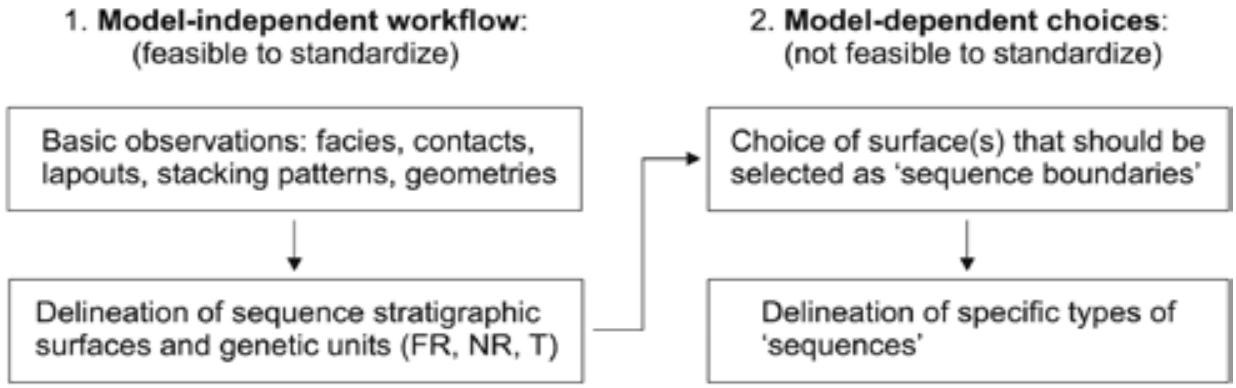

Figure 10: Model-independent workflow versus model-dependent choice in sequence stratigraphy presented in Catuneanu et al. (2009) and Catuneanu et al. (2010). The model-independent workflow leads to the subdivision of the stratigraphy into a succession of genetic units separated by sequence stratigraphic surfaces. After this sequence stratigraphic framework is built, the geoscientist may make model-dependent choices with respect to the selection of surfaces that should be elevated to the status of sequence boundary. In this study, after following a model-independent approach for the recognition of the stratal pattern of the basins, we propose the use of *magmatic sequences and stages* to subdivide the stratigraphic record of volcanic basins. Abbreviations: forced regressive (FR), normal regressive (NR) and transgressive (T) surfaces.

2.7 Sequence Volcano-Stratigraphy

Here, we propose an approach to subdivide the record of volcanic basins into three first-order volcano-stratigraphic intervals (i.e. pre, syn, and post-magmatic sequences). The pre-magmatic sequence predates magmatism and is cross-cut by the volcanic plumbing system. The syn-magmatic sequence comprises both intrusive and extrusive parts of the volcano. The post-magmatic sequence is characterised by degradation and burial of the volcanic structures after magmatism has ceased. These first-order sequences can be sub-divided into smaller-order magmatic stages (i.e. emplacement, constructional, degradational and burial stages), according to dominant magmatic or sedimentary processes that control the local basin architecture during each stage. Each one of these stages is characterised by a network of genetically related fundamental three-dimensional building blocks (i.e. architectural elements), formed by interactions between magma, external environments and sedimentation.

2.8 Seismic Geomorphology

Seismic geomorphology is a discipline that analyses the three-dimensional aspects of seismic facies from a geomorphological perspective. This analysis leads to the identification of depositional elements that are the fundamental building blocks of landscapes and seascapes (Posamentier and Kolla, 2003; Posamentier et al., 2007). Seismic geomorphology uses seismic reflection data to compose images that represent the geometry and morphology of geological bodies within seismic surveys (Figure 5; Figure 6; Figure 11; Figure 12).

Techniques such as opacity rendering, interval attribute analysis, horizon mapping and horizon and time/depth volume slices can produce insights in a range of fields, from igneous to sedimentary geology (e.g. Posamentier et al., 2007; Holford et al., 2012; Planke et al., 2017). Critical to the success of this approach lies in the “ground truth” calibration of the seismic images with lithofacies and depositional settings using borehole data and outcropping analogues (e.g. Planke et al., 1999; Single and Jerram, 2004; Klarne and Klarne, 2012; Millett et al., 2015; Schofield et al., 2016; Bischoff et al., 2017; Rabbel et al., 2018; Morley, 2018). When integrated with seismic and sequence stratigraphy, seismic geomorphology is a powerful tool for the prediction of lithologies, stratigraphic architecture, and geological processes in time and space (Davis et al., 2007). In this work, we applied seismic geomorphologic analysis to correlate the aspects of geobodies imaged in seismic data with potential analogue outcropping systems.

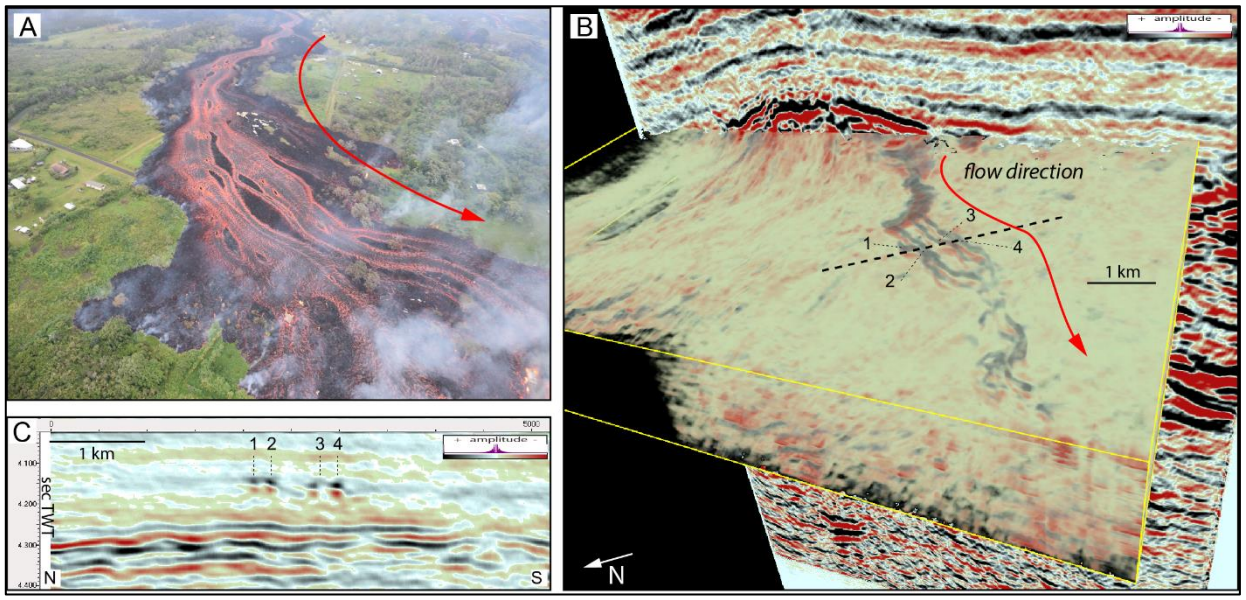

Figure 11: A) Channelized lava flow erupted from Kilauea Volcano, Lower East Rift Zone, Hawaii. B and C) 3D and 2D seismic images of an analogue channelized lava flow in Vulcan-3D, offshore Taranaki, New Zealand). This 3D volume together with the nearby Romney-3D reveal several large late Cretaceous polygenetic volcanoes that formed in association with rifting and opening of the Tasman Sea. Figures B and C from Bischoff (unpublished data, 2018).

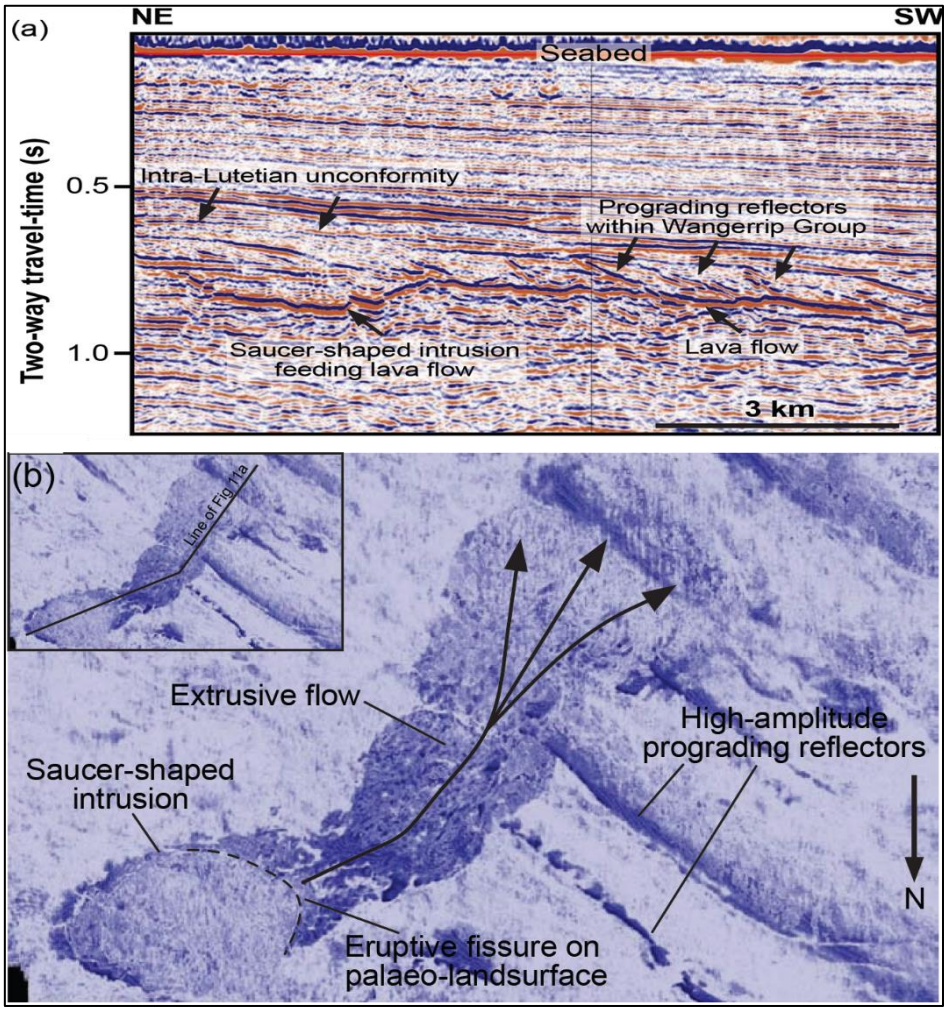

Figure 12: Seismic images showing the morphology of shallow intrusions that fed an extrusive flow at the early Paleocene paleosurface in Otway Basin, Southern Australia. (A) Arbitrary 2D seismic reflection profile. (B) 3D opacity-rendered view. From Holford et al. (2012).

2.9 Stratigraphic Record of Volcanism

The stratigraphic analysis of sedimentary basins requires the definition of a focal point of discussion. In sequence stratigraphy this focal point is usually the position of the shoreline through time. In sedimentary environments, terrestrial areas are typically the principal source of sediment accommodation (e.g. in fluvial systems it is the river channel, in deltas it is the river mouth). In volcanic systems, the focal point of discussion is the eruptive centre (Smith, 1991; Orton, 1996). The eruptive centre is the source of material from which co-genetic assemblages of lithofacies emanate during syn-eruptive and inter-eruptive periods of volcanism (Figure 13). In this study we observe how diverse volcanic and sedimentary architectural elements vary in time and space according to the distance from one or multiple eruptive centres.

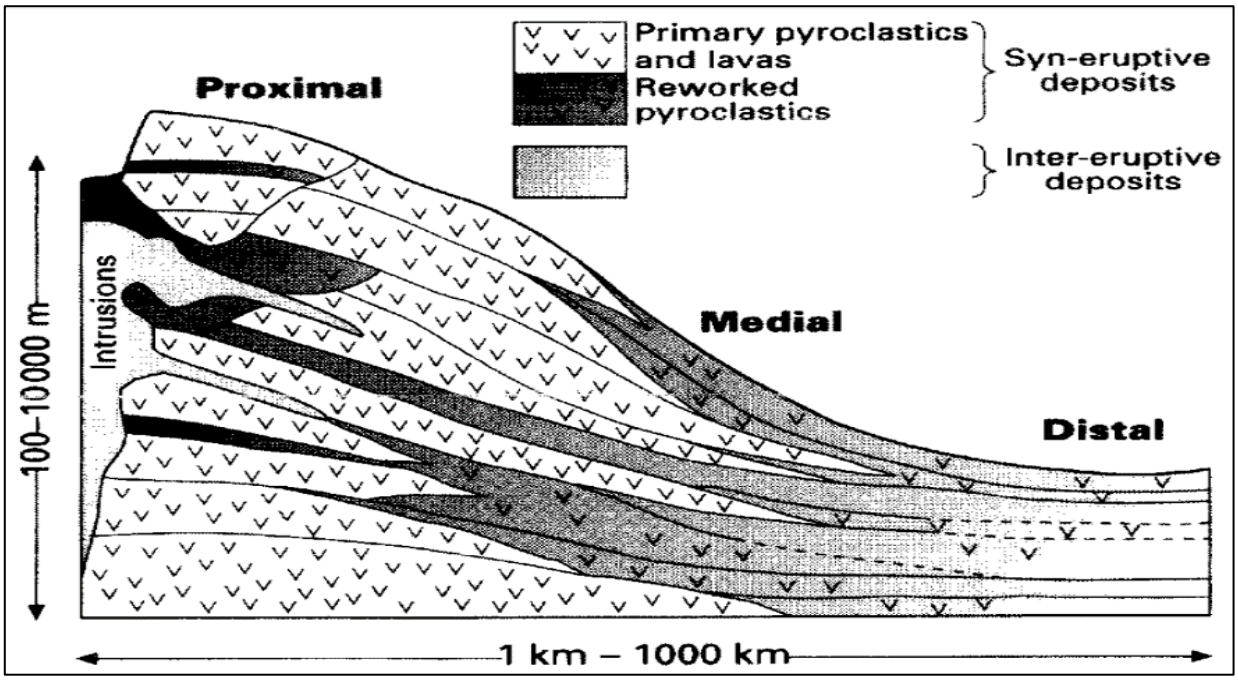

Figure 13: Stratigraphic model showing the faciological distribution and architecture of a hypothetical volcanic system. Deposits show lateral variation with increasing distance from the eruptive centre. Vertical succession occurs by the alternation of syn-eruptive and inter-eruptive deposits, bounded by proxies of chronostratigraphic surfaces. Figure from Orton (1996).

2.10 Sedimentary and Volcanic Architectural Elements

Architectural element is a term that was introduced to sedimentary geology during the early 1980's to document the fundamental building blocks of fluvial systems (Allen, 1983; Miall, 1985). The architectural elements approach focuses on the recognition of the internal structures and external bounding-surfaces that limit a body or an assemblage of genetically-related bodies, describing their geometry, lateral (spatial) variation, and vertical (time) succession. An

architectural element is defined as a "three-dimensional genetically related rock unit characterised by its geometry, facies, composition, scale and bounding-surfaces, and is the product of a particular process or suite of processes occurring within a depositional system (Miall, 2000).

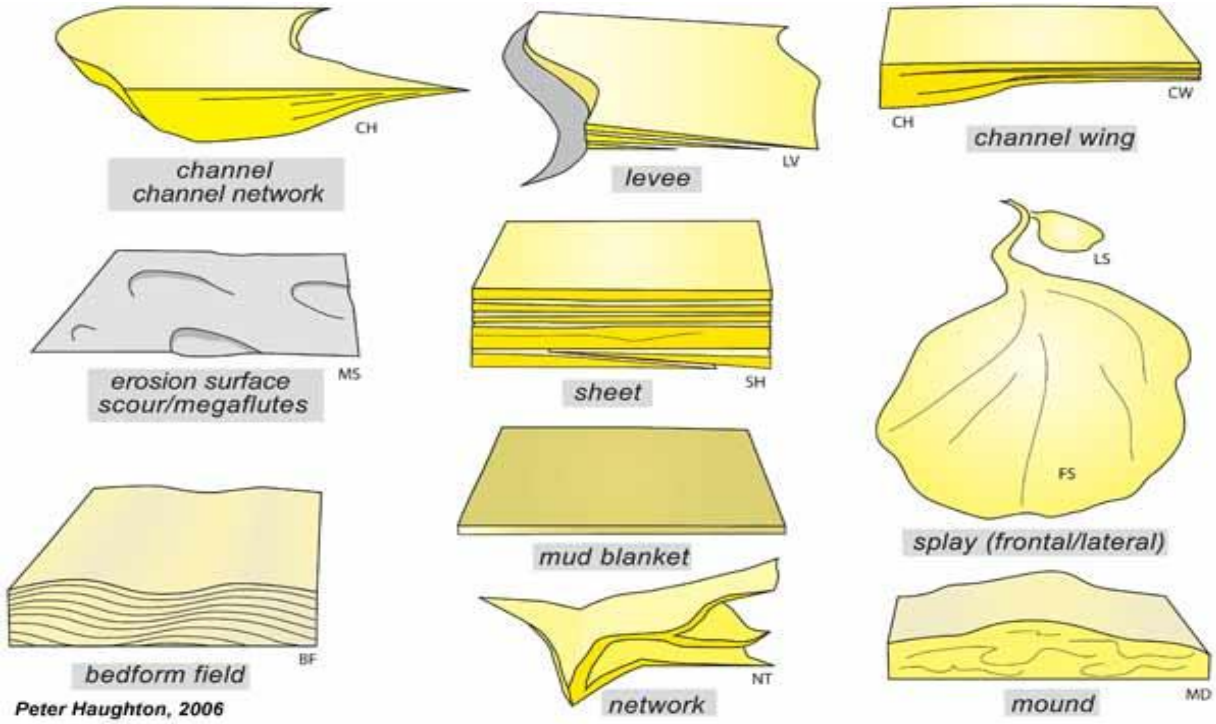

Figure 14: 3D representation of the main deep-water architectural elements. From Haughton (2006).

In early stages, recognition of architectural elements was difficult and mainly based on outcrop descriptions, which commonly lack 3D detailed information. Initially, representations of the architectural elements of fluvial systems, for example, were shown in single 2D sections (e.g. Miall, 1985). This raised distrust of the method (Bridge, 1993) and its application in subsurface analysis (Bridge and Tye, 2000). In the following years, the method was proven useful in both the surface and subsurface, especially due to advances in 3D seismic techniques such as geobody visualization and mapping of seismic bounding-surfaces. The application of the architectural element concept is now widely used for most clastic systems (e.g. Clark and Pickering, 1996; Prather et al., 2000; Posamentier and Kolla, 2003; Moraes et al., 2006; Slatt, 2013; Gamboa and Alves, 2015; Miall, 2016), and has also been successfully applied in carbonate systems (e.g. Kendall and Tucker, 2010; Catuneanu et al., 2011; Liu et al., 2018). In this study, the concept of an architectural element is applied to document the fundamental blocks of volcanic systems (Figure 15; Figure 16) buried in sedimentary basins. To our knowledge, Bischoff et al. (2017) was the first work to apply this concept to characterise the architecture of volcanic systems.

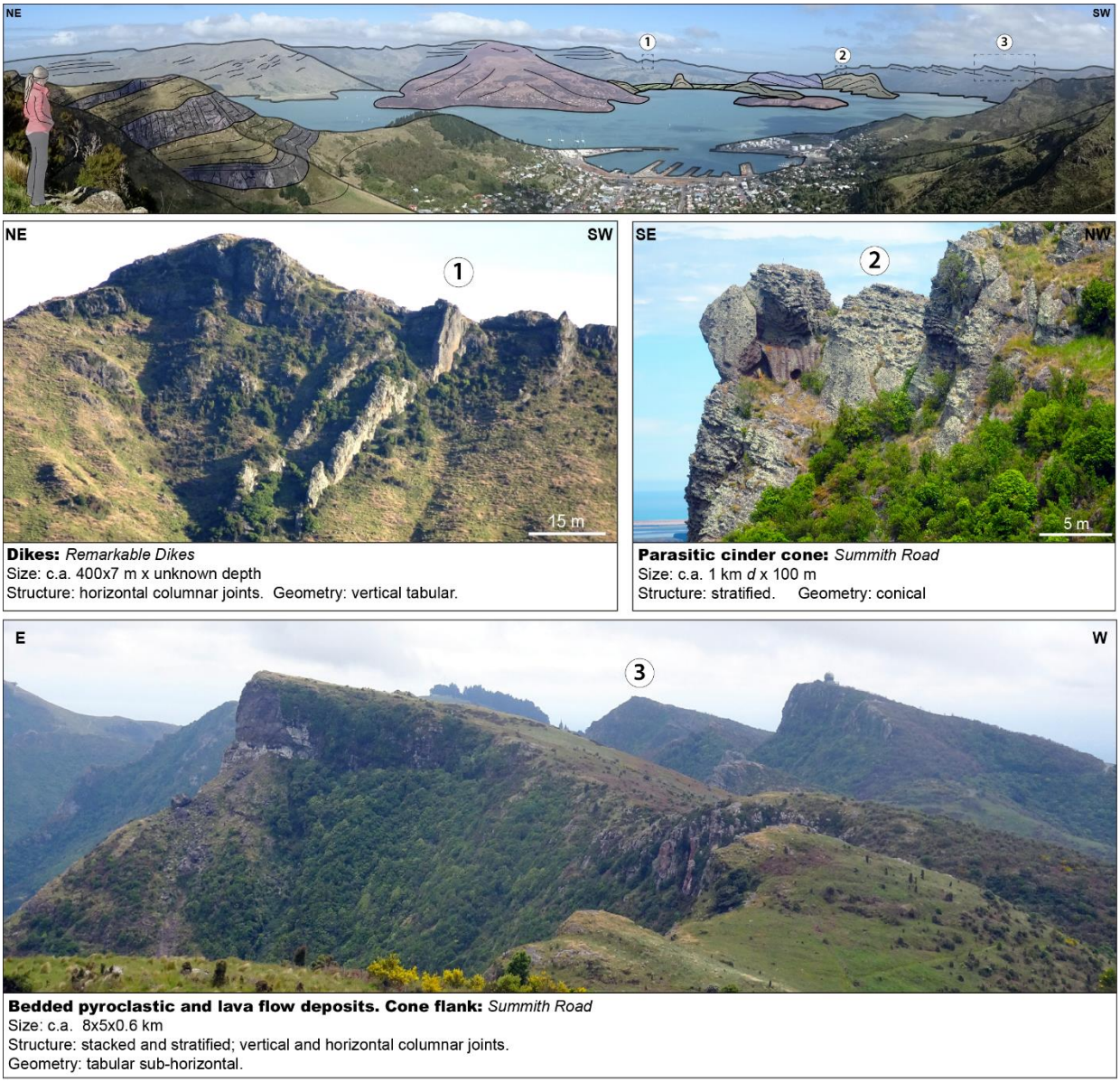

Figure 15: Examples of volcanic architectural elements in Lyttelton Volcano, Banks Peninsula Volcanic Complex. Each one of these elements is a three-dimensional rock unit genetically related to a particular process or a suite of processes occurring within the volcano. These elements are separated from each other by internal facies (e.g. composition, fragmentation, grain size), and external bounding-surfaces (e.g. cross-cutting relationship, angular or sharp contacts, changes in paleo-flow directions).

It is important to note that, despite similarity, architectural element and facies architecture are not synonymous. Facies architecture is a concept introduced in the late 1980's and early 1990's (e.g. Mutti and Normark, 1987; Miall and Tyler, 1991) to characterise the *heterogeneity and arrangement of lithofacies* within sedimentary systems, while architectural element was introduced to describe the *three-dimensional geometry of co-genetic rock units* (which are referred to as geobodies in seismic reflection studies). Today, both methods are widely applied to investigate the stratigraphic record of geological systems, however, facies architectural analysis focuses on the variation of physical properties within lithofacies (e.g. grain-sized

distribution, structures, composition), while architectural element analysis emphasizes the description of bounding discontinuities that limit genetically related rock units (e.g. channels, bars, crevasse splays, sand flats). Borgui (2000) presents a detailed review about these concepts.

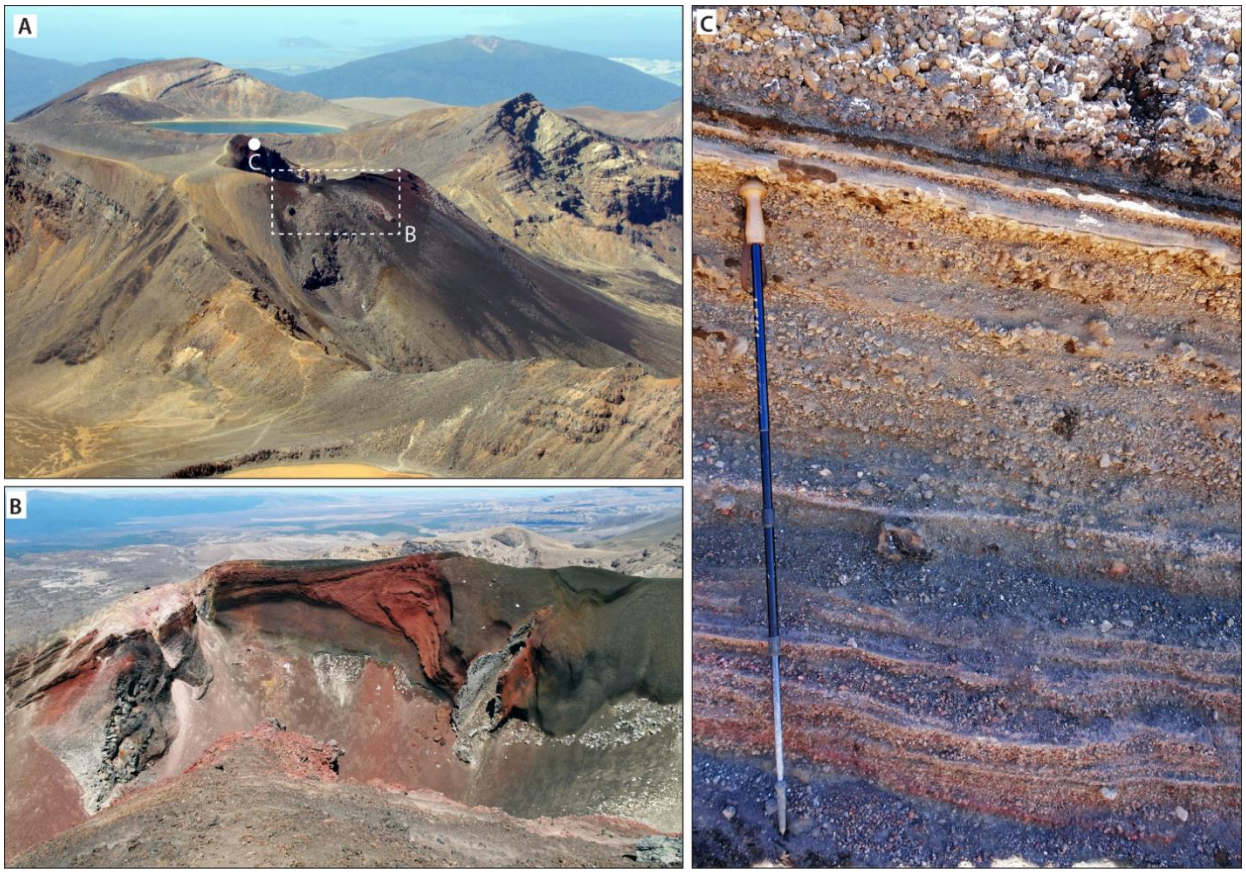

Figure 16: An example of the hierarchy of volcanic architectural elements in Tongariro Volcanic Complex, New Zealand. In a large-scale, the Red Crater (A) is one of several vents that compose the Tongariro Volcanic Complex. Downscaling, the flanks of the Red Crater are mainly composed by bedded inclined pyroclastic air-fall deposits, minor lava flows, and cross-cutting feeder dikes (B). A detailed view of part of the Red Crater flanks (C) show a succession of individual coarse-grained air-fall deposits, formed by changes in the dynamics of a single eruption, or by accumulation of tephra due to multiple eruption-cycles. At each scale, these sets of individual rock units (i.e. architectural elements) are formed in response to co-genetic processes occurring over a particular time-scale, and are physically separated from each other by a hierarchy of internal and external bounding surfaces.

2.11 Architectural Elements Analysis Applied in Geoenergy Exploration

The analysis of architectural elements enables the construction of predictive models for hydrocarbon exploration in sedimentary basins, with proven success since the 1980's (e.g. Miall, 1985; Clark and Pickering, 1996; Posamentier and Kolla, 2003; Moraes et al., 2006; Slatt, 2013; Gamboa and Alves, 2015). Oil and gas reservoirs are usually complex and highly variable. Understanding the distribution of architectural elements is critical to hydrocarbon exploration and development, because the elements determine the geometries, sizes, and internal heterogeneities of potential reservoirs, which provide guidelines for anticipated volumes and the

production behaviour of oil and gas (Slatt, 2013). Miall (1985) noted: “the architectural elements have become the norm for purposes of comparison, the framework and guide for future observations, the predictor in new geological situations, and the basis for hydrodynamic interpretation”. Because both sedimentary and volcanic architectural elements have strong impacts on fluid dynamics within a volcanic system, we propose that the architectural element method can be successfully applied in geothermal exploration as effectively as in petroleum exploration and development, which in this thesis is refer to as geoenergy exploration.

2.12 Conclusion

Interpretation of volcanic systems buried in sedimentary basins requires a multidisciplinary approach that combines insights from complementary disciplines such as structural geology, sedimentology, stratigraphy and volcanology into a unified model. During the last three decades, knowledge about sedimentary basins has improved significantly due to increasing advances in the fields of seismic and sequence stratigraphy. These advances have been particularly for characterising the architectural elements that compose the architecture of sedimentary systems. As noted in Cas and Wright (1993), “since the 1960’s attempts to make sense of the diversity of rocks, processes, stratigraphic models and deposition settings of volcanic successions have been aided by major advances in the field of sedimentology”. Here, we apply classical approaches used to characterise sedimentary basins such as architectural elements and stratigraphic sequences, to introduce the concepts of *magmatic sequences and volcanic architectural elements*. These concepts helps to characterise the spatio-temporal expression of volcanoes buried in sedimentary basins, and to reconstruct the paleo-environmental scenarios in which volcanic events occurred synchronously with basin sedimentation and erosion. We propose the construction of volcano-stratigraphic frameworks that represent the architecture of buried volcanic systems in sedimentary basins. These frameworks can be used to build models for the exploration of geoenergy resources such as hydrocarbons and geothermal power.

2.13 References

Abdelmalak, M. M., S. Planke., J. I. Faleide., D. A. Jerram., D. Zastrozhnov., S. Eide., R. Myklebust., 2016, The development of volcanic sequences at rifted margins: New insights from the structure and morphology of the Vøring Escarpment, mid-Norwegian Margin: Journal of Geophysical Research, Solid Earth, 121, 5212–5236, doi: 10.1002/2015JB012788.

Allen, J. R. L., 1983, Studies in Fluviatile Sedimentation: Bars, Bar-Complexes and Sandstone Sheets (Low-Sinuosity Braided Streams) in the Brownstones (L. Devonian), Welsh Borders: Sedimentary Geology, 33 (4): 237–93. doi:10.1016/0037-0738(83)90076-3.

Alves, T. M., Kamal'deen O., Phalene G., 2015, Volume Rendering of Enigmatic High-Amplitude Anomalies in Southeast Brazil: A Workflow to Distinguish Lithologic Features from Fluid Accumulations. Interpretation. doi:10.1190/INT-2014-0106.1.

Bischoff, A.P., A. Nicol, A. Barrier, M. Beggs., 2016, The Stratigraphic Record of Volcanism - Examples from New Zealand Sedimentary Basins. In 2016 Geoscience Society of New Zealand Conference, Wanaka, Abstract.

Bischoff, A.P., 2015, Igneous Features within Endurance-3D Survey and Their Impact on Barque Prospect. New Zealand Oil and Gas unpublished confidential report.

Blanke, S. J., 2010, "Saucer Sills" of the Offshore Canterbury Basin: GNS Publication, doi:10.1177/0094306114545742f.

Borghi, L., 2000, Visão geral da análise de fácies do ponto de vista da arquitetura deposicional. Boletim do Museu Nacional. Nova Série Geologia, Rio de Janeiro, v. 53, n.58, p. 1-26.

Bridge, J. S., 1993, Description and interpretation of fluvial deposits: a critical perspective: Sedimentology, doi:10.1111/j.1365-3091.1993.tb01361.x.

Bridge, J. S., and R. S. Tye., 2000, Interpreting the dimensions of ancient fluvial channel bars, channels, and channel belts from wireline-logs and cores: AAPG Bulletin, doi:10.1306/E4FD4B07-1732-11D7-8645000102C1865D.

Clark, J.D., Pickering, K.T., 1996, Architectural elements and growth patterns of submarine channels: application to hydrocarbon exploration. Am. Assoc. Petrol. Geol. Bull., 80, 194–221.

Cant, J. L., Siratovich, P. A, Cole, J. W., Villeneuve, M. C., Kennedy, B. M., 2018, Matrix permeability of reservoir rocks, Ngatamariki geothermal field, Taupo Volcanic Zone, New Zealand Geothermal Energy Science https://doi.org/10.1186/s40517-017-0088-6.

Cas, R. A. F., J. V. Wright., 1993, Volcanic Successions: Modern and Ancient - A Geological Approach to Processes, Products and Successions. Chapman and Hall, UK. doi:10.1007/978-0-412-44640-5.

Catuneanu, O., 2006, Principles of Sequence Stratigraphy. Changes, 375. doi:10.5860/Choice.44-4462.

Catuneanu, O., Abreu, V., Bhattacharya, J.P., Blum, M.D., Dalrymple, R.W., Eriksson, P.G.,Fielding, C.R., Fisher, W.L., Galloway, W.E., Gibling, M.R., Giles, K.A., Holbrook, J.M.,Jordan, R., Kendall, C.G.St.C., Macurda, B., Martinsen, O.J., Miall, A.D., Neal, J.E.,Nummedal, D., Pomar, L., Posamentier, H.W., Pratt, B.R., Sarg, J.F., Shanley, K.W., Steel, R.J., Strasser, A., Tucker, M.E., Winker, C., 2009, Towards the standardization of sequence stratigraphy. Earth-Science Reviews 92, 1–33. Elsevier B.V.: 1–33. doi:10.1016/j.earscirev.2008.10.003.

Catuneanu, O., J. P. Bhattacharya, M. D. Blum, R. W. Dalrymple, P. G. Eriksson, C. R. Fielding, W. L. Fisher, et al., 2010, Sequence Stratigraphy: Common Ground after Three Decades of Development. First Break. doi:10.3997/1365-2397.2010002.

Catuneanu, O., W. E. Galloway, C.G. St. C. Kendall, A. D. Miall, H. W. Posamentier, A. Strasser., M. E. Tucker., 2011, Sequence Stratigraphy: Methodology and Nomenclature. Newsletters on Stratigraphy. doi:10.1127/0078-0421/2011/0011.

Chopra, S., K. J. Marfurt., 2005, Seismic Attributes - A Historical Perspective. GEOPHYSICS. doi:10.1190/1.2098670.

Davies, R. J., H. W. Posamentier., L. J. Wood., J. A. Cartwright., 2007, Seismic Geomorphology: Applications to Hydrocarbon Exploration and Production. Geological Society Special Publications.

Emery, D., K. J. Myers., 1996, Sequence Stratigraphy, in Sequence Stratigraphy: doi:10.1002/9781444313710.fmatter.

Gamboa, D., T. M. Alves., 2015, Spatial and Dimensional Relationships of Submarine Slope Architectural Elements: A Seismic-Scale Analysis from the Espírito Santo Basin (SE Brazil). Marine and Petroleum Geology. doi:10.1016/j.marpetgeo.2015.02.035.

Hansen, D. M., J. Cartwright., 2006, Saucer-Shaped Sill with Lobate Morphology Revealed by 3D Seismic Data: Implications for Resolving a Shallow-Level Sill Emplacement Mechanism. Journal of the Geological Society 163 (3): 509–23. doi:10.1144/0016-764905-073.

Heap, M. J., B. M. Kennedy., 2016, Exploring the scale-dependent permeability of fractured andesite: Earth and Planetary Science Letters, doi:10.1016/j.epsl.2016.05.004.

Herzer, R. H., Seismic Stratigraphy of a Buried Volcanic Arc, Northland, New Zealand and Implications for Neogene Subduction. Marine and Petroleum Geology 12, no. 5 (January 1995): 511–31. https://doi.org/10.1016/0264-8172(95)91506-K.

Holford, S. P., N. Schofield, J. D. MacDonald, I. R. Duddy, P. F. Green., 2012, Seismic Analysis of Igneous Systems in Sedimentary Basins and Their Impacts on Hydrocarbon Prospectivity: Examples from the Southern Australian Margin. APPEA Journal, 52, 229–52.

Infante-Paez, L., and K. J. Marfurt, 2017, Seismic expression and geomorphology of igneous bodies: A Taranaki Basin, New Zealand, case study: Interpretation, v. 5, no. 3, p. SK121-SK140, doi:10.1190/INT-2016-0244.1.

Jervey, M.T., 1988, Quantitative geological modeling of siliciclastic rock sequences and their seismic expression. In: Wilgus, C.K., Hastings, B.S., Kendall, C.G.St.C., Posamentier, H.W., Ross C.A. and Van Wagoner, J.C. (Eds.) Sea Level Changes – An Integrated Approach. Society of Economic Paleontologists and Mineralogists (SEPM), Special Publication 42, 47-69.

Kendall, C. G. C., Tucker, M. E., 2010, SEPM STRATA website. http://www.sepmstrata.org/page.aspx?pageid=410

Klarner, S., O. Klarner., 2012, Identification of Paleo-Volcanic Rocks on Seismic Data, Updates in Volcanology. A Comprehensive Approach to the Volcanological Problems, 181–206, Prof. Francesco Stoppa (Ed.), InTech, DOI: 10.5772/24943.

Kennedy, B., M. Heap, A. P. Bischoff, A. Nicol, M. Villeneuve, J. Farquharson, J. Cole., 2017, Insights into Volcanic Rocks as Petroleum Reservoirs from Laboratory and Field Permeability Measurements. In AAPG GTW Influence of Volcanism and Associated Magmatic Processes on Petroleum Systems. Conference, Oamaru New Zealand.

Liu, J. Hou, Y. Li, Y. Dong, X. Ma, X. Wang., 2018, Characterization of architectural elements of Ordovician fractured-cavernous carbonate reservoirs, Tahe Oilfield, China J. Geol. Soc. India, 91 (3) (2018), pp. 315-322

Magee, C., E. Hunt-Stewart., C. A. L. Jackson., 2013, Volcano growth mechanisms and the role of sub-volcanic intrusions: Insights from 2D seismic reflection data: Earth and Planetary Science Letters, doi:10.1016/j.epsl.2013.04.041.

Marfurt, K., 2018, Seismic Attributes as the Framework for Data Integration Throughout the Oilfield Life Cycle: Society of Exploration Geophysicists, 508 p., doi:doi:10.1190/1.9781560803522.

Miall, A. D., 1985, Architectural-Element Analysis: A New Method of Facies Analysis Applied to Fluvial Deposits. Earth-Science Reviews Elsevier Science Publishers B.V 22: 261–308. doi:10.1016/0012-8252(85)90001-7.

Miall, A. D., Tyler, N., 1991, Three-Dimensional Facies Architecture of Terrigenous Clastic Sediments and Its Implications for Hydrocarbon Discovery and Recovery. 1–5. SEPM (Society for Sedimentary Geology). doi:10.2110/csp.91.03.0001.

Miall, A. D., 2000, Principles of Sedimentary Basin Analysis; Springer-Verlag, New York, 616p.

Miall, A. D., C. E. Miall., 2001, Sequence Stratigraphy as a Scientific Enterprise: The Evolution and Persistence of Conflicting Paradigms. Earth-Science Reviews. doi:10.1016/S0012-8252(00)00041-6.

Miall, A. D., 2016, Stratigraphy: A Modern Synthesis: Cham, Springer International Publishing, doi:10.1007/978-3-319-24304-7.

Millett, J., A. Wilkins., E. Campbell., M. Hole., R. Taylor., D. Healy., D. Jerram., D. Jolley., S. Planke., S. Archer., A. Blischke., 2016, The geology of offshore drilling through basalt sequences: Understanding operational complications to improve efficiency: doi:10.1016/j.marpetgeo.2016.08.010.

Mitchum, R M, P. R. Vail., 1977, Seismic Stratigraphy and Global Changes of Sea Level, Part 7 : Seismic Stratigraphic Interpretation Procedure. Seismic Stratigraphy: Applications to Hydrocarbon Exploration. AAPG Memoir 26 Memoir 26: 135–43.

Mordensky, S., M. Villeneuve., J. Farquharson., B. Kennedy., M. J. Heap., D. M. Gravley., 2018, Rock mass properties and edifice strength data from Pinnacle Ridge, Mt. Ruapehu, New Zealand: doi:10.1016/j.jvolgeores.2018.09.012.

Moraes, M. A. S., P. R. Blaskovski., P. L. B. Paraizo., 2005, Arquitetura de Reservatórios de Águas Profundas. Boletim de Geociencias Da Petrobras.

Morley, C., 2018, 3D seismic imaging of the plumbing system of the Kora volcano, Taranaki Basin, New Zealand: The influences of syn-rift structure on shallow igneous intrusion architecture: Geosphere, 2018. doi.org/10.1130/GES01645.1.

Mutti, E., W. R. Normark., 1987, Comparing Examples of Modern and Ancient Turbidite Systems: Problems and Concepts. In Marine Clastic Sedimentology. doi:10.1007/978-94-009-3241-8_1.

Nara, Y., Meredith, P.G., T. Yoneda., K. Kaneko., 2011, Influence of macro-fractures and micro-fractures on permeability and elastic wave velocities in basalt at elevated pressure. Tectonophysics, 503 (1-2) 52 - 59. 10.1016/j.tecto.2010.09.027.

Orton, G.J, 1996, Volcanic Environments. I n Reading, H. G., 1996, Sedimentary Environments: Processes, Facies and Stratigraphy: 688 p.

Planke, S., T. Rasmussen, S. S. Rey, and R. Myklebust, 2005, Seismic characteristics and distribution of volcanic intrusions and hydrothermal vent complexes in the Vøring and Møre basins, in Petroleum Geology: North-West Europe and Global Perspectives – Proceedings of the 6th Petroleum Geology Conference: doi:10.1144/0060833.

Planke, S., E. Alvestad, O. Eldholm., 1999, Seismic Characteristics of Basaltic Extrusive and Intrusive Rocks. The Leading Edge 18 (3): 342. doi:10.1190/1.1438289.

Planke, S., P. A. Symonds, E. Alvestad, J. Skogseid., 2000, Seismic Volcanostratigraphy of Large-Volume Basaltic Extrusive Complexes on Rifted Margins. Journal of Geophysical Research 105 (B8): 19335. doi:10.1029/1999JB900005.

Planke, S., J. M. Millett., D. Maharjan., D. A. Jerram., M. M. Abdelmalak., A. Groth., J. Hoffmann., C. Berndt., and R. Myklebust., 2017, Igneous seismic geomorphology of buried lava fields and coastal escarpments on the Vøring volcanic rifted margin: Interpretation, doi:10.1190/INT-2016-0164.1.

Posamentier, H. W., P. R. VAIL., 1988, Eustatic Controls on Clastic Deposition II – Sequence and Systems Track Models. In Sea-Level Changes. doi:10.2110/pec.88.01.0125.

Posamentier, H. W., R. J. Davies, J. A. Cartwright, and L. J. Wood, 2007, Seismic Geomorphology - an Overview. Geological Society, London, Special Publications 277: 1–14. doi:10.1144/GSL.SP.2007.277.01.01.

Posamentier, H. W., V. Kolla, 2003, Seismic Geomorphology and Stratigraphy of Depositional Elements in Deep-Water Settings. Journal of Sedimentary Research 73 (3): 367–88. doi:10.1306/111302730367.

Prather, B., F. Keller., M. A. Chapin., 2000, Hierarchy of Deep-Water Architectural Elements with Reference to Seismic Resolution: Implications for Reservoir Prediction and Modeling: pp. 817-835 p., doi:10.5724/gcs.00.15.0817.

Rabbel, O., O. Galland., K. Mair., I. Lecomte., K. Senger., J. B. Spacapan., R. Manceda., 2018, From field analogues to realistic seismic modelling: a case study of an oil-producing andesitic sill complex in the Neuquén Basin, Argentina: Journal of the Geological Society, doi:10.1144/jgs2017-116.

Rateau, R., N. Schofield, and M. Smith, 2013, The Potential Role of Igneous Intrusions on Hydrocarbon Migration, West of Shetland. Petroleum Geoscience 19 (3): 259–72. doi:10.1144/petgeo2012-035.

Reynolds, P., N. Schofield., R. J. Brown., S. P. Holford., 2016, The architecture of submarine monogenetic volcanoes - insights from 3D seismic data: Basin Research, v. 30, p. 437–451, doi:10.1111/bre.12230.

Reynolds, P., S., Holford, N. Schofield., A. Ross., 2017, Three-Dimensional Seismic Imaging of Ancient Submarine Lava Flows: An Example From the Southern Australian Margin: Geochemistry, Geophysics, Geosystems, doi:10.1002/2017GC007178.

Rohrman, M., M. Lisk., 2010, Geophysical delineation of volcanics and intrusives offshore NW Australia using global analogues. ASEG Extended Abstracts 2010, 1-3.

Schutter, S. R., 2003, Hydrocarbon Occurrence and Exploration in and around Igneous Rocks. Geological Society, London, Special Publications 214 (1): 7–33. doi:10.1144/GSL.SP.2003.214.01.02

Single, Richard T., 2004, The facies architecture of large igneous provinces: an integrated geological and geophysical approach to the characterisation of volcanic successions in 3-D, Durham theses, Durham University. Available at Durham E-Theses Online: http://etheses.dur.ac.uk/2978/

Silva, S. D., and J. M. Lindsay, 2015, Primary Volcanic Landforms. The Encyclopedia of Volcanoes. doi:10.1016/B978-0-12-385938-9.00015-8.

Slatt, R. M., 2013, Stratigraphic Reservoir Characterization for Petroleum Geologists. Developments in Petroleum Science. doi:10.1016/B978-0-444-56365-1.00013-4.

Sheriff, R.E, and Geldart, L.P., 1995, Exploration Seismology. Cambridge University Press, Cambridge

Smith G.A., 1991, Facies sequences and geometries in continental volcaniclastic sequences in Fisher, R.V., and Smith, G.A., eds., Sedimentation in volcanic settings: SEPM (Society for Sedimentary Geology) Special Publication 45, p. 109–121.

Schofield, N., D. A. Jerram., S. Holford., A. Stuart., M. Niall., A. Hartley., J. Howell., M. David., P. Green., D. Hutton., C. Stevenson, 2016, Sills in sedimentary basin and petroleum systems, in K. Németh, ed., The Series Advances in Volcanology, 1–22.

Schmiedel, T., S. Kjoberg., S. Planke., C. Magee., O. Galland., N. Schofield., C. A.-L. Jackson., and D. A. Jerram., 2017., Mechanisms of overburden deformation associated with the emplacement of the Tulipan sill, mid-Norwegian margin: Interpretation, doi:10.1190/INT-2016-0155.1.

Svensen, H. H., T. H. Torsvik., S. Callegaro., L. Augland., T. H. Heimdal., D. A. Jerram., S. Planke., and E. Pereira., 2017, Gondwana Large Igneous Provinces: plate reconstructions, volcanic basins and sill volumes: Geological Society, London, Special Publications, doi:10.1144/SP463.7.

Tipper, J. C., 1993, Do seismic reflections necessarily have chronostratigraphic significance? Geological Magazine, doi:10.1017/S0016756800023712.

Van Wagoner, J.C., Mitchum Jr., R.M., Campion, K.M., Rahmanian, V.D., 1990, Siliciclastic Sequence Stratigraphy in Well Logs, Core, and Outcrops: Concepts for High-Resolution Correlation of Time and Facies. In: American Association of Petroleum Geologists, Methods in Exploration Series 7, p. 55.

Vail, P.R., Mitchum Jr., R.M., Todd, R.G., Widmier, J.M., Thompson III, S., Sangree, J.B.,Bubb, J.N., Hatlelid, W.G., 1977, Seismic stratigraphy and global changes of sea-level. In: Payton, C.E. (Ed.), Seismic Stratigraphy – Applications to Hydrocarbon Exploration. AAPG Memoir 26, pp. 49–212

Walker, R. G., N. P. James., and 1992, Facies Models: Response to Sea Level Changes: Geological Association of Canada, doi:10.1097/00000433-198206000-00020.

Wright, K. A., 2013, Seismic Stratigraphy and Geomorphology of Palaeocene Volcanic Rocks, Faroe-Shetland Basin. PhD Thesis.

Yilmaz, O., 2001, Seismic Data Analysis: Processing, Inversion, and Interpretation of Seismic Data. No. 10, Investigations in Geophysics, Soc. of Exploration Geophysicists, Tulsa.

Chapter 3

Stratigraphy of Architectural Elements in a Buried Polygenetic Volcanic System and Implications for Hydrocarbon Exploration

3 Stratigraphy of Architectural Elements in a Buried Polygenetic Volcanic System and Implications for Hydrocarbon Exploration

3.1 Abstract

The interaction between magmatism and sedimentation creates a range of petroleum plays at different stratigraphic levels due to magma emplacement, eruptions and burial of volcanoes in sedimentary basins. This study characterises the spatio-temporal distribution of the fundamental building blocks (i.e. architectural elements) of a buried composite volcano and enclosing sedimentary strata, to provide insights for hydrocarbon exploration in volcanic systems. We use a large dataset of wells and 2D-3D seismic reflection surveys from the offshore Taranaki Basin, New Zealand, compared with outcropping volcanic systems worldwide to demonstrate the local impacts of magmatism on the evolution of the host sedimentary basin and petroleum system. Here we reveal the architecture of Kora Volcano, an andesitic polygenetic composite volcano that was erupted submarine during the Miocene and is currently buried by more than 1000 m of sedimentary strata.

Twenty two individual architectural elements have been characterised within three main stratigraphic sequences of the Kora Volcanic System (KVS). These sequences are referred to as pre-magmatic (predate magmatism), syn-magmatic (defined by the occurrence of intrusive, eruptive and sedimentary architectural elements) and post-magmatic (controlled by degradation and burial of the volcanic structures after magmatism ceased). Potential petroleum plays were identified based on the distribution of the architectural elements and on the geological circumstances resulting from the interaction between magmatism and sedimentation. At the endogenous level, emplacement of magma forms structural traps such as drag folds and strata jacked-up above intrusions. At the exogenous level, syn-eruptive, inter-eruptive and post-magmatic processes mainly form stratigraphic and paleogeomorphic traps such as interbedded volcano-sedimentary deposits, and upturned pinchout of volcanogenic and non-volcanogenic coarse-grained deposits onto the volcanic edifice. Potential reservoirs are located at systematic vertical and lateral distances from eruptive centres. This study demonstrates that identifying the architectural elements of buried volcanoes is necessary for building predictive models and for de-risking hydrocarbon exploration in sedimentary basins affected by magmatism.

3.2 Introduction

In recent years, petroleum exploration in and around volcanic systems have met with some commercial success, although understanding of how individual buried volcanoes perturb petroleum systems is often incomplete. The potential of volcanic systems to accumulate economic petroleum resources has been known since the middle of last century. Ongoing production from the Green Tuff formation in Japan, rhyolites, tuffs and conglomerates of the Qingshen field in China, volcano-sedimentary sequence of Rosebank Field in the North Sea, and fractured basalts of the Cabiúnas Formation offshore Brazil are examples of successful hydrocarbon exploration in volcanic settings.

Such "volcanic systems" are here defined as a "set of interrelated elements that form a complete magmatic-sedimentary complex, i.e. the pre-magmatic sedimentary strata deformed by magmatism, the syn-intrusive, syn-eruptive and inter-eruptive parts of the volcano, and the sedimentary strata that buried it". These systems typically form due to a combination of igneous and sedimentary processes, which can have both positive and negative impacts on petroleum systems. They have the potential to influence the geometry, locations and fluid-flow properties of source and reservoir units, the migration pathways of hydrocarbons, the integrity of traps, the maturity of hydrocarbons and the geothermal history of a basin (e.g. Stagpoole and Funnell, 2001; Schutter, 2002; Rohrman, 2007; Farooqui, 2009; Holford et al., 2012; Rateau et al., 2013). They also produce a wide variety of lithofacies with broad permo-porosity characteristics that can change laterally over distances of 10's to 100's of meters (Cas and Wright, 1993; Kennedy et al., 2017). Defining the large range of possible lithofacies in volcanic systems is very difficult during the initial exploratory phase of a prospect. The lack of information associated with the complexity of these systems leads to uncertainties that complicate the construction of models for predicting the occurrence of hydrocarbons. As a consequence of these knowledge gaps, exploration of some buried volcanoes may not be undertaken because they may have an unacceptably high commercial risk.

The present research examines the characteristics of intrusive and eruptive rocks for a buried polygenetic composite volcano (Kora Volcano) and their spatio-temporal relationships to background (non-volcanic) basin sedimentation. In this chapter we outline the distribution of the individual building blocks that compose the architecture of Kora Volcanic System (KVS). We show the location and relationship between diverse volcanic and sedimentary architectural elements,

discussing the main pre, syn and post-magmatic processes that control the morphology of the volcano and the distribution of associated sedimentary strata. These new insights help to de-risk hydrocarbon exploration of polygenetic volcanoes buried in sedimentary basins and improve the likelihood of finding commercially important petroleum resources both in New Zealand basins, which are studded with buried volcanoes, and internationally. In addition to hydrocarbon exploration in buried volcanoes, results from this research can provide important insights that can be applied to geothermal exploration.

3.3 Kora Volcano Geologic Setting and Exploration

Kora Volcano is part of a chain of more than 25 buried Miocene stratovolcanoes which form a NNE trending belt (here referred to as the Mohakatino Volcanic Belt or MVB) in the Northern Graben of the Taranaki Basin, New Zealand (Bergman et al., 1992; King and Thrasher, 1996; Seebeck et al., 2014; Figure 17).

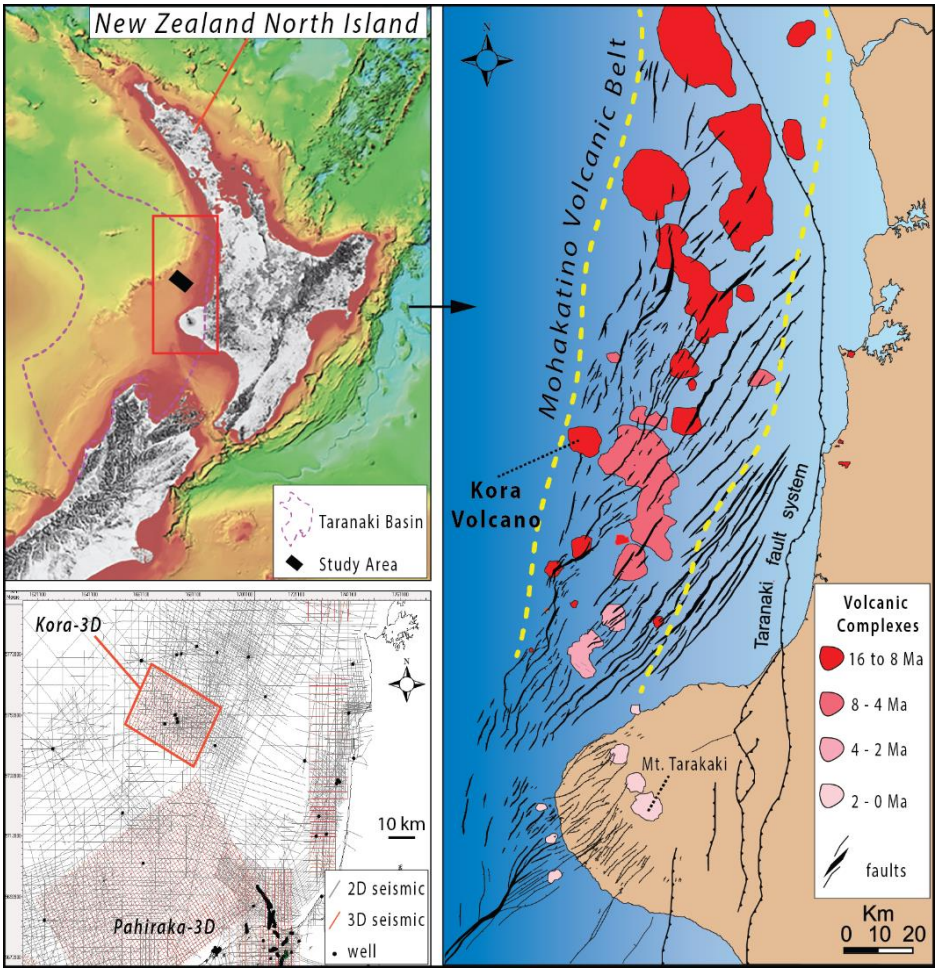

Figure 17: Location map of the study area and data set available. Kora is one of the volcanic complexes of the MVB, erupted from the Early Miocene to Late Pliocene in the Northern Taranaki graben. Detailed map modified from Giba et al. (2013).

These volcanoes young from Early Miocene in the north to the active Mount Taranaki volcano in the south (Giba et al., 2013). Based on their chemistry and location above the subducting Pacific plate, volcanoes in the MVB are interpreted to be part of an intra-arc system developed in response to dehydration of the westward subducting Pacific plate beneath the Australian plate (King and Thrasher, 1996; Seebeck et al., 2014). The southwest-dipping subduction zone in the northern part of New Zealand, associated with the subduction process along the Hikurangi margin (Nicol et al., 2007; Stagpoole and Nicol, 2008), uplifted and exposed large areas of Zealandia during the Neogene, providing voluminous sediment supply to the adjacent sedimentary basins. As a consequence, a thick sequence of slope and deep-water sediments were deposited in the offshore part of the Northern Taranaki graben. The composite volcanoes of the MVB were progressively buried by the shelf progradation during the last ca 20 Ma, producing a total basin fill thickness of up to 5 km thick for the Neogene interval. Basin-fill lithologies deposited during this time are dominated by interbedded mudstones, carbonates and deep-water sandstones that locally interfinger with volcanic rocks and volcaniclastic sediments originating from the MVB (King and Thrasher, 1996; Figure 18).

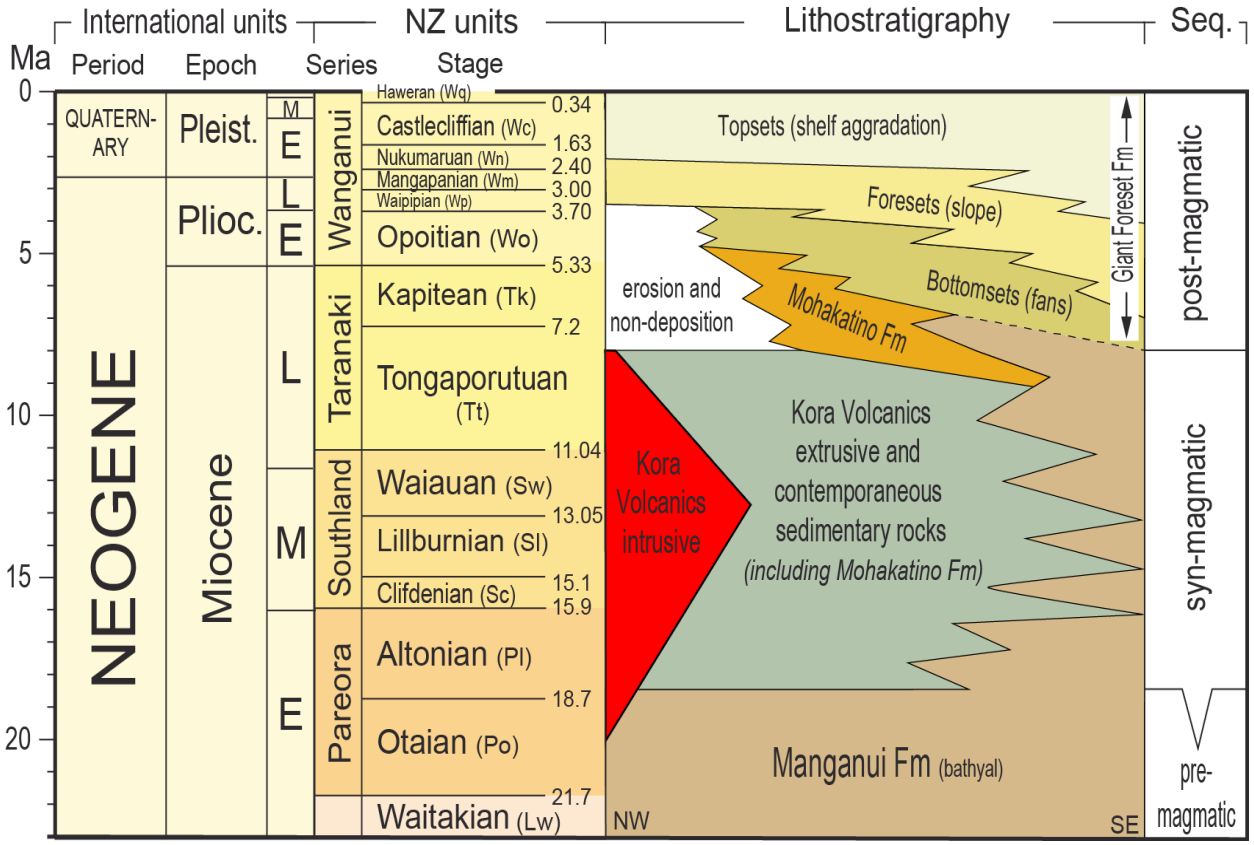

Figure 18: Local chronostratigraphic chart showing the age and occurrence of the main lithostratigraphic units in the study area. Compiled from Bergman et al. (1992), King and Thrasher (1996), OMV (2011), and insights from this study. Stratigraphic ages modified from the International Chronostratigraphic Chart 2014 and New Zealand Geological Time Scale 2015.

Kora Volcano has been drilled by five petroleum exploration wells which penetrated a range of lithologies including *sensu stricto* sedimentary rocks (non-volcanogenic), tuffs, lapilli-tuffs, hyaloclastites, tuff breccias, and epiclastic sandstones, conglomerates and breccias. Geochemical analyses show that the volcanic rocks mainly comprise low-to-medium potash, calc-alkaline andesites and subordinate basalts, suggesting that the magma was derived from partial melts of the asthenospheric mantle, and were not contaminated by continental crust during magma ascent (Bergman et al., 1992).

The age of these volcanic rocks has been constrained by radiometric dating of tuffaceous facies (K/Ar and Ar/Ar), foraminifera biostratigraphy and seismic stratigraphic analyses (Bergman et al., 1992; Giba et al., 2013; Seebeck et al., 2014). Radiometric dates indicate that intrusive magmatism commenced at ca 20 Ma. Kora Volcano was constructed on deep-water mudstones of the Early Miocene (18.7 - 15.9 Ma) Manganui Formation (previously called Mahoenui Formation). Volcanic style was predominate explosive, estimated to have started at ca 17 Ma, and eruptions continued until ca 8 Ma. The edifice is onlapped by both reworked volcaniclastic sediments onto the cone flanks, and by prograding marine sediments of the Giant Foreset Formation near the crest of the edifice. The youngest of the onlapping deep-water mudstones are 5.33 - 3.70 Ma in age, and the volcanic edifice was completely buried by no longer than 3.7 - 4.4 Ma (Bergman et al., 1992; King and Thrasher, 1996; Figure 18).

Oil and gas exploration of the MVB commenced in the 1960s with acquisition of 2D seismic reflection lines, while the first exploration well to encounter an offshore volcanic centre (Mangaa-1) was completed in 1970. In the mid 1980's petroleum company ARCO targeted a large structural dome at the level of potential Eocene deep-water reservoirs with the Kora-1 exploration well. Kora-1 penetrated a thick sequence of Miocene volcaniclastic rocks and encountered producible crude oil within proximal pyroclastic tuffs and volcanic conglomerate facies, confirming both the volcanic origin of the structural high and the hydrocarbon potential of the MVB (Bergman et al., 1992). Kora-1 was sidetracked by the well Kora-1A, recovering more than 100 m of continuous core to understand better the reservoir potential of the volcanic and associated sedimentary interval (Bergman et al., 1992). Three appraisal wells were subsequently drilled, recording only oil shows and the discovery was subsequently deemed subcommercial. Further exploration undertaken by OMV in 2006, with acquisition and processing of the Kora-3D seismic reflection survey, revealed a complex distribution of sedimentary and volcanic deposits and intense brittle deformation compartmentalizing the syn-magmatic sequence (OMV, 2005

and OMV, 2011). Despite previous exploration efforts, the potential of KVS to host commercial quantities of hydrocarbons remains incompletely understood.

3.4 Data and Methods

This chapter draws upon a dataset of 2D and 3D seismic reflection data and drill-holes (Figure 17) that penetrate Kora Volcano and the enclosing sedimentary rocks. Particular attention is given to the interpretation of 3D seismic reflection data which have been analysed using a range of geophysical techniques (e.g. mapping of chronostratigraphic surfaces, seismic facies and attribute analysis, geobody extraction and volume rendering), to reveal the main architectural elements of the volcanic system.

We utilize the sedimentological concept of architectural elements to understand better how volcanism interacts with sedimentation within the basin. In sedimentary geology, "architectural element" is a term used to describe individual depositional units that are the fundamental building blocks of landscapes and subsea morphology (Allen, 1983; Miall, 1985; Posamentier and Kolla, 2003). An architectural element is a three-dimensional genetically related rock unit characterised by its geometry, facies, composition and scale, and is the product of a particular process or suite of processes occurring within a depositional system (Miall, 2000). We analyse each one of these sedimentary and volcanic architectural elements individually, identifying the "best fit" interpretation for the geological processes that produced them. Each of these elements were positioned within a stratigraphic framework (Figure 19), which aids the identification of potential petroleum plays.

The techniques used to recognize the architectural elements follow two premises: i) characterisation of the three-dimensional seismic elements within the Kora-3D seismic reflection volume, and ii) analogy with elements outcropping in ancient and modern systems. The primary processes producing the 3D architecture of the KVS were inferred using both modern and fossil analogues and "ground truth" calibration of the seismic images with the lithofacies recovered from the drill-holes that penetrated Kora and the enclosing sedimentary strata. Analysis of the elements within the seismic reflection data include: mapping of seismic surfaces of chronostratigraphic and geotectonic significance, 3D volume visualization including techniques such as volume rendering, and (where possible) definition of criteria for interpretation of intrusive, extrusive or sedimentary bodies. Principles of seismic stratigraphy, sequence

stratigraphy, seismic geomorphology and structural analysis were applied to observe the lateral and vertical relationship between the architectural elements and to support interpretations of the geological system within the seismic volume (Mitchum et al., 1977; Planke and Alvestad, 1999; Catuneanu, 2006; Posamentier et al., 2007).

3.5 Stratigraphy of Architectural Elements of Kora Volcanic System

We have identified 22 individual architectural elements distributed in three distinctive stratigraphic sequences (pre, syn, and post-magmatic) associated with Kora Volcano and its enclosing strata (Figure 19 and Figure 20). They form by a combination of geological processes including magmatism, deformation, sedimentation, erosion and burial of the volcanic edifice, which control the occurrence and distribution of the architectural elements that together produce the three-dimensional architecture of the KVS. Sediments deposited during the pre-magmatic sequence and undeformed by magmatic processes are not considered further here. The syn-magmatic sequence is characterised by rock units formed during the emplacement of intrusive bodies, eruptions and time-equivalent sedimentation, as well as by deformation of pre-magmatic strata during magmatism. Sedimentary processes such as erosion and burial of the volcanic edifice are dominant during the post-magmatic sequence, after volcanism has ceased (Figure 19 and Figure 20).

3.5.1 Syn-Magmatic Sequence

The syn-magmatic sequence is bounded by the pre-and- post eruptive surfaces (PrErS and PoErS), which corresponds to the beginning and end of volcanism in the KVS respectively. At the intrusive realm, the syn-intrusive surface (SyInS) separates the KVS plumbing system from undeformed basinal sedimentary strata (Figure 19). This sequence comprises rock units formed during syn-intrusive, syn-eruptive and inter-eruptive events. Syn-intrusive architectural elements are characterised by both the magmatic intrusions and the resulting deformation of overlying strata. Syn-eruptive architectural elements are controlled by volcanic eruptions and include both the volcanic and the related sedimentary deposits triggered by eruptions, while inter-eruptive architectural elements are characterised by sedimentary deposits formed during periods of volcanic quiescence.

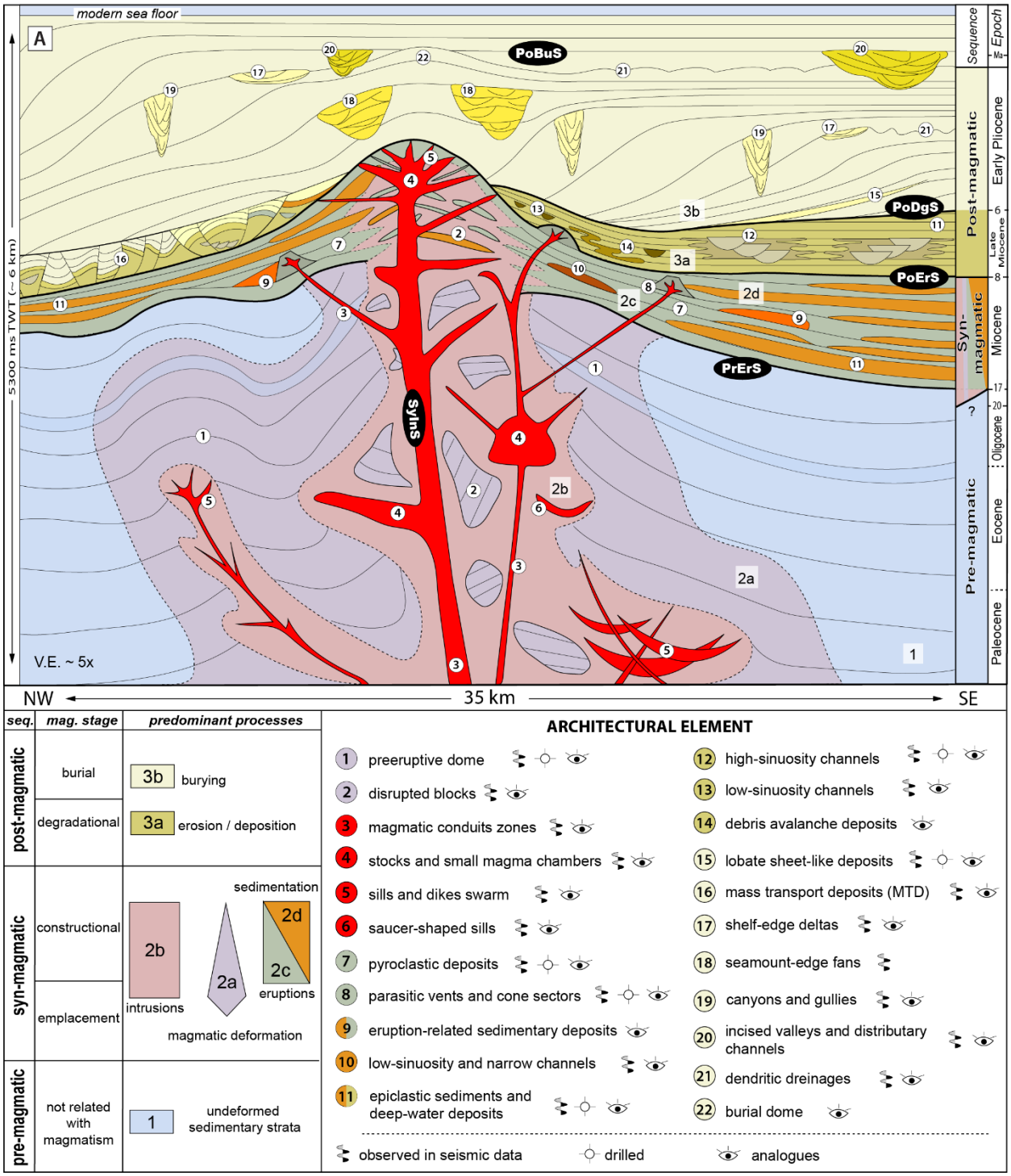

Figure 19: Schematic representation of the stratigraphic sequences, magmatic sequences, stages, architectural elements, and predominant processes associated with the Kora volcanic system. Numbers in circles represent the location of the architectural elements indicated in the key. Numbers in squares indicate predominant processes in the key. The symbols in the bottom part of the architectural elements key illustrate the database used on the interpretations. The terms “observed in seismic” represent architectural elements found in seismic data, “drilled” represent architectural elements sampled by wells, and “analogues” represent architectural elements recognized in modern and ancient analogues. Conduit zones and dikes have lateral thickness exaggerated for visualization proposes. Abbreviations are SyInS (syn-intrusive surface), PrErS (pre-eruptive surface), PoErS (post-eruptive surface), PoDgS (post-degradational surface) and PoBuS (post-burial surface). More details about these volcano-stratigraphic surfaces are in chapter 5.

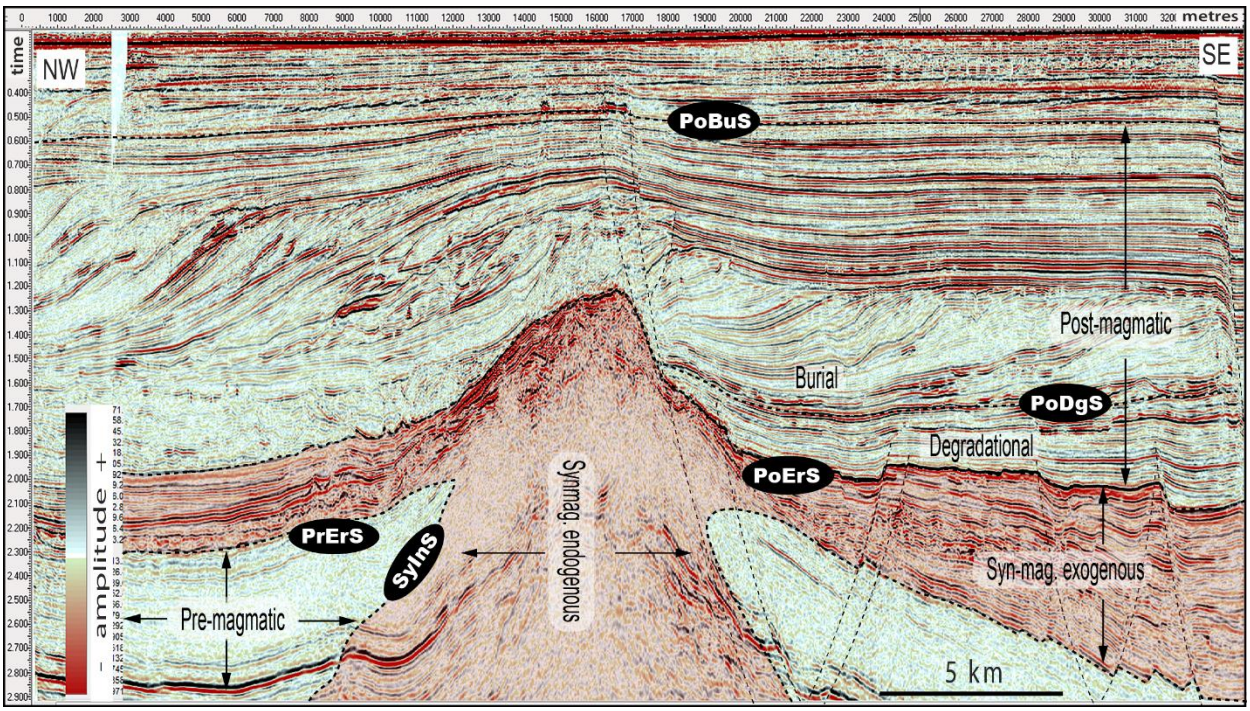

Figure 20: A 2D seismic section of the Kora volcano and a representation of the main stratigraphic sequences and processes. Note the progradation of clinoforms from the southeast to the northwest.

3.5.1.1 Syn-intrusive architectural elements: magma emplacement and deformation

Syn-intrusive architectural elements include saucer-shaped sills, sills and dikes swarms, stocks and small magma chambers, and magmatic conduits zones. These elements primarily occur at sub-volcanic depths (between 3000 to 5000 ms TWT on the seismic data) and are best imaged at the periphery of the volcanic core (Figure 21 to Figure 24). Saucer-shaped sills range from 1.5 to 4.5 km in cross-sectional width, have lobate geometries in plan view and magma finger structures at the terminations of the sills (Figure 22). When sills occur in isolation, they usually produce little deformation of the immediately overlying strata (Figure 22C), while intrusion of dike and sill swarms often dome overlying strata (Figure 23A and Figure 23B). Many of the deeper dike and sill complexes coincide with normal faults from Late Cretaceous and Miocene rifting, suggesting that magma may have utilized these structures to rise through the crust.

Shallow intrusions are not easily recognized from 3D seismic data beneath of the volcanic edifice due to its reflection-free and chaotic seismic character, which make composition of high resolution images difficult (Figure 23A and Figure 24B). One possible explanation for the loss of seismic reflectivity within the edifice is that the volcanic cores are highly anisotropic due to the presence of alternate lithologies (due to metasomatic and meteoric alteration), discontinuous intrusive geobodies with a range of size, shape (e.g. plugs, stocks and small magma chambers), and inclination (e.g. crystalline magmatic conduits, dikes, saucer-shaped and transgressed sills).

The presence of radial dike swarms is likely to occur at shallow levels associated with isolated cone sector and parasitic vents, which can be inferred by observation on outcropping ancient and modern volcanoes elsewhere (e.g., Hampton and Cole, 2009).

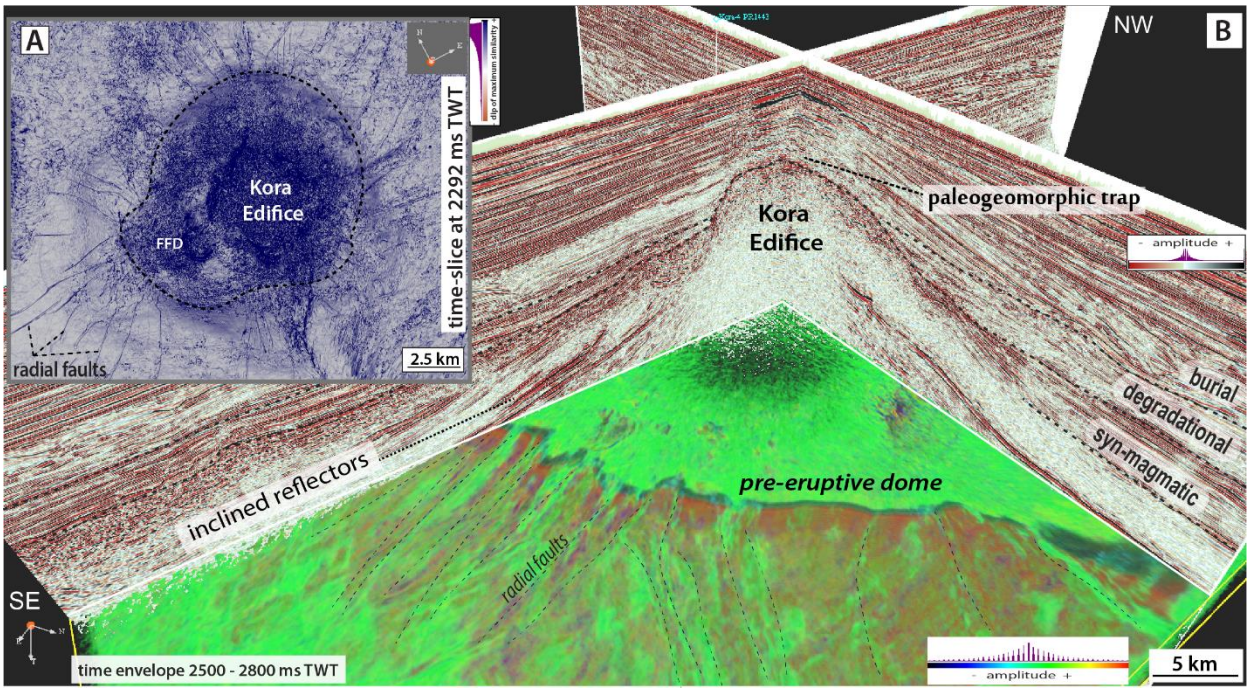

Figure 21: Seismic images of pre-magmatic strata deformed during magma emplacement. (a) Time slice in dip of maximum similarity seismic cube showing faults in radial pattern and the circular structure of the Kora volcano. The FFD is a forced-folded dome pushed up by underlying sills and dikes intrusions. (b) Inline and crossline sections of the Kora volcano combined with a volume rendering seismic envelope showing the pre-eruptive dome (evident in red, corresponding to the Tangaroa Formation).

Some seismic images of high amplitude reflectors with irregular morphology in plan view and 1 to 2 km in diameter have been observed beneath the Kora volcanic edifice. The reflectors enclosing these bodies are strongly deformed, being disrupted and cross-cut by a range of structures including folds, normal faults and reverse faults (Figure 24B). Drill-holes in the Kora Volcano do not sample either the high amplitude reflectors or the enclosing deformed strata, however, based on their seismic characteristics and analogy with outcropping volcanoes (e.g., Sewell, 1988) we interpret these features to be semi-spheroidal plutonic bodies such as stocks and small magma chambers that deformed pre-magmatic sedimentary rocks during their emplacement (Figure 24B).

Magmatic conduits or conduit zones are interpreted in the seismic data based on the occurrence of sub-vertical seismic discontinuities that cross-cut pre-magmatic strata beneath the volcano and are linked with mound-like structures at shallower stratigraphic levels, which have been interpreted to be parasitic and satellite vents, and cone sectors of Kora Volcano (Figure 24). In

plan view these features display a semi-circular shape varying in diameter from 0.1 to > 2 km and are best imaged at the periphery of the volcanic core, where we identify 69 potential magmatic conduits and their associated parasitic, satellite vents and cone sectors.

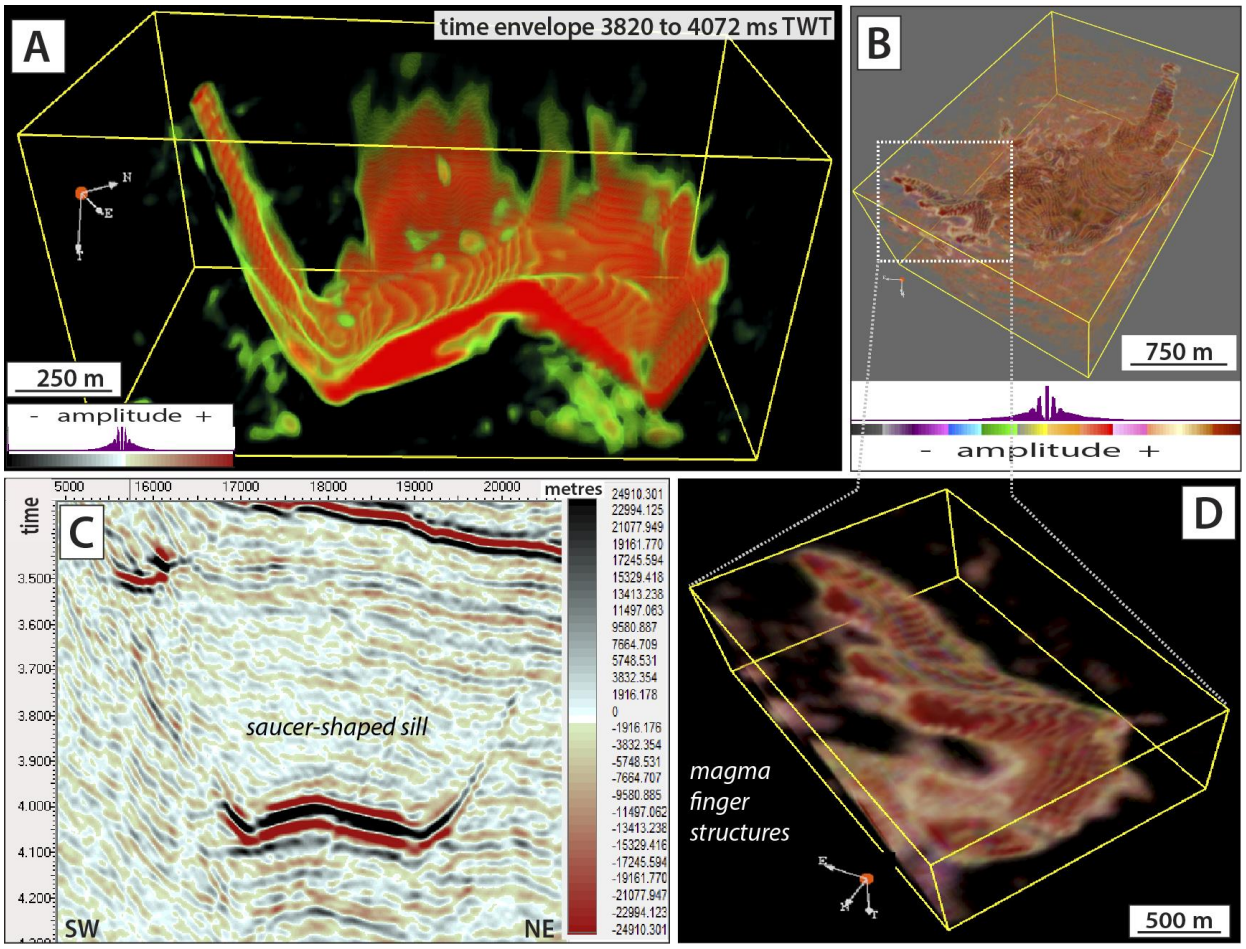

Figure 22: Seismic images of syn-intrusive architectural elements. (a) High-amplitude geobody extraction revealing the 3D geometry of a saucer-shaped intrusion. (b and d) Detail of the intrusion showing a semi lobate body in plan view with magma-fingers structures at the terminations. (c) The 2D cross section of the amplitude anomaly.

Magma ascent and emplacement can deform large areas of pre-magmatic strata in the sub-volcanic part of Kora edifice, forming a semi-circular structural high more than 25 km in diameter (Figure 19 and Figure 21), here referred to as the pre-eruptive dome. Cross-sections of the volcanic edifice show pre-magmatic sedimentary strata with symmetrical double-flapped geometry, tilted away from the main vent complex (Figure 23A). This dome structure formed in association with small displacement (e.g. < 50 ms) radial normal faults that diverge from the eruptive centre and accommodate radial extension of the Oligocene uplifted strata (Figure 21; OMV, 2010). The pre-eruptive dome underlies sub-horizontal reflectors from the exogenous part of the syn-magmatic sequence and is marked by an angular unconformity at the top (Figure 26). This angular relationship suggests that the area beneath the cone experienced inflation and

ground dilatation during the early syn-magmatic sequence and, prior to, the initial eruptive events, probably due to the emplacement of magma at the upper crust (e.g., < 10 km depth) beneath Kora Volcano. Ground dilatation and doming during magma emplacement is commonly observed in modern volcanoes (e.g. Wicks et al., 2002; Pritchard and Simmons, 2004; Lu et al., 2009). Similar structural styles are also observed in regions deformed by salt tectonics, which produce flexure and stretching of overburden strata above salt diapirs, forming positive structural relief due to vertical deformation (Schultz-Ela et al, 1993). In addition to intrusion, faulting and folding, seismic imaging of the sub-volcanic zone suggests the presence of disrupted pre-magmatic blocks among the syn-intrusive bodies.

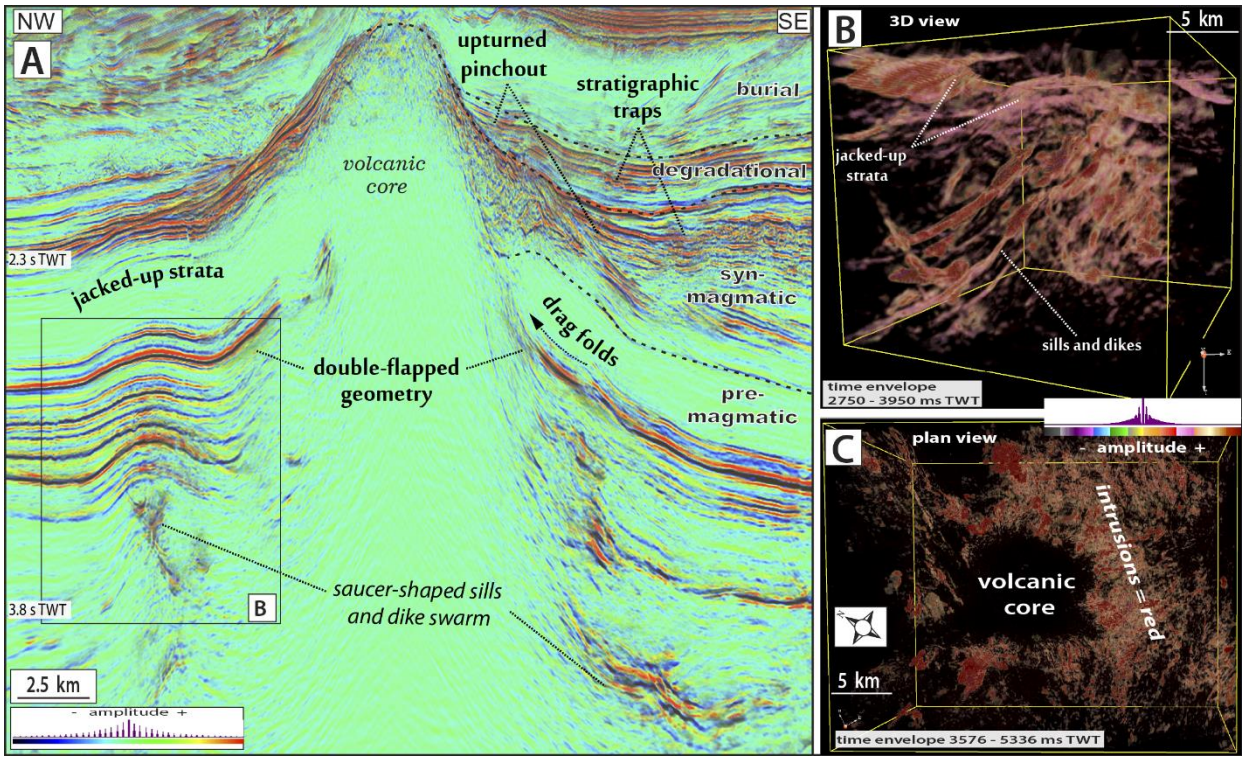

Figure 23: Seismic images of syn-intrusive architectural elements. (A) Cross section applying the optical stacking technique. (B) Geobody extraction of high-amplitude anomalies (red) showing sill and dikes jacking-up the overlaying sedimentary strata. (C) Volume rendering envelope showing the distribution of high-amplitude geobodies. Note that the bodies are concentrated toward the southern and eastern part of the seismic cube, region where the Miocene rift faults are more frequent and present larger displacement.

3.5.1.2 Syn-eruptive architectural elements: eruptive deposits and eruption-related sedimentary deposits

Syn-eruptive architectural elements of KVS occur on seismic data between 1300 to 2400 ms TWT and include volcanic cone sectors, parasitic and satellite vents, pyroclastic deposits and eruption-related sedimentary deposits (Figure 19 and Figure 24 to Figure 27). They comprise the exogenous part of the syn-magmatic sequence and are a direct consequence of volcanic

eruptions. Proximal to the main vent complex, high amplitude, inclined, discontinuous, disrupted and amalgamated reflectors diverge from the eruptive centres in a radial pattern, while distal from the volcanic cone a distinctive seismic facies of parallel, sub-horizontal and continuous high amplitude reflectors are intercalated in a stacking pattern (Figure 25). This geometric configuration is recognized in modern subaerial andesitic volcanoes, including those of the Tongariro Volcanic Complex, in New Zealand (Figure 25). In the proximal parts of the Ngauruhoe and Red Crater volcanic edifice, air fall, pyroclastic density currents and lava flow deposits show long, narrow and channelized geometry diverging in a radial pattern from the eruptive vents. With increasing distance from the vent and the decreasing topographic gradient of the cone, these channelized systems bifurcate to produce large lobate and continuous deposits. Over time, successive flows form amalgamated, inclined and discontinuous deposits on the flanks of the volcano, and stacked sub-horizontal and parallel deposits on distal parts of the cone (Figure 25).

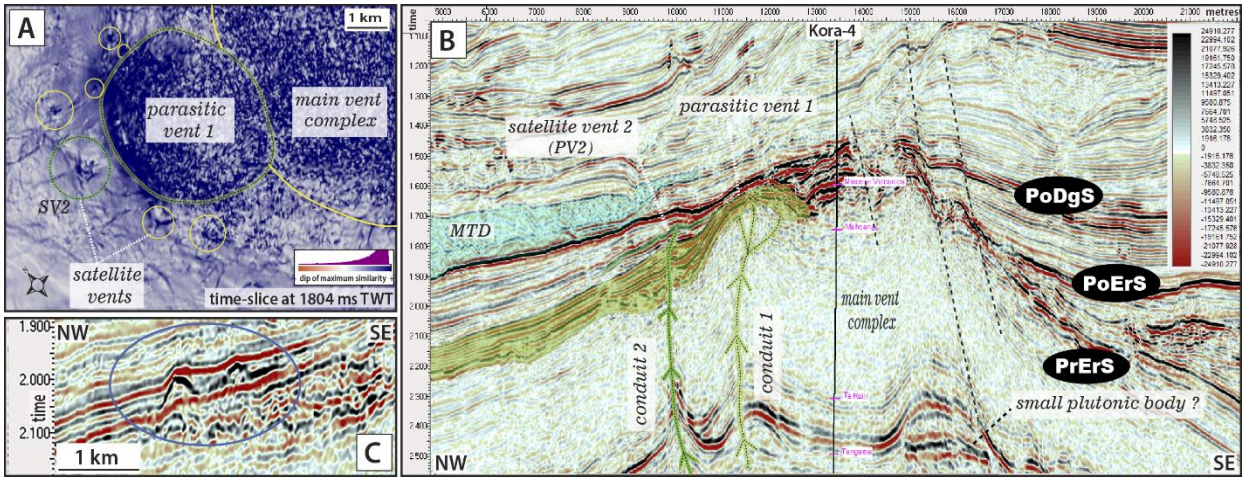

Figure 24: Seismic images of syn-intrusive and syn-eruptive architectural elements. (A) Time slice through the dip of maximum similarity seismic cube at 1084 ms TWT. The darker blue colours represent the core of parasitic vents and cone sectors, whereas the lighter blue colours represent sedimentary strata that onlap these structures. Note the radial pattern of lineaments associated with the smaller parasitic and satellite vents circled in yellow and green. (B) The 2D cross section showing the relationship of parasitic vents and conduit zones. (C) A 2D cross section showing mount-like structures interpreted to be small parasitic vents.

In 2D seismic sections the syn-eruptive interval contains several high amplitude reflectors with mound-like morphology onlapped by the above younger reflectors (Figure 24C). In plan view, these mound-like bodies display semi-circular geometry varying from 15 km in diameter (main Kora vent complex) to tens of meters around the margins (Figure 24A). Each mound-like seismic anomaly is usually rooted in an intrusive geobody interpreted to be related with a magmatic conduit (Figure 24). Based on the available seismic data and analogy with outcropping volcanoes (e.g. the large polygenetic Miocene andesitic volcanoes of Lyttelton and Akaroa, New Zealand

South Island; Hampton and Cole, 2009), we interpret these mound-like features to be small parasitic and satellite vents, and cone sectors, formed as a consequence of multiple eruptive centres building up the final morphology of the composite Kora Volcano in association with the main central vent zone.

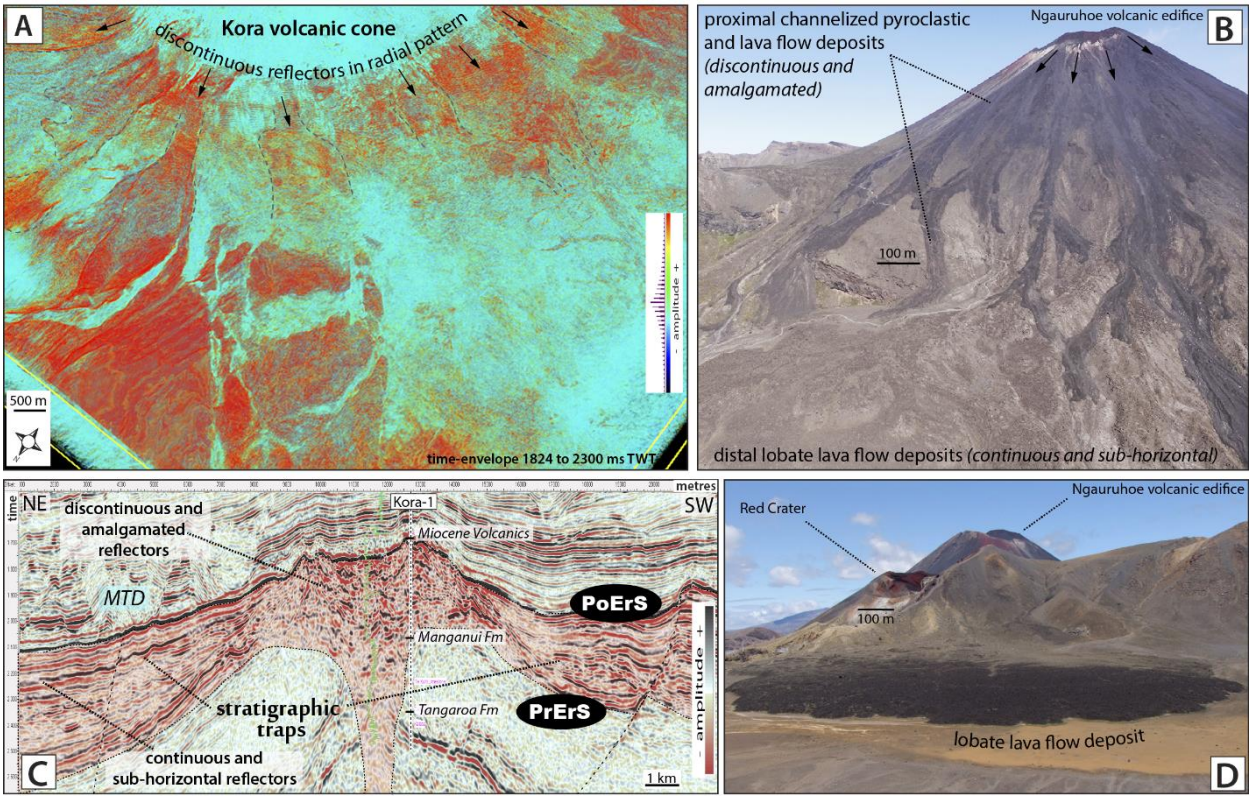

Figure 25: Seismic images and outcrop analogues representing the syn and inter-eruptive architectural elements of Kora volcanic system. (A) Volume rendering envelope showing the northwest part of Kora volcano. Note that discontinuous high-amplitude reflectors diverge outward from the main vent complex (red). (B and D) Geometry of eruptive (air fall, pyroclastic density currents, and lava flow deposits) and epiclastic deposits on Ngauruhoe volcano and Red Crater, Tongariro National Park, New Zealand. Note that on the flanks of the volcano, the deposits are amalgamated and discontinuous, and in the foothills, deposits form continuous and lobate bodies. (A and C) These geometric patterns are also recognized in seismic images of the Kora volcano.

Syn-eruptive architectural elements of KVS comprise a range of volcaniclastic lithologies sampled by five exploratory wells. Drill cores that penetrate the exogenous syn-magmatic sequence recovered pyroclastic lithologies such as tuffs, lapilli-tuffs, hyaloclastites and tuff breccias, as well as epiclastic sandstones, volcanic conglomerates and volcanic breccias (Bergmann et al., 1992; Figure 27). By analogy with processes observed on modern volcanoes we suggest that the syn-eruptive interval of KVS may contain volcanic eruptive deposits together with sedimentary deposits triggered by eruptions and earthquakes (e.g. eruption-related debris-avalanche deposits formed on 18 of May 1980 during the lateral blast of Mount St Helens; Lipman and Mullineaux, 1982). Based on the available seismic and well data, distinguishing eruptive volcanic

deposits (e.g. pyroclastic deposits) from eruption-related sedimentary deposits or from epiclastic inter-eruptive sedimentary deposits is not always possible.

The basal interval of the Kora wells shows very high density and low gamma ray signatures and may represent lava deposits (Bergmann et al., 1992). Seismic images of this basal interval shows a distinctive pattern of parallel, sub-horizontal and continuous high amplitude reflectors with lobate terminations confined to the base of the paleo-volcanic edifice, which may suggest that the initial stages of volcanism of the Kora Volcano had an effusive contribution.

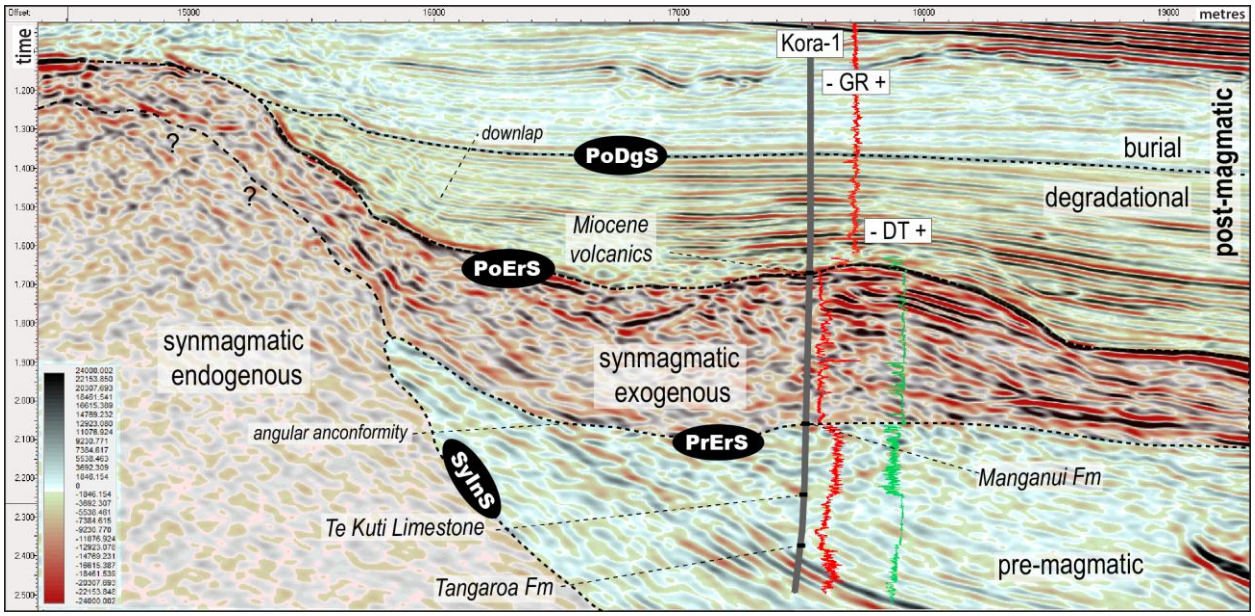

Figure 26: A 2D seismic section showing the endogenous and exogenous part of the syn-magmatic sequence, overlaying strata from the pre-magmatic sequence and covered by strata from the post-magmatic sequence. The 3D seismic cube is tied with lithofacies and well logs drilled on the wells (e.g., Kora-1, red = gamma ray and green = density).

3.5.1.3 Inter-eruptive architectural elements: epiclastic deposits and contemporaneous non-volcanogenic deposits

Volcanic eruptions are short-lived events compared to the total history of volcanism. During periods of eruptive quiescence, normal surface process of erosion, transportation and redeposition dominate in volcanic terranes and can operate at very high rates (Cas and Wright, 1993). Inter-eruptive architectural elements result from the interplay between the volcanic morphologies created during eruptions and the contemporaneous non-volcanogenic sedimentary systems that degrade and interact with the volcanic forms. In KVS, the interpretation of seismic reflection data and correlation with wells suggest that the inter-eruptive architectural elements comprise a succession of epiclastic and deep-water deposits. Lithologies recovered in the Kora wells confirm that the exogenous portion of KVS syn-magmatic sequence

contains an intercalation of sedimentary and eruptive deposits (Bergmann et al., 1992; Figure 27) that are the product of recurrent syn-eruptive and inter-eruptive processes over approximately 10 Ma. Wells tens of kilometres distal from Kora Volcano (e.g. Wainui-1, Awatea-1 and Ariki-1) demonstrate that the lithofacies recovered in Kora wells vary laterally from volcanogenic deposits (closer to the eruptive centre) to *sensu stricto* sedimentary rocks deposited in deep-marine environments away from the volcano, which is consistent with facies models proposed for terrestrial volcanic terranes (e.g. Cas and Wright, 1993; Orton, 1996; Figure 19). Seismic attribute analysis and volume rendering of Kora-3D reveal narrow and straight channels with lobate terminations on the flanks of the volcano that may represent gravitational deposits (e.g. debris avalanche deposits), however the lithology and origin of these deposits remains unclear and they could be formed either by sedimentary and/or volcanic processes.

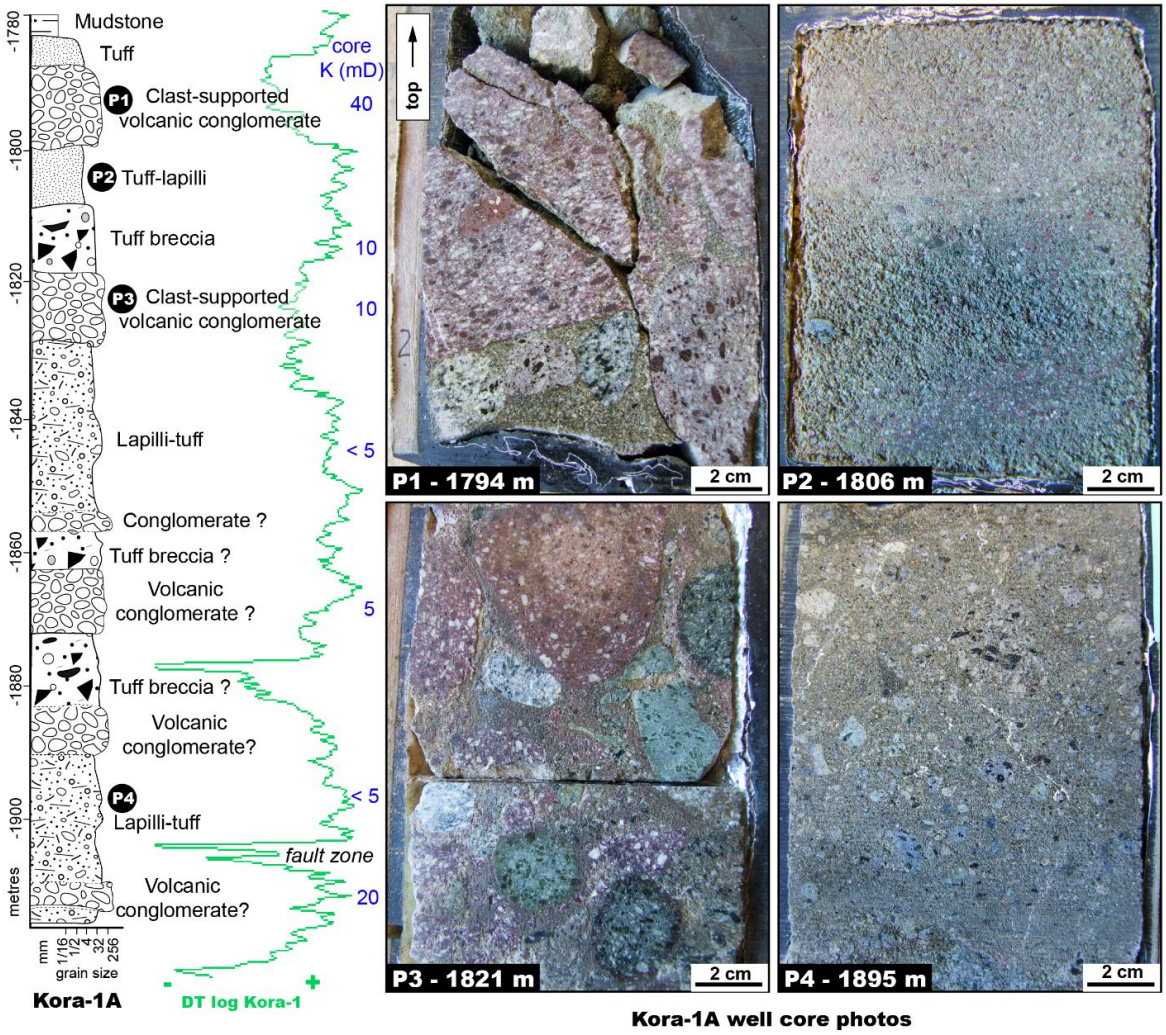

Figure 27: Well-core description and photographs of the main lithofacies recovered on the Kora-1A well. The green curve is the density log from Kora-1, located 50 m from Kora-1A. Numbers in blue are permeability measurements from Kora-1A cores. P1: Polymictic (more than three types of volcanic clasts) clast-supported, rounded volcanic conglomerate with sandy matrix; P2: well-sorted tuff; P3: polymictic clast-supported, well-rounded volcanic conglomerate; and P4: moderately sorted lapilli-tuff.

3.5.2 Post-Magmatic Sequence

Radiometric dating, changes in the pattern of seismic reflectors and correlation with biostratigraphic data from wells indicate that the volcanism in Kora ended around 8 Ma ago (Bergmann et al., 1992; King and Thrasher, 1996; Figure 18 and Figure 19). After volcanism had ceased, degradation and burial of the volcanic edifice controlled the local stratigraphic succession and the occurrence of specific architectural elements in KVS. This sequence can be sub-divided into degradational and burial stage.

3.5.2.1 Degradational stage: rate of erosion > rate of burial

The degradational stage is marked by high rates of degradation of the volcanic edifice. The top of the gradational stage is characterised by an arbitrary surface for which the rate of burial exceeds the rate of degradation (PoDgS). In KVS it is characterised by the last occurrence of chaotic seismic facies diverging from the cone with downlap termination covering syn-magmatic strata on the flanks of the volcanic edifice (Figure 26). These seismic facies vary laterally to continuous and parallel reflectors that represent the sediments deposited in deep-water settings, sampled in wells tens of kilometres from Kora Volcano. In the Parihaka-3D and Kora-3D seismic volumes (Figure 17), the degradational interval contains a range of architectural elements such as channels, lobes and fans that interact with the volcanic edifices (Figure 28 to Figure 30), demonstrating that erosion, transportation and re-deposition of materials sourced from volcanic centres impacted the local basin architecture. Some of these architectural elements (e.g. low-sinuosity channels and deposits with lobate terminations; Figure 28A and Figure 29C) appear to be sourced from the paleo-edifice, suggesting that sedimentation is not exclusively controlled by source-to-sink pathways, and in marine settings can also be influenced by the presence of volcanic highs. Strata deposited during the degradational stage are well preserved on the south eastern side of Kora Volcano, occurring between 1650 and 1950 ms TWT. Towards the northwest, the degradational sub-sequence has been completely deformed and eroded by younger gravitational flows (mass transport deposits of the burial period, subsequent described) due to seafloor collapses during the development of a slope and basin morphology (Figure 19, Figure 24B and Figure 25E).

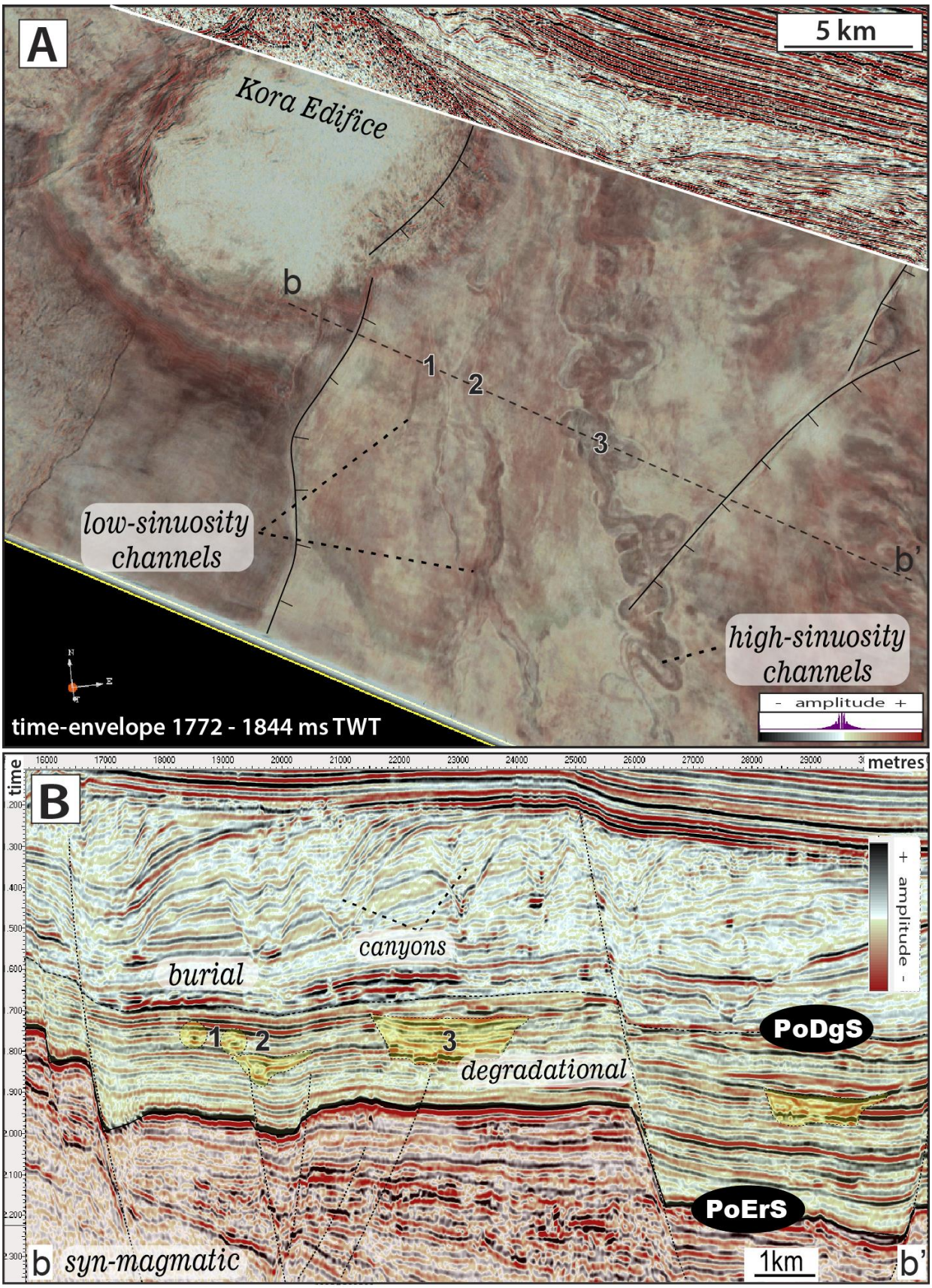

Figure 28: Seismic images of architectural elements formed during the degradational stage. (a) Composite cross section and volume rendering envelope showing the Kora volcano and the relationship with Late-Miocene to Pliocene deep-water channel systems. (b) Detailed 2D cross sections showing low sinuosity (1, 2) and high-sinuosity channels (3).

In the KVS region, the upper limit of the degradational stage is marked by reflectors that show progradation of clinoforms from southeast to northwest, known to as the Giant Foreset Formation (Figure 18, Figure 19, Figure 26, Figure 28B and Figure 30; Beggs, 1990). The timing of cessation of the degradational stage can be tentatively inferred from the Mangaa-1 and Awatea-1 wells (30 km NE of Kora) where the transition from volcaniclastic (Mangaa C sand) to siliciclastic and calcareous sands (Mangaa B and A sands) occurred in the Lower Opoitian at approximately 4-5 Ma (Fletcher, 1996; Figure 18).

High and low-sinuosity channels deposited in deep-water settings commonly occur in the KVS degradational stage (Figure 28 and Figure 29). The low-sinuosity channels are narrower (ca 300 m wide) and straighter closer to the flanks of the volcano, and are wider towards the south (ca 1000 m wide). Dispersed discontinuous high amplitude blocks trending parallel to the longitudinal axis of the low-sinuosity channels may correspond to debris avalanche deposits sourced from the Kora edifice (Figure 29C). High-sinuosity channels occur where the topographic seabed gradients are less steep, ca 5 km southeast of the flanks of Kora Volcano. These channels present a N-S longitudinal depositional axis varying from ca 1 km wide and less sinuous in the north part of the Kora-3D, to 3 km wide and very sinuous towards the south (Figure 28 and Figure 29). The high-sinuosity channels can be tracked for more than 60 km south of the Kora-3D area, within the same stratigraphic interval on the Parihaka-3D seismic volume. Towards the north, these channels have been incorporated into mass transport deposits (MTD) of the burial stage. In 3D seismic images, it is still possible to recognize parts of the meandering system preserved in large slumped blocks. The source of the sediments that feed the channels of the degradational stage remains unclear. Analysis of the seismic data together with sedimentation models proposed by Vonk and Kamp (2008) and Hansen and Kamp (2008) suggest that deep-water systems were at least partly sourced from the submarine volcanoes of MVB during Late Miocene to Early Pliocene, interfingering with deposits of the Mount Messenger Formation sourced from a land mass to the south (King and Thrasher, 1996; Shumaker, 2016).

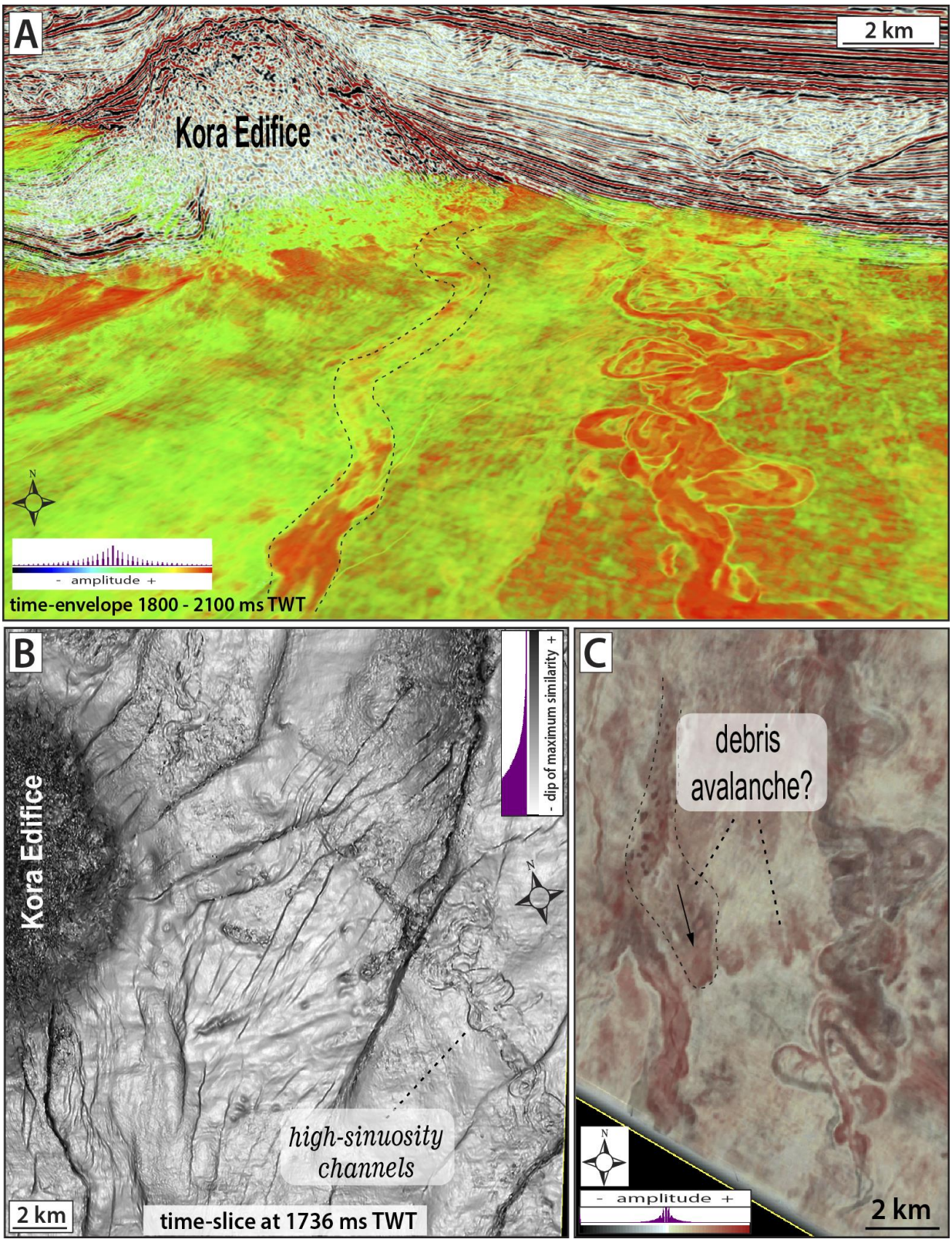

Figure 29: Seismic images of architectural elements formed during the degradational stage. (a) Composite cross section and volume rendering showing the Kora volcano and the relationship with deep-water channel systems. (b) Time-slice on the dip of the maximum similarity cube showing faults in the radial pattern (closer to the cone) interfering with the northeast faults from the Miocene rift. Note that some of the faults are compartmentalizing the high-sinuosity channel deposits. (c) Volume rendering envelope showing low and high deep-water channels and possible debris avalanche deposits.

3.5.2.2 *Burial stage: rate of erosion < rate of burial*

The beginning of the burial stage is marked by the PoDgS, which represent the time when the rate of burial exceed the rate of degradation, while its end is characterised by and arbitrary surface that limits the relative influence of MVF basin architecture (PoBuS). Data from wells in combination with seismic reflection analysis indicate that Kora Volcano was constructed in a deep-water setting and progressively buried in slope to shelf environments (Bergmann et al., 1992; King and Thrasher, 1996; Fletcher, 1996; Hansen and Kamp, 2008). In the Northern Taranaki graben, the base of the burial stage is marked by clinoforms prograding from southeast to northwest during the Late Neogene regression. Seismic attribute analysis and volume rendering images from Kora-3D reveal that the volcanic edifice strongly influenced the development of the enclosing sedimentary systems, persisting for some millions years after the complete burial of the volcano (Figure 30 to Figure 33).

Lobate sheet-like deposits occur at the base of the burial interval and are characterised by high amplitude and semi-continuous reflectors with bottomset terminations (Figure 30B and Figure 30C). In plan view, these deposits display narrow and straight channels ca 200 m wide with lobate terminations, varying from 3 to 5 km wide (Figure 30A). These bodies are stacked in front of the steep southeast facing flanks of the extinct volcanic edifice (Figure 30) and mark the initial stages of the installation of a slope-to-basin morphology in KVS area.

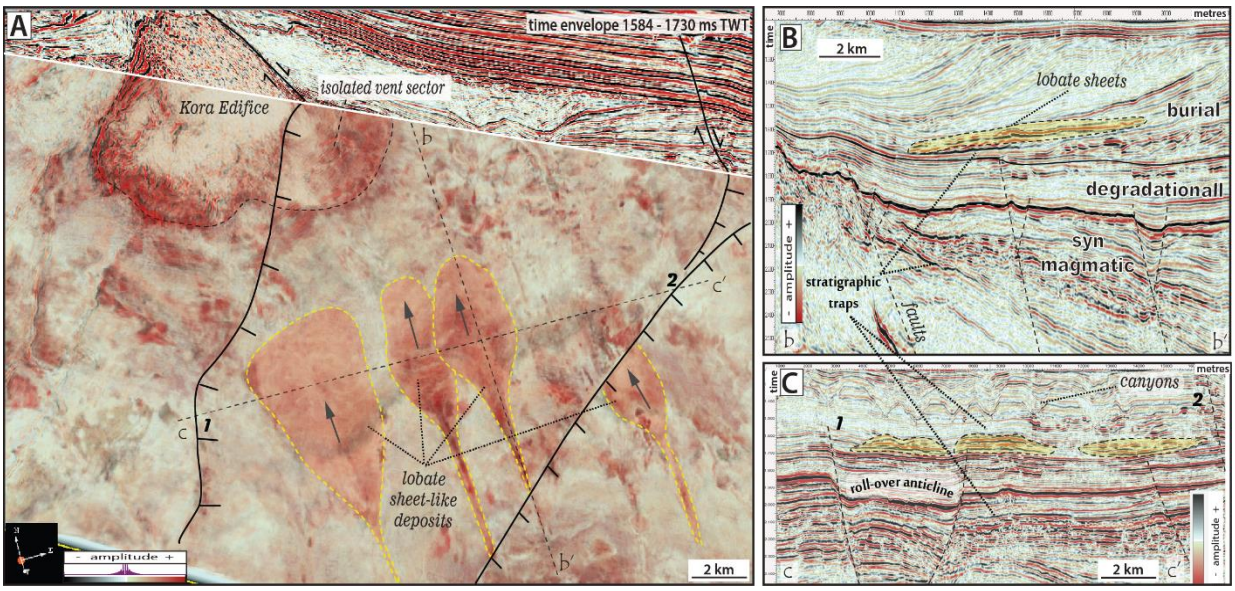

Figure 30: Seismic images of architectural elements formed during the burial stage. (a) Composite cross section and volume rendering envelope showing the Kora volcano and the lobate sheet-like deposits. (b) Dip section showing the lobate sheet-like deposits in detail. Note the foreset indicating migration of clinoforms from the southeast to northwest at the burial interval. (c) Cross section showing the lobate sheet-like deposits perpendicular to the paleo-depositional direction. Note that most of faults do not displace sediments deposited during the burial period.

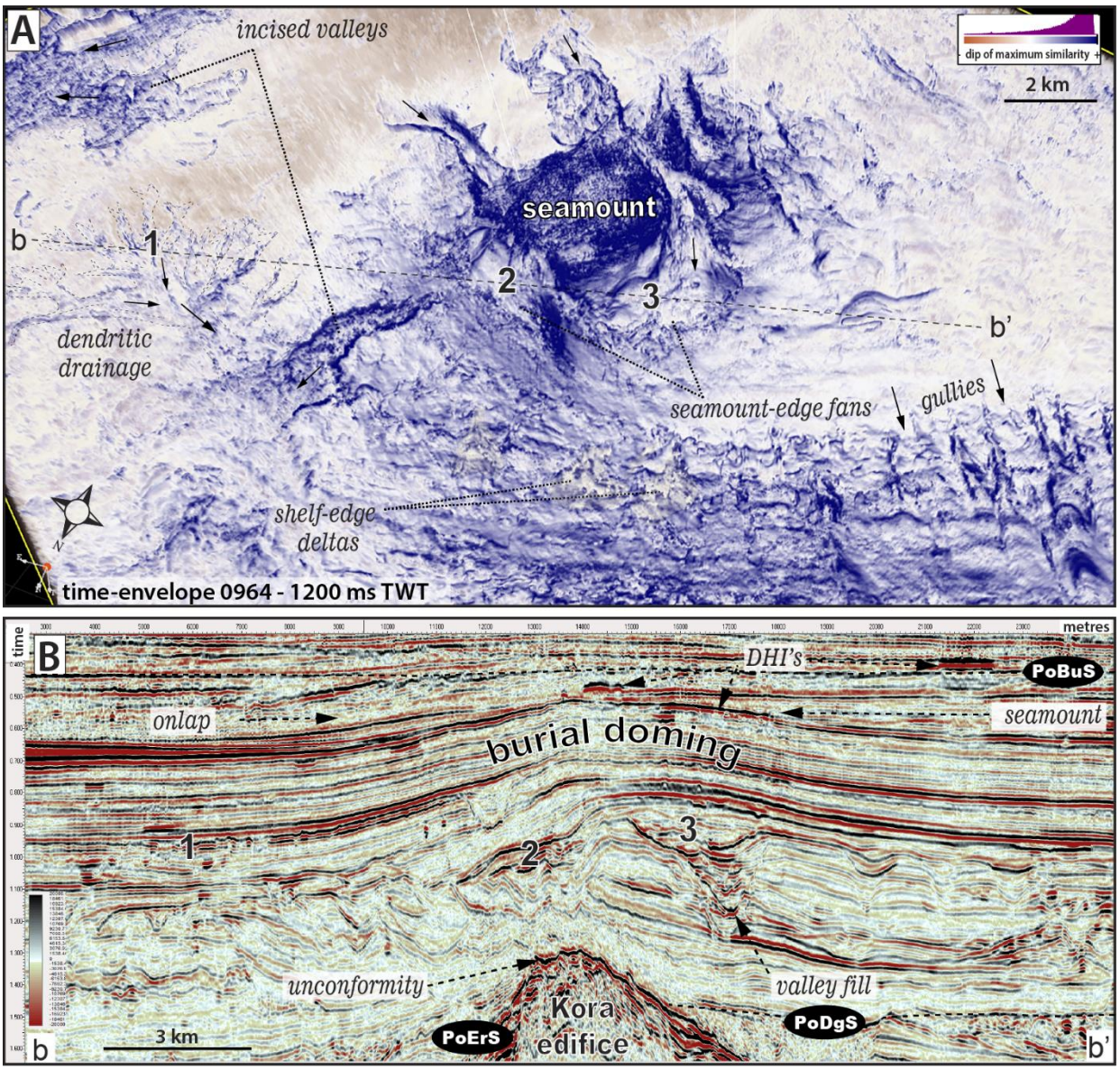

Figure 31: Seismic images of the architectural elements formed during the burial period. Note the dome over the buried Kora volcano and the sedimentary systems that interact with the second seamount. The volcanic edifice was completely buried by approximately 4 Ma ago and still had a strong influence on the development of sedimentary systems until at least the Pleistocene. (a) Dip of maximum similarity cube showing the location of the buried Kora volcano and the development of fans, deltas, dendritic drainages, gullies, and canyons during the progradation of the slope (northwest) and establishment of a shelf (southeast) in the region. (b) A 2D cross section showing the seamount over the volcanic edifice.

Towards the north western part of Kora Volcano, a large mass transport deposit (MTD) occurs between 1600 and 1950 ms TWT (Figure 19, Figure 24B and Figure 25C). This MTD deposit is characterised by chaotic and disrupted reflectors with internal normal and reverse faults. The inferred slide surface trace of the MTD is parallel to the NE-SW strike of Cretaceous faults, concordant with the strike of major Miocene and younger normal faults. Analysis of the seismic data shows that the transport direction of the MTD was from SE to NW, suggesting that this catastrophic event is related with the construction of a slope and basin morphology during the

Pliocene progradation. The deposit is thicker on the northwest flank of the volcano, demonstrating that a large part of the cone was incorporated into the MTD. However, this MTD event is likely to have been triggered by earthquakes associated with fault activity, rather than being a direct product of instability and collapse of the volcanic edifice due to direct association with rift faults and collapse of the slope-front.

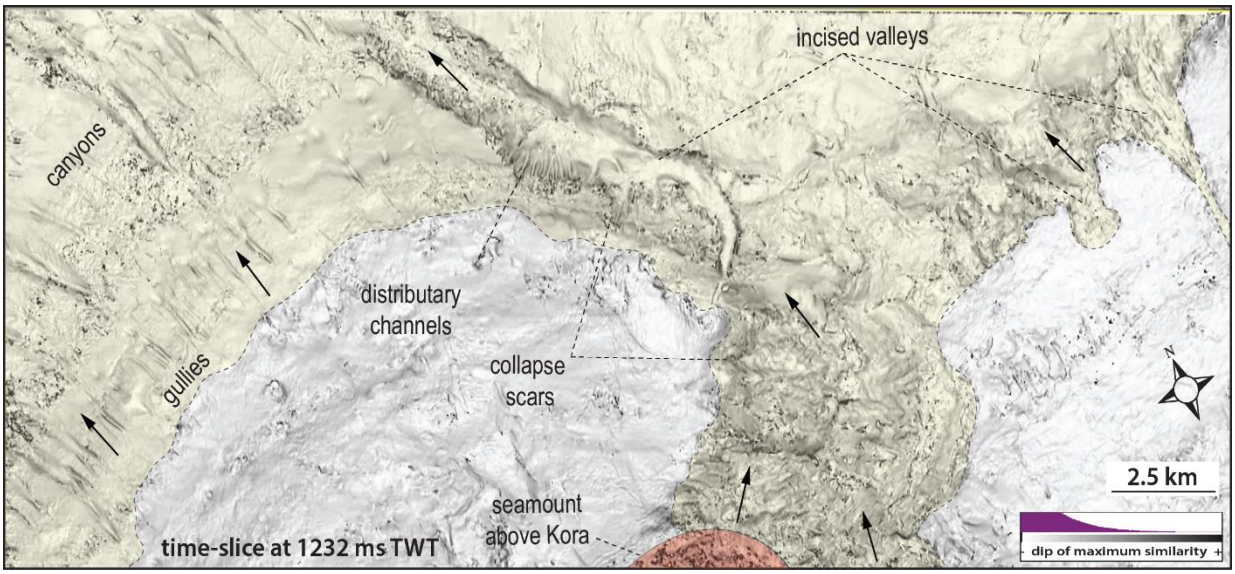

Figure 32: Seismic images of architectural elements formed during the burial stage. Time slice through the dip of maximum similarity cube showing the relationship of the buried Kora volcano and the enclosing sedimentary architectural elements. The dashed line represents the position of the shelf break.

Biostratigraphic data from wells (Bergmann et al., 1992; Fletcher, 1996) and seismic stratigraphic analysis suggest that the complete burial of Kora edifice occurs in an upper bathyal setting. Seismic attribute analysis, volume rendering and cross-section seismic images show canyons and gullies deeply cross-cutting reflectors from older strata (Figure 28B, Figure 30 and Figure 32) in this interval. Seismic reflectors above the volcano (after the complete burial volcanic structure) display a domal configuration around 550 ms TWT that is onlapped by younger reflectors, here referred to as the burial dome, suggesting the occurrence of a persistent bathymetric high above the buried volcano (Figure 19 and Figure 31B). The geometry of the domal structure together with the distribution, style and architecture of the sedimentary systems are strongly influenced by the location of the buried Kora Volcano. Onlap of seismic reflectors onto the structural high suggests that the domal structure was manifest on the seafloor as a seamount until at least the Pleistocene (about 6 Ma years after volcanism had ceased, and at least 2 Ma after the volcanic structure was completely buried at around 4 Ma). The processes, which resulted in the production of the dome structure on the seafloor long after burial of the edifice is likely product

of differential compaction between volcanic lithologies and enclosing sedimentary rocks. Also, erosion around the paleo-volcanic high and/or local carbonate bioconstruction installed on the top of the high can contribute on this process. In addition, two large fans 3 km wide and 5 km long were deposited from south to north on the edges of the burial dome, here referred to as "seamount-edge fans" (Figure 31 and Figure 33).

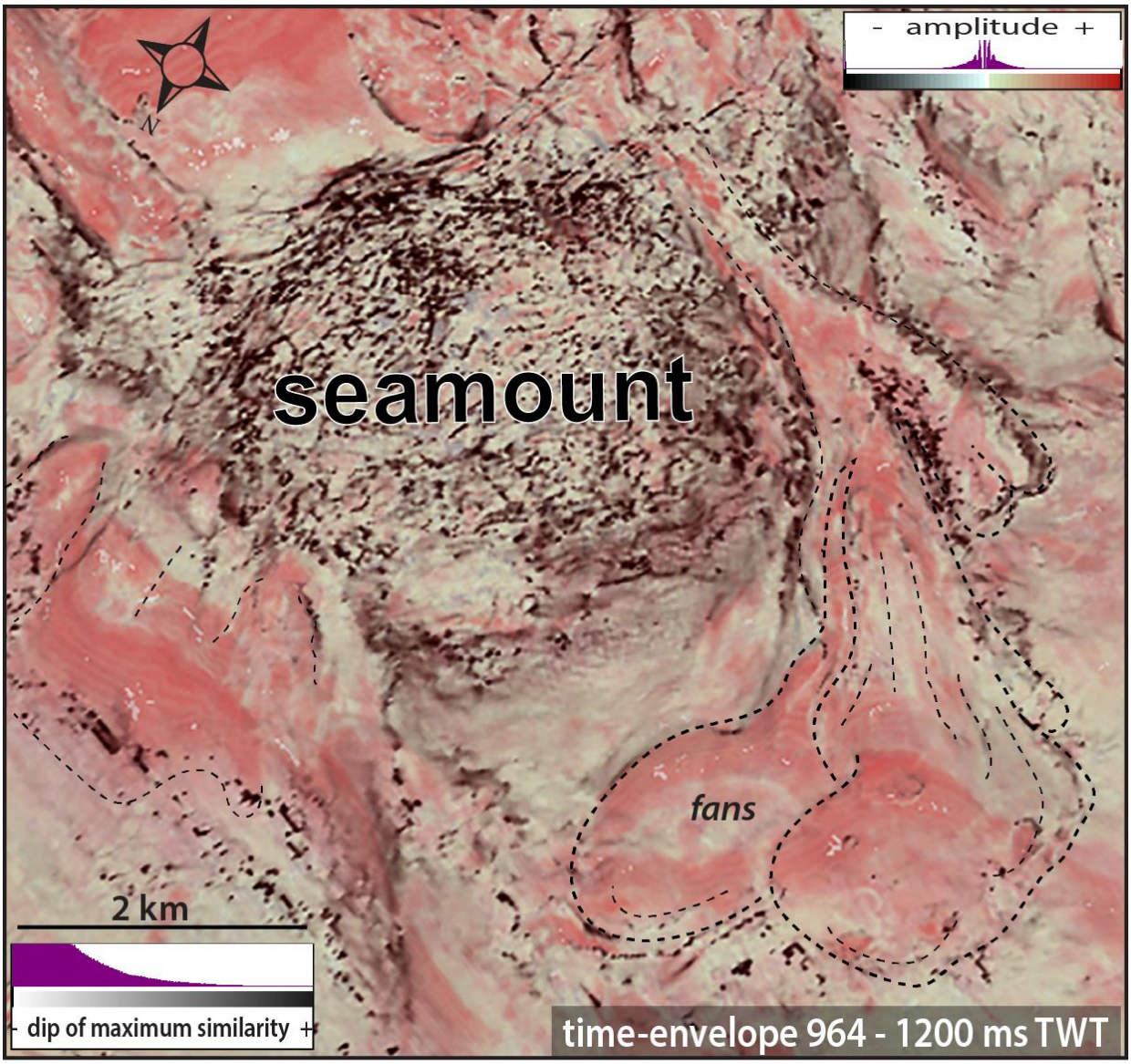

Figure 33: Overlap of the dip of the maximum similarity seismic cube and the amplitude volume rendering seismic cube showing the main geometrical shape of the seamount-edge fans and the relationship with the seamount produced due to the burial of Kora volcanic edifice.

Above the S-N prograding clinoforms (Figure 20 and Figure 31B), the seismic facies gradually change character to become parallel, continuous and horizontal, with reflectors terminating in topset relationship (Figure 20). The erosive truncations no longer form deep canyons but otherwise display a dendritic pattern over large areas (Figure 31A), which reflects a progradation

of shelf environments over the continental slope. Shelf-edge deltas, large incised valleys with internal distributary channels and collapsed scars are common features observed in 3D seismic images of this interval (Figure 32 and Figure 31), and reinforce the interpretation of shelf environments (possibly even costal environments and subaerial exposure during high-frequency base-level falls) dominating the sedimentary system in the wake of the migrating shelf-break and coastal line towards the north.

3.6 Economic Potential and Petroleum Plays

The potential of volcanic systems to accumulate economic petroleum resources has been known since the middle of last century. Ongoing production from the Green Tuff Formation in Japan, rhyolites, tuffs, and conglomerates of the Qingshen field in China, volcano-sedimentary sequence of Rosebank field in the North Sea, and fractured basalts of the Cabiúnas Formation offshore Brazil are examples of successful hydrocarbon exploration in volcanic settings. Kora Volcano hosts a sub-commercial discovery of crude oil with 32^{o} API from volcaniclastic rocks in the syn and inter-eruptive deposits, with 1,168 bopd (barrels/day) produced during a Kora-1 well formation test and 668 bopd produced in a long-term test from Kora-1A well. The Kora discovery indicates that oil has been expelled from the Late Paleocene Waipawa Formation in the Northern Graben Taranaki, and demonstrated the potential of the Mohakatino Volcanic Belt to host significant volumes of oil. The discovered Kora field remains undeveloped due to the complex distribution of reservoirs and traps, and also to its location in the offshore part of the basin, which makes development and production expensive compared with onshore fields. In the following sections we use the insights arising from the analysis of the architectural elements of KVS and enclosing strata to illustrate the great variety of traps and reservoirs that can occur in association with buried volcanic systems.

The knowledge obtained for exploration of hydrocarbons in buried volcanoes have direct application onto the geothermal industry. The heterogeneity observed by mapping petroleum reservoirs, traps and seals in buried volcanoes can help to define better the subsurface architecture and fluid dynamics of geothermal systems associated with modern volcanoes.

3.6.1 Syn-Magmatic Traps and Reservoirs

The events associated with emplacement of magma and eruptions of Kora Volcano formed several types of structural traps with variable sizes including, piercement domes, drag folds, upturned pinchouts, and jack-up of sedimentary strata above intrusions. Most of these traps have potential to form four-way closures that could host economic volumes of hydrocarbons. Drag folds and piercement domes are structural traps formed due to deformation and uplift of pre-magmatic sequences (pre-eruptive dome architectural element) and in the studied area have potential to form structures with ca 30 km^2 in size (Figure 21 and Figure 23A). Jack-up of sediments above intrusions occurs between 2500 and 3500 ms TWT in the seismic volume (Figure 23) and is more commonly associated with saucer-shaped sills and dike swarms than with isolated intrusions. The largest sub-volcanic jacked-up structure is located northwest of Kora Volcano and has a closure of about 10 km^2 (Figure 23). Upturned pinchout traps can occur where sub-horizontal strata from the syn-magmatic sequence pinch out against impermeable rocks deposited on the flanks of the volcano (Figure 23A) and are tilted upwards in the direction of the edifice (Figure 25C), possibly due to differential compaction, rotational block faulting or a combination of these processes.

Stratigraphic traps are likely to occur in the exogenous part of the syn-magmatic sequence due to the intercalation of porous and non-porous deposits formed during eruptions and associated sedimentary processes (Figure 25C and Figure 26). These stratigraphic traps usually comprise a reservoir unit pinching out against the volcanic edifice with higher level strata terminations inclined towards the eruptive centre, having the potential to entrap hydrocarbons from large areas around the volcano against the structural high (Figure 30B). The sub-commercial field found in Kora-1 and Kora-1A wells appears to be trapped in a combination of upturned pinchout strata and stratigraphic traps formed by the alternation of tuffs and volcaniclastic sedimentary deposits (Figure 25 to Figure 27). Distal to the edifice, the exogenous part of the syn-magmatic sequence is often interrupted by normal faults, which in some cases form roll-over anticlines that could store hydrocarbon fields (Figure 30C).

Potential reservoirs of KVS syn-magmatic sequence more likely form in intercalated volcanic and sedimentary deposits (Figure 27) and may form in fractured igneous rocks. Proven syn-magmatic hydrocarbon reservoirs of the KVS include primary pyroclastic and epiclastic deposits with porosity ranging from 9 to 28% and permeability from 0.1 to 200 mD (Figure 27). Production from

the Kora wells show highest values in clast-supported volcanic conglomerates and on lapilli tuffs intervals (Bergmann et al., 1992; Figure 27). Closer to the cone, seismic images show that these producing deposits are likely discontinuous, amalgamated and diverge outward from the main vent complex (Figure 25). At the same stratigraphic level but distal to the apex of the Kora edifice, in areas where seabed gradients were low (compared to the cone flanks), interpretation of the seismic data using analogous outcropping volcanoes suggests that potential reservoirs may be vertically stacked and more continuous, potentially forming large fans, lobes and sheet-like deposits (Figure 27) which are more likely producible plays. Fractured igneous bodies also have the potential to form reservoirs at sub-volcanic levels associated with the emplacement and fracturing by cooling of intrusive rocks (Figure 22 and Figure 23), and also in pyroclastic deposits (e.g. fractured welded ignimbrites if present), or at the base of the extrusive part of the syn-magmatic sequence (especially if vesicular and brecciated lava flows occur at this stratigraphic location in association with fractures).

3.6.2 Post-Magmatic Traps and Reservoirs

Stratigraphic traps are likely to form in the post-magmatic sequence due to pinchout of coarse-grained deep-water deposits onto the volcanic edifice, which are excellent petroleum plays because they usually contain the reservoir and the trap in the same structure. This kind of play shows intercalations of porous and non-porous deep-water sediments thinning and pinching-out against non-porous volcanic rocks on the flanks of the volcano. Seismic images of south eastern deep-water systems of KVS (Figure 19, Figure 28 to Figure 30) show a strong impedance contrast between channel bodies and the enclosing sedimentary strata, which suggests that the channels probably contain coarse-grained sediments. If these systems have closure in both directions along the paleo-depositional trend, they have the potential to store hydrocarbons, particularly in circumstances where normal faults compartmentalize the reservoirs (Figure 25C, Figure 28 to Figure 30) or promote up-sequence flow through hydrocarbon prone mudstones to charge the up-sequence channel deposits.

Paleogeomorphic traps in the form of unconformities, buried volcanic edifices, seamounts and valley fill may also locally promote hydrocarbon accumulation in the post-magmatic sequence. Paleogeomorphic traps are formed where positive or negative structures of ancient landscapes and sea-floors are buried by younger strata of different lithology (Halbouty, 1972). These traps likely form during the burial of volcanoes, reefs, channels, barrier sand bars, basement hills,

seamounts or erosive surfaces. After cessation of volcanism in Kora, a ca 1500 m high positive volcanic seamount commenced burial and continued to influence the sedimentary style of the area through the Pliocene to the Pleistocene (i.e. long after the volcano was completely buried). The burial of Kora Volcano formed two large 4-way closure traps, each one covering areas of more than 30 km^2 at different stratigraphic levels. The lower closure occurs at ca 1300 ms TWT (Figure 20, Figure 21B and Figure 31B), at the unconformity between volcanic rocks and younger burial sediments, and the shallower closure at ca 600 ms TWT (burial dome architectural element), which is marked by reflectors onlapping the domal structure (Figure 19, Figure 20, Figure 31B). Amalgamated high amplitude reflectors fill concave erosive features interpreted to be gullies, canyons and incised valleys, likely containing coarse-grained sediments (Figure 30 to Figure 33). In the Kora region, these deposits potentially form subtle traps varying in size from hundreds of meters to 2 km wide. Seismic amplitude anomalies suggest that DHI's (direct hydrocarbon indicators) are trapped in these structures at shallow levels, around 500 to 300 ms TWT (Figure 30; OMV, 2011).

Potential reservoirs of the post-magmatic sequence are controlled by the sedimentary processes of degradation and burial of Kora Volcano and can be related with the development of submarine channels and fans, seamount-edge fans and debris avalanche aprons enclosing the edifice. Late Miocene and Pliocene deep-water, slope and shelf-edge sedimentary bodies form fans and lobes pinching-out against the flanks and burying the volcano (Figure 30). These deposits are lithostratigraphically equivalents to the sands of Mangaa and Giant Foreset formations, composed of well sorted, very fine to fine grained sands with excellent reservoir qualities, including a porosity average around 25% and permeability from 60 to 500 mD (Fletcher, 1996). In addition, degradation and edifice sector collapses have potential to form a debris apron surrounding the volcano, which may include reservoir facies (Figure 29C).

3.7 Conclusions

Reconstruction of the architecture of KVS allows us to understand how igneous and sedimentary bodies interact and are distributed in time and space due to the piercement and burial of a polygenetic submarine composite volcano in a sedimentary basin. The architecture of the volcanic system is defined by the occurrence of specific three-dimensional building blocks (i.e. architectural elements) in different stratigraphic levels, related with the emplacement, construction, degradation and burial of the volcanic structure.

Both lateral and vertical relationships between architectural elements vary systematically. Syn-intrusive architectural elements cross-cut and deform pre-magmatic sequences. Syn and inter-eruptive architectural elements overlay pre-magmatic sequences and are controlled by the relative distance from the eruptive centres. Post-magmatic architectural elements overlay the syn-magmatic sequence and are formed by the interaction of regional basin fill processes with local degradation and burial of the volcanic edifice.

Analysing the architectural elements of KVS allows us to characterise in detail the variety of traps and reservoirs formed at each stratigraphic level, identifying potential plays to host economic volumes of hydrocarbons. The endogenous part of the volcano is characterised by traps and potential reservoirs created by magma emplacement and deformation of pre-magmatic strata. At the exogenous level, interplay between eruptions and base-level change control the distribution of reservoirs and traps. After volcanism has ceased, *sensu stricto* basinal sedimentation form reservoirs and traps controlled by the location of the volcanic structure.

This work demonstrates that in spite of its complexity, modern scientific and technological techniques enable us to reconstruct the architecture of a buried volcanic system. This helps to develop conceptual models for the location, variation, geometry, size and style of igneous and sedimentary deposits within the system, which is essential for reducing exploratory risk in sedimentary basins affected by magmatism. We have determined that identifying the architectural elements of buried volcanoes is necessary for building predictive models and for de-risking hydrocarbon exploration in sedimentary basins affected by magmatism.

3.8 References

Allen, J. R. L., 1983, Studies in Fluviatile Sedimentation: Bars, Bar-Complexes and Sandstone Sheets (Low-Sinuosity Braided Streams) in the Brownstones (L. Devonian), Welsh Borders: Sedimentary Geology, 33 (4): 237–93. doi:10.1016/0037-0738(83)90076-3.

Beggs, J.M., 1990, Seismic Stratigraphy of the Plio-Pleistocene Giant Foresets, Western Platform, Taranaki Basin. In 1989 New Zealand Oil Exploration Conference : Proceedings. Wellington., 201–7. Wellington.

Bergman, S.C., J.P. Talbot, and P.R. Thompson., 1992, The Kora Miocene Submarine Andesite Stratovolcano Hydrocarbon Reservoir, Northern Taranaki Basin, New Zealand. In 1991 New Zealand Oil Exploration Conference, 178–206.

Bischoff, A.P., A. Nicol, A. Barrier, M. Beggs., 2016, The Stratigraphic Record of Volcanism - Examples from New Zealand Sedimentary Basins. In 2016 Geoscience Society of New Zealand Conference, Wanaka, Abstract.

Bischoff, A.P., 2015, Igneous Features within Endurance-3D Survey and Their Impact on Barque Prospect. New Zealand Oil and Gas unpublished confidential report.

Cas, R. A. F., J. V. Wright., 1993, Volcanic Successions: Modern and Ancient - A Geological Approach to Processes, Products and Successions. Chapman and Hall, UK. doi:10.1007/978-0-412-44640-5.

Catuneanu, O., 2006, Principles of Sequence Stratigraphy. Changes, 375. doi:10.5860/CHOICE.44-4462.

Farooqui, M Y., 2009., Evaluating Volcanic Reservoirs. Oilfield Review Schlumberger 21 (1): 36–47.

Fletcher Challenge Energy Taranaki., 1996, Awatea-1 Well Completion Report, PEP384557. New Zealand Geological Survey unpublished open-file PR-2262.

Giba, M., A. Nicol, and J. J. Walsh., 2010, Evolution of Faulting and Volcanism in a Back-Arc Basin and its Implications for Subduction Processes. Tectonics 29 (4): 1–18. doi:10.1029/2009TC002634.

Giba, M., J. J. Walsh, Andrew Nicol, V. Mouslopoulou, H. Seebeck., 2013, Investigation of the Spatio-Temporal Relationship between Normal Faulting and Arc Volcanism on Million-Year Time Scales. Journal of the Geological Society 170 (6): 951–62. doi:10.1144/jgs2012-121.

Halbouty, T. M., 1972, Rationale for Deliberate Pursuit of Stratigraphic, Unconformity and Paleogeomorphic Traps. AAPG Bulletin 56 (3): 537–41.

Hampton, S. J., J. W. Cole., 2009, Lyttelton Volcano, Banks Peninsula, New Zealand: Primary Volcanic Landforms and Eruptive Centre Identification. Geomorphology 104 (3–4). Elsevier B.V.: 284–98. doi:10.1016/j.geomorph.2008.09.005.

Hansen, R.J., P.J.J. Kamp, 2008, New Insights into the Condensed Nature and Stratigraphic Significance of the Late Neogene Ariki Formation, Taranaki Basin. New Zealand Petroleum Conference Proceedings, 1–13.

Holford, S. P., N. Schofield, J. D. MacDonald, I. R. Duddy, P. F. Green., 2012, Seismic Analysis of Igneous Systems in Sedimentary Basins and Their Impacts on Hydrocarbon Prospectivity: Examples from the Southern Australian Margin. APPEA Journal, 52, 229–52.

Hunt, D., M. E. Tucker., 1992, Stranded Parasequences and the Forced Regressive Wedge Systems Tract: Deposition during Base-Level Fall. Sedimentary Geology 81 (1–2): 1–9. doi:10.1016/0037-0738(92)90052-S.

King, P.R., G.P. Thrasher., 1996, Cretaceous-Cenozoic Geology and Petroleum Systems of the Taranaki Basin. Lower Hutt, New Zealand, Institute of Geological and Nuclear Sciences Limited, Monography, 243p.

King, P. R., G. P. Thrasher., 1992, Post-Eocene Development of the Taranaki Basin, New Zealand: Convergent Overprint of a Massive Margin. Geology and Geophysics of Continental Margins 53: 93–118. doi:10.2307/1485072.

Kennedy, B., M. Heap, A. P. Bischoff, A. Nicol, M. Villeneuve, J. Farquharson, J. Cole., 2017. Insights into Volcanic Rocks as Petroleum Reservoirs from Laboratory and Field Permeability Measurements. In AAPG GTW Influence of Volcanism and Associated Magmatic Processes on Petroleum Systems. Conference, Oamaru New Zealand.

Klarner, S., O. Klarner., 2012, Identification of Paleo-Volcanic Rocks on Seismic Data, Updates in Volcanology. A Comprehensive Approach to the Volcanological Problems, 181–206, Prof. Francesco Stoppa (Ed.), InTech, DOI: 10.5772/24943.

Lipman, P. W, D. R. Mullineaux., 1982, The 1980 Eruptions of Mount St. Helens, Washington. Geological Survey Professional Paper 77 (1250): 844.

Lu, Zhong, D. Dzurisin, J. Biggs, C. Wicks, S. McNutt., 2010, Ground Surface Deformation Patterns, Magma Supply, and Magma Storage at Okmok Volcano, Alaska, from InSAR Analysis: 1. Inter-eruption Deformation, 19970-2008. Journal of Geophysical Research: Solid Earth 115 (5): 1–14. doi:10.1029/2009JB006969.

Miall, A. D., 1985, Architectural-Element Analysis: A New Method of Facies Analysis Applied to Fluvial Deposits. Earth-Science Reviews Elsevier Science Publishers B.V 22: 261–308. doi:10.1016/0012-8252(85)90001-7.

Miall, A. D., 1995, Whither Stratigraphy? Sedimentary Geology 100 (1–4): 5–20. doi:10.1016/0037-0738(95)00100-X.

Miall, A. D., 2000, Principles of Sedimentary Basin Analysis; Springer-Verlag, New York, 616p.

Mitchum, R M, P. R. Vail., 1977, Seismic Stratigraphy and Global Changes of Sea Level, Part 7 : Seismic Stratigraphic Interpretation Procedure. Seismic Stratigraphy: Applications to Hydrocarbon Exploration. AAPG Memoir 26 Memoir 26: 135–43.

Nicol, A., C. Mazengarb, F. Chanier, G. Rait, C. Uruski, L. Wallace., 2007, Tectonic Evolution of the Active Hikurangi Subduction Margin, New Zealand, since the Oligocene. Tectonics 26 (4). doi:10.1029/2006TC002090.

OMV New Zealand Limited., 2005, Kora 3D Seismic Survey, Offshore NZ. New Zealand Geological Survey. Unpublished open-file report PR-3302.

OMV New Zealand Limited., 2011, Final Seismic Interpretation Report for PEP 38485 (Kora). New Zealand Geological Survey. Unpublished open-file report PR-4318.

Orton, G.J., 1996, Volcanic Environments. In Reading, H. G., 1996, Sedimentary Environments: Processes, Facies and Stratigraphy: 688 p.

Palladino, D M, S. Simei, G. Sottili., 2010, Integrated approach for the reconstruction of stratigraphy and geology of Quaternary volcanic terrains: An application to the Vulsini Volcanoes (central Italy). Geological Society of America Special Papers, 2010, 464, p. 63-84, doi:10.1130/2010.2464(04)

Planke, S., E. Alvestad, O. Eldholm., 1999, Seismic Characteristics of Basaltic Extrusive and Intrusive Rocks. The Leading Edge 18 (3): 342. doi:10.1190/1.1438289.

Planke, S., P. A. Symonds, E. Alvestad, J. Skogseid., 2000, Seismic Volcanostratigraphy of Large-Volume Basaltic Extrusive Complexes on Rifted Margins. Journal of Geophysical Research 105 (B8): 19335. doi:10.1029/1999JB900005.

Posamentier, H. W., R. J. Davies, J. A. Cartwright, L. J. Wood., 2007, Seismic Geomorphology - an Overview. Geological Society, London, Special Publications 277: 1–14. doi:10.1144/GSL.SP.2007.277.01.01.

Posamentier, H. W., V. Kolla., 2003, Seismic Geomorphology and Stratigraphy of Depositional Elements in Deep-Water Settings. Journal of Sedimentary Research 73 (3): 367–88. doi:10.1306/111302730367.

Pritchard, M. E., M. Simons., 2004, An InSAR-Based Survey of Volcanic Deformation in the Southern Andes. Geophysical Research Letters 31 (15). doi:10.1029/2004GL020545.

Rateau, R., N. Schofield, M. Smith., 2013, The Potential Role of Igneous Intrusions on Hydrocarbon Migration, West of Shetland. Petroleum Geoscience 19 (3): 259–72. doi:10.1144/petgeo2012-035.

Rohrman, M., 2007, Prospectivity of Volcanic Basins: Trap Delineation and Acreage de-Risking. AAPG Bulletin 91 (6): 915–39. doi:10.1306/12150606017.

Schultz-Ela, D. D., M. P. A. Jackson, B. C. Vendeville., 1993, Mechanics of Active Salt Diapirism. Tectonophysics 228 (3–4): 275–312. doi:10.1016/0040-1951(93)90345-K.

Schutter, S. R., 2003, Hydrocarbon Occurrence and Exploration in and around Igneous Rocks. Geological Society, London, Special Publications 214 (1): 7–33. doi:10.1144/GSL.SP.2003.214.01.02.

Seebeck, H. C., 2012, Normal Faulting, Volcanism and Fluid Flow, Hikurangi Subduction Plate Boundary, New Zealand. P.h.D Thesis, University of Canterbury.

Seebeck, H. C., A. Nicol, P. Villamor, J. Ristau, J. Pettinga., 2014, Structure and Kinematics of the Taupo Rift, New Zealand. Tectonics 33 (6): 1178–99. doi:10.1002/2014TC003569.

Sewell, R. J., 1988, Late Miocene Volcanic Stratigraphy of Central Banks Peninsula, Canterbury, New Zealand. New Zealand Journal of Geology and Geophysics 31 (March 2015): 41–64. doi:10.1080/00288306.1988.10417809.

Shumaker, L. E., 2016, Sedimentology, Seismic Geomorphology and Provenance Investigations of Deep-Water Deposits: Taranaki Basin, New Zealand. P.h.D Thesis, Stanford University.

Silva, S. D., J. M. Lindsay., 2015, Primary Volcanic Landforms. The Encyclopedia of Volcanoes. doi:10.1016/B978-0-12-385938-9.00015-8.

Smith G.A., 1991, Facies sequences and geometries in continental volcaniclastic sequences in Fisher, R.V., and Smith, G.A., eds., Sedimentation in volcanic settings: SEPM (Society for Sedimentary Geology) Special Publication 45, p. 109–121.

Stagpoole, V. M., R. H. Funnell., 2001, Arc Magmatism and Hydrocarbon Generation in the Northern Taranaki Basin, New Zealand. Petroleum Geoscience 7: 255–67. doi:10.1144/petgeo.7.3.255.

Stagpoole, V. M., A. Nicol., 2008, Regional Structure and Kinematic History of a Large Subduction Back Thrust: Taranaki Fault, New Zealand. Journal of Geophysical Research: Solid Earth 113 (1): 1–19. doi:10.1029/2007JB005170.

Vonk, A. J., P. J. J. Kamp., 2008, The Late Miocene Southern and Central Taranaki Inversion Phase (SCTIP) and Related Sequence Stratigraphy and Paleogeography. New Zealand Petroleum Conference Proceedings, no. 1996: 1–17.

Wicks, C, D. Dzurisin, S. Ingebritsen, W. T. Z. Lu, J. Iverson., 2002, Magmatic Activity Beneath the Quiescent Three Sisters Volcanic Centre, Central Oregon Cascade Range, USA. Geophysical Research Letters 29 (7): 26 1-4. doi:10.1029/2001GL014205.

Chapter 4

Seismic Reflection and Petrographic Characterisation of a Buried Monogenetic Volcanic Field

4 Seismic Reflection and Petrographic Characterisation of a Buried Monogenetic Volcanic Field

4.1 Abstract

Buried volcanoes occur in great numbers within sedimentary basins around the globe. Over the last two decades, the knowledge about these 'fossil' volcanic systems has increased significantly, mainly due to continuous improvements and availability of high-quality seismic reflection data. Today, a growing number of studies demonstrate that "seismic volcanology" is becoming a feasible science, especially when seismic analysis is combined with borehole data and seismic-scale outcrop analogues. Interpretation of buried volcanoes from seismic data typically requires information from very large datasets and integration of disciplines such as sedimentology, seismic and sequence stratigraphy, tectonics, and volcanology. The integration of these disciplines create a unified model that explain these systems in their totality, from emplacement to complete burial in the host sedimentary basin.

In chapters 4 and 5, we characterise the complete geological record of a cluster of 31 middle Miocene volcanoes, currently buried by ca 1000 m in sedimentary strata in the offshore Canterbury Basin, New Zealand. These volcanoes were imaged by high-quality 2D seismic lines and drilled by the petroleum exploration well Resolution-1, which recovered a monzogabbro intrusion and correlative volcaniclastic rocks. For the purposes of this thesis, we refer to these volcanoes as the Maahunui Volcanic Field (MVF).

In Chapter 4, we introduce the topic and the regional geological setting, explaining the methods and their limitations for characterising buried volcanoes from seismic and well data, and presenting the results from detailed petrographic analysis, seismic interpretation, seismic morphologic characterisation, and paleo-environmental reconstruction of MVF area. Integration of these dataset allows us to interpret that the eruptions in MVF were entirely submarine (ca 500 to 1500 m), producing subaqueous equivalents of maar-diatreme and tuff cone volcanoes. The morphology of the volcanoes is interpreted to be primarily controlled by phreatomagmatic explosions, in which variations in the eruptive mechanisms such as water/magma ration and the characteristics of the pre-eruptive substrate probably have an important role in the fragmentation and dispersion of material. In addition, differential post-eruptive degradation has changed the original volcanic morphology, which was controlled by the height, and by the

position of the volcanic edifices in relation to a late Miocene base-level fall. Reconstruction of the paleo-physiography of the MVF area suggests that eruptions were short-lived, and controlled by a plumbing system that fed magma to dispersed eruptive centres, which are characteristic of monogenetic volcanic fields. The results from chapter 4 improves understanding of the geological processes that control the architecture of the MVF. Chapter 5 will apply these results to build a comprehensive volcano-stratigraphic framework of the MVF.

4.2 Introduction

Buried volcanoes are common in New Zealand and in sedimentary basins and around the globe (e.g. Field et al., 1989; Bergman et al., 1992; Single and Jerram, 2004; Giba et al., 2013; Plank et al., 2017; Reynolds et al., 2017). Geological characterisation of these buried systems relies on the integration of subsurface geophysical interpretations, drill-hole data analysis, and observations from outcropping volcanic analogues (e.g. Planke et al., 1999; Jerram et al., 2009; Klarne and Klarne, 2012; Holford et al., 2012; Schofield et al., 2012; Schofield et al., 2016). Today, continuous improvement of subsurface imaging allows us to compose seismic images with horizontal and vertical resolutions down to tens of metres in both sedimentary basins with or without buried volcanoes (e.g. Posamentier and Kola, 2000; Bischoff, 2017; Rabbel et al., 2018).

However, all remote-sensing techniques have limitations which places constraints on the resulting interpretations. For example, the quality and resolution of seismic surveys are primarily controlled by geophysical parameters such as signal scattering due to changes in rock velocities and densities, energy attenuation with depth, geobody thickness and lateral continuity being small relative to the signal wavelength, and instrumentation limits imposed by navigation during seismic acquisition and computing power (e.g. Sheriff and Geldart, 1995; Planke et al., 1999; Abdelmalak et al., 2016; Marfurt, 2018). Loss in seismic resolution may be amplified in sedimentary basins impacted by volcanism due to the presence of volcanic rocks with similar acoustic impedance and geometries to the enclosing sedimentary rocks (Klarner and Klarner, 2012), and by intrusive bodies that are too steeply inclined to be resolved seismically. The loss of seismic signal is particularly important beneath volcanic cones, as the rocks are typically highly deformed by multiple intrusive events (Holford et al., 2012; Jackson, 2012; Bischoff et al., 2017; Infante-Paez and Marfurt, 2017; Morley, 2018).

To address these limitations, seismic data are frequently interpreted together with observation from rock samples and petrophysical wireline-logs collected from drillholes (e.g. Planke et al., 1999). However, drillholes are typically scarce and motivated by a resource exploration, thus borehole data provides little information about the geometries and lateral variations of rock units that typically form complex three-dimensional bodies. This is especially true in volcanic systems, which commonly contain a variety of litho-types that can include examples from intrusive, extrusive, and sedimentary rocks. Thus, many rock-types present in buried volcanoes may not be recognized or could be misinterpreted. In recent studies, the approach adopted to fill this information gap has been to integrate observations from seismic-scale outcrop analogues into the interpretation workflow (e.g. Schofield et al., 2016; Planke et al., 2017). In this chapter, we apply this methodology to correlate seismic images with potential analogues from subaerial and submarine outcropping volcanoes.

In outcrop, the morphology of volcanoes provide insights into past eruptive styles, edifice growth mechanisms, and cone degradation experienced during their complete history (e.g. Fornaciai et al, 2012). Volcanic morphology is well studied in modern and ancient subaerial systems (e.g. Cas and Wright, 1993; Orton, 1996; Kereszturi et al., 2010; Németh, 2010; Kereszturi and Németh, 2013; Silva and Lindsay, 2015), but is still a work-in-progress for the marine realm (e.g. Cas and Giordano, 2014; Jutzeler et al., 2014).

Despite differences in volcanology processes at subaerial and subaqueous environments, their products can share many similarities (e.g. Cas et al., 1989; Cas et al., 1993; White et al., 2015). In both environments, volcanic morphology is likely controlled by the interplay of many competing processes, such as steady versus dynamic mechanisms of fragmentation, fixed versus variable location of explosion locus, and single versus multiple eruption phases, which can complicate their interpretation (e.g. Kereszturi and Németh, 2013). This is especially true for buried volcanoes, because in addition to volcanic complexity and limitations of sub-surface interpretation, these “fossilized” volcanoes are likely influenced by superimposed post-eruptive processes (e.g. degradation, compaction and diagenesis), which can have alter their original form. For these reasons, assumptions and generalizations are generally required to interpret the seismic morphology of buried volcanoes.

In this chapter, we present the first part of a case-study on a cluster of 31 middle Miocene volcanoes, currently buried by ca 1000 m of sedimentary strata in the offshore Canterbury Basin, eastern side of Zealandia (Figure 34). For the purposes of this thesis, we refer to this volcanic

field as the Maahunui Volcanic Field (MVF)[1], which is the Māori name for the stretch of coast south of Banks Peninsula (aka Canterbury Bight) and immediately adjacent to the study area. To conduct this study, we have utilised a collection of high-quality 2D seismic lines, data from six petroleum exploration wells, and insights from dozens of outcropping, submerged, and buried volcanic systems imaged by 3D seismic surveys from New Zealand sedimentary basins and elsewhere. The compiled datasets are complementary, with each providing different information about the rock-types, characteristic eruptive styles, magma-sediment interactions, volcanic morphologies, and architecture of the volcanic system within the basin strata. Most data from analogue volcanic systems were compiled from the literature, although we also have made our own observations and interpretations from onshore (e.g. Waiareka-Deborah Volcanic Field and Banks Peninsula Volcanic Complex) and offshore examples in the Canterbury (e.g. Waka-3D seismic survey) and Taranaki basins (e.g. Romney and Vulcan-3D seismic surveys). We contrast information from sedimentology, seismic and sequence stratigraphy, tectonics and volcanology into a unified model, to evaluate the large-scale processes that control the morphology of volcanoes buried in MVF, and to produce insights into buried volcanic systems elsewhere.

The work outlined in Chapter 4 demonstrates that despite limitations, the large-scale geologic history and morphology of buried volcanoes can be interpreted from good quality 2D seismic reflection data, based on a multidisciplinary approach that integrates complementary information into a unified model. Insights from this work helps improve prediction of the locations of architectural elements for buried monogenetic submarine volcanic systems in a comprehensive volcano-stratigraphic framework, which is the topic of Chapter 5.

[1] *The name Maahunui is derived from the legendary canoe that the demigod Maui used to sail the Pacific Ocean. In the legend Maui was fishing and hooked the great fish Waro, which dragged him for a long distance during an intense fight. Eventually Maui started to win the battle and hauled Waro to the surface, which immediately transformed into land, the North Island of New Zealand. Maui's canoe named Maahunui, then became the South Island of New Zealand. Local Māori people use the name Maahunui for the coast south of Banks Peninsula and, in consultation with members of the Ngāi Tahu Research Centre of the University of Canterbury, we have adopted the name for the volcanic field studied.*

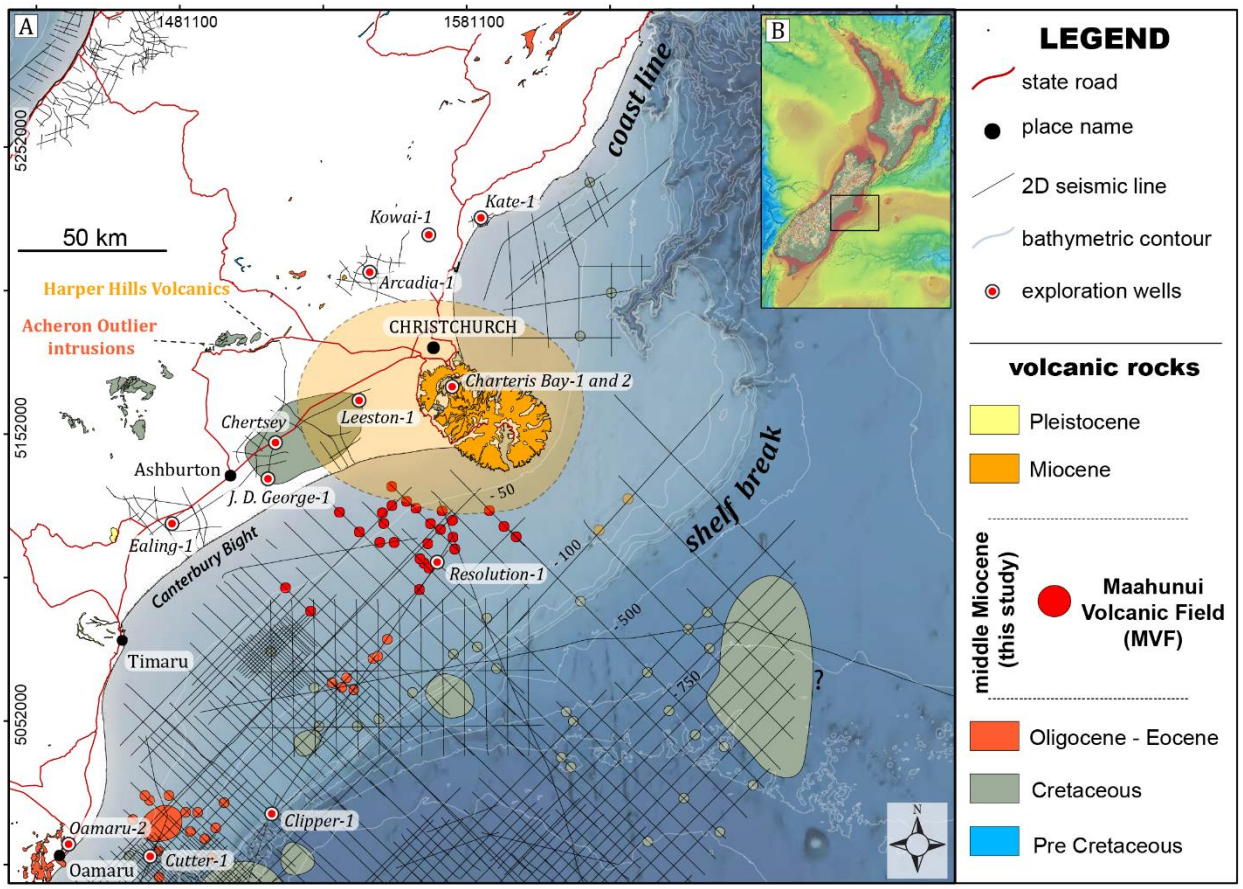

Figure 34: A) Map showing the age and location of volcanic rocks onshore and offshore northern Canterbury Basin, together with the main seismic and well data used in this work. Red dots indicate the locations of volcanoes in the Maahunui Volcanic Field, which is the focus of this study (Chapters 4 & 5). Location of Paleogene to Cretaceous offshore volcanoes were mapped in association with Andrea Barrier (University of Canterbury PhD candidate in structural geology). Onshore volcanoes are from GNS geologic map (Forsyth et al., 2008). B) New Zealand topographic and bathymetric map from the NZ Petroleum Exploration 2018 datapack. Black square in B) shows the location of the detailed map in A.

4.3 Geological Setting

Volcanic rocks of the MVF pierce basement rocks of the Torlesse Supergroup and are emplaced within sedimentary rocks of the Canterbury Basin, on the eastern side of Zealandia (Figure 34; Figure 35). The basement comprises of low-grade meta-sedimentary rocks and minor igneous rocks that were deformed in an accretionary prism of a long-lived arc-trench system that was active on the eastern border of the Gondwanan supercontinent, from the Permian to the early Cretaceous (Suggate et al., 1978). Sedimentation in the Canterbury Basin began in the mid Cretaceous (ca 112-105 Ma) and was synchronous with rifting, prior to the separation of Zealandia from west Antarctica and Australia (e.g. Mortimer et al., 2004). Lithospheric extension created NE-SW and E-W grabens in the Canterbury Basin, predominately infilled by non-marine late Cretaceous sediments (Strogen et al, 2017). Post-rift quiescence and thermal subsidence

promoted the deposition of marine sediments during the Paleogene, culminating with maximum transgression during the late Oligocene (Field et al., 1989; Ballance, 1993). Since the early Miocene, the present oblique-convergent boundary between the Pacific and Australian tectonic plates has produced several tectonic cycles of uplift and erosion of the western border of the basin, with rapid progradation of a thick sequence of continental and marine sediments into the Canterbury Basin (Suggate et al., 1978; Field et al., 1989; Kamp et al., 1992; Batt et al., 2004; Lu et al, 2005; Hart et al., 2008; Strogen et al, 2017; Barrier, in prep; Figure 35; Figure 36).

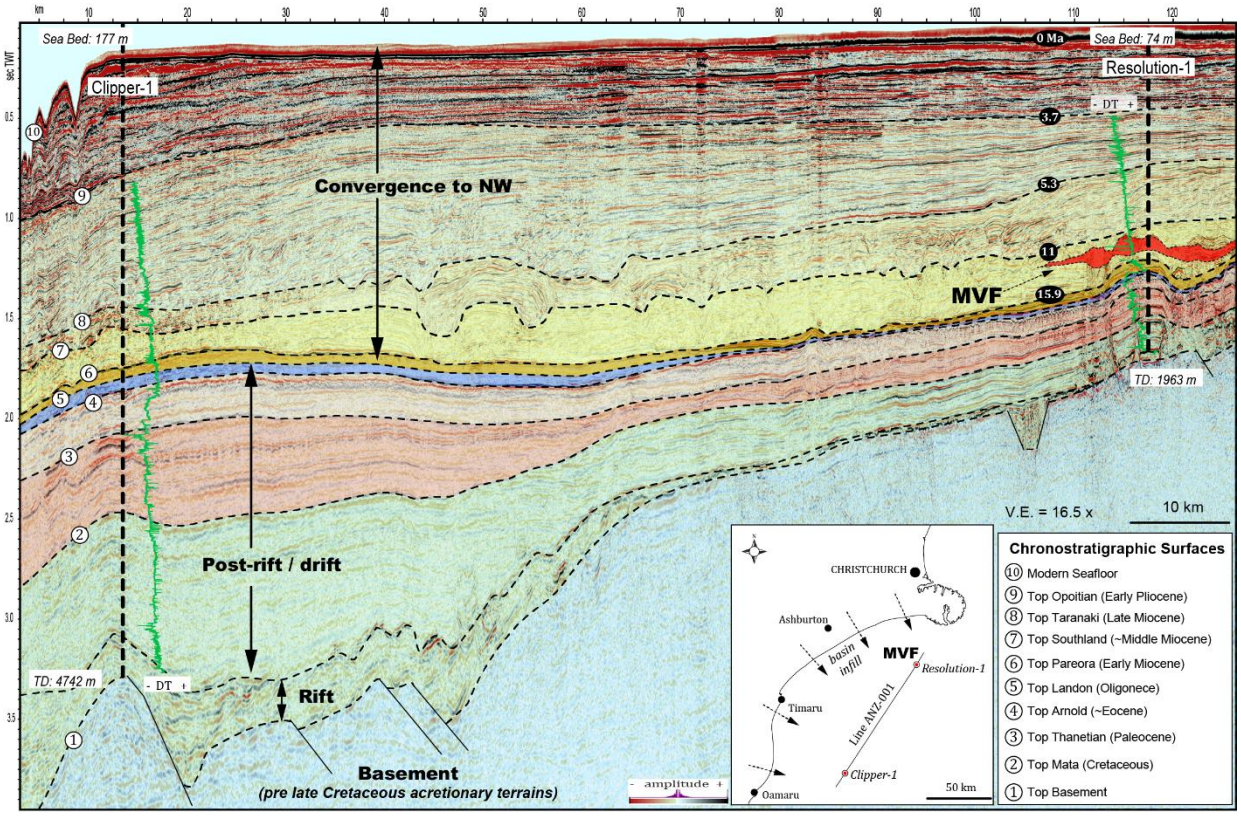

Figure 35: 2D regional strike/oblique seismic line showing the stratigraphic architecture, the main geotectonic events in the northern part of the Canterbury Basin, and the occurrence of the MVF (red). The Resolution-1 and Clipper-1 wells were used to tie the seismic data to chronostratigraphic surfaces that represent important changes during the basin evolution. Cretaceous-Paleogene surfaces and rift faults courtesy of Andrea Barrier, UC PhD candidate in structural geology.

Volcanism occurred semi-continuously during the geological evolution of Canterbury Basin (Figure 34). The earliest volcanic events associated with the basin date from the late Cretaceous, represented by the products of silicic to intermediate magma erupted from several sparse volcanic centres in the central and northern parts of the basin (i.e. Mount Somers volcanics, ca 95 Ma). During the Cenozoic, the Canterbury Basin and eastern South Island experienced widespread and long-lived intraplate volcanism. These magmatic events are not adequately explained by mantle plume or extensive lithosphere thinning models (e.g. Morgan, 1971; Weaver

and Smith, 1989 apud Timm et al., 2010). Mantle plumes typically create a track of volcanoes with age progression correlated with the direction of plate motion, however, this is not observed in the Canterbury Basin. In addition, the lithosphere underneath Zealandia is estimated to be ca 70 to 100 km thick (Stern et al., 2002) and does not show extensive thinning. Two different models have been proposed to explain the atypical magmatism in the Canterbury region: sudden detachment and sinking of a remnant late Cretaceous subducted slab (Finn et al., 2005), and asthenosphere upwelling induced by removal of parts of the subcontinental lithosphere throughout the Cenozoic (Hoernle et al., 2006; Timm et al., 2010). Independent of the geodynamic processes that control this magmatism, the observed products are primarily mafic in composition, and formed both monogenetic volcanic fields such as the Waiareka/Deborah and Waipiata Volcanic Fields (Coombs et al., 1986; Németh and White, 2003), and large polygenetic volcanic complexes like those from Banks and Otago Peninsulas (Coombs et al., 1960; Sewell, 1988). In the offshore Canterbury Basin, several late Cretaceous to Pleistocene buried volcanoes and intrusive bodies have been mapped using seismic reflection data (Field et al., 1989; Blanke, 2010; Bischoff, 2016; Barrier et al., 2017; Figure 1), however, little is known about the eruptive histories of these systems, which is mainly due to a lack of detailed studies and direct geological information.

The MVF study area is located ca 40 km south (and offshore) of Banks Peninsula. In this location, volcanic and intrusive rocks were first identified in the petroleum exploratory Resolution-1 well, which was drilled in 1975, about 75 km offshore from Ashburton (Figure 34; Figure 36). This borehole penetrated volcaniclastic rocks interbedded with bathyal siltstones of Waiauan age (12.7 to 11 Ma) from 1103.5 to 1220 m, and intersected an intrusive body at 1911 m, which was K-Ar dated at 12 ± 2 Ma (Milne, 1975). These rocks were tentatively correlated by successive authors with outcropping volcanic rocks of Banks Peninsula, Acheron Outlier intrusions (Milne, 1975), and Harper Hills volcanics (Field et al., 1989). The location of the proposed outcrops is shown in Figure 34. Banks Peninsula is a large polygenetic composite-shield volcanic complex mainly erupted subaerially during the late Miocene (Sewell, 1988). Harper Hills Basalts comprise a sequence of subaerial tholeiitic lava flows K-Ar dated at 10.5 ± 0.3 Ma (Carlson et al., 1980; Browne, 1983), and associated volcanic muds (Coalgate Bentonites), basalt dikes (Bluff Basalt), and well bedded volcaniclastic rocks (Sandpit Tuff). Biostratigraphic dating suggests that the Sandpit Tuff dates from Waiauan (12.7 to 11 Ma) or Tongaporutuan (11 to 7.2 Ma, according to Carlson et al., (1980) and Browne (1983). Acheron Outlier intrusions are tholeiitic gabbros

forming a large irregular laccolith emplaced along bedding planes in Cretaceous to Paleocene carbonaceous sedimentary rocks of the Eyre Group, and were most likely intruded into these rocks during the Oligocene (Eady, 1995). Results from the present study indicate that the MVF is an independent cluster of deep submarine monogenetic volcanoes. Further studies and new seismic data would be necessary to map the total area of MVF and a possible correlation with co-genetical outcrops.

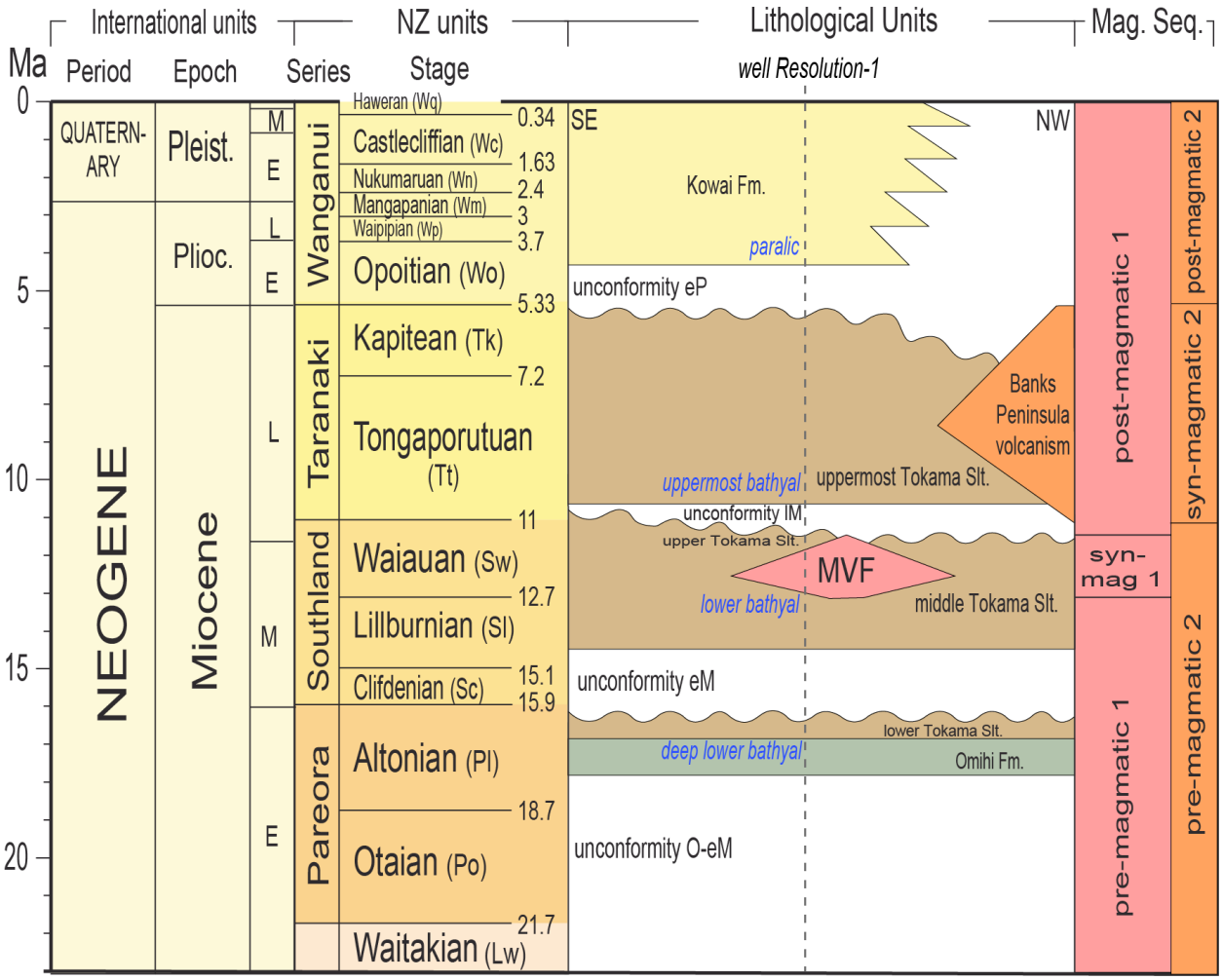

Figure 36: Local chronostratigraphic chart of the study area. We subdivide Tokama Siltstone into 4 depositional units according to their depositional setting (blue italic label). Two main volcanic events within northern Canterbury basin during the Miocene emplaced MVF and Banks Peninsula. The main magmatic events are each represented by pre, syn and post-magmatic sequences, and are shown in the right part of the figure. Magmatism in pink is related with MVF, while in orange is related with Banks Peninsula. Stratigraphic ages follow the International Chronostratigraphic Chart 2014 and New Zealand Geological Time Scale 2015 (Raine et al., 2015).

4.4 Dataset, Methods and Limitations

Many important aspects of the geology of the study area rely on consideration of biostratigraphic and lithologic data from the Resolution-1 well. Because of this, the structure of this chapter is designed to initially provide the reader with small-scale petrographic and paleo-environmental

information, and to progressively up-scale interpretations to a regional scale[2], based on seismic stratigraphic mapping techniques. In this section, we present the data set used in Chapters 4 and 5, as well as the methods, limitations and assumptions that may be necessary to characterise volcanoes buried in sedimentary basins.

4.4.1 Data Set

Seismic reflection and well data used in this thesis were sourced from the 2017 New Zealand Petroleum and Minerals petroleum exploration data pack, which includes a large database of reports, maps, wells and seismic surveys loaded in Kingdom© software. We used both industry and government surveys, with special attention given to interpretation of PPL38202 and PPL38203 surveys, known as CB-82. We use more than 40,000 km of moderate to high-quality onshore and offshore 2D seismic lines acquired during the 1970's and 1980's, tied to six petroleum exploration and stratigraphic wells drilled in the northern Canterbury Basin (Leeston-1, Clipper-1, Ealing-1, Resolution-1; Charteris Bay-1 and 2; Figure 34). Seismic line spacing typically ranges from 1 to 8 km, with good vertical resolution up to 6 seconds penetration (ca 5 km) and samples recorded at 0.004 second intervals. The well information varies in data-type and quality. Resolution-1 and Clipper-1 contain a more complete dataset that includes lithological, geochemical, geochronological, petrographic and biostratigraphic information from cuttings, cores and wireline logs for the stratigraphic intervals drilled. For this study, detailed petrographic and elemental geochemistry analysis of MVF rocks were conducted on select intervals that could potentially contain Miocene igneous rocks, initially based on the description of the Resolution-1 well from Milne (1975).

4.4.2 Petrography, RXF and SEM-EDS Methods and Limitations

We described and photographed relevant intervals of the Resolution-1 well at the New Zealand Petroleum and Minerals core-store, located in Featherston, North Island of New Zealand. Samples collected by Jane Newman from the well material provided us with one drill-core of an intrusive rock from a depth of 1962.25 m, and 13 composite ditch-cutting samples of volcaniclastic rocks at 10 m intervals between 1100 to 1230 m depth.

[2] Representative to the proxy extension of MVF and enclosing sedimentary strata

Petrographic characterisation of these cutting samples may have limitations due to a number of factors including: their small original grain size, potential break-up of material during drilling operations, composite sample intervals that likely blend material from diverse beds, and difficulty to separate drilling mud from altered *in situ* volcanic fragments. Due to the high degree of alteration of the cutting samples, conventional sample washing to separate drilling mud from sample material was not applied because most of the soft rock material would have been lost during the sieving process. Therefore, to prepare the samples for analysis the following steps were taken in the University of Canterbury Sedimentary Laboratory:

1. Dry analysis of samples under a binocular microscope and photograph documentation with a magnification of 105x;
2. Selection of unwashed material with volcanic texture and structures from the measured depth interval of 1130 to 1150 m;
3. Part of this unwashed material was separated to perform petrographic macro and microscopic characterisation “in nature”;
4. The other part was immersed in water to hydrate and manually wash the sample;
5. Manual grain-by-grain wet separation of potential volcanic fragments from drilling mud;
6. Sample drying;
7. Immersion of loose selected material in resin, follow by cutting and polishing to a thickness of ca 0.3 mm for transmitted light petrographic description. Two samples were selected from the measured depth interval of 1130 to 1140 m (1 washed and 1 unwashed), and seven samples from the depth interval of 1140 to 1150 m (4 washed and 3 unwashed). One sample of the intrusion was well indurated and could be thin-sectioned without the above steps;
8. Petrographic description and photograph documentation using a Meiji transmitted light microscope with 400x magnification.

To estimate the thickness of the volcanic deposits, we tentatively correlate wireline-logs of the Resolution-1 well, mud-logging descriptions presented in Milne (1975), and new insights from this work. Intervals with abundant volcanic fragments described in Milne (1975) show low-gamma and low-density log character, and may reach thicknesses of ca 10 m (e.g. interval from 1103.5 to 1114 m). However, samples from our dataset do not contain abundant volcanic rocks in this supposedly volcanic thicker interval, rather, we observe similar rock description and log character in the interval from 1130 to 1150 m. During sample collection, we observed that some

intervals were incomplete in the core store, perhaps due to extensive sampling of cutting samples since the original collection of the core in 1975 (e.g. Schiøler et al., 2011). Despite the paucity of the sample material, sufficient cutting samples were available to petrographically characterise possible volcanic rock types in the MVF.

X-ray fluorescence (XRF), Scanning Electron Microscope (SEM) and Energy Dispersive Spectroscopy (EDS) were then performed on samples from selected intervals that contain igneous rocks. XRF analysis was conducted using an Olympus Vanta handheld analyser for one sample from 1962.25 m depth (intrusion) and three samples from 1130 to 1160 m depth in the Resolution-1 well. XRF is a non-destructive analytical technique used to determine the elemental composition of materials by measuring the fluorescence (or secondary) X-ray emitted from a sample when it is excited by a primary X-ray source. The XRF gun was calibrated to perform a bulk geochemistry analysis of the total samples. Each sample was analysed four times to ensure that the results were consistent and reproducible. The results were used to compare the geochemistry of the intrusive and extrusive rocks sampled. SEM and EDS analysis was also conducted using the JEOL JSM IT-300 variable pressure SEM at the Electron Microscopy Centre at the University of Canterbury. SEM analysis produces high definition morphologic images by scanning the surface of the samples using a focused beam of electrons. The interaction of the emitted electrons with the sample atoms produces signals that contain information about the surface topography and composition of the sample. We used the SEM to analyse the elemental geochemistry of fragments collected from a depth range of 1140 to 1150 m in Resolution-1, and to produce microscopic images of their morphology.

4.4.3 Methods and Limitations to Reconstruct Buried Volcanoes from Seismic Data

Detailed seismic morphologic characterisation was conducted for each seismic anomaly that could represent a middle Miocene volcano buried in the study area, and for all anomalies that could represent intrusive bodies within strata of the Canterbury Basin. To recognize which anomalies could date from the middle Miocene, we mapped the pre-eruptive (PrErS) and post-eruptive (PoErS) surfaces of these volcanoes based on seismic volcanic stratigraphy and volcaniclastic occurrences in the Resolution-1 well (more details in section 4.4.4). Table 3 shows the attributes and parameters applied in this characterisation.

Table 3: Attributes and parameters used on the seismic morphological Characterisation and reconstruction of MVF volcanoes.

Seismic morphometric parameters	Shape of the anomaly after burial, basal diameter (m), height after burial (s) for cone-like anomalies, depth after burial (s) for crater-like anomalies.
Assumptions and estimations	Post-eruptive degradation, degree of compaction during burial, seismic wave velocity (m/s) within the anomalies.
Other considerations	Data quality, position of the 2D seismic line relative to the "summit" of the seismic anomaly, cone-like anomalies associated with underlying funnel-like anomalies, evidence for large intrusions underneath anomalies, paleo-geographic position relative to major base-level falls, presence of canyons that may have eroded part of the anomalies.

First, we classify the buried seismic anomalies into two main groups: positive and negative morphologies (e.g. Figure 37). Positive morphologies are seismic anomalies characterised by a convex-up shape of PoErS immediately above a relatively flat PrErS horizon (Figure 37A). Negative morphologies are recognisable on seismic lines by pit-like excavations into PrErS (Figure 37B). We sub-classify these anomalies into six classes as: positive symmetric cone, positive asymmetric cone, positive trapezium, positive mound, negative funnel-like structures and negative basin-like structures[3].

Basal width (W) of positive volcanoes were defined by the horizontal distance between the inflection points of the PoErS horizon in relation to a relatively flat PrErS horizon (Figure 37A). The radius of positive volcanoes corresponds to W/2, or the radius of the steeper flank for asymmetric cones. The width of negative volcanoes was defined as the horizontal distance between the sides of the funnel-like or basin-like structures at the PrErS horizon (Figure 37B). The height and depth (profundity of crater excavations) of volcanoes after burial were initially recorded in seconds two-way-time (sec TWT). The height (in TWT) of positive volcanoes was defined as the vertical time-distance between PrErS and PoErS at the apex of the anomaly imaged on 2D lines. The depth (in TWT) of negative volcanoes was measured by the vertical time-wave-transit between the PrErS horizon and the inverse apex of funnel-like or basin-like structures (Figure 37A and B).

[3] After preliminary interpretation, we sub-classify these anomalies as crater-type and crater-type. Crater-type are all negative anomalies that excavate PrErS. Crater-type are all positive anomalies showing upward-convex shape of PoErS (e.g. volcano-types presented in Kereszturi and Nemeth, 2013), despite the fact that cone, mound and trapezium anomalies may contain a crater zone.

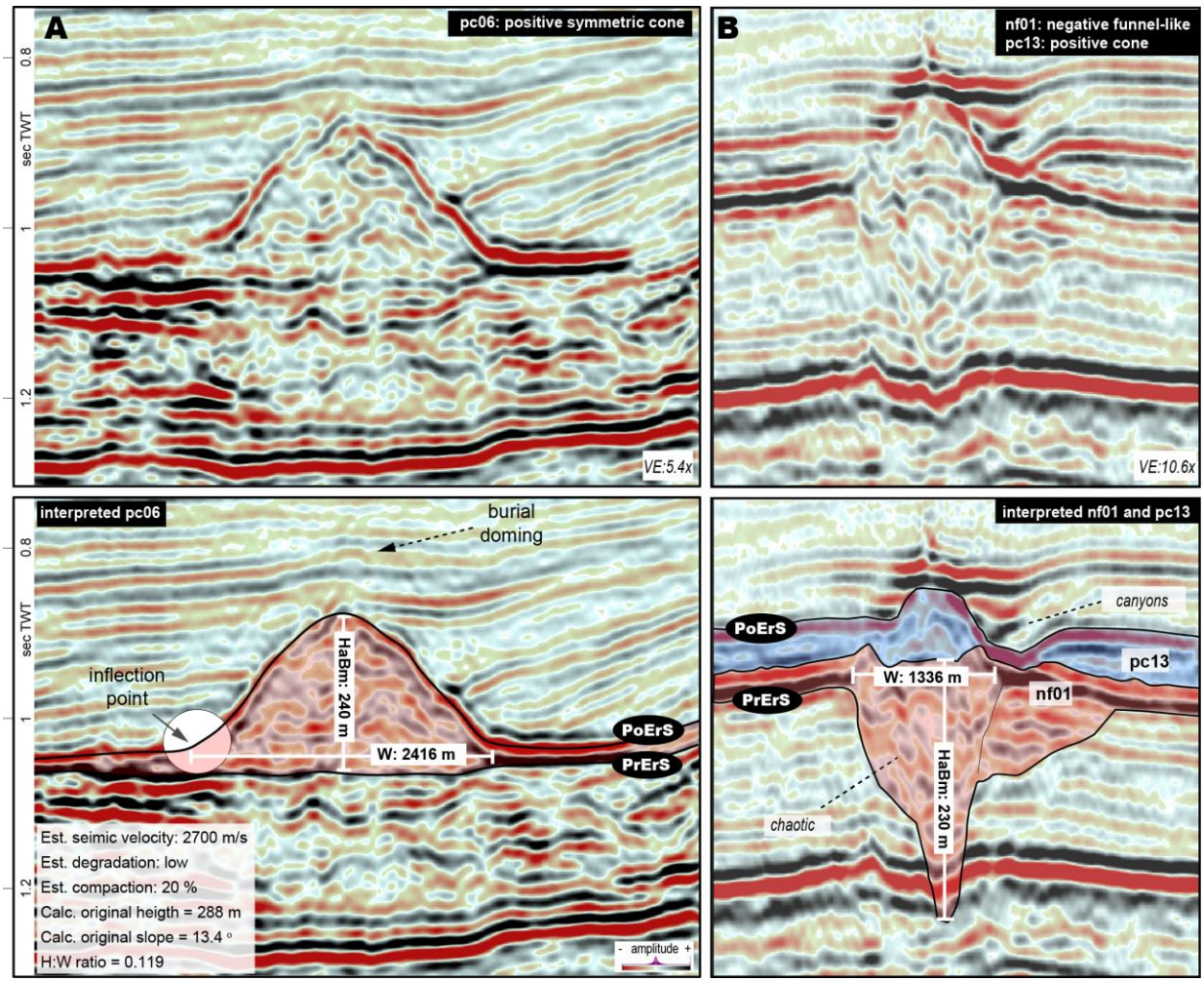

Figure 37: Seismic morphometric measurements and example of morphology classification of MVF volcanoes. A) shows a positive symmetric cone (crater-type). B) shows a compound morphology. Bottom part (nf01 in light red) has a negative funnel-like shape (crater-type) and its lateral association. Upper part (pc13 in light blue) shows a positive asymmetric cone shape (crater-type) and its lateral association. Note that pc13 have one of the flanks eroded by canyons. TWT in the seismic lines are convert to distance in metres using the method in section 4.4.3.1.

4.4.3.1 Methods, limitations and assumptions to reconstruct buried volcanoes from seismic data

As briefly discussed in the introduction chapter, characterisation of buried volcanoes from seismic data have some limitations imposed by the complexity of these systems and the associated difficulties resolving the subsurface geology at an acceptable resolution. To reconstruct the original morphology and edifice heights at the time of the formation of volcanoes now buried in the subsurface, three key parameters have to be addressed: i) the acoustic velocity of the material (volcanic and sedimentary rocks) that comprise and enclose the seismic anomalies; ii) the amount of post-eruptive degradation of the edifice before burial; and iii) how much compaction the volcanoes experienced during their burial, from the surface to their actual depth in the basin. Information on the quantification of these parameters is outlined below.

Estimation of acoustic velocities of buried volcanoes

Estimates the acoustic velocity of volcanic rocks buried in the subsurface are usually made using petrophysical data such as wireline-logs and rock samples from boreholes (e.g. Planke et al., 1999; Klarner and Klarner, 2012; Millett et al., 2015; Cant et al. 2018). Acoustic velocities can also be obtained through laboratory simulations (e.g. Nara et al., 2011), or by pre-and-post stacking of the acoustic velocities using geophysical techniques (e.g. Sheriff and Geldart, 1995). Estimation of the acoustic velocity is one of the most difficult parameters to establish to quantitatively characterise the morphology of buried volcanoes. Studies using borehole data show that parameters such as P-wave (compressional waves) velocity in igneous rocks produced by the same melt can vary as much as 1500 to 7500 m/s (Planke et al., 1999). In addition, boreholes are usually scarce and cannot reproduce the enormous variability of volcanic and sedimentary rocks of buried volcanic systems. Acoustic velocity can also change rapidly across volcanic rocks, in some cases varying several orders of magnitude in a few metres. This variations in acoustic velocities can be consequence of changes in lithology (e.g. Nara et al., 2011; Heap et al., 2017), fracture spacing (e.g. Heap and Kennedy, 2016; Cant et al., 2017), or metasomatism and weathering (Rohrman and Lisk, 2010; Mordensky et al., 2018; Sun et al., 2018). Because of these variations, some assumptions are necessary to indirectly estimate the seismic velocity of rocks that comprise buried volcanoes. In the absence of a dataset that can represent the rock variability within these buried volcanoes, and because seismic reflectors are usually a geophysical representation of amalgamated rock layers (i.e. due to restricted vertical seismic resolution), the standard procedure used to estimate acoustic velocities is to pre-define minimum, maximum and average ranges of expected velocities, based on the available data from wells and using analogues from data in wells elsewhere (e.g. Magee et al., 2013; Reynolds et al., 2016, 2017). As a rule of thumb, poorly consolidated and altered tuffs are in the low-velocity range, while intrusions are in the high-velocity range (Planke et al., 1999; Holford et al., 2012). This is certainly the case in MVF. The sonic-log in the Resolution-1 well shows velocity values ranging from 2100 to 2200 m/s in volcaniclastic rocks, and 5000 to 6000 m/s in intrusive rocks.

Although useful, this conventional method has inherent errors due to limited knowledge about the *in situ* rocks. Jackson (2012) and Magee et al. (2013) propose a method to estimate the velocities within buried volcanoes based on the characteristics of a geophysical artefact known as velocity pull-up. This artefact occurs when seismic waves travel faster within certain rock layers in relation to enclosing strata. Thus, volcanoes showing high impedance contrast

compared to their enclosing sedimentary strata may show velocity pull-up artefacts. The authors successfully applied the method in southern Australian marginn sedimentary basins, however, we cannot reproduce their results using data from the MVF for a series of reasons. First, seismic images of MVF volcanoes show both high and low impedance contrasts relative to the enclosing sedimentary strata. Sonic-logs from the well demonstrate that volcaniclastic rocks of the MVF can have slower acoustic velocities compared to the enclosing strata (which range from 2400 to 2700 m/s). This suggests that volcanoes in the MVF are unlike to produce velocity pull-up artefacts. A second issue is that seismic reflectors beneath volcanic cones are often highly deformed and seismically anisotropic, which usually causes loss of reflectivity and poor quality imaging of these zones (e.g. Jackson, 2012; Reynolds et al., 2016; Bischoff et al., 2017). Third, sub-volcanic zones can be associated with uplift and arching of pre-eruptive strata deformed by shallow magmatic chambers, laccoliths, sills, and dikes, which are frequently observed in the MVF and in other volcanic systems (e.g. Wicks et al., 2002; Pritchard and Simmons, 2004; Lu et al., 2009; Bischoff, et al., 2017; Infante-Paez and Marfurt, 2017; Schmiedel et al., 2017; Morley, C., 2018).

To overcome these problems and to derive an acceptable estimate of acoustic velocities of the MVF, we have developed a new approach, referred here to as the *Relative Impedance Index* (RII). This method comprises two steps: i) evaluate the acoustic impedance contrasts of the volcanic and sedimentary strata at the location drilled by the Resolution-1 well, and compare these differences to the internal and external acoustic impedances of the seismic anomalies that represent buried volcanoes of the MVF, and ii) estimate acoustic velocity values for the anomalies based on the sonic-data in the well (sonic wireline-log is presented in Figure 42, section 4.5.1). Thus, in the MVF, volcanic anomalies presenting similar impedance contrasts to the enclosing sedimentary rocks were assigned a velocity of 2500 m/s (average velocities of the sedimentary rocks enclosing the middle Miocene volcaniclastics in the Resolution-1 well). Volcanic anomalies with impedance contrasts comparable to the high impedance of enclosing sedimentary strata were assigned a velocity of 2700 m/s (high velocities in sedimentary rock enclosing the middle Miocene volcaniclastics in the Resolution-1 well). Volcanic anomalies with higher impedance contrasts compared to the high impedance values of enclosing strata were assigned velocities of 3000 m/s. Velocities of 3500 m/s were exclusively assigned to two small volcanoes with extremely high impedance contrasts in relation to sedimentary strata. It is important to mention

that these extremely high impedance volcanoes (pc10 and pc07) were classified as having low seismic data quality).

To validate this method, we perform a separate analysis using the standard approach to estimate the height of the buried volcano from pre-defined maximum and minimum velocities. Thus, the minimum value for the MVF extrusive sequence was estimated to be 2000 m/s and a maximum of 3500 m/s. These values are based on the velocities of volcanic rocks sampled in eight wells drilled in the Canterbury Basin and from measurements available in the literature from international studies (e.g. Planke et al., 1999; Schutter, 2003; Nara et al., 2011; Klarner and Klarner, 2012; Holford et al., 2012; Millett et al., 2015; Heap and Kennedy, 2016; Reynolds et al., 2016; Heap et al., 2017; Cant et al. 2018). For both methods, the height of the anomaly after burial was measured in seconds (HaBs), and these values were multiplied by the estimated acoustic velocity (m/s) to calculate the height of the anomaly in metres (HaBm). Appendix 1 present additional information of the RII method.

Estimation of the amount of post-eruptive degradation

After the eruptive life cycle of a volcano, erosion may impact the original morphology until the edifice is completely erased from the geological record, or until the remaining volcanic structure is buried and "fossilized" in a sedimentary basin. To estimate the amount of degradation experienced by volcanoes before burial, we develop a method here referred to as the *Cone Apex Technique* (Figure 38). This technique was applied where positive-like volcanoes display flattened tops coincident with the stratigraphic position of major base-level-falls, and contain reflectors that downlap from the volcanoes onto the PrErS horizon, or top lap from the PoErS horizon onto the volcano flanks, which could indicate that some material has eroded from the volcano. Erosion of volcanic cones may also occur due to canyon incision and by collapsed of the edifices by gravitational processes, thus, we also characterise the potential amount of erosion based on the morphology of the canyons that degrade volcanoes, and on the presence of localized seismic facies that could represent debris deposits close to the edifice flanks. Volcanoes that do not show evidences of erosion in seismic lines were assumed to be rapidly buried and preserved.

In all cases of inferred cone erosion, we have estimated the amount of edifice erosion by measuring the TWT between the top of the eroded edifice and the intersection of lines projected along the volcano flank, to the apex of the PoErS above the degraded volcano (Figure 38). The TWT measurement was converted to a vertical distance in metres using a constant acoustic

velocity of 2500m/s (average velocities in sedimentary rock enclosing the middle Miocene volcaniclastics at Resolution-1). Thus, the amount of degradation was classified as low (< 20 vertical m), moderate (20 to 100 m), high (> 100 m), or "unsure" in cases where the volcano geometry could not be well defined, perhaps because of inadequate seismic resolution. This technique can only be applied after a preliminary analysis of the possible eruptive and post-eruptive controls on volcanic morphology in the area. In MVF, we interpreted that trapezium and mound morphology are progressively eroded forms of cone-type volcanoes (more details in section 4.5.5). Here, morphological classifications as cone, trapezium and mound are applied in their geometric sense to describe the morphologies of the seismic images, and should not be confused with typical volcanic morphology terminology used to classify outcropping volcanoes.

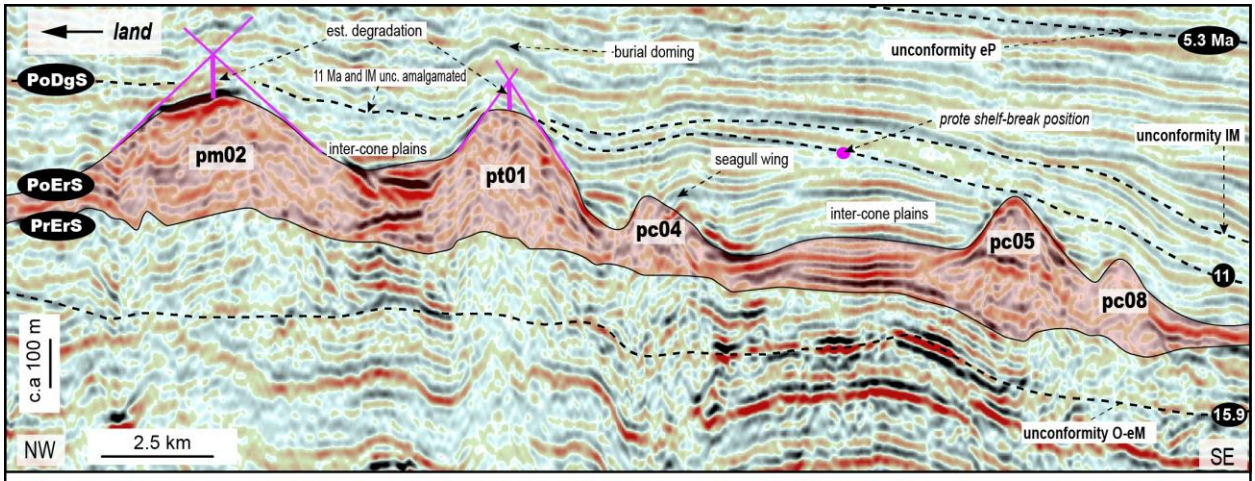

pm02	pt01	pc04	pc05	pc08
positive mound	positive trapezium	positive asymetric cone	positive symetric cone	positive symetric cone
W: 5472 m	W: 2696 m	W: 1583 m	W: 2562 m	W: 1405 m
HaBs: 0.189 s	HaBs: 0.196 s	HaBs: 0.085 s	HaBs: 0.151 s	HaBs: 0.157 s
Vel: 2700 m/s	Vel: 2700 m/s	Vel: 3000 m/s	Vel: 3000 m/s	Vel: 2500 m/s
HaBm: 255 m	HaBm: 262 m	HaBm: 128 m	HaBm: 277 m	HaBm: 198 m
comp: 30 %	comp: 20 % (burial doming)	comp: 40% (seagull wing)	comp: 30%	comp: 30%
HbBm: 332 m	HbBm: 314 m	HbBm: 179 m	HbBm: 294 m	HbBm: 255 m
est. degr: 84 m	est. degr: 49 m	est. degr: unsure	est. degr: no evidence	est. degr: no evidence
oHm: 416 m	oHm: 363 m	oHm: 179 m	oHm: 294 m	oHm: 255 m
HW: 0.076	HW: 0.135	HW: 0.113	HW: 0.112	HW: 0.182
oS: 8.6 °	oS: 15.1 °	oS: 12.7 °	oS: 12.9 °	oS: 20 °

Figure 38: 2D dip section (line CB-82-06) showing evidence of differential degradation related with the late Miocene (IM) unconformity and of differential compaction (burial doming and "seagull wings"). PrErS is the pre-eruptive surface, while PoErS is the post-eruptive surface. PoDgS[4] is the post-gradational surface.

[4] In Chapter 5 we discuss the volcano-stratigraphic surfaces in detail.

Estimation of the amount of compaction during burial

Estimating the compaction of buried volcanoes can be difficult based on limited data from the subsurface area. Volcanic rocks do not show predictable compaction trends with progressive burial as is typically observed in sedimentary rocks. Compaction of volcanic rocks depends largely on the original texture and structures of primary rocks, such as the amount of fragmentation or degree of welding. Compaction also depends on the secondary alteration of the rocks due to diagenesis during burial, the presence of interstitial fluids and exposure to meteoric or hydrothermal alteration (Heap et al., 2015; Wyering et al., 2014; Cant et al., 2017).

To estimate the compaction of volcanoes in the MVF, we developed a method based on the differential compaction between buried volcanoes and the sediments that enclose them. This method has two steps. First, we describe the geometries of reflectors above, and lateral to MVF volcanic edifices, to search for evidence of differential compaction between the volcanoes and their enclosing strata (strata enclosing MVF is mainly represented by the Tokama Siltstone lithostratigraphic unit). Reflectors that domed above volcanoes during progressive burial (Figure 38) indicate that enclosing strata compacted more than the volcanic rocks. No doming of the reflectors above volcanoes indicate no differential compaction. Reflectors with a 'seagull wing' configuration above volcanoes (Figure 38) suggest that the enclosing strata compacted less than the volcano (e.g. Planke et al, 2005; Bischoff et al., 2017; Holford et al., 2017). Second, we assign values of compaction based on compaction curves presented in Field et al. (1989), which suggest that in the Canterbury Basin, siltstones buried at 1000 m (i.e. the current burial depth of MVF) typically have compacted around 30% relative to seabed sediments of similar grain size and composition. Thus, we assume 30% compaction of volcanoes associated with no seismic evidence of differential compaction, 20% compaction of volcanoes associated with burial doming, and 40% compaction for volcanoes with "seagull wing" reflector configurations. These estimates of compaction are order-of-magnitude only and uncertainties in these values do not significantly impact the first-order results of this method. Examples of differential compaction are presented in Figure 38.

Calculating seismic morphometric parameters of buried volcanoes

With the available dataset, we reconstruct the near original morphologies of volcanic edifices in the MVF. Table 4 shows the equations applied to calculate morphometric parameters of the volcanoes. Note that we do not calculate parameters that consider crater width or crater slopes

of positive volcanoes because these values are in many cases unknown due to limitations in the interpretation of 2D seismic data. Direct comparison between seismic morphology analyses with the morphology of submarine and subaerial volcanoes observed at the present Earth surface, is a powerful tool for the interpretation of buried volcanoes. However, it is important to remember that morphometric parameters of distinct volcano-types can overlap in many cases (e.g. Silva and Lindsay, 2015). In addition, seismic morphometric analysis has a great number of variables with associated uncertainties, thus, we do not recommend direct comparison between the morphometry of reconstructed buried volcanoes with values observed from their surface counterparts. The morphometric parameters of reconstructed buried volcanoes may have application for establishing guidelines for their interpretation and for further investigation of volcanic processes (as long as the limitations of the methods are acknowledged).

Table 4: Equations used to calculate seismic morphometric parameters of the MVF volcanoes.

Abbreviations	Equations
HaBs: height after burial in seconds **Vel:** estimated acoustic velocity in m/s **HaBm:** height after burial in meters **comp:** estimated amount of compaction (%) **HbBm:** height before burial in metres **degr:** estimated amount of degradation in metres **oHm:** estimated eruptive height in metres **W:** Basal width **Rt:** basal radius **HW:** height vs. basal width ratio **oS:** estimated eruptive flank slope **atan:** arc cotangent	$HaBm = \frac{HaBs \times Vel}{2}$
	$HbBm = HaBm + (HaBm \times comp)$
	$oHm = HbBm + degr$
	$HW = \frac{oHm}{W}$
	$oS = 180^0 \times \frac{\text{atan}(oHm/Rt)}{\pi}$

4.4.4 Seismic Stratigraphy Methods

The seismic interpretation procedure was as follows.

1. Seismic-well tie correlation: seismic reflection lines from the NZPAM Kingdom© project were checked and calibrated with checkshot surveys from the Resolution-1 and Clipper-1 wells (Milne, 1975 and Hawkes and Mound, 1984). The depths of chronostratigraphic markers and formation tops were verified and, where necessary, corrected using the revised biostratigraphy of Canterbury Basin published by Schiøler et al. (2011).

2. Chrono and sequence stratigraphic mapping: Mapping of chrono and sequence stratigraphic surfaces was based on interpretation of 2D seismic lines over an area of ca 23,000 km^2 enclosing the MVF, correlated to biostratigraphic data from the Resolution-1, Clipper-1 and Leeston-1 wells when possible. Five chronostratigraphic surfaces for early Miocene to Modern Seabed were mapped in detail: top Pareora (ca 15.9 Ma), top Southland (ca 11 Ma), top Taranaki (ca 5.3 Ma), top Opoitian (ca 3.7 Ma) and modern seafloor (Figure 35). We named these surfaces to their correlated geological ages, following the New Zealand Geological Time Scale 2015. The surfaces mapped from reflectors picked on 2D seismic lines were interpolated using the *flex gridding algorithm* embedded in the Kingdom© software, to produce grids (horizons) that are proxies for chronostratigraphic boundaries of the study area (e.g. Tipper, 1993). Next, we mapped two important early Miocene (eM) and late Miocene (lM) unconformities, based on the observation of seismic criteria such as types of stratal terminations (e,g. onlap, toplap) and depositional trends (e.g. progradational, retrogradation) associated with that surface, that are recorded below and above that stratigraphic contact (e.g. Catuneanu, 2006). Because the study area was located in a submarine setting related to the formation of a slope-and-basin morphology, it was important to stablish the criteria for "sequence boundary", prior to seismic stratigraphic mapping of these unconformities. Here, we follow the methodology presented in Hunt and Tucker (1992), who correlate the marine surface to the timing of the end of base-level fall at the correlative shoreline. These surfaces are the basis for establishing the chronostratigraphic framework of the northern Canterbury Basin in this study, which helps us to compare volcano and sedimentary stratal patterns in different parts of the basin, and provide insights into the paleo-physiography of the basin at the time of formation of each surface. Our mapping (and others; e.g. Field et al., 1989; Adrian, 1997; Lu et al., 2005; Barrier, in prep) do not identify significant post-Cretaceous structural deformation in the area. The only events that deform the seismic reflectors in the study area are related to magmatism of the MVF (and maybe Banks Peninsula), which reinforces the use of maps on chronostratigraphic surfaces as proxies for paleo-physiography. Regional surfaces from Basement to early Oligocene (top Basement, top Mata, top Arnold and top Landon; Figure 35), were provided courtesy of Andrea Barrier.
3. Seismic facies characterisation: Seismic anomalies that could represent middle Miocene intrusive and extrusive igneous rocks were characterised based on criteria such as geometry,

internal and external configuration of seismic reflectors, deformation of enclosing strata, and stratigraphic position of the anomaly in relation to the chronostratigraphic surfaces.

4. Seismic volcano-stratigraphic analysis: Detailed seismic mapping of the pre- and post-eruptive surfaces (PrErS, PoErS) of MVF were calibrated with middle Miocene extrusive rocks penetrated by Resolution-1. The lateral continuity of PrErS and PoErS from the well were mapped in the 2D seismic lines following principles of seismic stratigraphy such as continuity of seismic reflectors, contact terminations, and the location of sedimentary and volcanic seismic facies (e.g. Mitchum et al., 1977; Planke and Alvestad, 1999). From these maps, we compose chronostratigraphic and isochron maps that represent the approximate physiography and thickness of each interval in seismic-time. Figure 39 shows the method to produce the syn-eruptive isochron map (between PrErS and PoErS). Mapping of post-eruptive surfaces such as the post-degradational surface (PoDgS) and the post-burial surface (PoBuS) is an innovation of the seismic volcano-stratigraphic method introduced in this work. This approach was first presented in Bischoff et al. (2017), and is outlined in Chapter 3 of this thesis. These surfaces are based on evidence of important erosional events that degrade the volcanic edifices (PoDgS) after volcanism had ceased, and on evidence of disturbances to basin sedimentation due to progressive burial of the edifices (PoBuS).

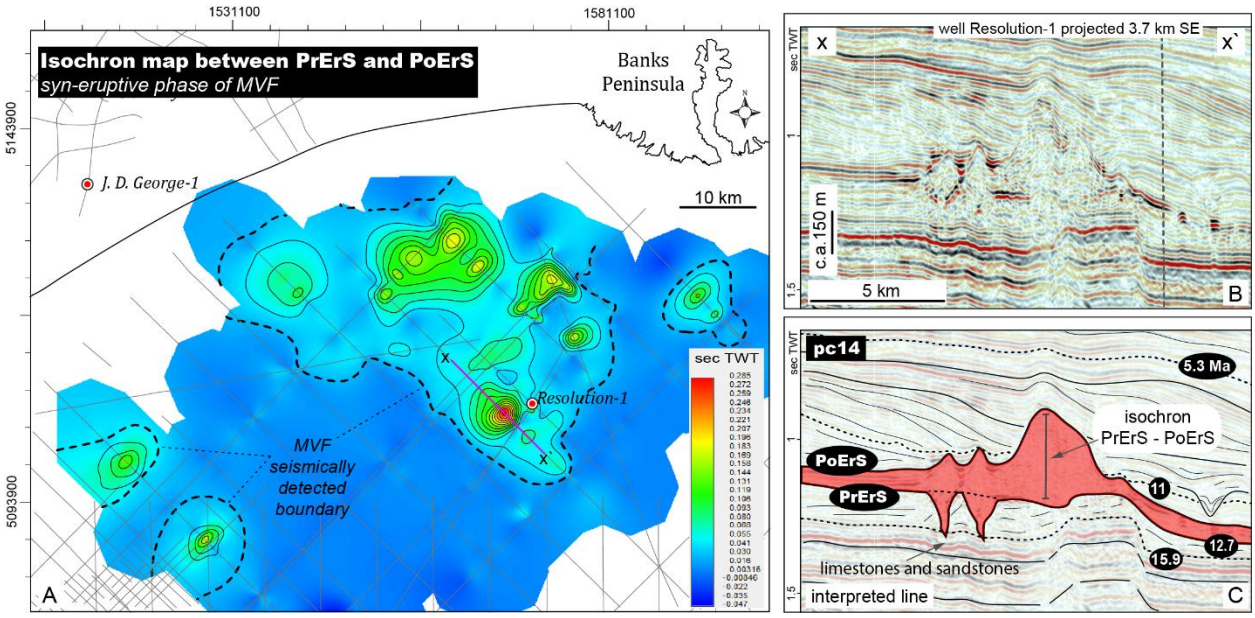

Figure 39: A) Isochron map between pre-eruptive (PrErS) and post-eruptive surfaces (PoErS) of MVF showing the location of MVF cone-type volcanoes. Note that the surfaces thin and amalgamate with increasing distance from individual or clusters of volcanoes, defining the seismic detectable boundaries of MVF. B) Uninterpreted seismic section across volcano pc-14. C) Interpretation of seismic section in B) showing the PrErS and PoErS surfaces and the associated isochron. Diatremes were excluded during mapping of the PrErS surface due to computer limitations, as they would have shown a false positive structure in the isochron map.

4.5 Geological Characterisation of Maahunui Volcanic Field

This section present the results obtained from petrographic, XRF, SEM-EDS and seismic reflection analysis of the MVF. Geological characterisation of this volcanic field was undertaken by combining results from petrographic analysis of volcanic and sedimentary rocks recovered from Resolution-1 and the interpretation of 2D seismic lines in the studies area (Figure 34).

4.5.1 Results from Petrography, XRF and SEM-EDS Analysis

In this section, we describe the characteristics of five main groups of rocks related to the MVF: (1) intrusive rocks emplaced into (2) host paralic to neritic sedimentary rocks, (3) bathyal mudstones and carbonates, and (4) bathyal siltstones interbedded with (5) volcaniclastic rocks.

4.5.1.1 Intrusive rocks (1911.5 to 1963 m)

The Resolution-1 well penetrates 51.5 m of intrusive rocks, approximately 5 m of which was cored from 1958 to 1963 m. Macro and microscopic description of a core sample collected from a depth of 1962.25 m indicated a leucocratic, medium-grained hypidiomorphic medium-grade altered rock (Figure 40; Figure 41). Primary minerals in this sample are plagioclase (70%) and augite (20%), with subordinate orthoclase and olivine (<10%). Plagioclases usually form 0.5 to 2.5 mm elongated euhedral to subhedral crystals of andesine to labradorite based on their extinction angle, and are commonly altered to smectite, illite and zeolite. Augite occurs as subhedral prismatic crystals up to 6 mm in diameter, which form an ophitic texture with plagioclase. These textures and compositions are common in diabase rocks, and suggest an intermediate magma cooling rate at shallow depths (Walker, 1957). Clinopyroxenes in some cases are replaced by amphibole and biotite. Chlorite alteration is pervasive in some parts of the rock or associated with opaque minerals, and may indicate magma hydration and high temperature (ca 250° C) hydrothermalism. Olivine can be partially or totally replaced by iddingsite, which suggests alteration in the presence of water (Smith et al, 1987). Miarolitic cavities occur in several parts of the core and reinforce the interpretation of a hypabyssal rock injected at shallow depths, which indicates that MVF melts were enriched in volatiles (Peretyazhko, 2010). Accessory minerals include apatite, opaques (ilmenite?) and zircon. We classify this rock using the QAPF diagram as an olivine-monzogabbro. Petrographic description presented in Milne (1975) classified some parts of this intrusion as a quartz-monzogabbro (however we did not identify quartz in our samples), and as a teschenite, due to the presence of analcite. Analcite (or analcime)

is a tectosilicate from the zeolite group and can form as a primary igneous mineral in under-saturated volcanic rocks associated with hydrated magmas (Pearce, 1993). We describe rare crystals of analcite associated with radial zeolite, which always fill residual space and cavities. This suggests that analcite more likely is a secondary product of hydrothermalism rather than a primary mineral from the magma. However, a complete microscopic and nanoscopic analysis of the well core is required to test this interpretation.

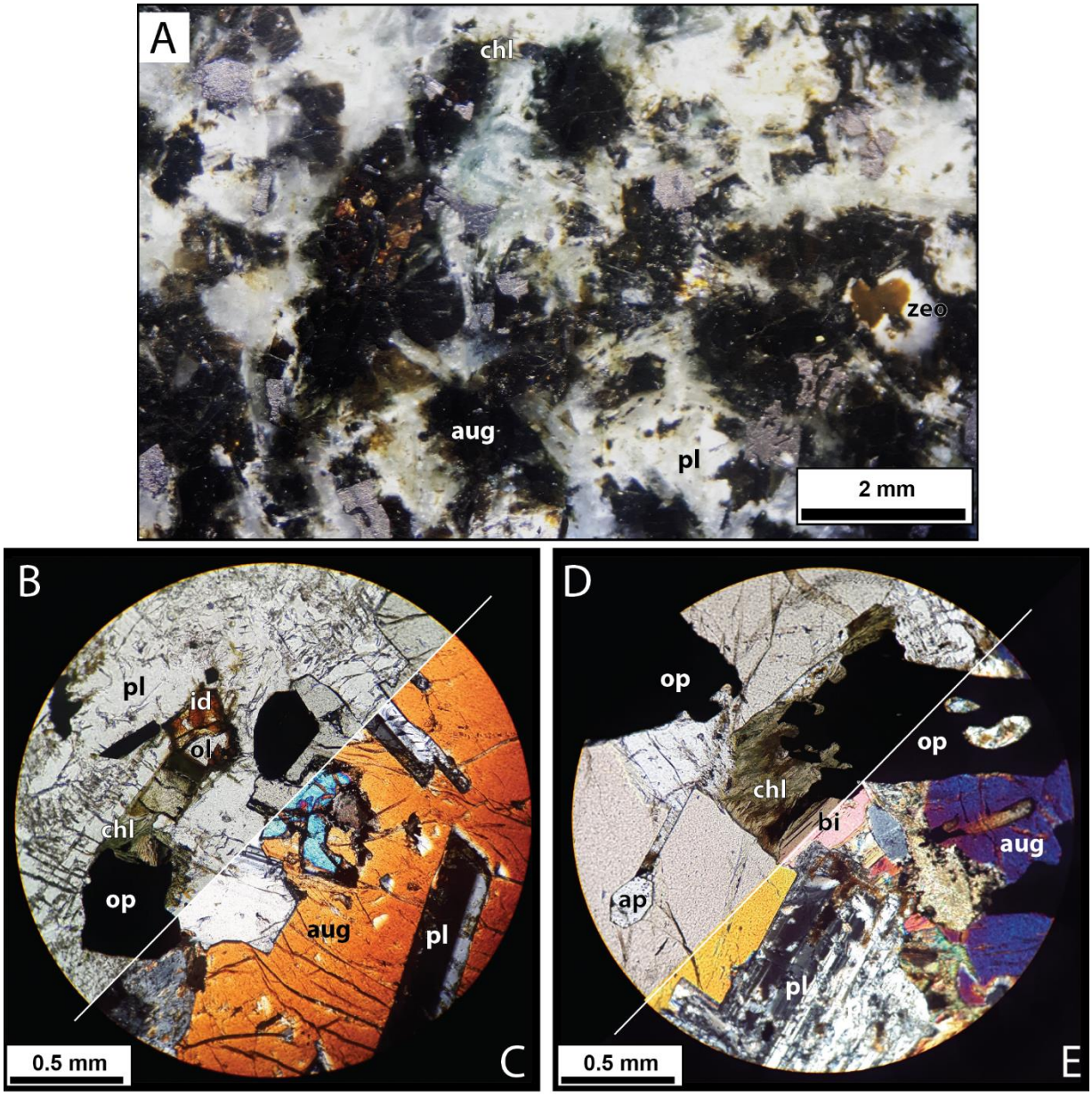

Figure 40: Macroscopic and microscopic photographs of the monzogabbro recovered from a depth of -1962.25 m in the Resolution-1 well. A) Photograph of a medium-grained leucocratic intrusive rock composed of plagioclase (pl) and pyroxene (aug). Zeolite analcite (zeo) occurs filling cavities. Chlorite (chl) occurs as an alteration of primary minerals. Thin-section photographs in plain (B and D) and cross-polarized light (C and E) showing ophitic texture of plagioclase (pl) and augite (aug), olivine (ol) crystals partially replaced by iddingsite (id), and clinopyroxenes (aug) replaced by biotite (bi) and chlorite (chl), which suggests magma crystallization at shallow depths and H_2O interaction. Accessory minerals are: opaques (op) and apatite (ap). Photographs and petrographic identifications were made in conjunction with Marcos Rossetti (UC PhD candidate in physical volcanology).

Results from the XRF analysis indicate a bulk composition of ca 50% of silica (SiO_2), ca 17% of Al_2O_3, and high content of Fe, Mg, K, Ca and Ti, which may suggest a calc-alkaline magmatic series. Geochemical analysis was conducted only with the attempt to verify a possible correlation between the middle Miocene intrusive and extrusive rocks. Further sampling and analyses would be required to characterise the complete geochemistry of MFV. Radiometric dating (K-Ar) presented in Milne (1975) indicate a crystallization age of 12 ± 2 Ma.

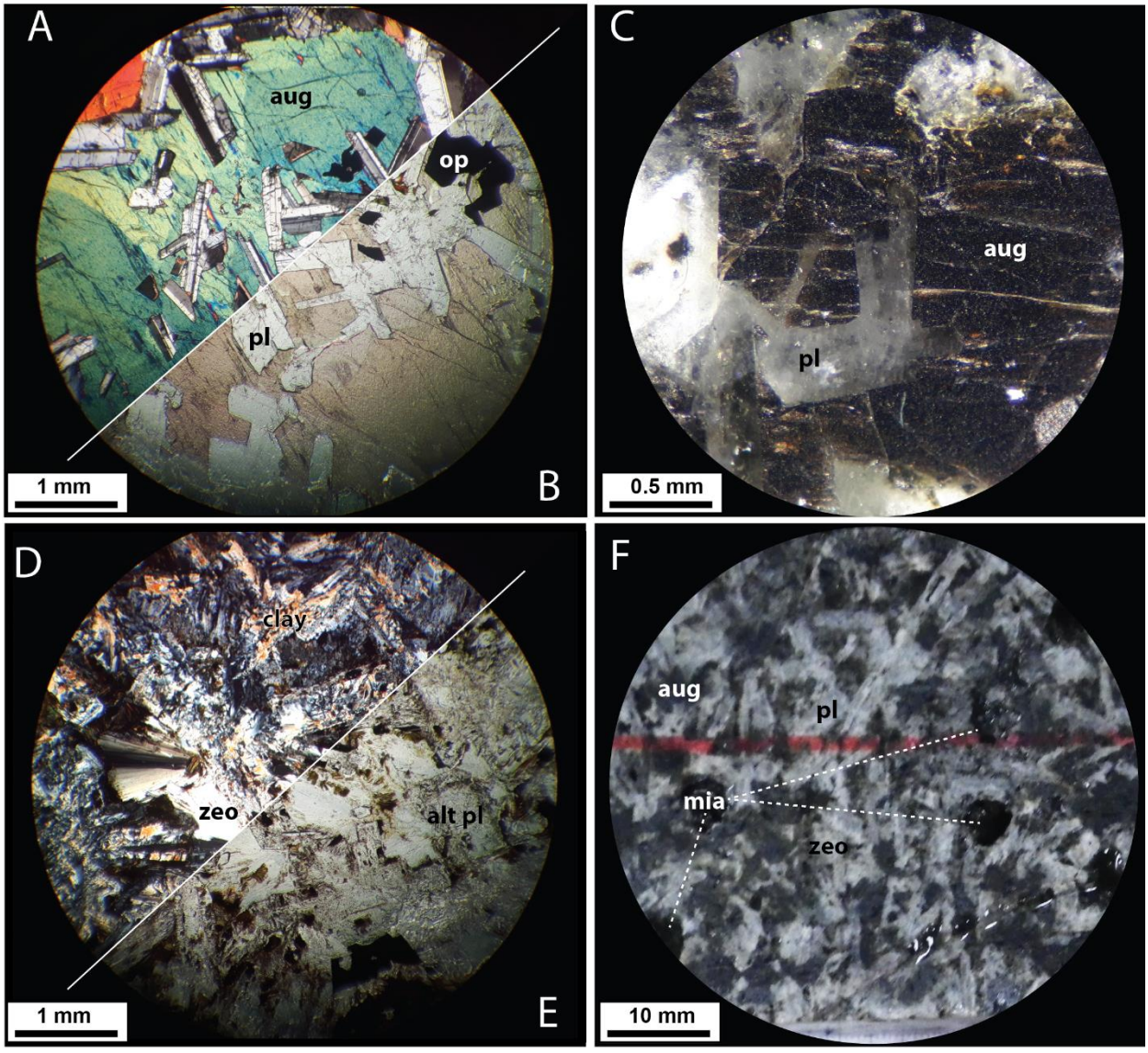

Figure 41: Macroscopic and microscopic photographs of the monzogabbro recovered at -1962.25 m in the well Resolution-1. Thin-section in cross-polarized light (A), plain polarised light (B) and macroscopic polished section (C) showing augite (aug) and plagioclase (pl) with ophitic texture. Thin section in cross-polarized light (D) and plain-polarized light (E) showing zeolite (zeo) filling interstitial space and plagioclase altered to clays. Macroscopic photograph of Resolution-1 core at the depth of 1663 m (C) showing augite, plagioclase, acicular crystals of zeolite and miarolitic cavities (mia). Photographs and petrographic identifications were made in conjunction with Marcos Rossetti (UC PhD candidate in physical volcanology).

4.5.1.2 Paralic to neritic host sedimentary rocks (1911.5 to ca 1335 m)

The monzogabbro sampled from the Resolution-1 well intruded Cretaceous-Paleocene paralic to middle neritic sedimentary rocks of the Broken River and Conway formations. These sedimentary rocks are composed of granular pebble size conglomerates, fine-grained white quartz-sandstones, associated with dark grey pyritic siltstones, and thin layers of carbonaceous mudstones. Hydrothermal effects are observed in these rocks extending ca 34 m above the intrusion, based on the occurrence of siltstones cross-cut by carbonate veins and abundant zeolites (Milne, 1975). Palynomorphs and miospores show an increasing degree of thermal alteration towards the intrusion (Schiøler et al., 2011). Onshore, analogue gabbroid outcrops from the Oligocene(?) Acheron Outlier intrusions show evidence of thermal effects extending several tens of metres from the igneous rocks (Eady, 1995). Intrusions emplaced in organic-rich sedimentary rocks have the potential to elevate the temperature near the igneous bodies sufficiently high to generate thermogenic gas (e.g. Aarnes et al., 2015). This heating process can generate methane (CH_4), and can release high amounts of CO_2 (e.g. Delmelle et al., 2015; Sversen et al., 2018), together with sulfidic acids such as H_2S (e.g. Iacono-Marziano et al., 2013; Robertson et al., 2015; Arnorsson et al., 2015). The upper Paleocene-Eocene part of this rock association is characterised by mudstones and fine-grained sandstones (Charteris Bay Sandstone), interpreted to be deposited in transgressive shallow-marine environments, in association to passive tectonic subsidence in the basin (Field et al., 1989; Schiøler et al., 2011). This rock association is locally interbedded with thin layers of tuffaceous rocks that probably correspond to material erupted from scattered vents in the Canterbury Basin (Figure 34) or to localized peperitic material.

4.5.1.3 Bathyal mudstones and carbonates (ca 1335 to 1284.1 m)

Bathyal mudstones and carbonates deposited from the Oligocene to early Miocene comprises light grey to brown mudstones (Ashley Mudstone) and light grey massive carbonate rocks (Amuri Limestone and Omihi formations). These units are typically poorly indurated and show gradual variation from silty mudstones to calcareous mudstones and wackestones (Milne, 1975; Figure 42). This rock association represents a period of maximum inundation of Zealandia, and in the study area, corresponds to the development of a condensed section attributed to a very low supply of terrigenous materials (e.g. Field et al., 1989). The contact between the Amuri and Omihi formation is unconformable with a time break of ca 13.5 million years, from the early Oligocene to early Miocene (unconformity O-eM; Figure 36; Figure 42).

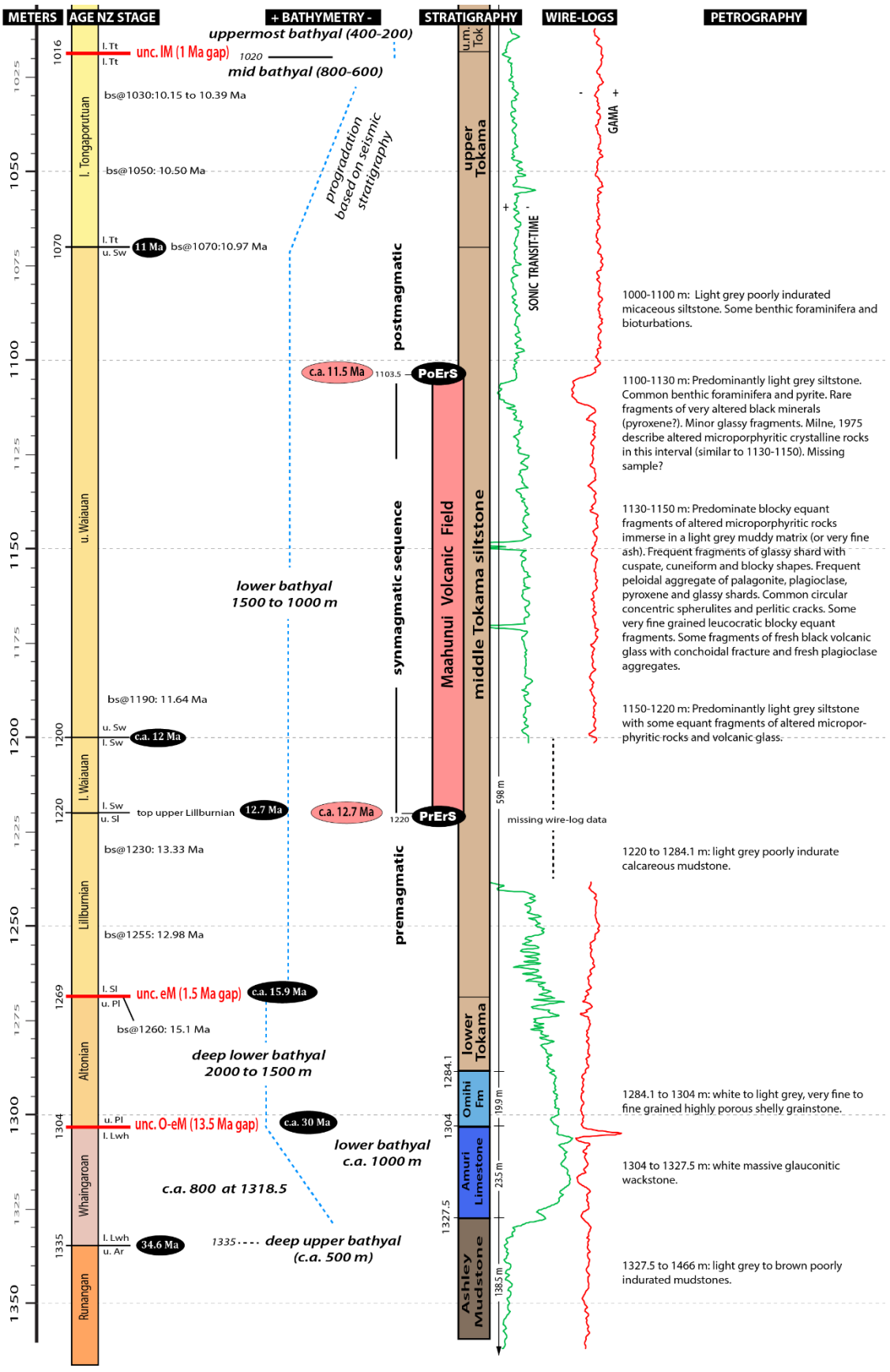

Figure 42: Composite well data of the Oligocene-Miocene interval of Resolution-1 well showing the lithologies, ages, paleo-environments, stratigraphy and wire-logs. Symbol bs@ is the given biostratigraphic age in Schiøler et al. (2011). Blue dashed lines show the bathymetry trend. Numbers in black ellipses are ages according to the 2015 NZ Geologic Time Scale (Raine et al., 2015). Numbers in red ellipses are estimated ages of the MVF based on the integration of these dataset.

The origin of the O-eM unconformity is controversial and successive authors have interpreted it as the product of glacio- or tectonic-eustatic changes, sediment starvation during a high stand period, volcanism, or action of sea-bottom currents (e.g. Lever, 2007). Seismic reflection analysis shows that some funnel-like anomalies interpreted to represent maar-diatreme volcanoes have excavated into the upper part of these sedimentary rocks, which is the topic of Chapter 5. Rare tuffaceous material is locally described interbedded within this rock association, which likely was erupted from scattered vents in the Canterbury Basin (Figure 34).

4.5.1.4 Bathyal siltstones (1284.1 to 686.1 m)

From 1284.1 to 686.1 m, the dominant rock in Resolution-1 is a soft light grey siltstone (Tokama Siltstone) with sparse bioclasts and benthonic foraminifers (Figure 43A), deposited in a bathyal setting from the early Miocene to early Pliocene (Milne, 1975; Schiøler et al., 2011; Figure 42). These rocks are locally interbedded and blended with volcaniclastic material of the MVF (Figure 43B), which we characterised separately in the section 4.5.1.5. During the time period of formation of Tokama Siltstone (early Miocene to early Pliocene), three main biostratigraphic unconformities have been identified in the Resolution-1 well, each representing hiatuses of 1 to 3 Ma (Schiøler et al., 2011). These unconformities are interpreted to be formed by different tectonic pulses during the onset of basin inversion and compressional tectonics to NW of the study area, which is related to southward propagation of the Neogene Hikurangi subduction zone (Field et al., 1989; Kamp et al., 1992; Lu et al, 2005; Schiøler et al., 2011). Here we refer to these unconformities as eM (early Miocene), lM (late Miocene), and eP (early Pliocene), according to their ages of formation (Figure 36).

To characterise the paleo-environment in which MVF has erupted in detail, we subdivide the Tokama Siltstone into four depositional units, according to major paleo-bathymetric shifts identified in the biostratigraphic data (Schiøler et al., 2011) of the Resolution-1. These shifts are strictly related to the position of unconformities, and are distributed in Resolution-1 as follows: lower Tokama (1284.1 to 1260), middle Tokama (1260 to 1070), upper Tokama (1070 to 1016), and uppermost Tokama (1016 to 686.1). Table 5 shows the main stratigraphic and paleo-environment characteristics of these units.

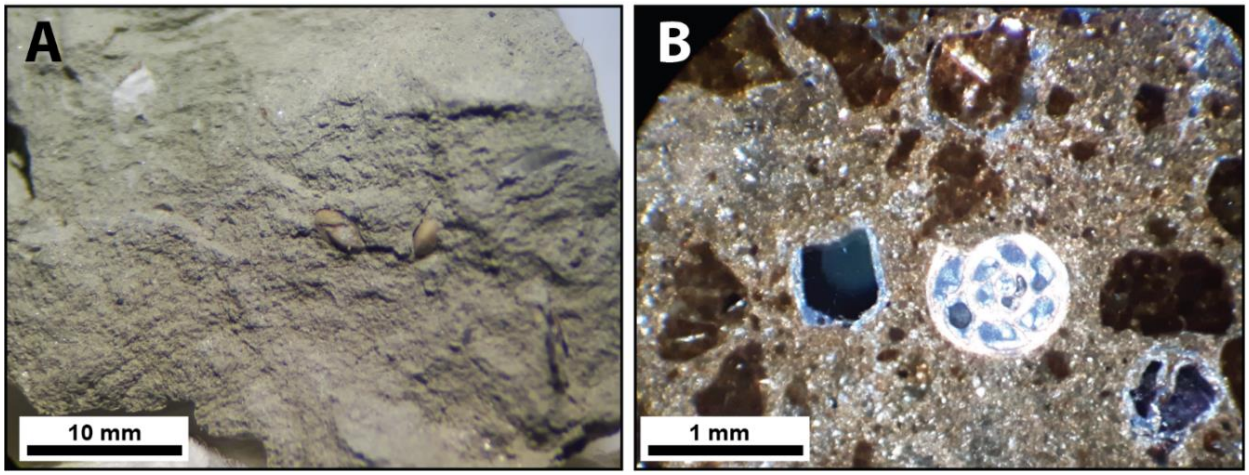

Figure 43: A) Macroscopic photograph of an unwashed cuttings sample of a massive siltstone containing benthonic foraminifera recovered from the interval 1120 to 1130 m from the Resolution-1 well (middle Tokama). B) Microscope photograph in crossed-polarized light of unwashed cutting samples of volcanic clasts and a gastropod in a muddy matrix from the interval of 1130 to 1140 m in Resolution-1.

The lower Tokama was deposited during the late early Miocene, in a deep lower bathyal setting, with water depths ranging from 2000 to 1500 m (Figure 42). Its upper boundary is marked by a sharp transition to a lower bathyal setting (1500 to 1000 m), which is represented by the unconformity eM and its ca 1.5 Ma hiatus in the study area (Figure 42). The middle Tokama (which is interbedded with volcaniclastic rocks of the MVF) was deposited during the middle Miocene, in a relatively steady lower bathyal setting (1500 to 1000 m deep), which is evident by the biomarker species *Sigmoilopsis schlumbergeri* and *Eggerella bradyi,* often associated with *Cibicides robertsonianu*, although the decrease in planktics towards the top of the middle Miocene interval points to an overall up-hole decrease in water depths (Schiøler et al., 2011; Figure 42). We place the onset of this base-level fall at ca 11 Ma, based on seismic stratigraphic analysis that shows a NW-SE progradation of clinoforms in a downlap relationship onto sub-horizontal reflectors, which indicate decreasing water depths in the area of Resolution-1 (Figure 39).

The onset of decreasing water depths marks the base of the upper Tokama, which is interpreted to represent a progressive shift from a lower bathyal to a middle bathyal setting (800-600 m), due to increasing sedimentary supply from the NW. During this period, all volcanic activity in MVF was extinct. The top of upper Tokama is marked by a sharp transition to an uppermost bathyal setting (400-200 m) and associated hiatus of ca 1 Ma in the study area (unconformity lM), which is the most important post-eruptive erosional event that impacts the morphology of the volcanoes in the MVF (details in section 4.6). The uppermost Tokama (Figure 42) was deposited during the late Miocene to early Pliocene in an uppermost bathyal setting. Seismic stratigraphic

interpretation suggests a progressively shallowing in water depths up-sequence. The top of this depositional unit is evident by the occurrence of bioclastic mudstones, coquinas and sandstones of the Kowai Formation starting at 686.1 m, which marks the establishment of an outer neritic setting (100 to 200 m) in the area of Resolution-1, around 5.3 Ma (unconformity lM, Figure 36).

Table 5: Main stratigraphic and paleo-environmental characteristics of the Tokama Siltstone depositional units. Highlighted middle Tokama unit (red) is interbedded with the volcaniclastic rocks described in the section 4.5.1.5.

Depositional unit	Depth in the well	Age	Depositional setting	Lower bound	Upper bound	Thickness (m)
Uppermost Tokama	1016 to 686.1	Late early Miocene to late Pliocene	Uppermost bathyal	Unc. lM	Unc. eP	329.9
Upper Tokama	1070 to 1016	Late early Miocene	Mid bathyal	Onset of slope progradation	Unc. lM	54
Middle Tokama	1269 to 1070	Middle Miocene	Lower bathyal (1500-1000 m)	Unc. eM	Onset of slope progradation	190
Lower Tokama	1284.1 to 1269	late early Miocene	deep lower bathyal	Omihi Fm	Unc. eM	24

4.5.1.5 Volcaniclastic rocks (-1220 to - 1103.5 m)

The Resolution-1 well penetrates a 116.5 m (1220 to 1103.5) thick sequence containing fragments of volcaniclastic rocks interbedded with siltstones of the middle Tokama depositional unit (Figure 42; Figure 43; Figure 44; Figure 45; Figure 46; Figure 47; Figure 48; Figure 49; Table 5). Macro and microscopic description of cuttings sampled from this interval indicates poorly sorted (< 0.1 to 5 mm), hyalocrystalline, highly altered, non-welded fragments of leucocratic rocks, glass and disaggregated crystals. Grain-size distribution is variable, usually comprising fragments with microcrystalline, microporphyritic and vitrophyric texture, and less common vitriclastic textures (Figure 45). Primary components include crystals of plagioclase and pyroxene, shards of glass (Figure 46; Figure 47; Figure 48), and common spheroidal aggregates (armoured lapilli?; Figure 49). Sandstone and limestone lithics (probably from Amuri and Omihi limestones, and Charteris Bay sandstone) are relatively abundant (Figure 49). Pervasive palagonite alteration is dominant, which is typically interpreted as devitrification of sideromelane glass (Stroncik and Schmincke, 2002), although some fresh fragments also occur (Figure 46; Figure 47).

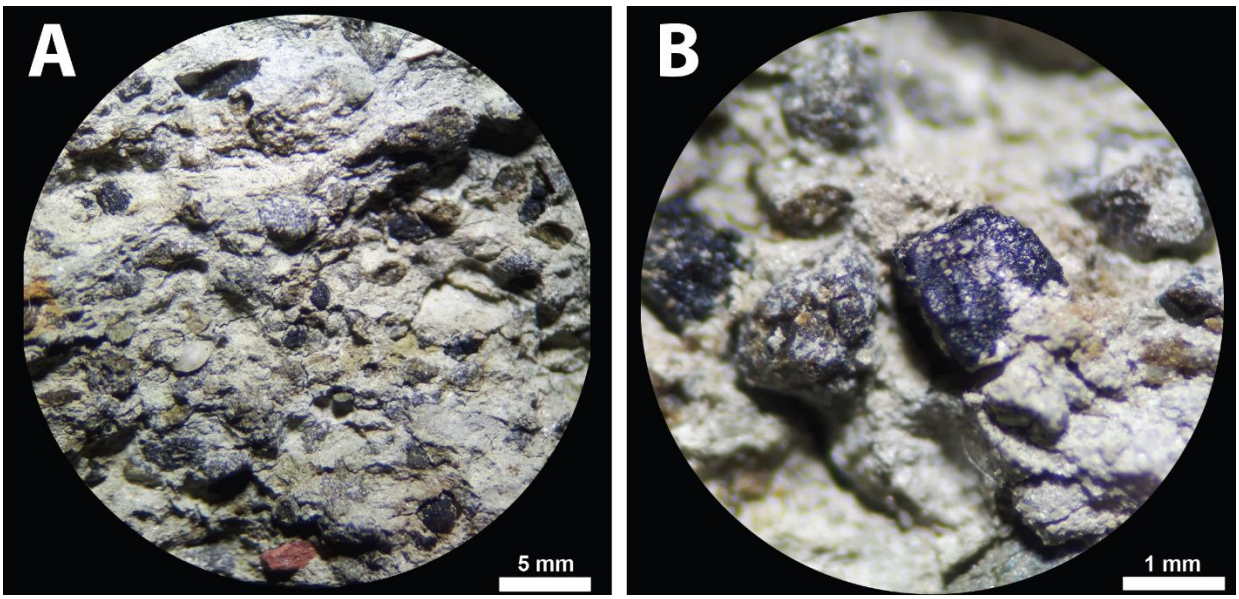

Figure 44: Macroscopic photographs of unwashed cutting samples from the interval of -1130 to -1140 m in Resolution-1. A) Volcanic fragments and bioclasts immersed in a muddy matrix. Black fragments are mainly altered pyroxenes (B).

Plagioclase usually forms <0.1 to 1.5 mm elongated euhedral crystals, typically associated with microporphyritic and vitrophyric textures (Figure 45A and C). Often, plagioclase occurs as euhedral to anhedral broken phenocrysts in sharp contacts with the groundmass (Figure 45B and D), which could represent fragments of holocrystalline material crystallized in the magma chamber that was disaggregated during explosive eruptions (Best and Christiansen, 1997). Less commonly, some phenocrysts show rounded margins (Figure 45D), which may be a consequence of abrasion due to particle collision during magmatic transport, or mixing and recycling of material associated with multiple explosions into the deep crater zones of maar-diatremes volcanoes (e.g. White and Ross, 2011; Graettinger et al., 2016). Some rare phenocrysts show sieve texture and devitrified glass inclusions (Figure 45C), which could indicate disequilibrium phases in the magma chamber, high volatile content of the original melts, or rapid magma decompression (Nelson and Montana, 1992).

Glassy shards are very common in the samples of this interval, and occur in a wide range of shapes and textures. Most commonly, shards are non-welded and present blocky and cuneiform shapes, and less frequently, cuspate, platy, splintery shapes, and relics of bubble walls. Spall shards form friable fragments usually with cuneiform, blocky, splintery shapes, and minor relics of bubble-walls (Figure 46). These fragments commonly show jigsaw-fit texture and occur in association with blocky fragments that contain microporphyritic cores (Figure 46). These textures are typically interpreted to indicate quenching and breakup of larger and less altered

hyaloclastite fragments formed by thermal shock during rapid cooling (MacPhie et al., 1993). However, these textures could also represent resedimented fragments of spatter clasts originally deposited around the margins of submarine vents during a process equivalent to fire fountains, which formed by an expanding flare of magma above the vent, and quenching of erupted magma due to its interaction with the ambient water (e.g. Cas and Giordano, 2014). Shards with cuspate, platy, splintery shapes and relics of bubble walls sometimes occur associated with poorly sorted and vesiculated rocks (Figure 47), which could be indicative of submarine strombolian eruptions, although examples elsewhere show that these features are also observed in hyaloclastites and in deposits of eruption-fed density currents (e.g. MacPhie et al., 1993; White, 2010; Cas and Giordano, 2014). Blocky, cuspate and platy shards also occur in association with fragments that contain very fine broken crystals, low vesicularity, pervasive alteration to palagonite, and lithics (Figure 48) which could indicate (but not define) phreatomagmatic fragmentation processes (e.g. Walker and Croasdale, 1971; MacPhie et al., 1993).

Often, fragments in this interval display a circular concentric spheroidal texture in two distinctive styles: i) very friable spherules that easily disintegrate from contact with water, show an inner core (lithic?) and external aggregate of very fine particles circled by a palagonite film (Figure 49); and ii) spherules moderately-to-well indurated and associated with pseudo-perlitic cracks, show a devitrified (palagonite) inner core, a single concentric outer rim, and an external array of acicular crystals in a radial pattern (Figure 50). In both cases, the spherules are associated with pervasive alteration to palagonite. The forms and texture of these spherules resembles both armoured lapilli that could be the product of eruption-fed density currents (e.g. White, 2000), or spherulites, which are commonly interpreted to indicate high-temperature devitrification of coherent volcanic glass and/or the presence of aqueous solutions in the magma (e.g. Marshall, 1961; Lofgren, 1970; apud MacPhie et al., 1993).

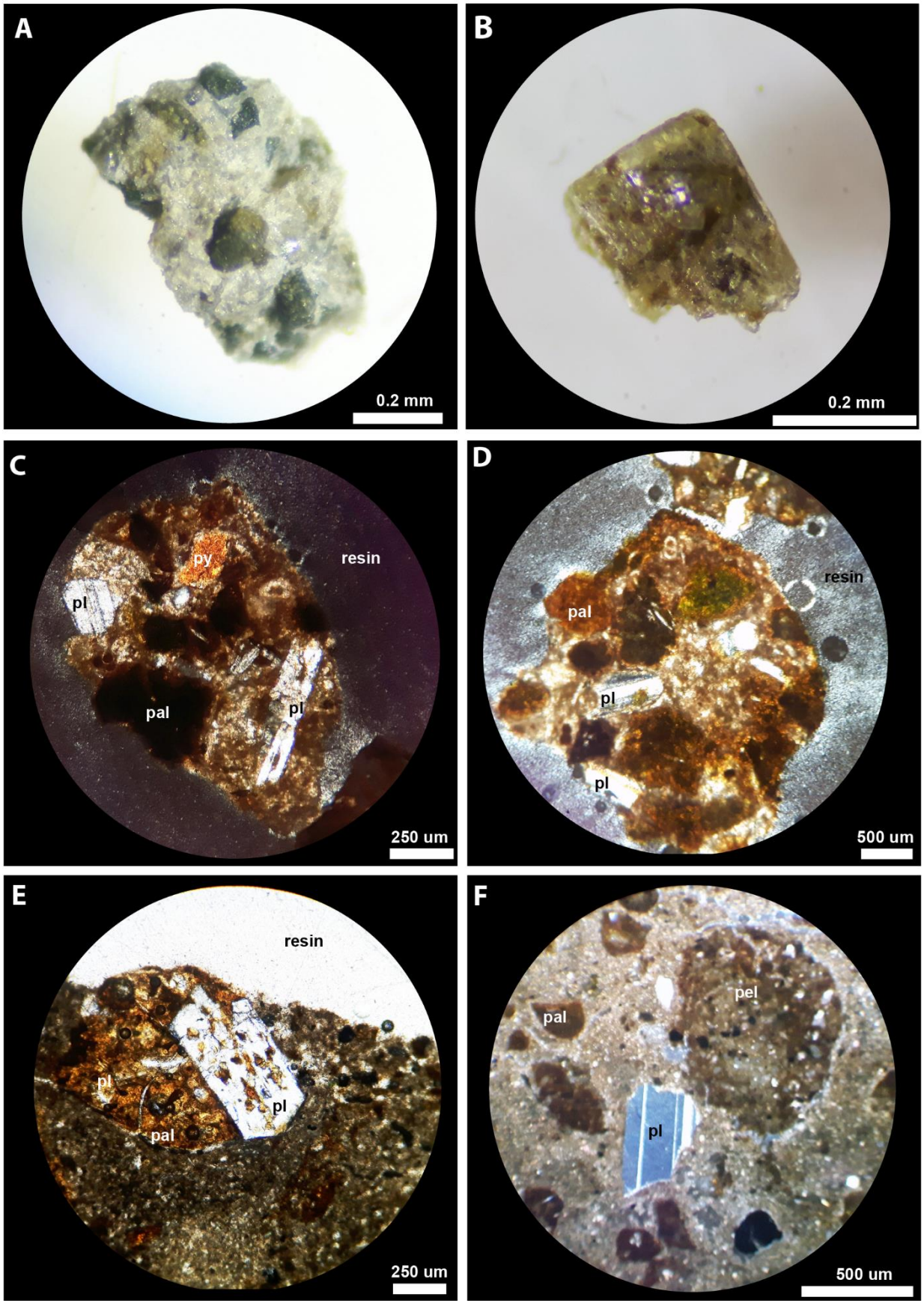

Figure 45: Macroscopic photographs of plagioclase (pl) and pyroxene (py) phenocrysts in microporphyritic texture (A), and an example of broken plagioclase fragments (B). C to F show photographs of rocks with microporphyritic and vitrophyric textures in cross-polarized light of. Note that phenocrysts with broken angular borders (C and F) are associated with peloidal (pel) and palagonite (pal) clasts.

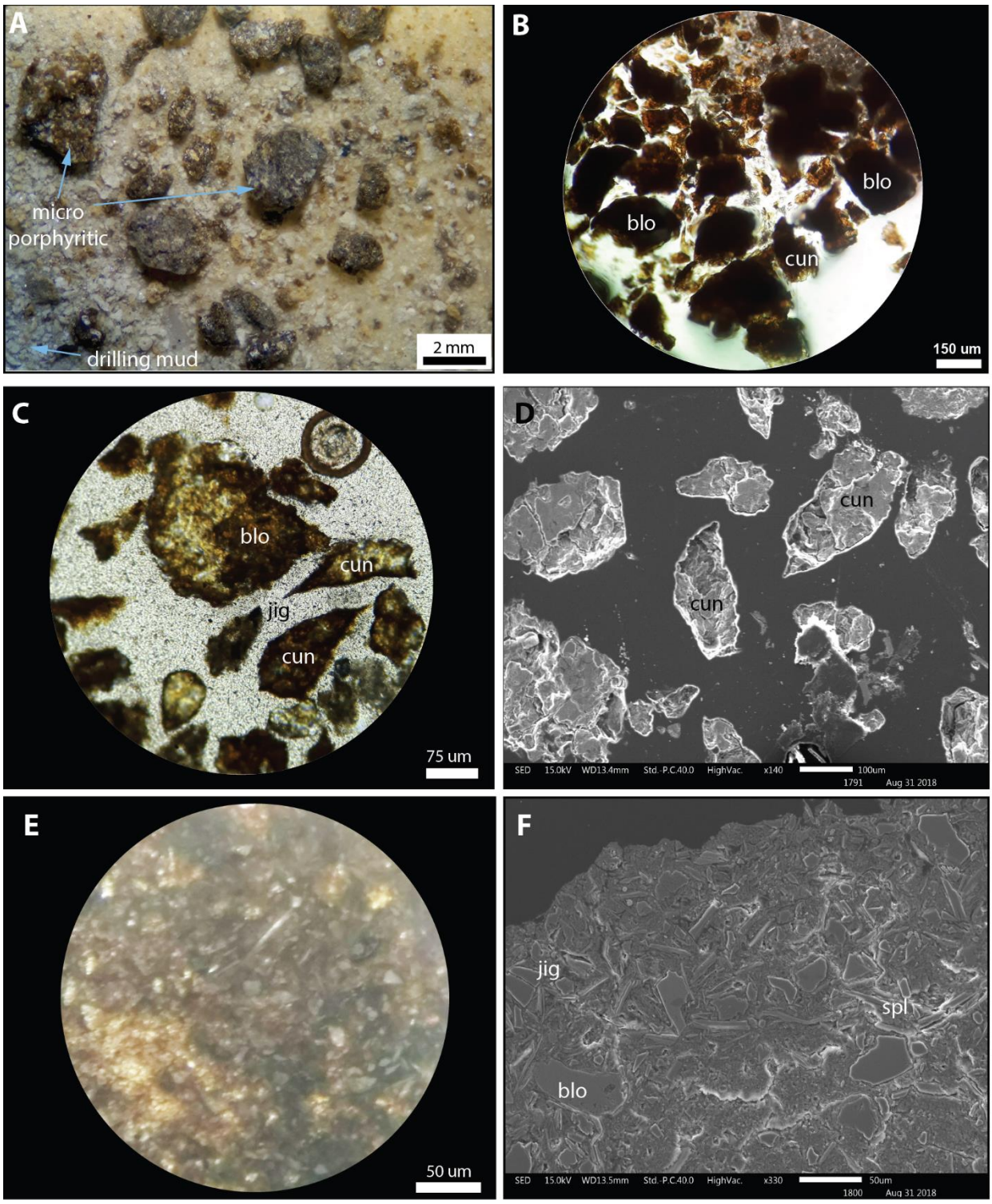

Figure 46: Macroscopic images of volcanic fragments submerged in water (A) during the washing process of samples from the interval of -1130 to -1140 m in Resolution-1. These rocks show altered microporphyritic texture with blocky equant and jigsaw-fit texture. Microscope (B and C) and SEM (D) images of spall shards with cuneiform (cun), and blocky (blo) shapes in jigsaw-fit (jig) texture. Microscope (E) and SEM (F) images of loose glassy shards with blocky and splintery (spl) shapes in vitriclastic and jigsaw-fit jig texture.

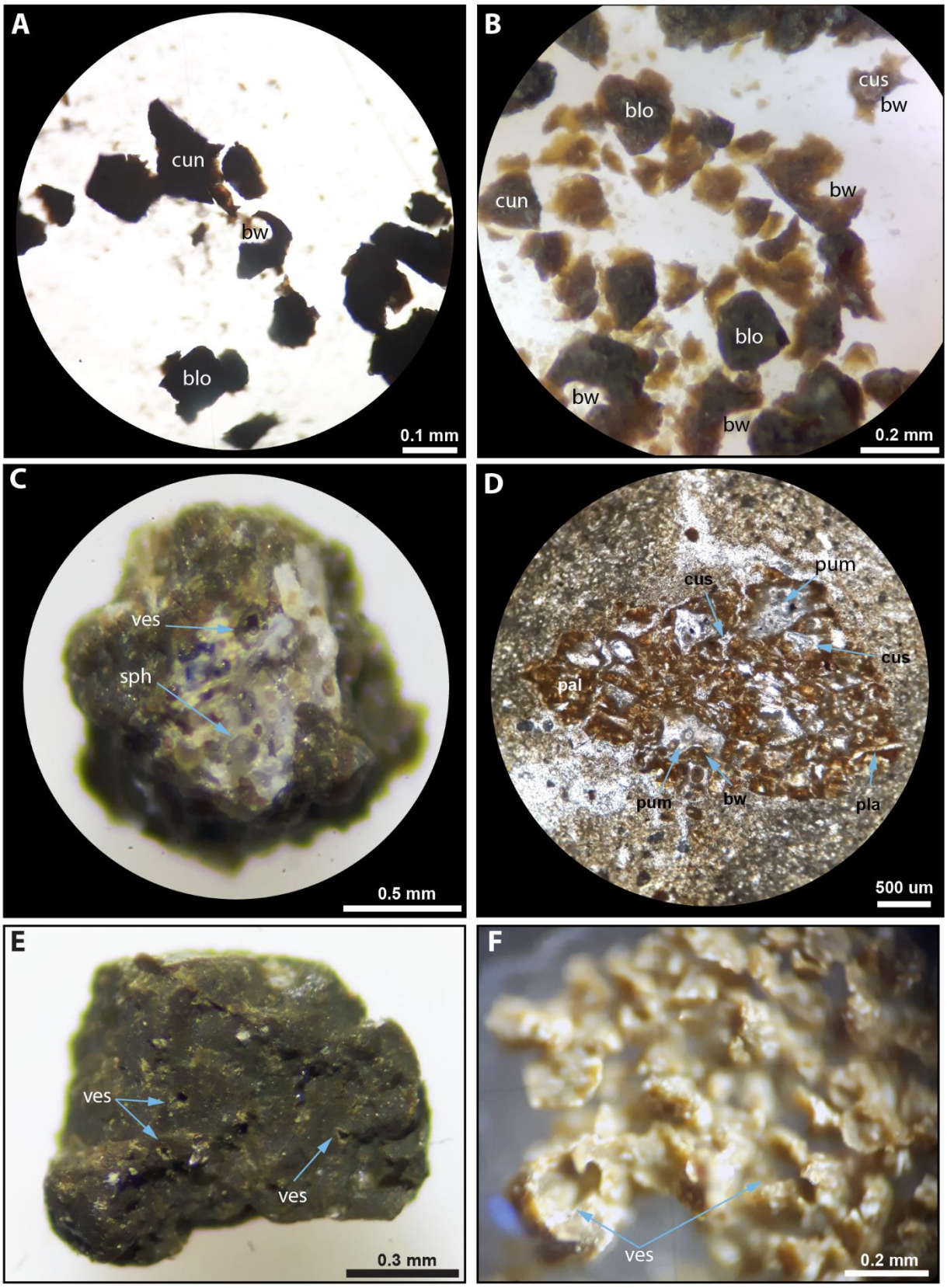

Figure 47: A and B) Macroscopic images of loose shards with cuspate, cuneiform, blocky (blo) and platy (pla) shapes, and common relic bubble walls (bw). C) Hypocrystalline fragment containing concentric spherules (sph) and vesicles (ves). D) Photograph of thin-sections in plain light showing palagonite (pal) and glassy shards with, cuspate (cus), platy (pla) and pumice (pum) shapes, and relics of bubble walls (bw). E) Macroscopic image of microcrystalline blocky equant fragment with some micro-vesicles. F) Macroscopic photograph of loose and poorly indurated spalls of shards with common vesicles.

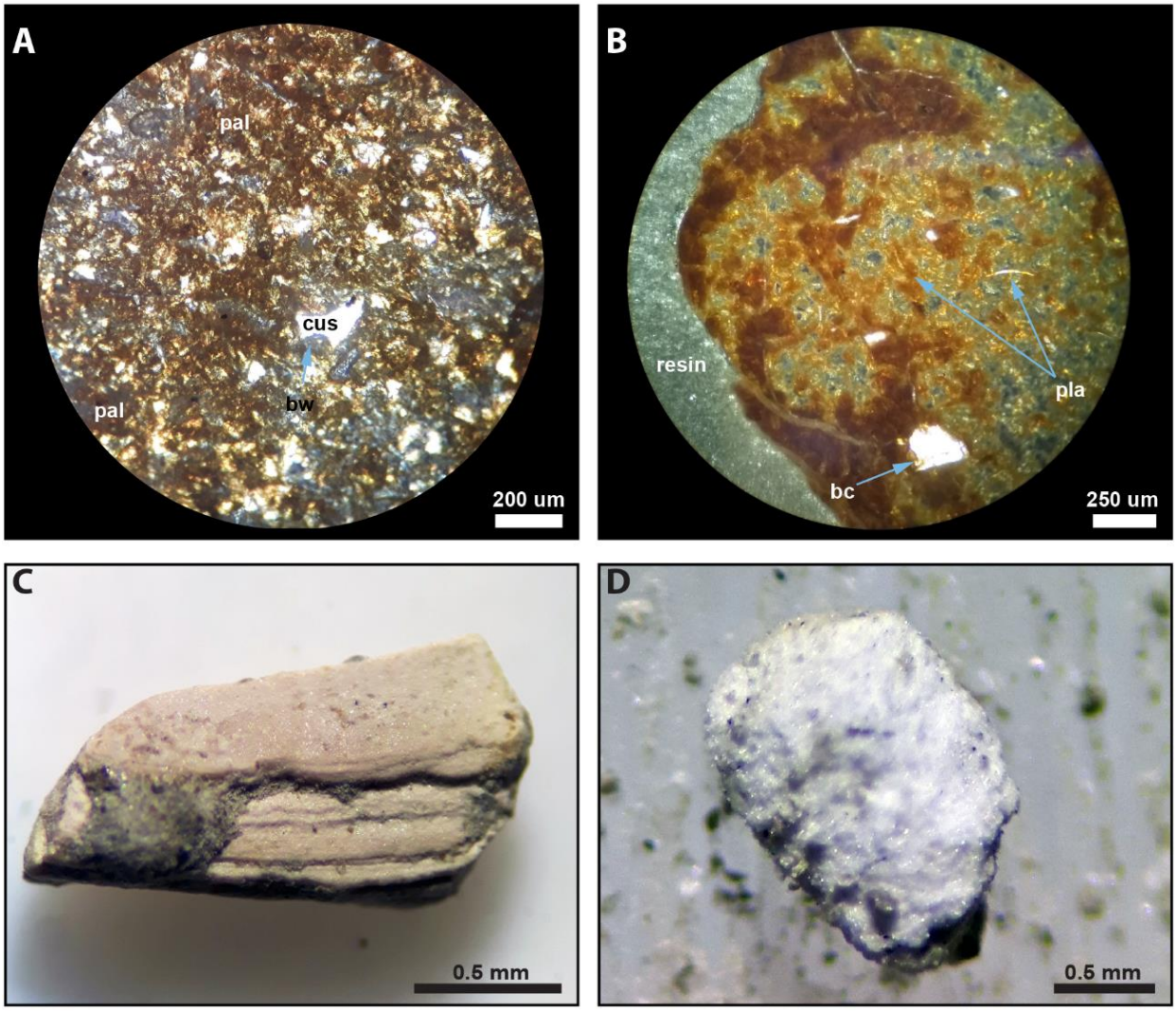

Figure 48: A and B) Thin-sections in plain-polarised light showing fragments of very-fine grained rocks with a pervasive alteration to palagonite (pal), shards with cuspate (cus) and platy (pla) shapes, and fragments of broken crystals (bc). Macroscopic images of limestone (C) and sandstone lithics (D), which may correspond to rocks of Amuri and Omihi limestones, and Charteris Bay sandstone.

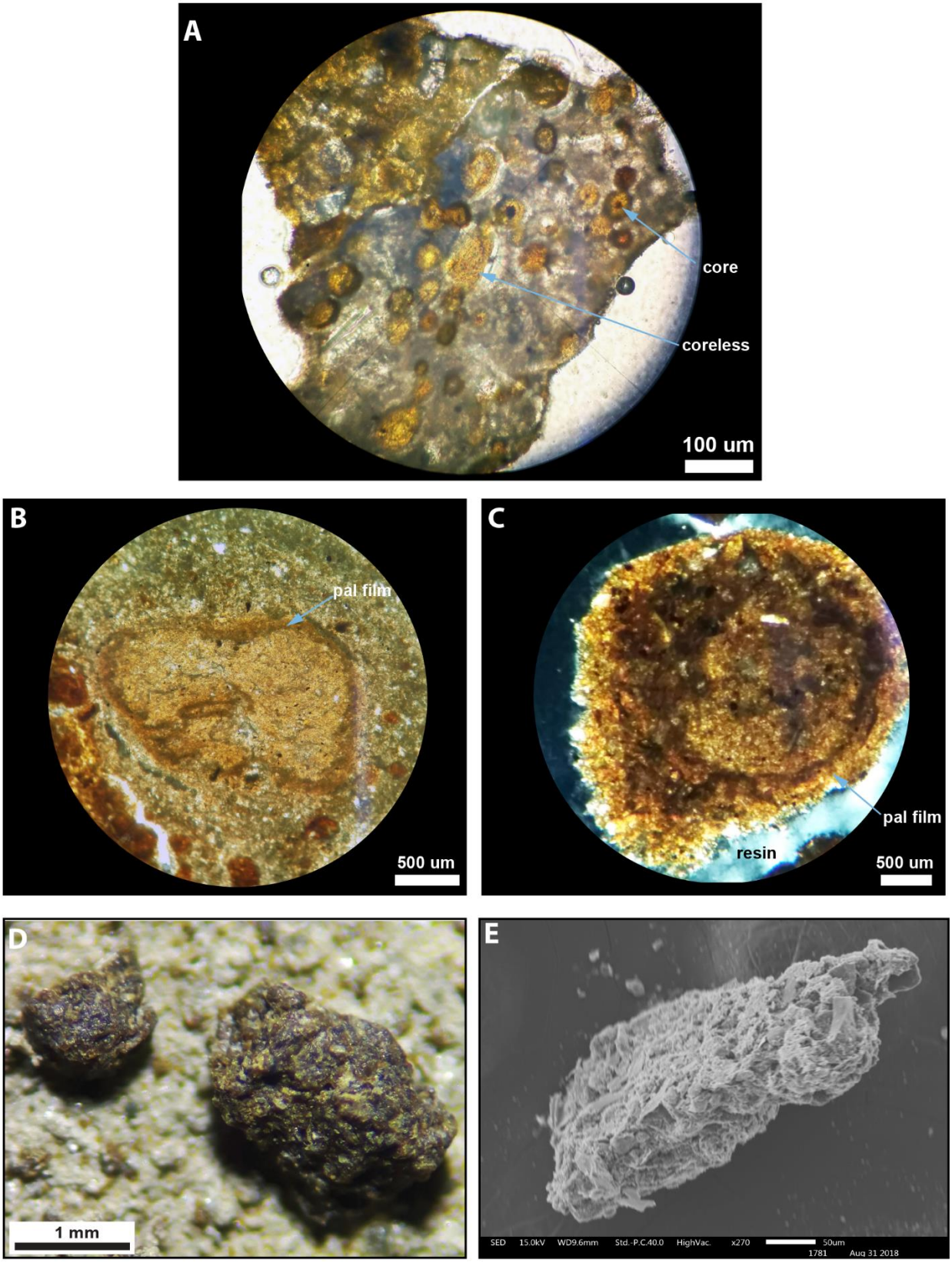

Figure 49: Thin-sections in plain-polarised light (A and B) and cross-polarized light (C) showing spherules with and without an inner core enveloped in a palagonite (pal) film. Macroscopic (D) and SEM (E) examples of poorly indurated highly porous glassy aggregate are also displayed.

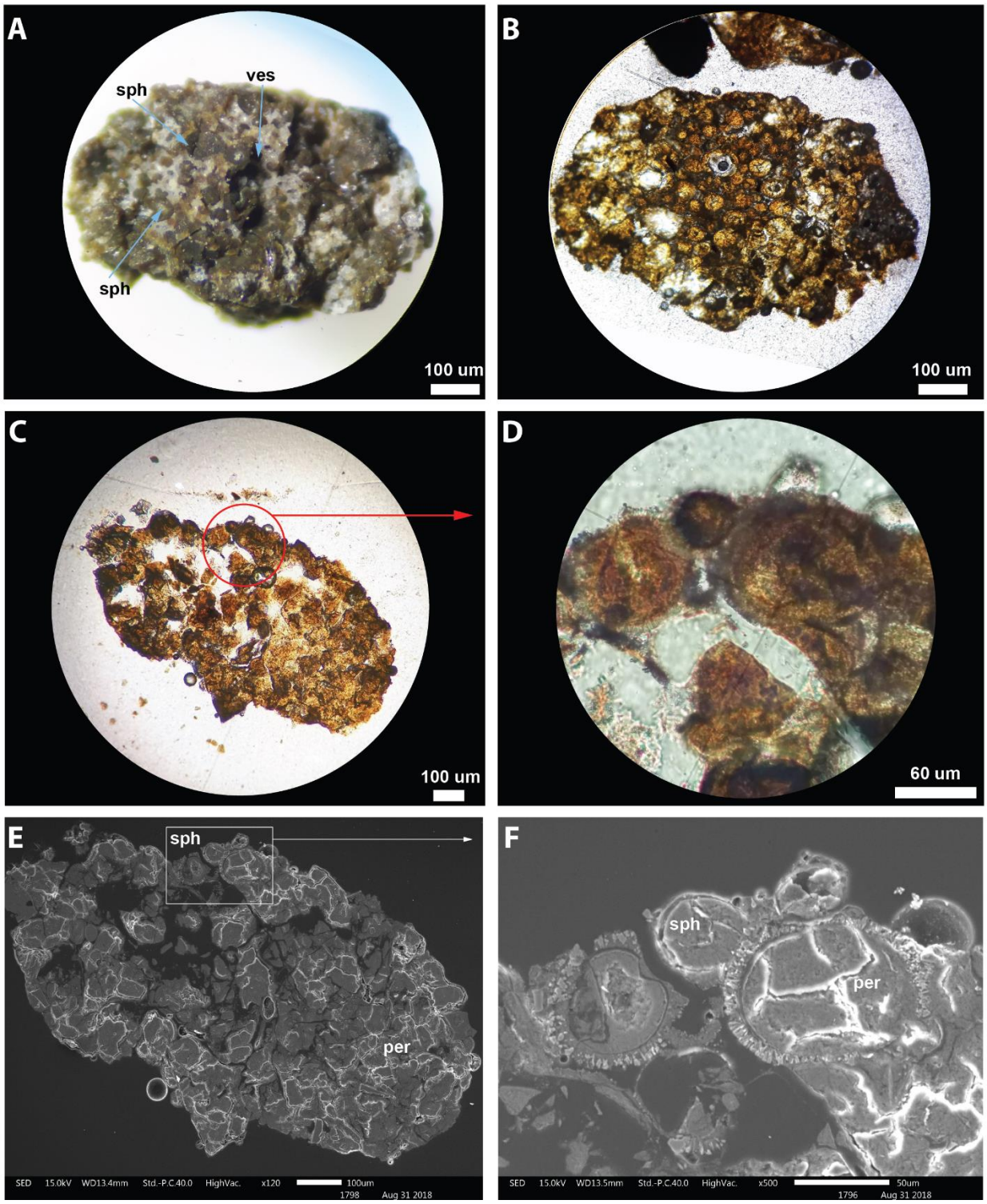

Figure 50: Macroscopic (A) and plain-polarised light microscopic (B) examples of well indurated aggregate of cored spherules (sph), associated with vesicles (ves) and intense palagonite alteration. Plain light (B), cross-polarized and SEM (E and F) images of spherule with a glassy devitrified (palagonite) inner core, enveloped in a single concentric outer rim associated with an array of acicular crystals in radial pattern and pseudo-perlitic (per) cracks.

Given the uncertainties and limitations presented in the section 4.4, it was not possible to confidently interpret these rocks as primary eruptive or resedimented volcaniclastics. Some petrographic features (poorly sorted and polymictic material blended with Tokama Siltstone, and

presence of rounded clasts) suggested resedimented volcaniclastics. However, material blending could be simply caused by drilling issues, or represent the distal products of submarine pyroclastic plumes that incorporated lithoclasts during magma fragmentation and transport (e.g. White, 2000). In contrast, wireline-logs of Resolution-1 show sharp log-facies contacts at the boundaries between volcaniclastics and siltstones (Figure 42), which commonly represent abrupt composition changes in lithofacies and could point towards a primary volcaniclastic source. In addition, seismic facies show constant lateral thickness in the volcaniclastic interval (Figure 51) and are not confined to valleys, which is characteristic of subaerial pyroclastic surges (e.g. Cas and Wright, 1992), and may indicate a similar process as observed in eruption-fed density currents (e.g. White, 2000). In any case, what is evident from the integration of petrography, seismic stratigraphy and biostratigraphic data is that these volcaniclastic rocks were: i) erupted in relatively deep-water depths (bathyal; ca 1000 to 1500 m), ii) experienced volcanic fragmentation processes (explosive and maybe autoclastic), iii) may or may not have been reworked, and iv) were deposited in the cone apron of the volcano pc14 and near the ring plain of nf01, nf02 and nf03 (these morphologies are the topic of Chapter 5), which reinforces that both end members, primary and reworked volcaniclastics, could be present in the well.

XRF results indicate a bulk composition of ca 45% of silica (SiO_2), ca 14% of Al_2O_3, and contain Fe, Mg, K, Ca and Ti. SEM-EDS analyses in the volcanic glass show an average composition of ca 55% of silica (SiO_2), ca 17% of Al_2O_3 and contents of Fe, Mg, K, Ca, Ti and Na. These results are consistent with the analyses in the monzogabbro intrusion and also indicate a basaltic composition, and together with interpretation from seismic lines (e.g. Figure 51), reinforce a genetical correlation between both intrusive and extrusive rocks.

4.5.2 Age of the MVF and depth of the monzogabbro intrusion

To estimate the age of active volcanism in the MVF, we consider biostratigraphic data (Schiøler et al., 2011), a K-Ar date of the monzogabbro intrusion (Milne, 1975), sedimentological aspects of the strata that enclose both intrusive and volcaniclastics (e.g. amount of compaction and sedimentation rates), and results from seismic stratigraphic mapping (Figure 42; Figure 51).

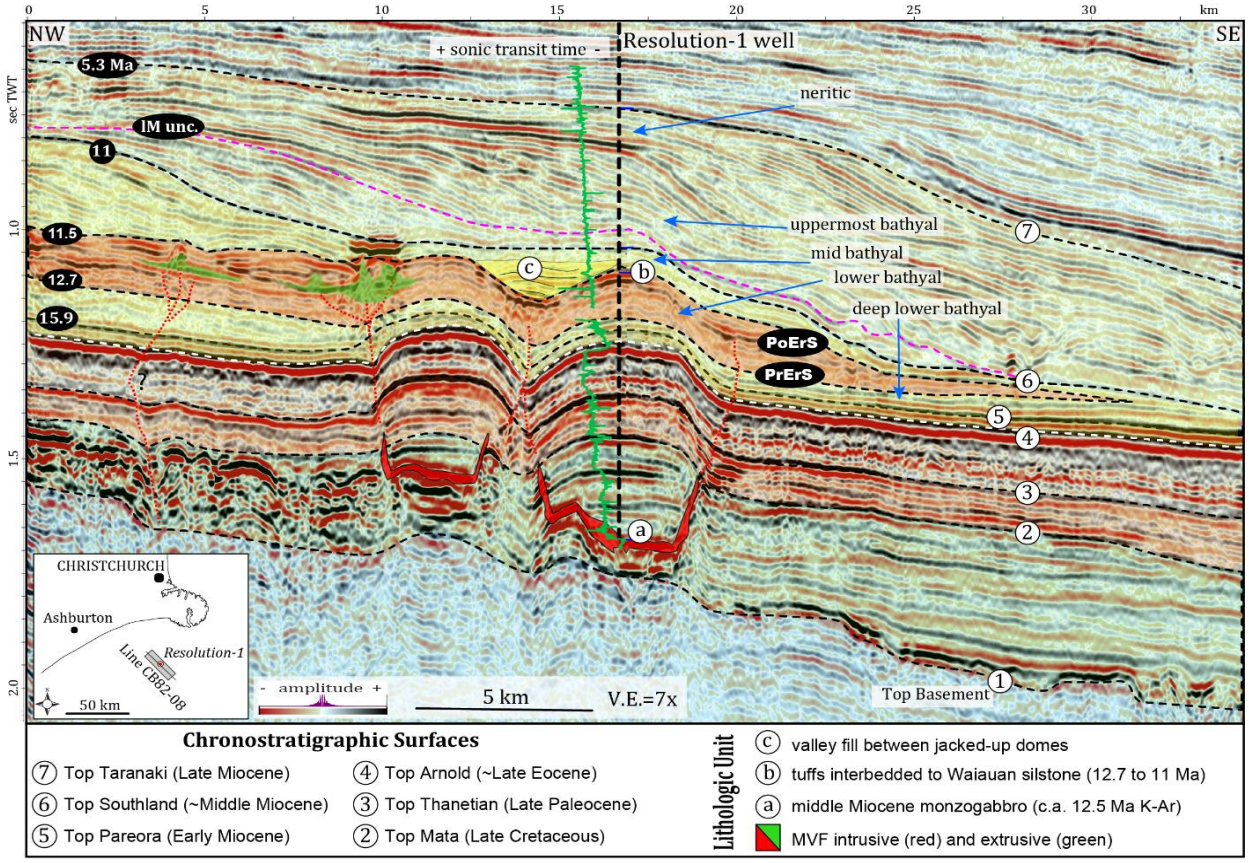

Figure 51: Interpreted 2D dip seismic section at the Resolution-1 well (thick dashed line). Saucer-shaped sills (a) were intruded into Cretaceous sedimentary strata during the middle Miocene (ca 12.5 Ma K-Ar) and caused doming of the overlying strata. The doming consequentially changed the sea-floor topography and promoted deposition as channelized systems (c) next to the dome structures. The syn-eruptive interval (between PrErS and PoErS) is defined by the occurrence of volcanic material (b) interbedded with sedimentary rocks of the Tokama Siltstone of Waiauan age (ca 12.7 to 11 Ma) and seismic stratigraphic analysis. At the border of the domed strata, disrupted reflectors and faults suggest magma and hydrothermal fluid pathways that fed eruptions onto the middle Miocene paleo-seafloor. All seismic anomalies interpreted to correspond to buried volcanoes of the MVF occur between PrErS and PoErS surfaces, which merge to form a single reflector in all directions away from the MVF. Seismic anomalies interpreted to correspond to intrusions are located below PrErS. The available evidence together with geochemical and petrographic analysis demonstrate that the intrusive and extrusive rocks penetrated by the Resolution-1 well have a co-genetic relationship, which together with estimations of sedimentation rate in the area allow us to propose that the MVF was formed from ca 12.7 to 11.5 Ma. Cretaceous to Paleogene horizons courtesy of Andrea Barrier.

The oldest MVF volcaniclastic rocks (1220 m in Resolution-1) correlate to the transition from the Lillburnian to the lower Waiauan New Zealand stages (ca 12.7 Ma), thus, we assume an onset of MVF volcanism at 12.7 Ma (Figure 42). The youngest volcaniclastics occur at 1103.5 m in the well, however, there is no direct biostratigraphic age correlation at this depth (Figure 42). To define the end of MVF volcanic activity, we calculate the sedimentation rates of the middle and upper Tokama, from the depth interval between 1255 and 1030 m in the well (Figure 42). The difference in thickness and age on this interval are 215 m and 2.59 Ma, respectively. To reduce the effect of the thickness of volcanic rocks on sedimentation rates, we subtract 10 m, which was estimated from the density and gamma logs in the well (Figure 42). This gives us an average sedimentation

rate of 83 m/Ma (or 0.0120 Ma/m). Assuming that the sedimentation rate was constant, we multiply the siltstone thickness of the MVF interval (106.5 m) per calculated sedimentation rate (0.0120 Ma/m), which suggests that MVF was active for ca 1.2 Ma. Thus, the estimated onset of MVF volcanism (12.7 Ma) minus its calculated active time, suggest that the cessation of volcanism in the MVF was around 11.5 Ma, which is consistent with the K-Ar age of crystallization of the intrusion (12 ± 2 Ma; Milne, 1975). To extrapolate this result regionally, we mapped the chronostratigraphic surfaces that correspond to 12.7 Ma (PrErS) and 11.5 Ma (PoErS), and characterise the seismic anomalies that potentially represent volcanoes within this interval, which is the topic of sections 4.5.3 and 4.5.4.

To estimate the depth of emplacement of the monzogabbro penetrated by Resolution-1, we first subtract the depth of the surface marking the onset of volcanism in the MVF (1220 m in the well), from the depth of the intrusion (1911.5 m in the well), which produces a difference of 691.5 m. Next, we assume a constant compaction for these rocks of 40%, which is based on compaction curves for sediments in the Canterbury Basin presented in Field et al. (1989). These calculations give us an emplacement depth of ca 968.1 m below the contemporary paleo sea-bed, which is consistent with petrographic observations that suggest a shallow level intrusion.

4.5.3 Volcanic and Hypabyssal Seismic Facies

We describe five seismic facies interpreted to represent buried volcanoes or hypabyssal bodies in the study area (Figure 52). In this section, we briefly present the main aspects of the seismic facies, while detailed characterisation and interpretation of the morphology of intrusions and volcanoes in the MVF is the focus of section 4.6 and Chapter 5.

Negative Crater-like Disrupted (NCD) seismic facies are characterised by funnel and basin-shaped geometries with shallow to deep excavations into the PrErS horizon. Internal reflectors within these negative anomalies have moderate amplitude, chaotic, disrupted, and sub-parallel seismic features at the top of the structure. External reflectors below the PrErS horizon are parallel and semi-continuous. Immediately above the PrErS, a very high amplitude reflector occurs next to the negative anomaly. The amplitude of this reflector decreases with increasing distance from the negative anomaly (Figure 52B). The formation of NCD's is likely associated with large phreatomagmatic eruptions, evident from deep pit-like excavations into the PrErS. Further evidence is the laterally related seismic facies that suggest dispersal of material adjacent to the crater-like structure. Both deep excavations and lateral related facies with highly dispersed

material are common features observed in maar-diatremes and tuff rings, and their related ejecta rings (e.g. Lorenz, V., 1985; White and Ross, 2011). Intense fragmentation of rocks below the PrErS requires considerable energy (e.g Zimanowski et al., 1997; Zimanowski and Büttner, 2003), and it is widely accepted that subaerial basaltic maar-diatremes result from phreatomagmatic eruptions (e.g. White and Valentine, 2016). In addition, the funnel-like structures in MVF (e.g. Figure 52B) share many similarities with the Foulden Maar imaged by seismic reflection data in the Waipiata Volcanic Field, South Island of New Zealand (Jones et al., 2017). The basin-like geometries maybe correspond to tuff ring volcanoes, however, due to limitations in seismic resolution, this interpretation is uncertain.

Positive Cone, trapezium and Mound-like (PCM) anomalies are characterised by concave downward projections between the PrErS and PoErS horizons, forming seismic morphologies such as mounds, trapeziums and cone-like structures. In MVF, the central part of PCM's typically show disrupted and chaotic internal facies, which is interpreted to represent a central vent zone. Deposits of the central vent grade laterally to chaotic, semi-continuous and/or inclined reflectors dipping in opposite directions and downlapping onto the PrErS horizon with increasing distance from the vent (Figure 20C), which correspond to the flanks of positive-like structures. These flanks are characterised by a stacked set of seismic reflectors that accumulate near to the interpreted vent zone, which are a common stratal relationship observed in submarine and subaerial monogenetic "cone-type" volcanoes elsewhere (e.g. Cas et al., 1989; Cas et al., 1993; Kereszturi and Németh, 2013; Jutzeler et al., 2014; Reynolds et al, 2016; White and Valentine, 2016). PCM's are interpreted to correspond to submarine equivalents of crater-type volcanoes (apud Kereszturi and Németh, 2013), which can include tuff and spatter cones, formed by accumulation of tephra above the PrErS and near an interpreted vent. Tuff cones are typical products of phreatomagmatic eruptions (e.g. Kereszturi and Németh, 2013; Silva and Lindsay, 2015), in which block and bomb ballistics, and turbulent jets represent the main mechanisms of particle dispersal and deposition of material (e.g. Cas et al., 1989; Kaulfuss et al., 2012). Spatter cones usually are the products of Hawaiian and Strombolian eruptions (e.g. Kereszturi and Németh, 2013; Silva and Lindsay, 2015). These volcano-types have been report in both subaerial and subaqueous environments (e.g. Deardoff et al., 2011; White et al., 2015b; Cas and Giordano, 2014). In MVF, the shallow slope angle ($< 16^{o}$) of the flanks of PCM's suggest that they may correspond to tuff cones, however, the seismic expression of tuff and spatter cones may difficult to characterise based on morphometric parameters. Thus, we do not discard the occurrence of

spatter cones in the MVF. Mound and trapezium-like seismic anomalies are interpreted to represent progressive degradation of cone-like volcanoes (Figure 38), due to exposure of the cone crest to wave erosion during the 11 Ma fall in base-level.

Saucer High Amplitude (SHA) are high-amplitude reflectors characterised by a saucer-shaped morphology. In cross-sectional view, this seismic facies usually show a sub-horizontal inner sheet parallel to the enclosing strata, and two peripheral inclined sheets cross-cutting the enclosing strata (Figure 23D). This seismic facies is interpreted to correspond to igneous intrusions in sedimentary rocks. They occur in great number in the Canterbury Basin (Blanke, 2010; Barrier et al., 2017), and are described in the literature as saucer-shaped sills (e.g. Hansen and Cartwright, 2006; Holford et al., 2012; Magee et al., 2016), although their contact with enclosing strata typically shows both sill and dike relationships. Minor sills and dike swarms are likely to occur in spatial association with saucer-sills.

Complex Disrupted Cross-cut (CDC) facies are characterised by disrupted reflectors with frequent cross-cutting relationships (Figure 23E). These seismic facies shows internal low to high amplitude, continuous to discontinuous, parallel to cross-cutting reflectors. Upper CDC reflectors are usually domed, while lower reflectors have cross-cutting relationships, which commonly produces loss of seismic reflectivity (e.g. Jackson, 2012; Schofield et al., 2016; McLean et al., 2017). These seismic facies typically occur below eruptive vents and are interpreted to correspond to disrupted blocks of pre-magmatic strata deformed by intrusions, which may be associated with magmatic conduit zones and emplacement of thin (up to 20 m) intrusive bodies.

Tabular Inclined Moderate-amplitude (TIM) seismic facies are inclined moderate amplitude reflectors with tabular geometries that usually occur below the top basement chronostratigraphic surface. These sub-vertical anomalies are aligned with pre-Cretaceous structures and are commonly located below larger intrusions, or below middle Miocene volcanoes (Figure 52F). They are interpreted as dikes and magmatic conduits that eventually fed intrusions and/or eruptions to the middle Miocene paleo submarine surface.

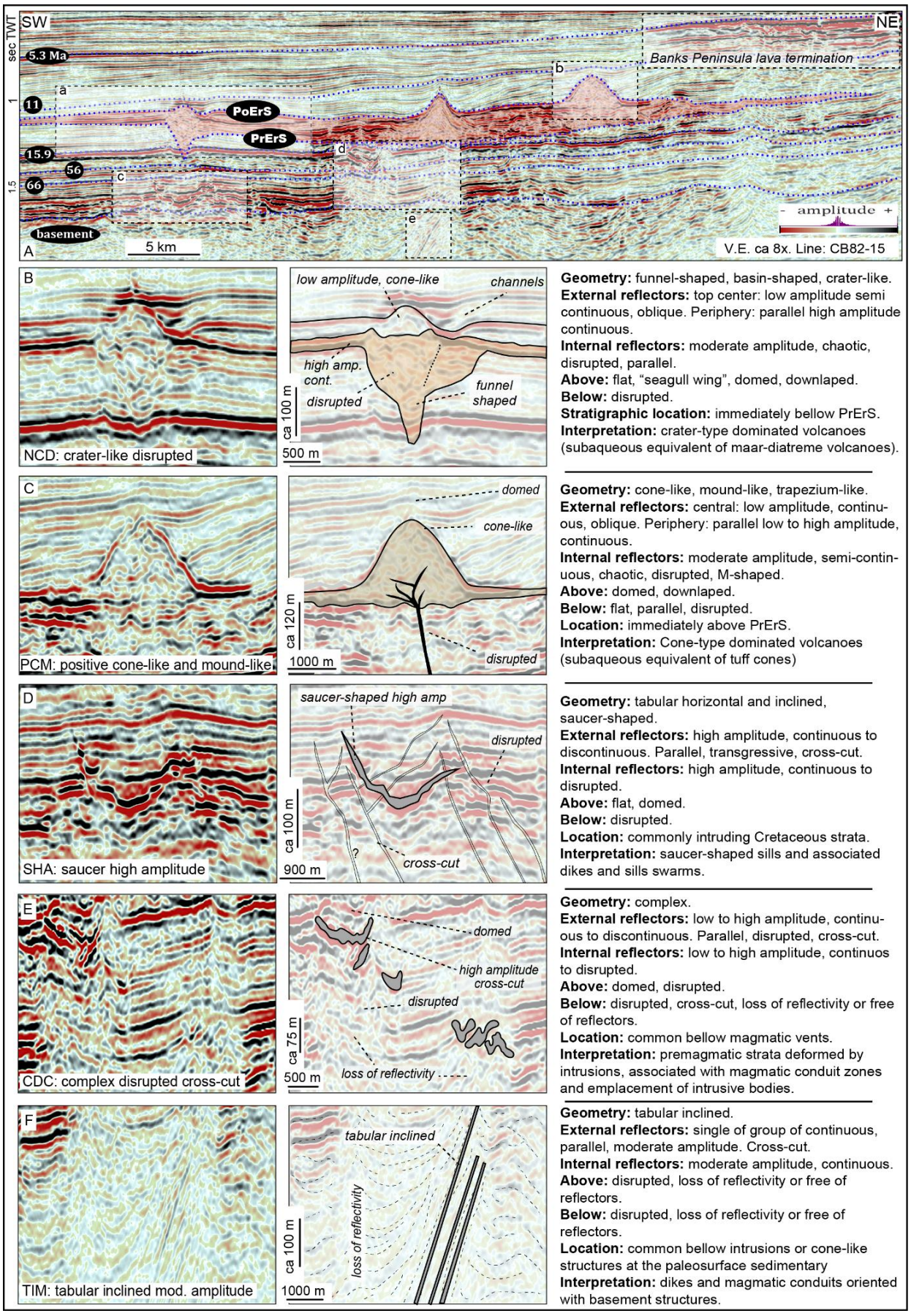

Geometry: funnel-shaped, basin-shaped, crater-like.
External reflectors: top center: low amplitude semi continuous, oblique. Periphery: parallel high amplitude continuous.
Internal reflectors: moderate amplitude, chaotic, disrupted, parallel.
Above: flat, "seagull wing", domed, downlaped.
Below: disrupted.
Stratigraphic location: immediately bellow PrErS.
Interpretation: crater-type dominated volcanoes (subaqueous equivalent of maar-diatreme volcanoes).

Geometry: cone-like, mound-like, trapezium-like.
External reflectors: central: low amplitude, continuous, oblique. Periphery: parallel low to high amplitude, continuous.
Internal reflectors: moderate amplitude, semi-continuous, chaotic, disrupted, M-shaped.
Above: domed, downlaped.
Below: flat, parallel, disrupted.
Location: immediately above PrErS.
Interpretation: Cone-type dominated volcanoes (subaqueous equivalent of tuff cones)

Geometry: tabular horizontal and inclined, saucer-shaped.
External reflectors: high amplitude, continuous to discontinuous. Parallel, transgressive, cross-cut.
Internal reflectors: high amplitude, continuous to disrupted.
Above: flat, domed.
Below: disrupted.
Location: commonly intruding Cretaceous strata.
Interpretation: saucer-shaped sills and associated dikes and sills swarms.

Geometry: complex.
External reflectors: low to high amplitude, continuous to discontinuous. Parallel, disrupted, cross-cut.
Internal reflectors: low to high amplitude, continuos to disrupted.
Above: domed, disrupted.
Below: disrupted, cross-cut, loss of reflectivity or free of reflectors.
Location: common bellow magmatic vents.
Interpretation: premagmatic strata deformed by intrusions, associated with magmatic conduit zones and emplacement of intrusive bodies.

Geometry: tabular inclined.
External reflectors: single of group of continuous, parallel, moderate amplitude. Cross-cut.
Internal reflectors: moderate amplitude, continuous.
Above: disrupted, loss of reflectivity or free of reflectors.
Below: disrupted, loss of reflectivity or free of reflectors.
Location: common bellow intrusions or cone-like structures at the paleosurface sedimentary
Interpretation: dikes and magmatic conduits oriented with basement structures.

Figure 52: Igneous seismic facies in the study area. A) Regional 2D strike/oblique seismic section showing the lower (PrErS) and upper (PoErS) stratigraphic limits of the MVF (see chapter 4.5.5 for details). B and C show images interpreted as volcanoes erupted in the MVF, while figures D, E and F show images of interpreted intrusions.

4.5.4 Volcano Morphology and Relationship with Intrusions and Diatremes

Volcanic morphology can provide insights about processes such as past eruptive styles, edifice growth mechanisms and cone degradation (e.g. Dohrenwend et al., 1986; Takada, 1994; Tibaldi, 1995; Vesperman and Schmincke, 2000; Martin and Németh, 2006; Corazzato and Tibaldi, 2006; Valentine et al., 2007; apud Fornaciai et al, 2012). To evaluate the syn- and post-eruptive processes that impact the morphology of the MVF volcanoes, we have undertaken a detailed qualitative-quantitative analysis and seismic morphometric characterisation for each volcano in the MVF.

We classify the post-burial morphology (i.e. as the volcanoes appear in seismic lines) of 31 individual volcanoes as positive symmetric cone, positive asymmetric cone, positive trapezium, positive mound, negative funnel-like, or negative basin-like (Figure 53A). Results show that 81% of the MVF volcanoes have a positive morphology, interpreted to represent crater-type volcanoes, while volcanoes that excavate into the PrErS (crater-type) are less frequent. The basal widths (W) of MVF volcanoes range from 550 to 6350 m. Most volcanoes (22) have a W between 1000 and 3000 m (Figure 53B). The anomalous volcano with W > 6000 m was interpreted from a low confidence seismic anomaly and may correspond to two or three amalgamated and highly eroded volcanoes.

Estimated magnitude of degradation shows that most MVF volcanoes experienced low (<20 vertical metres of erosion) and moderate degradation (20 to 100 m), while seven volcanoes were interpreted to be highly eroded (>100 m). It was not possible to determine the degree of degradation due to the poor seismic quality for five volcanoes (Figure 53C). Most positive volcanoes (25) have overlying domed reflectors or show no evidence of differential compaction, relative to the enclosing siltstones (ca 30% compaction at a depth of 1000; Field et al., 1989). This result suggests that the positive volcanoes have compacted less than, or a similar amount to the Tokama siltstone. Only two volcanoes display upper reflectors with “seagull wing” geometries, which suggests that they have compacted more than the enclosing sedimentary strata (Figure 53D). Reconstructed volcanic heights (oHm) vary from 60 to 430 m (Figure 53E) and original slopes (oS) range from 5^{o} to 24^{o} (Figure 24F). Positive cone-like volcanoes mostly range in oHm from 100 to 300 m, with only 16% of the volcanoes outside this range. Slope angles of cone-type volcanoes usually range between 5^{o} and 15.9^{o} (84%). These morphometric ranges are typical of monogenetic volcanoes (e.g. Kereszturi and Németh, 2013; Silva and Lindsay, 2015).

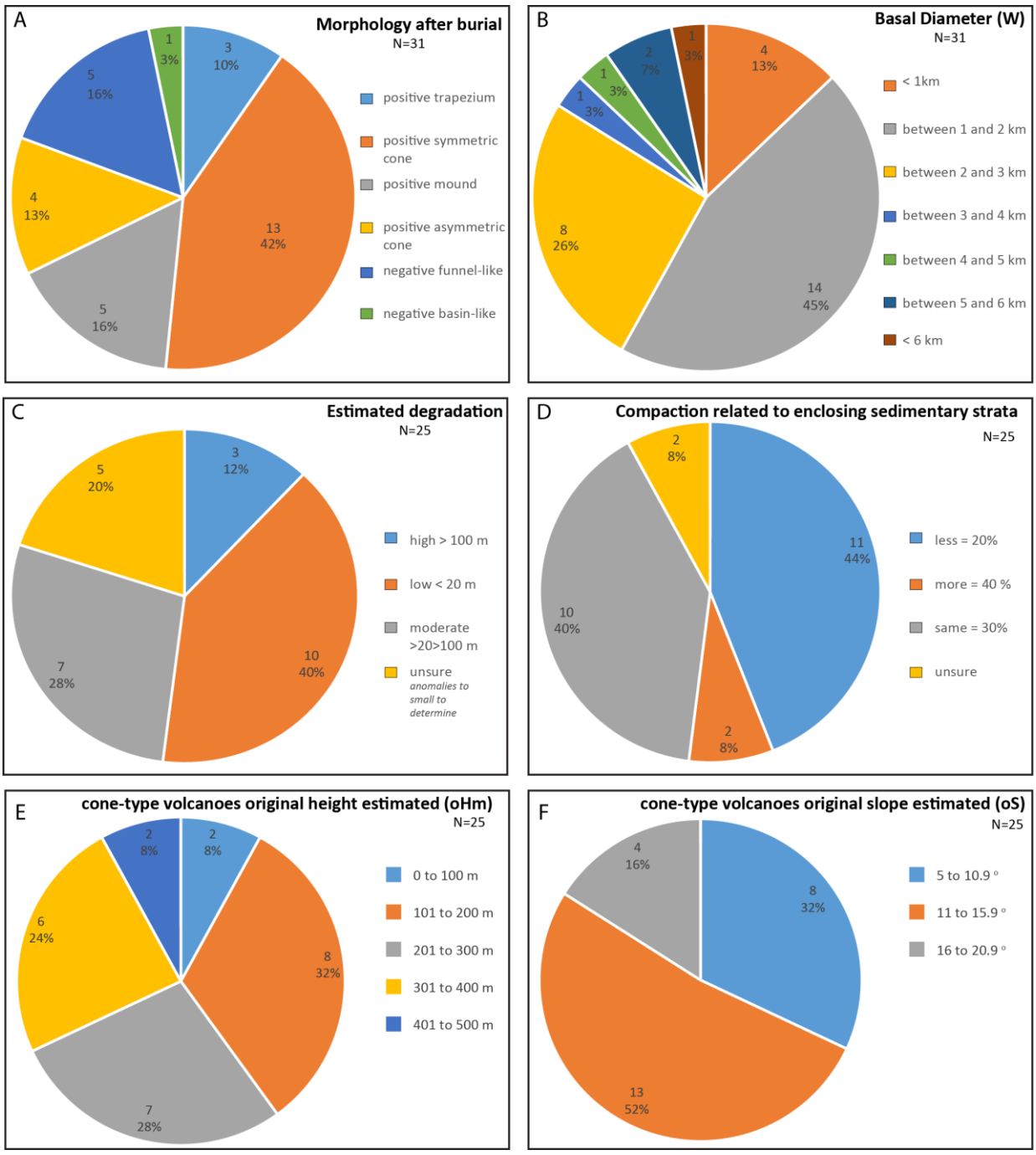

Figure 53: Pie diagrams showing the qualitative-quantitative morphometric results from MVF volcanoes. See text for details.

The total depth of negative basin and funnel-like anomalies range between 90 to 230 m (Figure 54A), which is into the morphometric ranges of maar-diatreme volcanoes (e.g. Lorenz, 1985; Kereszturi and Németh, 2013; Silva and Lindsay, 2015). Three of these negative anomalies show small cone-type volcanoes located above them, which could represent intra-crater volcanoes formed by late eruptive events on the top of a larger diatreme structure (Figure 37), which is commonly observed in maar-diatreme volcanoes (e.g. Lorenz, 1985; Kereszturi and Németh, 2013). We also evaluate the potential for MFV volcanoes to have formed in association with large

intrusions emplaced in lower sedimentary sequences (Figure 54B). Most volcanoes (68%) are likely related to large (> 2 km), shallow intrusions (ca 1 km at emplacement time and mainly saucer-shaped), suggesting that these igneous bodies could have fed eruptions in the MVF. This deduction is reinforced by petrographic and geochemical interpretation from the igneous rocks in Resolution-1. Volcanism fed by intrusion is common in sedimentary basins, with examples observed in southern Australian marginn (Holford et al., 2012; Jackson, 2012; Reynolds et al, 2016) and the North Sea (e.g. Hansen, 2008; McLean et al., 2017).

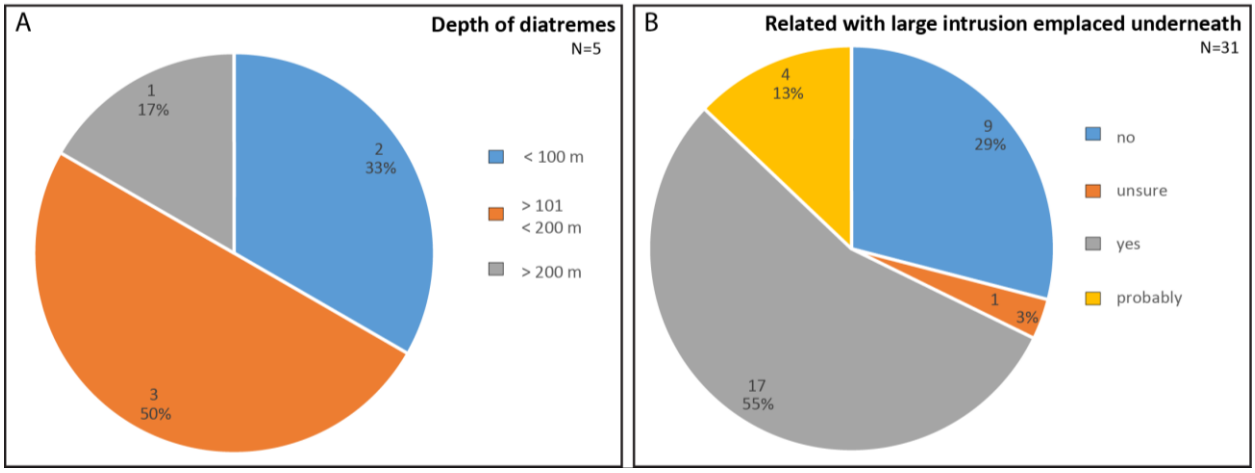

Figure 54: Pie diagrams showing the depth of diatreme craters (A), and number of volcanoes interpreted to be underlain by large (> 2 km) and shallow (ca 1 km) intrusions (B).

4.5.5 Paleo-Physiography and Paleo-Environmental Reconstruction

In this section, we extrapolate the observations from the Resolution-1 well to a regional scale, based on seismic stratigraphic analyses in correlation with biostratigraphic data from the Resolution-1, Clipper-1, Leeston-1, Ealing-1 and Charteris Bay-1 and 2 wells, as well as insights from rocks outcropping in the northern Canterbury Basin region (Figure 34; Figure 35; Figure 55; Figure 57; Figure 58; Figure 51; Figure 56). The integration of this dataset provides information about the areal distribution of volcanoes within the MVF, and about the external paleo-environments that precede, interact with and post-date the eruptions in the field (Figure 55).

Pre-eruptive stage (priory 12.7 Ma)

During the early Miocene and prior to ca 12.7 Ma (onset of volcanism in the MVF; Figure 42), the northern Canterbury Basin paleo-seafloor was controlled by a low-gradient smooth ramp that gently dipped towards the regional basin depocenter in the SE (Figure 35; Figure 55D; Figure 58), and aligned with the Chatham and Endeavour structural highs (Field et al., 1989; Barrier, in prep).

This paleo-physiography is indicated by the chronostratigraphic map presented in Figure 55D, and by the shape of the seismic horizon that represents the early Miocene ramp shown in Figure 58. At the location of the Resolution-1 well, the transition from deep to middle Tokama siltstone (Table 5; Figure 42) suggests water-depths dropping from deep-lower bathyal to lower bathyal (Table 6), which occurs in association with the unconformity eM, and prior to the onset of MVF eruptions around 12.7 Ma (Figure 42; Figure 51; Figure 55D). Integration of well data and chronostratigraphic indicate that the near pre-eruptive bathymetry of the study area ranges from 500-750 m at its shallowest, and from 1000-1500 m at its deepest segment (red dashed lines in Figure 56).

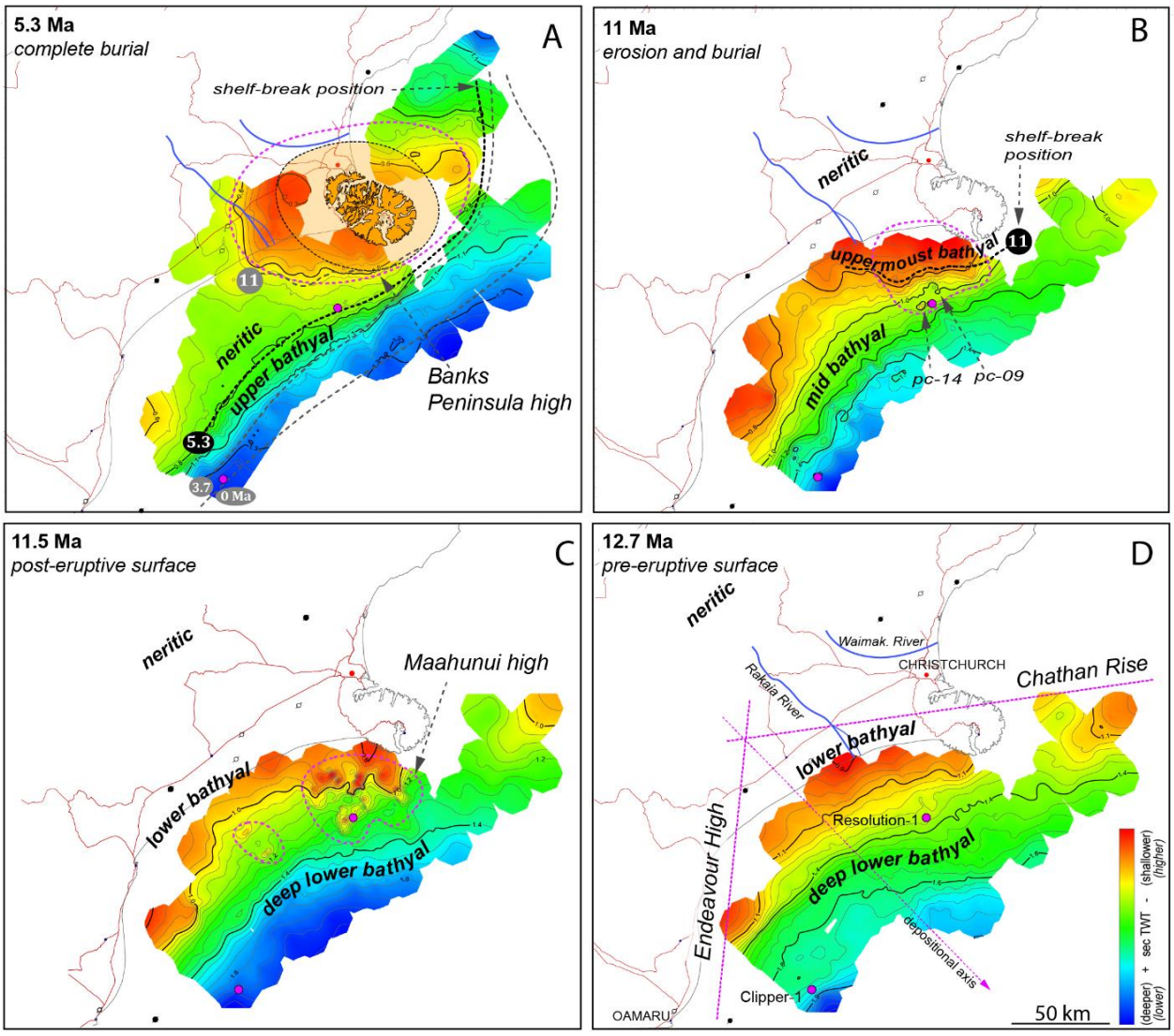

Figure 55: Chronostratigraphic maps of the northern Canterbury Basin. The MVF erupted entirely in a lower bathyal setting (D and C), and was buried in a lower to uppermost bathyal setting (B) due to rapid SE progradation in the northern Canterbury Basin. During the Neogene, the physiography of the basin evolved from a ramp to a basin-slope morphology (C to A). Outcropping paleo-environments compiled from Field et al. (1989). During mapping of the PrErS chronostratigraphic horizon, we corrected the effects of local deformation underneath eruptive vents and near shallow intrusions.

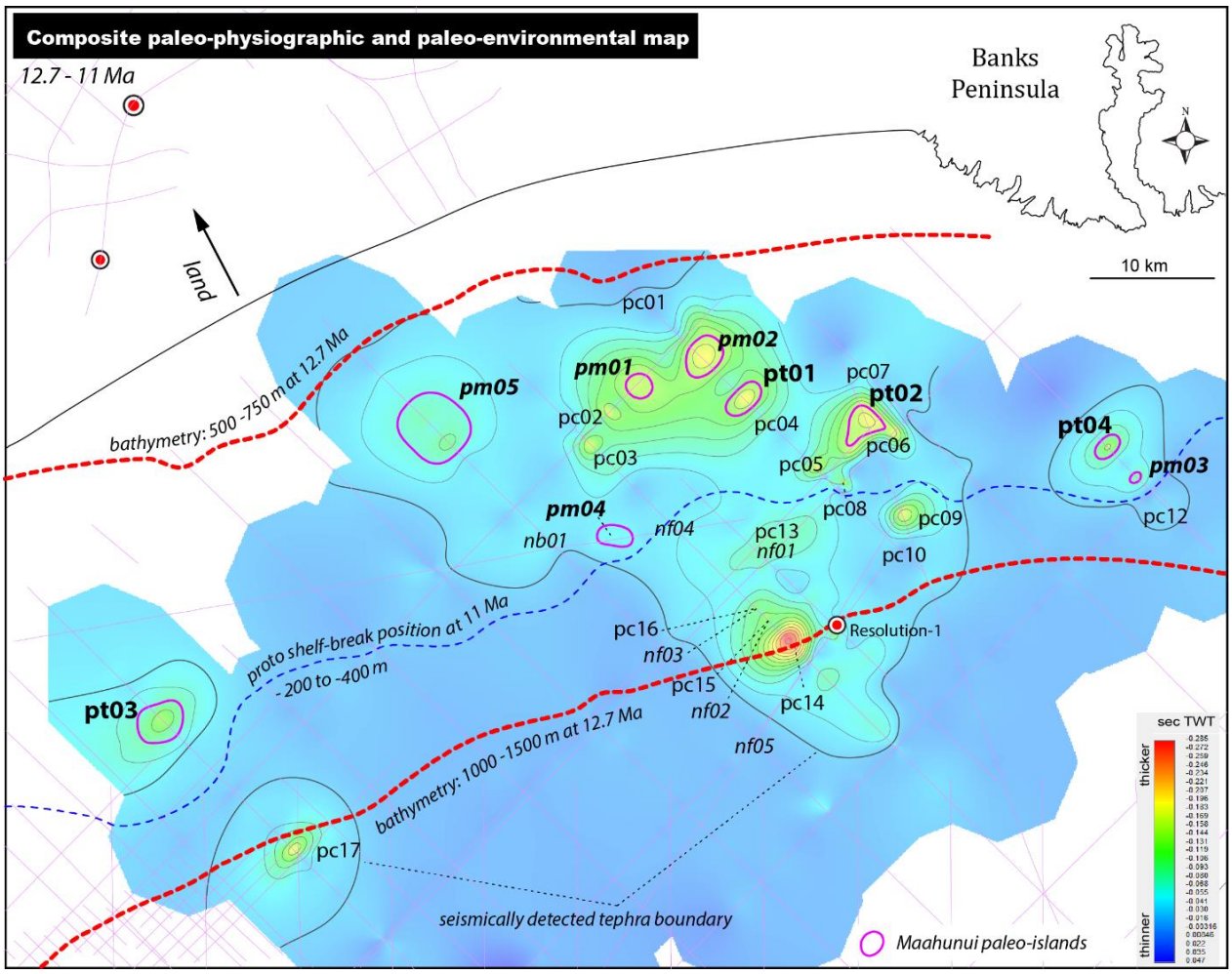

Figure 56: Composite paleo-physiographic and paleo-environmental map of the study area from ca 12.7 to 11 Ma. Abbreviations are plotted at the position of MVF volcanoes and correspond to their morphology. Pc's are positive cones, pt's are positive trapezium, pm's are positive mounds, nf's are negative funnel-like structures and nb's are negative basin-like seismic anomalies. Red dashed lines show the approximate bathymetry at the onset of eruptions in the MVF. Blue dashed line shows the position of the shelf-break at 11 Ma. Note that all pm's and pt's are located within relatively shallower waters, proximal the 11 Ma shelf-break. To construct this map, we combine information from the pre-, syn-, and post-eruptive stages of MVF in a single map. First, we produce an isochron map of the syn-eruptive stage of MVF (background rainbow colours), which correspond to the interval (in TWT) between PrErS (12.7 Ma) and PoErS (11.5 Ma). This isochron map was produced by applying a mathematical algorithm embedded in the Kingdom Software, which subtracts the time of the PoErS from time of the PrErS (Figure 39). The isochron background map shows the location of each volcano in the MVF. We opt for the non-reconstructed forms of the volcanoes (PoErS using HaBs heights) for two reasons: first, computational limitation to map a theoretical reconstructed morphology, which could create several interpolation errors and artefacts. Second, because the degraded morphology of the volcanoes is related to the position of the 11 Ma proto shelf-break, we decided to show the effects of erosion in the composite map. To estimate the 12.7 Ma (onset of volcanism) bathymetric contours of the study area, we first integrate biostratigraphic data at the location of the Resolution-1 well, with the local chronostratigraphic map of 12.5 Ma (Figure 55D). The distal contour in MVF is highlighted by the red dashed line on the right hand corner of the map, which corresponds to water depths ranging from 1000 to 1500 m. The proximal bathymetric contour (red dashed lines showing bathymetry ranging from 500 to 750 m deep) was estimated by calculating the slope angle (ca 1.5 degree) of the pre-eruptive regional ramp from seismic data, and in relation to the distance from neritic rocks of similar age outcropping in the Canterbury plains (Figure 55D), which was compiled from paleogeographic maps presented in Field et al. (1989). The position of the 11 Ma shelf-break (blue dashed line), was mapped from 2D seismic lines in the study area, and adjusted using the contours of the chronostratigraphic map of 11 Ma as required (Figure 55B). Note that volcanoes distal the 11 Ma proto-shelf break show a sharp increase in slope towards their summit, while volcanoes located proximal to this line show shallower slopes. Compare the contours that represent the morphology of pt03 vs. pc17 in the right-hand corner of the map. We interpret that volcanoes highlighted in a purple correspond to an ancient archipelago comprising nine small extinct volcanic islands.

Syn-eruptive stage (12.7 to 11.5 Ma).

During the volcanic activity, the regional lower bathyal setting remained relatively stable in the MVF area (Figure 42; Figure 51; Table 6), however, eruptions and shallow intrusions in the MVF locally raised the paleo-seafloor by ca 12.7 to 11.5 Ma (Figure 55C). Paleo-environmental reconstruction of the area enclosing the MVF (Figure 56) shows that by ca 12.5 Ma to 11.5 Ma water depths range from a minimum of 500 m and maximum of 1500 m deep, which indicate that the eruptions were entirely submarine. However, it is important to remember that the higher the volcanic edifices grow (due to the addition of material on their flanks and tops by successive eruptions), the shallower their summits become. Conversely, these volcanoes are unlikely to have reached the paleo sea-level during their syn-eruptive stage. This is evident by the volcano named pm02, the highest of the shallower edifices (Figure 56; Figure 59). This volcano had an estimated post-eruptive height (oHm) of ca 420 m, and was located in water depths certainly > 500 m (Figure 56), which suggests that its summit was at least 80 m deep at that time (Table 6). Although our dataset clearly indicates entirely submarine volcanism in the MVF, we cannot discard the possibility of minor subaerial or Surtseyan eruptions had occurred, mainly from volcanoes located in an ultra-proximal setting or from volcanoes not imaged on our seismic dataset.

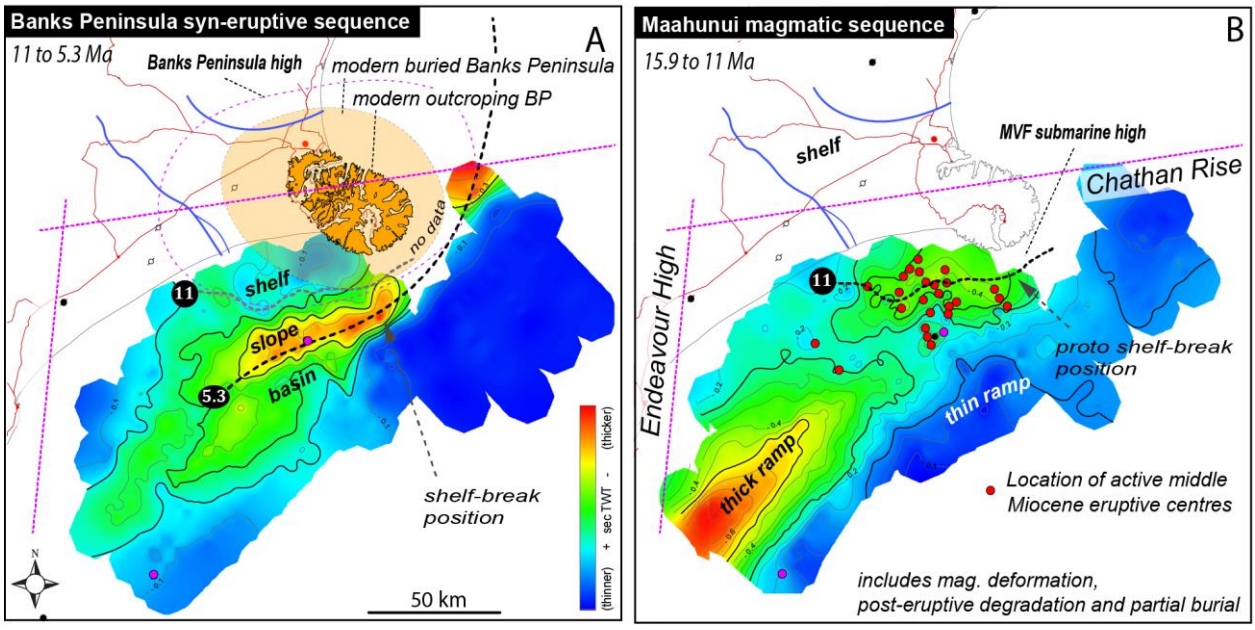

Figure 57: Isochron maps of the northern Canterbury Basin. By 11 Ma and younger, most volcanoes were buried by the slope progradation associated with increasing sediment supply from the NW (A), simultaneously with the installation of the Banks Peninsula. Note in (B) that a thicker pile of sediments was deposited at the location of the edifices of the MVF during their erosion and partial burial (MVF submarine high).

Post-eruptive stage (11.5 to 11 Ma)

After volcanism ceased around 11.5 Ma, MVF edifices were progressively buried by an increase in sediment influx from the NW which derived from the early uplift events of a proto New Zealand Southern Alps (e.g. Field et al., 1989). The presence of the extinct submarine volcanic field had a local influence on the distribution of sediments in the area, which is evident by a thick sequence of sediments deposited within the MVF during the erosion and burial stages (Figure 57B). Seismic images show that sedimentation among the volcanic edifices produced a distinctive depositional setting, here referred to as intra-cone plains (Figure 38; more details about this morphology in section 5.4.2). We interpret these local cumulative sediment thickness to result from the interplay of increasing NW-derived sediment supply from the Southern Alps and decrease in accommodation space in the MVF area (this last, either by introduction of volcanic material sourced by the eruptions, or by erosion of the volcanic edifices). Reduction of accommodation space in the north Canterbury Basin may also have been influenced by crustal arching related to the initial stages of Banks Peninsula magmatism (pre-eruptive doming on our volcanic-stratigraphic model; Bischoff et al., 2017), however, further investigation is necessary to test this hypothesis.

By 11 Ma, most volcanoes in the MVF were completely buried in a lower to uppermost bathyal setting (Figure 52A), with the exception of the pc14 and pc09, as both of these volcanoes were partially buried and located in deeper waters (Figure 55B; Figure 57B). Images from seismic lines in the MVF area show that volcanoes proximal to a proto shelf-break have their tops flattened (Figure 38). This is consistent with the position of unconformity lM, which suggests that these volcanoes experienced degradation due to wave-base erosion and possibly in some cases by subaerial exposure above the 11 Ma paleo sea-level. After 11 Ma, the remaining deep water volcanoes (pc09 and pc14) were buried by the progressive NW-SE basin-slope progradation, which occurred simultaneously with the establishment of Banks Peninsula in the late Miocene (Figure 34; Figure 35; Figure 55A; Figure 57A; Figure 58). Table 6 summarizes the paleo-geography and paleo-environmental evolution in the study area.

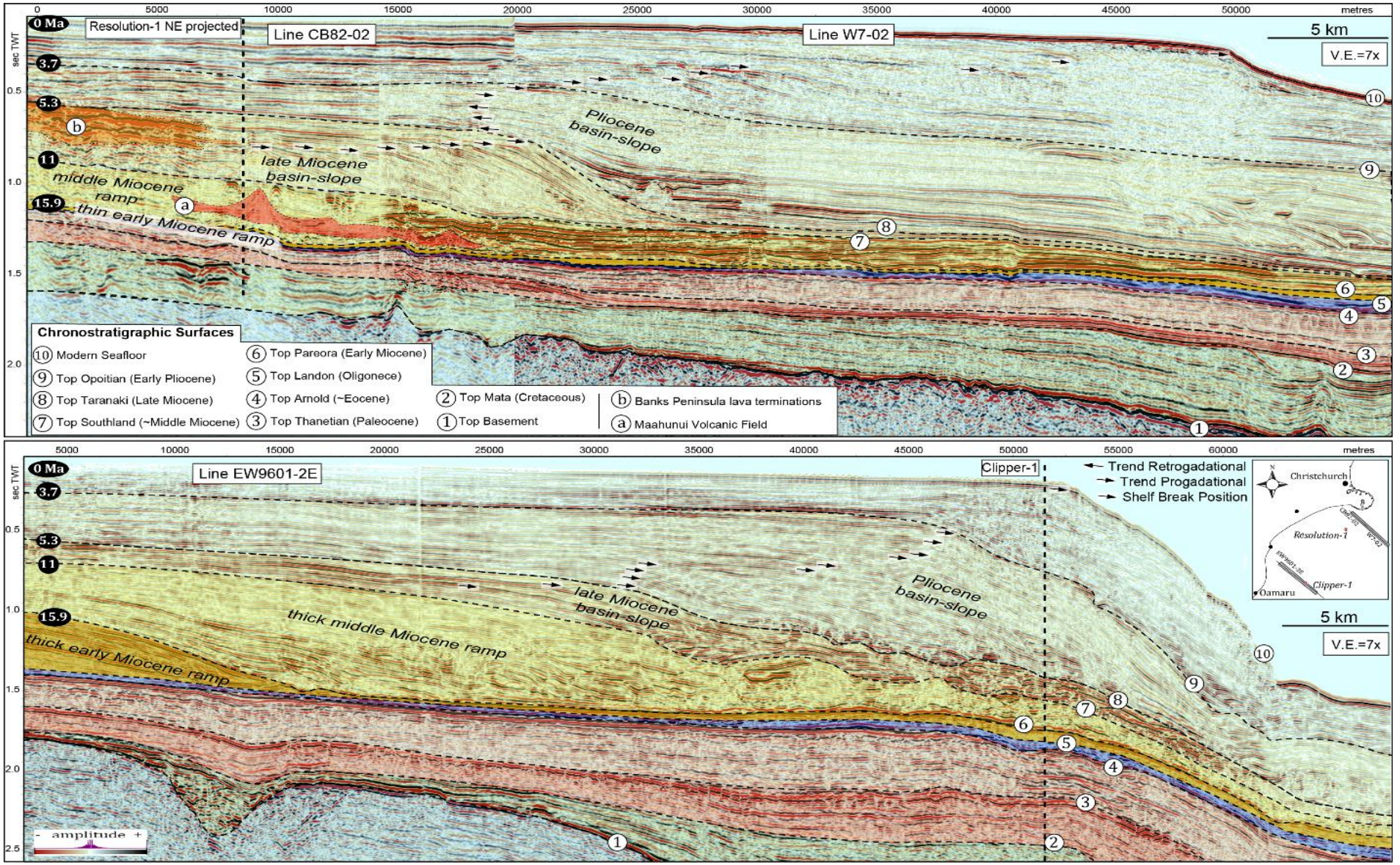

Figure 58: 2D regional seismic lines showing the location of the MVF in relation to the regional chronostratigraphic horizons mapped in the study area from the Cretaceous to Recent, and the main physiography of the basin. Neogene to Recent shelf-break migration is indicated by arrows that show the location of the shelf-break at each time, with the arrowhead pointing in the direction of migration. Cretaceous-Paleogene horizons were supplied by Andrea Barrier.

Table 6: Main stratigraphic and paleo-environmental characteristics of the MVF area. Interval highlighted in red corresponds to the active eruptive time in the volcanic field.

Age	Physiography	Magmatic stage	Depositional setting	NW shallower paleo-bathymetry	SE deeper paleo-bathymetry
11 Ma and younger	Slope and basin morphology	Complete burial	Neritic to uppermost bathyal	100 to 200 m and progressively shallower	200 to 400 m and progressively shallower
Post-degradational surface (unconformity lM) and rapid progradation					
11.5 to 11 Ma	Onset of slope-and-basin morphology (proto shelf-break)	Degradational and part of the burial	Uppermost bathyal to mid bathyal	200 to 400 m (volcanoes ≥ 200 m exposed to sea-level)	600 to 800 m (≥ 100 m at volcano summits)
Post-eruptive surface and onset of progradation					
12.7 to 11.5 Ma	Ramp, rugged at MVF location	Syn-eruptive	Lower bathyal	500 to 750 m (≥ 80 m at volcano summits)	1000 to 1500 m (≥ 200 m at volcano summits)
Pre-eruptive surface					
Early Miocene and priory to 12.7	Smooth ramp	Pre-eruptive	Lower to deep bathyal	1000 to 1500 m	1500 to 2000 m

4.5.6 Vent Distribution and Eruptive Fingerprint

The isochron map for the MVF active stage (Figure 56) shows the location of crater-type volcanoes mapped in this study. The cluster distribution of individual or overlapping volcanoes provides evidence that the MVF plumbing system fed magma to dispersed eruptive centres (which is characteristic of monogenetic volcanic fields; e.g. Kereszturi and Németh, 2013), rather than feeding eruptions at a fixed spot (which is typical of polygenetic volcanoes; e.g. Silva and Lindsay, 2015). Reconstruction of edifices using the morphometric parameters of two volcanoes (pc14 and pc17) with low magnitudes of degradation indicate that about 5.7 km^3 of magma erupted from the pc14 (biggest volcano in the area), and about 1.6 km^3 from pc17 (average size volcano in the area). These volumes are typical for monogenetic volcanoes (e.g. Kereszturi and Németh, 2013; Silva and Lindsay, 2015). Appendix 1 present additional information of the method used to calculate the volumes of buried volcanoes from seismic data.

The seismic reflection fingerprint of the MVF volcanism in the Canterbury Basin differs significantly from observations of long-lived polygenetic volcanoes imaged in seismic surveys offshore Taranaki Basin (e.g. Kora volcano, presented in Chapter 3). The transition from light to dark blue colours in the map shows where the amalgamation of PrErS and PoErS occurs, which we interpret as the seismically detected tephra boundary of the MVF (Figure 56). The map in Figure 56 demonstrates that the volcanoes in the MVF characteristically show rapid thinning and

amalgamation of the interval between the PrErS and PoErS surfaces, with increasing distance from eruptive centres (Figure 37A; Figure 39; Figure 51). This phenomenon is observed for both individual and overlapped volcanoes in the MVF. Subtle thinning indicates that volcanoes of the MVF experienced relatively short-lived eruptive-cycles, compared to background sedimentation rates. Polygenetic buried volcanoes do not show drastic PrErS and PoErS amalgamation with increasing distance from eruptive centres, because the products of volcanism are interbedded and contemporaneous with thicker sequences of basinal deposits (Bischoff et al., 2017), which suggests long-lived volcanism with recurrent eruptive-cycles at a relatively fixed location.

4.6 Controls on MVF Morphology

Integration of the results from petrography and seismic reflection analysis allow us to understand that two main processes controlled the morphology of the MVF buried volcanoes: i) eruptive-style, which produced predominately cone and crater-type volcanoes, and ii) post-eruptive degradation of crater-type volcanoes, which is a consequence of the interplay between edifice height and the external paleo-environmental conditions that affect the volcanoes (Figure 59).

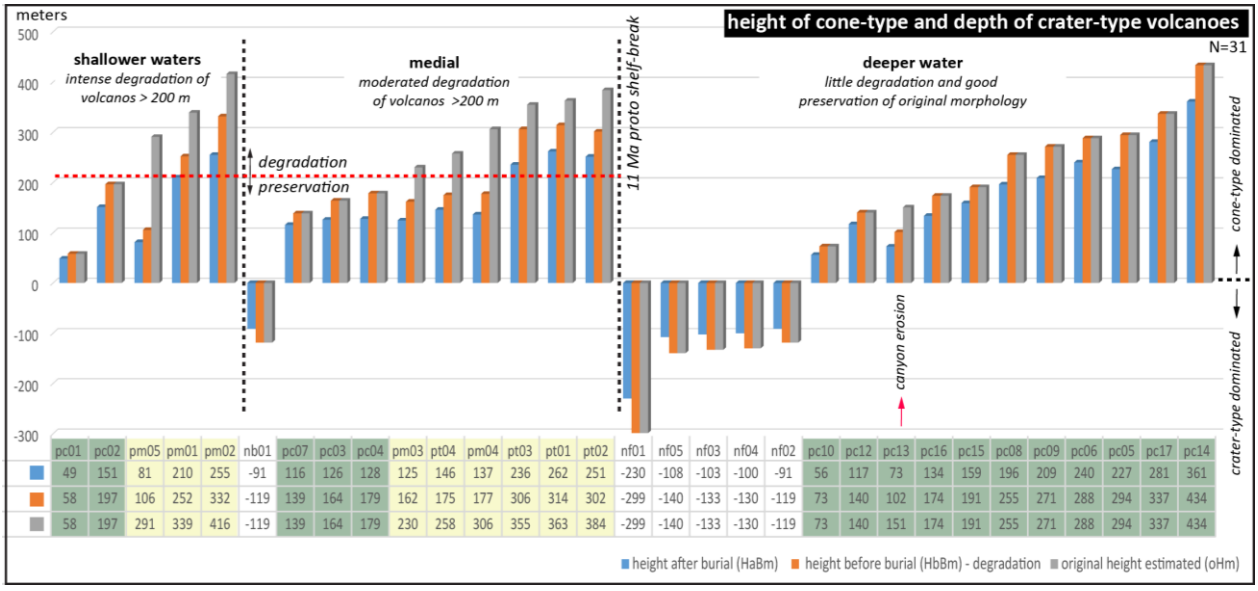

Figure 59: Morphometric analysis of MVF volcanoes relative to their post-eruptive paleo-environmental location. Blue bars show the height of volcanoes after burial (HaBm, as they were measured in seismic lines and converted to metres using the RII method). Orange bars show decompacted height values (HbBm). Grey bars show reconstructed original height of the MVF volcanoes (oHm). Red dashed line shows the limit between preservation and degradation of the edifices. Compare pm03 versus pc04 for example. Note that all pm's and pt's show evidences of degradation. Red arrow points to the only pc volcano with evidence of canyon erosion located at deeper waters.

4.6.1 Eruptive Styles and Edifice Growth Mechanisms

Results from seismic morphology and petrographic characterisation of the volcanoes in the MVF suggest the presence of two main volcano-types: cone- and crater-type volcanoes. Figure 60 shows the main morphologic aspects of these volcano-types along with photos of possible examples of their subaerial equivalents. We opt for comparison to modern subaerial examples because they are better preserved and exposed than outcrops of submarine volcanoes. Despite differences in eruption trigger and edifice growth mechanisms, it is notable that the products of submarine and subaerial eruptions share morphological similarities. Submarine examples that resemble subaerial spatter cones, tuff cones, and maar-diatreme volcanoes are common in the literature (e.g. Cas et al., 1989; Jutzeler et al., 2014; Cas et al., 1993; Head and Wilson, 2003; White et al., 2015b; Reynolds et al, 2016). In the following section we present the main seismic characteristics of cone and crater-type volcanoes of the MVF. In chapter 5 we present the complete characterisation of these volcano-types, defining the main building blocks (i.e. architectural elements) that compose each one of these morphologies.

Crater-type volcanoes are characterised by funnel and basin-like depressions into pre-eruptive strata (Figure 37B; Figure 52A and B; Figure 60A), likely caused by brittle deformation and mass collapse of material into a large crater zone (e.g. Lorenz, 1985). The basin-like seismic morphology maybe represent tuff rings, but they are difficult to characterise due to limitations in seismic resolution. We interpret the funnel-like morphology to be the seismic expression of subaqueous equivalents of maar-diatreme volcanoes based on:

- Large size of excavations into pre-eruptive strata, e.g. 1300 m in width versus 230 m in depth (see unbedded diatreme in Figure 60A), which indicate intense fragmentation of the host rock below the PrErS (e.g. White and Valentine, 2016);
- Deep craters in association with seismic facies that indicate extensive lateral dispersion of material and deposition at a low angle of repose, ca 2.5 km from the vent, with an average slope dips of 5^{o} increasing to ca 20^{o} near the vent (see tephra ring and tephra plain in Figure 60A);
- Sub-volcanic zone with downward-dipping reflectors, which suggests post-eruptive subsidence and mass adjustment of material into diatremes (e.g. White and Ross, 2011);
- Rock samples from Resolution-1 that suggest intense fragmentation and dispersal processes, which could indicate phreatomagmatic eruptions. This is evident by fragments

with very fine-grained texture and platy shards, and by the presence of limestone and sandstone lithics (Figure 48). These lithics are likely derived from lithologies located at the root of the diatremes nf02 and nf03, which are situated ca 3.5 km SW from the well (Figure 39).

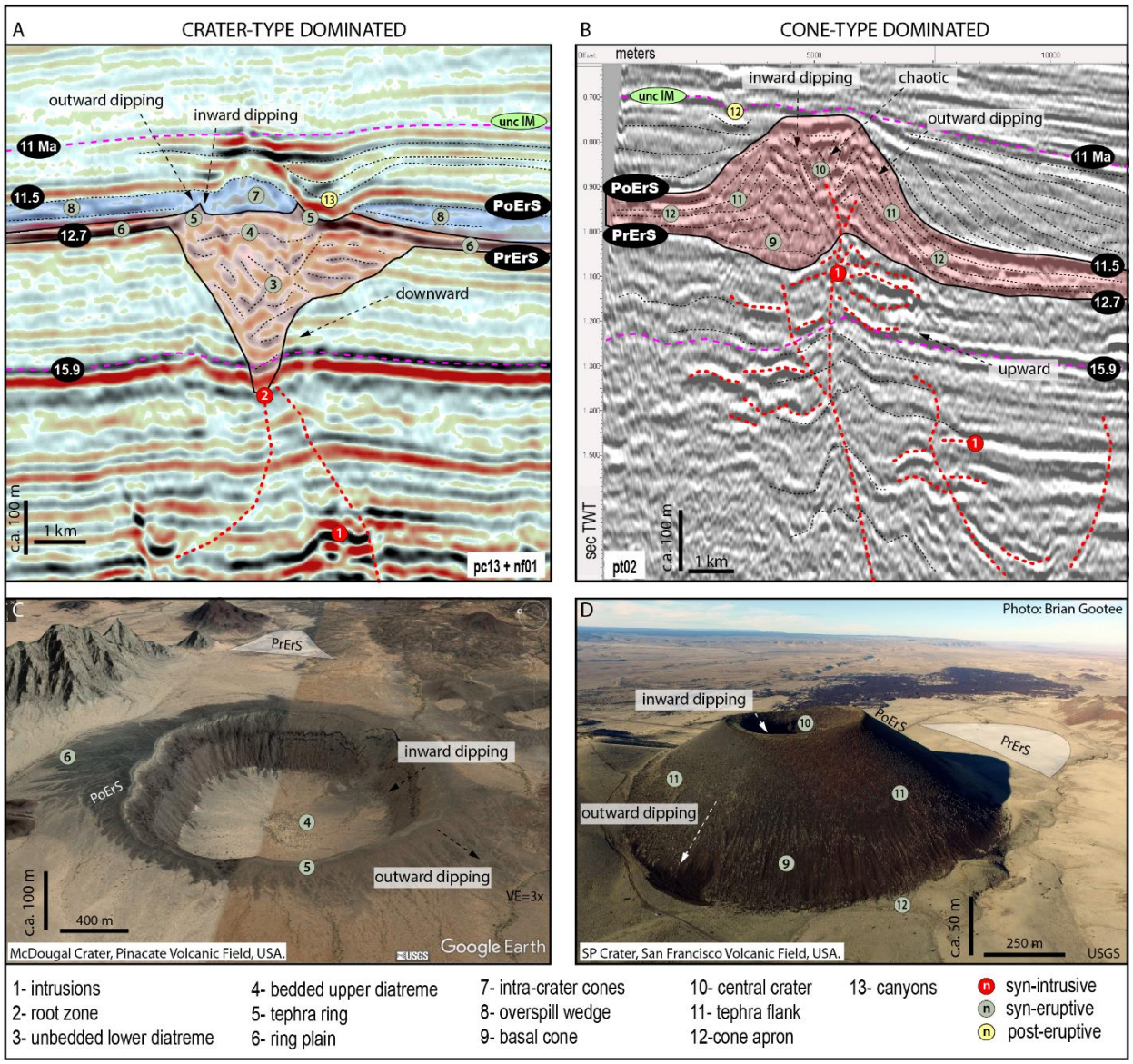

Figure 60: Top images show 2D seismic sections of crater (left) and cone (right) type dominated volcanoes. In the seismic sections, crater-type is characterised by deep funnel and basin-like excavations into the PrErS horizon, while cone-type is characterised by upwards deflection of the PoErS above the PrErS and reflectors that pile-up above PrErS. Bottom images correspond to interpreted subaerial analogues. The crater-type is a classic maar-diatreme volcano (McDougal Crater, in USA), while the cone-type is a well-known scoria cone (SP Crater, USA). Despite morphometric differences, tuff cones and scoria cones share many morphologic similarities, such as the presence of a crater zone with layers inward dipping, and peripheral flanks with layers outward dipping. Note the geometric similarity between the volcanoes in seismic and analogue images. Complete interpretation of the different types of volcanoes is presented in Chapter 5.

Crater-type volcanoes are represented by upwards deflection of the PoErS horizon above PrErS (Figure 37A; Figure 52A and C; Figure 60B). We interpret this morphology to be the seismic expression of subaqueous equivalents of tuff cones based on:

- The occurrence of stacked reflectors sets superimposed onto and above pre-eruptive strata, proximate to a vent (i.e. basal cone, tephra flank and cone apron in Figure 60A);
- Minor excavations into pre-eruptive strata;
- Sub-volcanic zone with upward-dipping reflectors;
- Cone-like morphology with abrupt topographic inflections and average reconstructed slope angles < 16° (i.e. tephra flank in Figure 60A);
- Rock samples from Resolution-1 that suggest explosive eruptions (Figure 47).

Observations in the MVF show that both cone and crater-type volcanoes have a random distribution in relation to water-depths (Figure 56). Decompression and fragmentation mechanisms at deep-water settings are still not completely understood (e.g. Cas and Giordano, 2014; Cas and Simmons, 2018). Observations from the Kermadec island arc suggest a transition from explosive to effusive volcanism around 1000 m water depth (Wright et al., 2006), however, products of explosive eruptions were also reported in water depths above 1000 m (e.g. Head and Wilson, 2003; White et al., 2003; Clague et al., 2000; Cas and Giordano, 2014). The crucial challenge of modern submarine volcanology is the need to improve understanding of how different processes of fragmentation, dispersal and deposition of magmatic particles are affected not only by changes in hydrostatic pressure, but also by changes in other physical proprieties, such as bulk modulus (deformability versus compressibility of water), thermal conductivity, heat capacity and the critical point of water (e.g. White et al., 2003; Cas and Giordano, 2014).

4.6.2 Post-Eruptive Paleogeography

After the MVF eruptions ceased around 11.5 Ma seismic stratigraphic and biostratigraphic analysis indicates a progressive shallowing in water depths. This event occurs simultaneously with the wake of the basin-slope progradation from NW to SE. By ca 11 Ma, the MVF can be divided in two halves by the position of a proto shelf-break (Figure 56). The shallower NW part of the area was located in a neritic environment (< 200-400 m), while the deeper SE part remained in an uppermost bathyal setting (> 200-400 m). Volcanoes with oHm >200 m and located proximal to the 11 Ma proto shelf-break show increasing amounts of degradation while

volcanoes located distal to the proto shelf-break were buried and well preserved independently of their post-eruptive height (Figure 38; Figure 59; Figure 61). In addition, volcanoes classified to have had a low amount of degradation always show a cone morphology, independent of external paleo-environmental factors, while highly degraded volcanoes are always located proximal to the proto shelf-break position (Figure 56), which suggest that their tops may have been eroded.

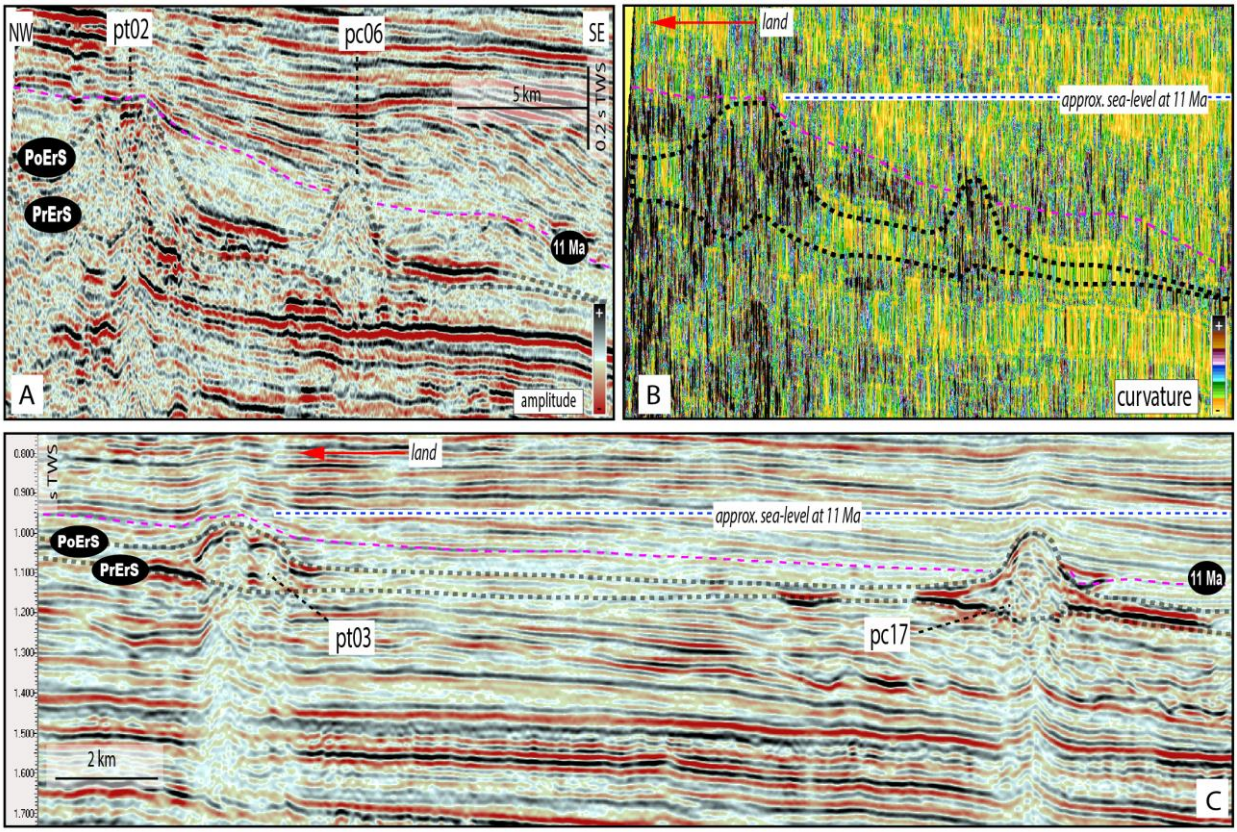

Figure 61: A and B show attribute analysis of pt02 and pc06 volcanoes and their seismic morphology. The curvature (B) attribute suggests that the internal and external parts of the volcanoes (black) are composed by rocks with similar acoustic properties, which are interpreted to represent volcaniclastic rocks eroded from the pt02 and deposited next to its flanks. C shows the morphological contrast between pt03 and pc17. Note that in both cases, extinct volcanic edifices located at shallow water (pt02 and pt03) show flattened tops in relation to the position of the 11 Ma unconformity, while volcanoes located at deeper water (pc06 and pc17) do not show a morphological relationship with this unconformity. This suggests that distal volcanoes were below sea-level and were well preserved. Blue dashed lines show the interpreted position of the sea-level at ca 11 Ma, based on the flattened top of proximal volcanoes.

These eroded volcanoes typically show trapezium and mound seismic morphologies, and have flattened-tops concordant with the lM unconformity. Buried mounds show H:W ratio < 0.05, while trapezium and cone-like volcanoes have H:W ratios between 0.058 and 0.172. We observe that H:W shows inverse proportionality with the degree of estimated degradation (Figure 62), which reinforces the relationship between the amount of degradation and volcanic morphology. Therefore, the higher degree of degradation gives a lower H:W ratio which we interpret to

produces the mounds and trapezium-like morphologies from an original cone-like morphology. Clague et al., (2000a) demonstrate that flat-topped cones in Hawaii can form as continuously overflowing lava ponds. This situation is unlike to explain the flatten-tops of the MVF crater-type volcanoes because accumulation of lava deposits typically form high-amplitude reflectors in seismic data (e.g. Planke et al., 1999; Holford et al., 2012; Reynolds et al., 2016). In addition, the volcanoes with "flatten-tops" in MVF always have their tops associated with the lM unconformity. We interpret that some originally high cone-like volcanoes could have emerged above sea-level during the late Miocene sea-level drop and experienced degradation by wave erosion. These emergent extinct volcanoes may have formed an archipelago of at least nine small volcanic islands by ca 11 Ma (Figure 56).

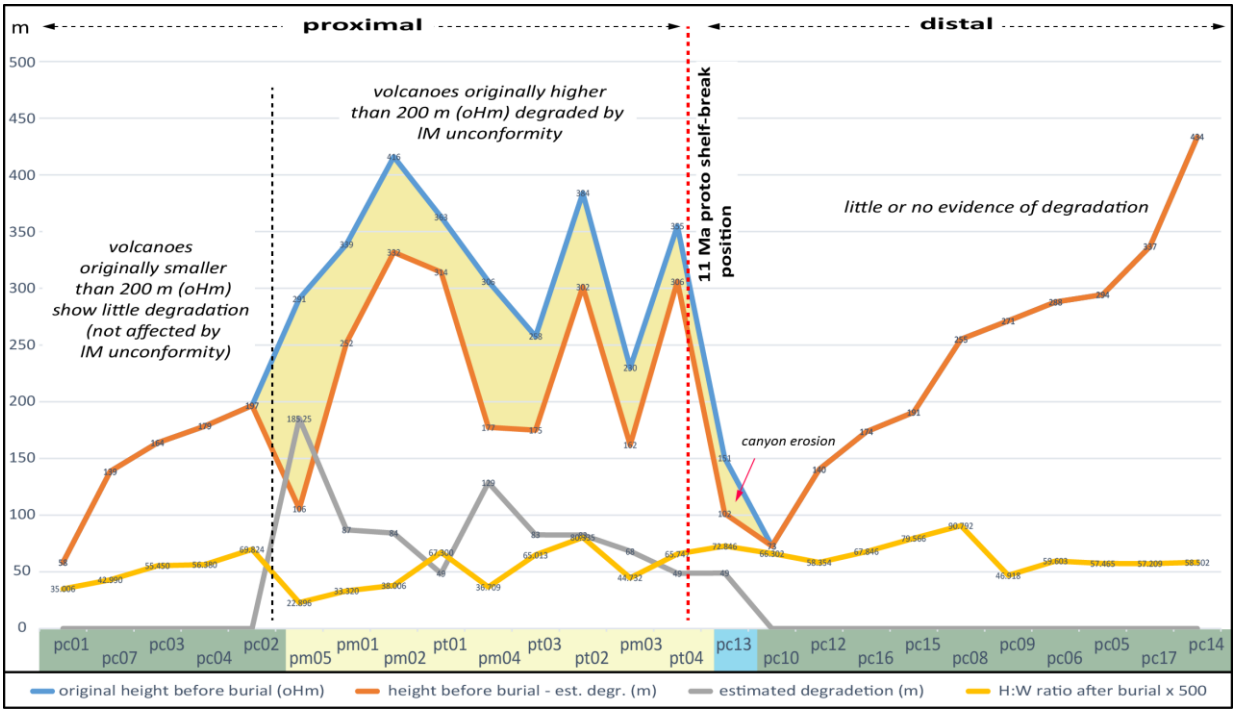

Figure 62: Morphometric analysis of crater-type MVF volcanoes in relation to the lM unconformity. Data have been organised by the position of volcanoes relative to the 11 Ma shoreline (proximal and distal). They were then organized by the estimated degree of degradation from the highest to smallest values, and finally by oHm from smallest to highest values. The yellow fill represents volcanoes with a moderate to high degree of degradation. At the left-hand side of the graph, all volcanoes are pc's of < 200 m oHm and show little degradation. All pt's and pm's are located on the shelf at 11 Ma and have oHm > 200 m. We interpret that at ca 11 Ma, these volcanoes were volcanic islands and experienced wave erosion. All volcanoes located on the slope do not show significant evidence of degradation, with the exception of pm03 which was eroded by canyons. The H:W ratio was multiplied by 500 for visualisation proposes. Note that the estimated degradation (grey) and the H:W (yellow) curves are inversely proportional, which indicates that a higher degree of degradation produced volcanoes with smaller H:W ratios, due to their loss in height (H) and gain in diameter (W).

4.7 Conclusions

Volcanism in the Maahunui Volcanic Field (MVF) occurred over an area of ca 1,520 km^2, comprising of a cluster of at least 31 middle Miocene volcanoes. These volcanoes are currently buried by around 1000 m of sedimentary strata in the offshore Canterbury Basin. Representative products of this volcanism are basaltic (possibly alkaline) in composition, and the volcanoes typically have small-volume (< 6 km^3) immediately after their eruptive phase. Reconstruction of the paleo-physiography of the MVF area indicate that eruptions were short-lived and controlled by a plumbing system that fed magma to dispersed eruptive centres, a characteristic of monogenetic fields. The MVF plumbing system emplaced a number of shallow (< 1000 m depth) intrusive bodies, commonly within Cretaceous-Paleocene sedimentary strata. Saucer-shaped sills are the most typical intrusion-type presenting sizes up to 5 km in width, and likely have fed magma to some of the volcanoes in the MVF. Eruptions were entirely submarine (500 to 1500 m), most likely producing subaqueous equivalents of maar-diatreme and tuff cone volcanoes. The morphology of the volcanoes are interpreted to be primarily controlled by phreatomagmatic explosions in which variations in the eruptive mechanisms such as water/magma ration and the mechanical behaviour of the pre-eruptive substrate likely have an important role in the fragmentation and dispersion of material. However, the occurrence of spatter cones and pillow mounds in the MVF is not discarded. In addition, post-eruptive degradation has changed the original volcanic morphology, which was controlled by the height, and by the position of the volcanic edifices in relation to a late Miocene base-level fall. After volcanism ceased, volcanoes located in a bathyal setting were rapidly buried and preserved, while volcanoes located in a neritic setting and with edifice heights > 200 m were possibly emergent at the paleo sea-surface, in this case, forming an archipelago with at least nine small extinct volcanic islands. Insights from the seismic morphological, petrographical characterisation and reconstruction of the volcanoes in the MVF has facilitated the prediction of potential architectural elements of buried monogenetic volcanic systems, which is the subject of Chapter 5.

4.8 References

Aarnes, I., Planke, S., Trulsvik, M., Svensen, H., 2015. Contact metamorphism and thermogenic gas generation in the Vøring and Møre basins, offshore Norway, during the Paleocene-Eocene thermal maximum. Journal of the Geological Society, 172(5), 588-598.

Abdelmalak, M. M., S. Planke., J. I. Faleide., D. A. Jerram., D. Zastrozhnov., S. Eide., R. Myklebust., 2016, The development of volcanic sequences at rifted margins: New insights from the structure and

morphology of the Vøring Escarpment, mid-Norwegian Margin: Journal of Geophysical Research, Solid Earth, 121, 5212–5236, doi: 10.1002/2015JB012788.

Adrian, A.B., 1997. Sea caves, relict shore and rock platforms: evidence for the tectonic stability of the Banks Peninsula, New Zealand. N.Z. J. Geol. Geophys. 40, 299-305.

Arnórsson, S., S. Thórhallsson., A. Stefánsson., 2015, Utilization of Geothermal Resources, in The Encyclopedia of Volcanoes: doi:10.1016/B978-0-12-385938-9.00071-7.

Ballance, P.F., 1993, The New Zealand Neogene forearc basins, in Ballance, P.F., ed., South Pacific Sedimentary Basins, Sedimentary Basins of the World 2: Amsterdam, Elsevier Science, p. 177–193.

Barrier,.A., A. Nicol, A. P. Bischoff., 2017, Volcanism Occurrences in the Canterbury Basin, New Zealand and Implication for Petroleum Exploration. In AAPG GTW Influence of Volcanism and Associated Magmatic Processes on Petroleum Systems. Conference, Oamaru New Zealand.

Barrier, in prep. Tectonic, structure and sedimentary evolution of the Canterbury Basin, New Zealand. PhD Thesis, University of Canterbury.

Batt, G. E., S. L. Baldwin., M. A, Cottam., P. G, Fitzgerald., M. T, Brandon., T. L. Spell., 2004, Cenozoic plate boundary evolution in the South Island of New Zealand: New thermochronological constraints: Tectonics, doi:10.1029/2003TC001527.

Bergman, S.C., J.P. Talbot, and P.R. Thompson., 1992, The Kora Miocene Submarine Andesite Stratovolcano Hydrocarbon Reservoir, Northern Taranaki Basin, New Zealand. In 1991 New Zealand Oil Exploration Conference, 178–206.

Best, M. G., E. H. Christiansen., 1997, Origin of broken phenocrysts in ash-flow tuffs: Bulletin of the Geological Society of America, doi:10.1130/0016-7606(1997)109<0063:OOBPIA>2.3.CO;2.

Bischoff, A.P., A. Nicol, A. Barrier, M. Beggs., 2016, The Stratigraphic Record of Volcanism - Examples from New Zealand Sedimentary Basins. In 2016 Geoscience Society of New Zealand Conference, Wanaka, Abstract.

Bischoff, A. P., A. Nicol, M. Beggs., 2017, Stratigraphy of architectural elements in a buried volcanic system and implications for hydrocarbon exploration: Interpretation, doi:10.1190/INT-2016-0201.1.

Blanke, S. J., 2010, “Saucer Sills” of the Offshore Canterbury Basin: GNS Publication, doi:10.1177/0094306114545742f.

Browne, G. H., 1983, A new interpretation of brecciation in the sandpit tuff, harper hills, Canterbury: New Zealand Journal of Geology and Geophysics, doi:10.1080/00288306.1983.10422258.

Carlson, J. R., J. A. Grant-Mackie., K. A. Rodgers., 1980, Stratigraphy and sedimentology of the coalgate area, canterbury, new zealand: New Zealand Journal of Geology and Geophysics, doi:10.1080/00288306.1980.10424205.

Cas, R. A. F., Landis, C. A., and Fordyce, R. E., 1989, A monogenetic, Surtla-type, Surtseyan volcano from the Eocene-Oligocene Waiareka-Deborah volcanics, Otago, New Zealand: A model: Bulletin of Volcanology, v. 51, no. 4, p. 281-298.

Cas, R., Satō, H., Simpson., C.J., 1993, Newer Volcanics province-processes and products of phreatomagmatic activity: Iavcei, Canberra 1993: excursion guide. Aust. Geol. Survey Organisation.

Cas, R. A. F., J. V. Wright., 1993, Volcanic Successions: Modern and Ancient - A Geological Approach to Processes, Products and Successions. Chapman and Hall, UK. doi:10.1007/978-0-412-44640-5.

Cas, R. A. F., G. Giordano., 2014, Submarine volcanism: A review of the constraints, processes and products, and relevance to the Cabo de Gata volcanic succession: doi:10.3301/IJG.2014.46.

Catuneanu, O., 2006, Principles of Sequence Stratigraphy. Changes, 375. doi:10.5860/CHOICE.44-4462.

Cant, J. L., Siratovich, P. A, Cole, J. W., Villeneuve, M. C., Kennedy, B. M., 2018, Matrix permeability of reservoir rocks, Ngatamariki geothermal field, Taupo Volcanic Zone, New Zealand Geothermal Energy Science https://doi.org/10.1186/s40517-017-0088-6.

Clague, D. A., J. G. Moore., J. R. Reynolds., 2000a, Formation of Submarine Flat-Topped Volcanic Cones in Hawai'i. In: Explosive Subaqueous Volcanism, edited by J.D.L. White, J.L. Smellie, and D.A. Clague, American Geophysical Union, Washington D.C., 200. Bulletin of Volcanology. doi.org/10.1029/140GM05.doi:10.1007/s004450000088.

Clague, D., R. Batiza., J.W. Head., A. Davis.,2000b, Pyroclastic and Hydroclastic Deposits on Loihi Seamount, Hawaii, in Explosive Subaqueous Volcanism, edited by J.D.L. White, J.L. Smellie, and D.A. Clague, American Geophysical Union, Washington D.C., 200. Bulletin of Volcanology. doi.org/10.1029/140GM05.

Coombs, D. S., A. J. R. White., D. Hamilton., and R. A. Couper., 1960, Age relations of the Dunedin volcanic complex and some paleogeographic implications—Part II: New Zealand Journal of Geology and Geophysics, doi:10.1080/00288306.1960.10420145.

Coombs, D.S., Cas, R.A., Kawachi, Y., Landis, C.A., McDonough, W.F., Reay, A., 1986, Cenozoic volcanism in north, east and central Otago. In: Smith, I.E.M. (Ed.), Late Cenozoic Volcanism in New Zealand. R. Soc. N.Z. Bull. 23, pp. 278-312.

Deardorff, N. D., K. V. Cashman., W. W. Chadwick., 2011, Observations of eruptive plume dynamics and pyroclastic deposits from submarine explosive eruptions at NW Rota-1, Mariana arc: Journal of Volcanology and Geothermal Research, doi:10.1016/j.jvolgeores.2011.01.003.

Delmelle, P., E. Maters., C. Oppenheimer., 2015, Volcanic Influences on the Carbon, Sulfur, and Halogen Biogeochemical Cycles, in The Encyclopedia of Volcanoes: doi:10.1016/B978-0-12-385938-9.00050-X.

Eady, A. E., 1995, The Petrology and Geochemistry of the Acheron Intrusion. Thesis, Canterbury University, 183 p. http://hdl.handle.net/10092/6783

Field, B.D., Browne, G.H., Davy, B.W., Herzer, R.H., Hoskins, R.H., Raine, J.I., Wilson, G.J., Sewell, R.J., Smale, D., Watters, W.A., 1989 Cretaceous and Cenozoic sedimentary basins and geological evolution of the Canterbury region, South Island, New Zealand. Lower Hutt: New Zealand Geological Survey. New Zealand Geological Survey basin studies 2. 94 p.

Finn, C. A., R. D. Müller., K. S. Panter., 2005, A Cenozoic diffuse alkaline magmatic province (DAMP) in the southwest Pacific without rift or plume origin: Geochemistry, Geophysics, Geosystems, doi:10.1029/2004GC000723.

Fornaciai, A., M. Favalli., D. Karátson., S. Tarquini., E. Boschi., 2012, Morphometry of scoria cones, and their relation to geodynamic setting: A DEM-based analysis: Journal of Volcanology and Geothermal Research, doi:10.1016/j.jvolgeores.2011.12.012.

Forsyth, P.J., Barrell, D.J.A., Jongens, R., 2008, Geology of the Christchurch area. Institute of Geological and Nuclear Sciences 1:250,000 Geological Map 16. Lower Hutt, GNS Science. 67 p1 sheet.

Giba, M., J. J. Walsh, Andrew Nicol, V. Mouslopoulou, H. Seebeck., 2013, Investigation of the Spatio-Temporal Relationship between Normal Faulting and Arc Volcanism on Million-Year Time Scales. Journal of the Geological Society 170 (6): 951–62. doi:10.1144/jgs2012-121.

Graettinger, A.H., G.A. Valentine, I., Sonder., 2016, Recycling in Debris-Filled Volcanic Vents. Geology 44, no. 10 (2016): 811. https://doi.org/10.1130/G38081.1.

Hansen, D. M., J. Cartwright., 2006, Saucer-Shaped Sill with Lobate Morphology Revealed by 3D Seismic Data: Implications for Resolving a Shallow-Level Sill Emplacement Mechanism. Journal of the Geological Society 163 (3): 509–23. doi:10.1144/0016-764905-073.

Hart, D. E., Marsden, I. D., and Francis, M., 2008, Coastal systems from Winterbourn, M. J., The Natural History of Canterbury, Canterbury University Press, p. 653-684.

Hawkes, P. W., D. D. Mound., 1984, BP Shell Todd (Canterbury) Services Limited, Clipper-1 Geological Completion Report PR1036.

Heap, M. J., B. M. Kennedy., 2016, Exploring the scale-dependent permeability of fractured andesite: Earth and Planetary Science Letters, doi:10.1016/j.epsl.2016.05.004.

Heap, M. J., B. M. Kennedy., J. I. Farquharson., J. Ashworth., K. Mayer., M. Letham-Brake., T. Reuschlé., H. A. Gilg., B. Scheu., Y. Lavallée., P. Siratovich., J. Cole., A. D. Jolly., P. Baud., D. B. Dingwell., 2017, A multidisciplinary approach to quantify the permeability of the Whakaari/White Island volcanic hydrothermal system (Taupo Volcanic Zone, New Zealand): Journal of Volcanology and Geothermal Research, doi:10.1016/j.jvolgeores.2016.12.004.

Head, J. W., L. Wilson., 2003, Deep submarine pyroclastic eruptions: theory and predicted landforms and deposits: Journal of Volcanology and Geothermal Research, v. 121, no. 3, p. 155–193, doi:https://doi.org/10.1016/S0377-0273(02)00425-0.

Holford, S. P., N. Schofield, J. D. MacDonald, I. R. Duddy, P. F. Green., 2012, Seismic Analysis of Igneous Systems in Sedimentary Basins and Their Impacts on Hydrocarbon Prospectivity: Examples from the Southern Australian Margin. APPEA Journal, 52, 229–52.

Hunt, D., and M. E. Tucker., 1992, Stranded parasequences and the forced regressive wedge systems tract: deposition during base-level fall: Sedimentary Geology, v. 81, no. 1–2, p. 1–9, doi:10.1016/0037-0738(92)90052-S.

Iacono-Marziano, G., Morizet, Y., Le Trong, E., Gaillard, F., 2013, New experimental data and semi-empirical parameterization of H2O-CO2 solubility in mafic melts. Geochimica Et Cosmochimica Acta 97. 145-157.

Infante-Paez, L., and K. J. Marfurt, 2017, Seismic expression and geomorphology of igneous bodies: A Taranaki Basin, New Zealand, case study: Interpretation, v. 5, no. 3, p. SK121-SK140, doi:10.1190/INT-2016-0244.1.

Jackson, C. A.-L., 2012, Seismic reflection imaging and controls on the preservation of ancient sill-fed magmatic vents: Journal of the Geological Society, doi:10.1144/0016-76492011-147.

Jerram, D. A., R. T. Single., R. W. Hobbs., C. E. Nelson., 2009, Understanding the offshore flood basalt sequence using onshore volcanic facies analogues: An example from the Faroe-Shetland basin: Geological Magazine, doi:10.1017/S0016756809005974.

Jutzeler, M., J. McPhie., S. R. Allen., 2014, Submarine eruption-fed and resedimented pumice-rich facies: the Dogashima Formation (Izu Peninsula, Japan): Bulletin of Volcanology, doi:10.1007/s00445-014-0867-x.

Jones, A., D., G. Wilson., A. Gorman., B. Fox., D. Lee., U. Kaulfuss., 2017, A drill-hole calibrated geophysical characterisation of the 23 Ma Foulden Maar stratigraphic sequence, Otago, New Zealand: 1-13 p., doi:10.1080/00288306.2017.1369130.

Kamp, P. J. J., P. F. Green., J. M. Tippett., 1992, Tectonic architecture of the mountain front-foreland basin transition, South Island, New Zealand, assessed by fission track analysis: Tectonics, doi:10.1029/91TC02362.

Kaulfuss, U., K. Németh, and J. White., 2012, Field Guide Miocene subaerial to subaqueous monogenetic volcanism in Otago, New Zealand.

Kereszturi, G., G. Csillag., K. Németh., K. Sebe., K. Balogh., and V. Jáger., 2010, Volcanic architecture, eruption mechanism and landform evolution of a Plio/Pleistocene intracontinental basaltic polycyclic monogenetic volcano from the Bakony-Balaton Highland Volcanic Field, Hungary: Central European Journal of Geosciences, doi:10.2478/v10085-010-0019-2.

Kereszturi, G., K. Németh., 2013, Monogenetic Basaltic Volcanoes: Genetic Classification, Growth, Geomorphology and Degradation: Updates in Volcanology - New Advances in Understanding Volcanic Systems, doi:http://dx.doi.org/10.5772/51387.

Klarner, S., O. Klarner., 2012, Identification of Paleo-Volcanic Rocks on Seismic Data, Updates in Volcanology. A Comprehensive Approach to the Volcanological Problems, 181–206, Prof. Francesco Stoppa (Ed.), InTech, DOI: 10.5772/24943.

Lever, H., 2007, Review of unconformities in the late Eocene to early Miocene successions of the South Island, New Zealand: Ages, correlations, and causes: New Zealand Journal of Geology and Geophysics, v. 50, no. 3, p. 245-261.

Lorenz, V., 1985. Maars and diatremes of phreatomagmatic origin, a review. Transactions of the Geological Society of South Africa, 88: 459-470.: 459-470 p.

Lu, H., C. S. Fulthorpe., P. Mann., M. A. Kominz., 2005, Miocene-Recent tectonic and climatic controls on sediment supply and sequence stratigraphy: Canterbury basin, New Zealand: Basin Research, v. 17, no. 2, p. 311–328, doi:10.1111/j.1365-2117.2005.00266.x.

Lu, Zhong, D. Dzurisin, J. Biggs, C. Wicks, S. McNutt., 2010, Ground Surface Deformation Patterns, Magma Supply, and Magma Storage at Okmok Volcano, Alaska, from InSAR Analysis: 1. Inter-eruption Deformation, 19970-2008. Journal of Geophysical Research: Solid Earth 115 (5): 1–14. doi:10.1029/2009JB006969.

Magee, C., E. Hunt-Stewart., C. A. L. Jackson., 2013, Volcano growth mechanisms and the role of sub-volcanic intrusions: Insights from 2D seismic reflection data: Earth and Planetary Science Letters, doi:10.1016/j.epsl.2013.04.041.

Marfurt, K., 2018, Seismic Attributes as the Framework for Data Integration Throughout the Oilfield Life Cycle: Society of Exploration Geophysicists, 508 p., doi:doi:10.1190/1.9781560803522.

McLean, C. E., N. Schofield., D. J. Brown., D. W. Jolley., and A. Reid, 2017, 3D seismic imaging of the shallow plumbing system beneath the Ben Nevis Monogenetic Volcanic Field: Faroe–Shetland Basin: Journal of the Geological Society, doi:10.1144/jgs2016-118.

McPhie, J., M. Doyle., R. Allen., 1993, Volcanic textures - a guide to the interpretation of textures in volcanic rocks. Centre for Ore Deposit and Exploration Studies, University of Tasmania

Mordensky, S., M. Villeneuve., J. Farquharson., B. Kennedy., M. J. Heap., D. M. Gravley., 2018, Rock mass properties and edifice strength data from Pinnacle Ridge, Mt. Ruapehu, New Zealand: doi:10.1016/j.jvolgeores.2018.09.012.

Nelson, S. T., A. Montana., 1992, Sieve-textured plagioclase in volcanic rocks produced by rapid decompression: American Mineralogist.

Németh, K., 2010, Monogenetic volcanic fields; origin, sedimentary record, and relationship with polygenetic volcanism: Special Paper Geological Society of America, doi:http://dx.doi.org/10.1130/2010.2470(04).

Németh, K., J. D. L. White., 2003, Reconstructing eruption processes of a Miocene monogenetic volcanic field from vent remnants: Waipiata Volcanic Field, South Island, New Zealand: Journal of Volcanology and Geothermal Research, doi:10.1016/S0377-0273(03)00042-8.

Milne, A.D., 1975. Well completion report Resolution, for BP, Shell, Todd Canterbury Service Limited. New Zealand Geological Survey Open-file Petroleum Report No. 648.

Mitchum, R M, P. R. Vail., 1977, Seismic Stratigraphy and Global Changes of Sea Level, Part 7 : Seismic Stratigraphic Interpretation Procedure. Seismic Stratigraphy: Applications to Hydrocarbon Exploration. AAPG Memoir 26 Memoir 26: 135–43.

Morley, C., 2018, 3D seismic imaging of the plumbing system of the Kora volcano, Taranaki Basin, New Zealand: The influences of syn-rift structure on shallow igneous intrusion architecture: Geosphere, 2018. doi.org/10.1130/GES01645.1.

Mortimer, N., 2004, New Zealand's Geological Foundations: Gondwana Research, v. 7, no. 1, p. 261-272.

Nara, Y., Meredith, P.G., T. Yoneda., K. Kaneko., 2011, Influence of macro-fractures and micro-fractures on permeability and elastic wave velocities in basalt at elevated pressure. Tectonophysics, 503 (1-2) 52 - 59. 10.1016/j.tecto.2010.09.027.

Orton, G.J., 1996, Volcanic Environments. In Reading, H. G., 1996, Sedimentary Environments: Processes, Facies and Stratigraphy: 688 p.

Pearce, T.H., 1993, Analcime phenocrysts in igneous rocks: Primary or secondary? Discussion. Am. Mineral. 78, 225-229.

Peretyazhko, I. S., 2010, Genesis of mineralized cavities (Miaroles) in granitic pegmatites and granites: Petrology, doi:10.1134/S0869591110020062.

Planke, S., E. Alvestad, O. Eldholm., 1999, Seismic Characteristics of Basaltic Extrusive and Intrusive Rocks. The Leading Edge 18 (3): 342. doi:10.1190/1.1438289.

Planke, S., J. M. Millett., D. Maharjan., D. A. Jerram., M. M. Abdelmalak., A. Groth., J. Hoffmann., C. Berndt., and R. Myklebust., 2017, Igneous seismic geomorphology of buried lava fields and coastal escarpments on the Vøring volcanic rifted margin: Interpretation, doi:10.1190/INT-2016-0164.1.

Posamentier, H. W., V. Kolla., 2003, Seismic Geomorphology and Stratigraphy of Depositional Elements in Deep-Water Settings. Journal of Sedimentary Research 73 (3): 367–88. doi:10.1306/111302730367.

Pritchard, M. E., M. Simons., 2004, An InSAR-Based Survey of Volcanic Deformation in the Southern Andes. Geophysical Research Letters 31 (15). doi:10.1029/2004GL020545.

Rabbel, O., O. Galland., K. Mair., I. Lecomte., K. Senger., J. B. Spacapan., R. Manceda., 2018, From field analogues to realistic seismic modelling: a case study of an oil-producing andesitic sill complex in the Neuquén Basin, Argentina: Journal of the Geological Society, doi:10.1144/jgs2017-116.

Raine, J. I., A. G. Beu., A. F. Boyes., H. J. Campbell., R. A. Cooper., J. S. Crampton., M. P. Crundwell., C. J. Hollis., H. E. G. Morgans., N. Mortimer., 2015, New Zealand Geological Timescale NZGT 2015/1: New Zealand Journal of Geology and Geophysics, v. 58, no. 4, p. 398–403, doi:10.1080/00288306.2015.1086391.

Reynolds, P., N. Schofield., R. J. Brown., S. P. Holford., 2016, The architecture of submarine monogenetic volcanoes - insights from 3D seismic data: Basin Research, v. 30, p. 437–451, doi:10.1111/bre.12230.

Reynolds, P., S., Holford, N. Schofield., A. Ross., 2017, Three-Dimensional Seismic Imaging of Ancient Submarine Lava Flows: An Example From the Southern Australian Margin: Geochemistry, Geophysics, Geosystems, doi:10.1002/2017GC007178.Rohrman, M., M. Lisk., 2010, Geophysical delineation of

volcanics and intrusives offshore NW Australia using global analogues. ASEG Extended Abstracts 2010, 1-3.

Robertson, J., E. M. Ripley., S. J. Barnes., C. Li, 2015., Sulfur liberation from country rocks and incorporation in mafic magmas: Economic Geology, doi:10.2113/econgeo.110.4.1111.

Schofield, N., L. Heaton, S. P. Holford., S. G. Archer., C. A.-L. Jackson., and D. W. Jolley., 2012, Seismic imaging of "broken bridges": linking seismic to outcrop-scale investigations of intrusive magma lobes: Journal of the Geological Society, doi:10.1144/0016-76492011-150.

Schofield, N., D. A. Jerram., S. Holford., A. Stuart., M. Niall., A. Hartley., J. Howell., M. David., P. Green., D. Hutton., C. Stevenson., 2016, Sills in sedimentary basin and petroleum systems, in K. Németh, ed., The Series Advances in Volcanology, 1–22.

Schmiedel, T., S. Kjoberg., S. Planke., C. Magee., O. Galland., N. Schofield., C. A.-L. Jackson., and D. A. Jerram., 2017, Mechanisms of overburden deformation associated with the emplacement of the Tulipan sill, mid-Norwegian margin: Interpretation, doi:10.1190/INT-2016-0155.1.

Schutter, S. R., 2003, Hydrocarbon Occurrence and Exploration in and around Igneous Rocks. Geological Society, London, Special Publications 214 (1): 7–33. doi:10.1144/GSL.SP.2003.214.01.02.

Sewell, R. J., 1988, Late Miocene volcanic stratigraphy of central Banks Peninsula, Canterbury, New Zealand: p. 41–64, doi:10.1080/00288306.1988.10417809.

Silva, S. D., J. M. Lindsay., 2015, Primary Volcanic Landforms. The Encyclopedia of Volcanoes. doi:10.1016/B978-0-12-385938-9.00015-8.

Single, R.T., Jerram, D.A., 2004. The 3-D facies architecture of flood basalt provinces and their internal heterogeneity: examples from the Palaeogene Skye Lava Field. Journal of the Geological Society 161, 911-926

Sheriff, R.E, and Geldart, L.P., 1995, Exploration Seismology. Cambridge University Press, Cambridge

Smith, K. L., A. R. Milnes., R. A. Eggleton., 1987, Weathering of basalt: formation of iddingsite. Clays Clay Miner. 35, 418– 428.

Schiøler, P., Raine, J.I., A. Griffin., C.J. Hollis., D.K. Kulhanek., H.E.G. Morgans., L. Roncaglia., C.P. Strong., C. Uruski., 2011. Revised biostratigraphy and well correlation, Canterbury Basin, New Zealand. GNS Science Consultancy Report 2011/12. 142 p.

Stern, T., S. Kleffmann., D. Okaya., M. Scherwath., S. Bannister., 2002, Low seismic-wave speeds and enhanced fluid pressure beneath the Southern Alps of New Zealand: Geology, doi:10.1130/0091-7613(2001)029<0679:LSWSAE>2.0.CO;2.

Strogen, D. P., H. Seebeck., A. Nicol, P. R. King., 2017, Two-phase Cretaceous–Paleocene rifting in the Taranaki Basin region, New Zealand; implications for Gondwana break-up: Journal of the Geological Society, doi:10.1144/jgs2016-160.

Stroncik, N. A., H. U. Schmincke., 2002, Palagonite - A review: International Journal of Earth Sciences, doi:10.1007/s00531-001-0238-7.

Suggate, R.P., Stevens, G.R.,Te Punga, M.T., 1978, The geology of New Zealand. Govt Printer, Wellington.

Sun, X., S. Cao, X. Pan, X. Hou, H. Gao, and J. Li., 2018, Characteristics and prediction of weathered volcanic rock reservoirs: A case study of Carboniferous rocks in Zhongguai paleouplift of Junggar Basin, China: Interpretation, v. 6, no. 2, p. T431–T447.

Svensen, H. H., T. H. Torsvik., S. Callegaro., L. Augland., T. H. Heimdal., D. A. Jerram., S. Planke., and E. Pereira., 2017, Gondwana Large Igneous Provinces: plate reconstructions, volcanic basins and sill volumes: Geological Society, London, Special Publications, doi:10.1144/SP463.7.

Timm, C., K. Hoernle., R. Werner., F. Hauff., P. van den Bogaard., J. White., N. Mortimer., D. Garbe-Schönberg., 2010, Temporal and geochemical evolution of the Cenozoic intraplate volcanism of Zealandia: doi:10.1016/j.earscirev.2009.10.002.

Tipper, J. C., 1993, Do seismic reflections necessarily have chronostratigraphic significance? Geological Magazine, doi:10.1017/S0016756800023712.

Walker, F., 1957, Ophitic Texture and Basaltic Crystallization. The Journal of Geology, 65(1), 1-14. Retrieved from http://www.jstor.org/stable/30064199.

Walker, G. P. L., R. Croasdale., 1971, Characteristics of some basaltic pyroclastics: Bulletin Volcanologique, doi:10.1007/BF02596957.

Wicks, C, D. Dzurisin, S. Ingebritsen, W. T. Z. Lu, J. Iverson., 2002, Magmatic Activity Beneath the Quiescent Three Sisters Volcanic Centre, Central Oregon Cascade Range, USA. Geophysical Research Letters 29 (7): 26 1-4. doi:10.1029/2001GL014205.

White, J. D. L., 2000, Subaqueous eruption-fed density currents and their deposits: Precambrian Research, 101 (2000) 87–109 doi:10.1016/S0301-9268(99)00096-0.

White, J. D. L., J. L. Smellie., D. A. Clague., 2003, Introduction: A deductive outline and topical overview of subaqueous explosive volcanism, in Geophysical Monograph Series: doi:10.1029/140GM01.

White, J. D. L., P. S. Ross., 2011, Maar-diatreme volcanoes: A review: doi:10.1016/j.jvolgeores.2011.01.010.

White, J. D. L., J. McPhie., S. A. Soule., 2015a, Submarine Lavas and Hyaloclastite, in The Encyclopedia of Volcanoes: doi:10.1016/B978-0-12-385938-9.00019-5.

White, J. D. L., C. I. Schipper., K. Kano., 2015b, Submarine Explosive Eruptions, in The Encyclopedia of Volcanoes: doi:10.1016/B978-0-12-385938-9.00031-6.

White, J. D. L., G. A. Valentine., 2016, Magmatic versus phreatomagmatic fragmentation: Absence of evidence is not evidence of absence: Geosphere, doi:10.1130/GES01337.1.

Wright, I. C., T. J. Worthington., J. A. Gamble., 2006, New multibeam mapping and geochemistry of the 30°-35° S sector, and overview, of southern Kermadec arc volcanism: Journal of Volcanology and Geothermal Research, doi:10.1016/j.jvolgeores.2005.03.021.

Wyering, L. D., M. C. Villeneuve., I. C. Wallis., P. A. Siratovich., B. M. Kennedy., D. M. Gravley., J. L. Cant., 2014, Mechanical and physical properties of hydrothermally altered rocks, Taupo Volcanic Zone, New Zealand: Journal of Volcanology and Geothermal Research, v. 288, p. 76–93, doi:10.1016/j.jvolgeores.2014.10.008.

Zimanowski, B., R. Büttner., V. Lorenz., H. G. Häfele., 1997, Fragmentation of basaltic melt in the course of explosive volcanism: Journal of Geophysical Research: Solid Earth, doi:10.1029/96JB02935.

Zimanowski, B., R. Büttner., 2003, Phreatomagmatic explosions in subaqueous volcanism, in Geophysical Monograph Series: doi:10.1029/140GM03.

Chapter 5

Stratigraphy of Architectural Elements in a Buried Monogenetic Volcanic System

5 Stratigraphy of Architectural Elements in a Buried Monogenetic Volcanic System

5.1 Abstract

Large volumes of magma emplaced and deposited within sedimentary basins can have an impact on their architectural style and geological evolution. Over the last decade, continuous improvement in techniques such as seismic volcano-stratigraphy and 3D seismic visualization of igneous rocks buried in sedimentary basins has helped increase knowledge about these "volcanic basins". Today, challenges remain in understanding how magmatism can influence the stratigraphic record of sedimentary basins from large to small scale. In this PhD thesis, we propose a volcanic-stratigraphic framework that divides volcanic basins into three first-order magmatic sequences (i.e. pre, syn and post-magmatic), which can be further divided into second-order magmatic stages related with the emplacement, construction, degradation and burial of the volcanoes. Each one of these stages is characterised by a network of genetically related fundamental building blocks (i.e. architectural elements), formed by interactions between magma, external environments and sedimentation.

Here, in the second part of this study, we apply the previous results from Chapter 4 to unravel the complete architecture of the Maahunui Volcanic System (MVS), situated in the offshore Canterbury Basin, South Island of New Zealand. We show the location, geometry, size, and relationships between 25 main architectural elements in a comprehensive volcano-stratigraphic framework that explains the evolution of the MVS from emplacement to complete burial. The plumbing system of the MVS comprises of seven main architectural elements, including saucer-shaped sills, dikes and sills swarms, minor stocks and laccoliths, and strata deformed by intrusions. These intrusive elements occur in five distinctive plumbing-types, controlled by the emplacement depth, and by the geometric relationships between the intrusions and the enclosing strata. The extrusive volcanic architecture is defined by a combination of eruptive and associated sedimentary architectural elements, with minor and localized shallow intrusions. Characteristic volcano-types of the MVS are interpreted as the submarine equivalents of crater and crater-type volcanoes. Crater-type volcanoes have eight main architectural elements (i.e. root zone, lower and upper diatreme, tephra ring, tephra plain, intra-crater cones, overspill wedge and tephra fallow carpets). Crater-type volcanoes have five main architectural elements (i.e. basal cone, central crater, tephra flank, cone apron and tephra fallout carpets). After

volcanism has ceased, the process of degradation and burial of the volcanic edifices produces five main sedimentary architectural elements (i.e. inter-cone plains, epiclastic plumes, canyons and gullies, burial domes and seamount-edge fans).

Understanding the relationships between these diverse architectural elements allow us to reconstruct the complete architecture of the MVS, and to recognize the main volcano-stratigraphic trends in the study area. The characterisation of architectural elements of the MVS can be then by applied to the exploration of geoenergy resources such as oil, gas and geothermal power, which is the topic of Chapter 6. Improving our understanding of the architectural elements of volcanic systems is important for assessing exploration risks, and for increasing the likelihood of finding commercial geoenergy resources in association with buried and active monogenetic volcanic systems.

5.2 Introduction

Volcanoes buried in sedimentary basins can form very complex magmatic-sedimentary systems (e.g. Planke et al., 1999; Holford et al., 2012; Schofield et al., 2012; Bischoff et al., 2017; Morley, 2018). The large-scale architecture of volcanoes can be divided into two main realms: i) the intrusive, or endogenous realm, is defined by sub-volcanic zones where magma crystallizes in the subsurface, and ii) the eruptive, or exogenous realm, is characterised by magma erupted at the Earth's surface (e.g. LaFemina, 2015). In the endogenous realm, magma migration and emplacement with the sedimentary strata can form a great variety of intrusive bodies, each with different morphologies, sizes and contact relationships with the host rocks, typically controlled by the equilibrium of magma pressure versus lithostatic pressure (e.g. Lister et al., 1991; Rubin, 1995; O'Neill et al., 2010; apud Kereszturi and Németh, 2013). Magma that reaches the Earth's surface can produce diverse terrestrial and submarine morphologies, largely defined by the interplay between magma composition, eruptive styles, edifice growth mechanisms, interaction with external environments, and tectonic settings (e.g. Cas and Wright, 1993; Kereszturi et al, 2011; Silva and Lindsay, 2015; Rogers, 2015; Planke et al., 2017). Large volumes of magma (typically > 10 km^3) erupted during multiple cycles from a relatively stationary plumbing system form polygenetic volcanoes, such as the iconic composite cones of Mt Fuji in Japan and Mt Taranaki in New Zealand (e.g. Silva and Lindsay, 2015). In contrast, monogenetic volcanic fields form when magma is dispersed to scattered vents. This process normally produces clusters of

small-volume volcanoes (< 10 km^3), which are related to a single[5] short-lived eruptive cycle with minor interruptions, such as those of the Auckland Volcanic Field in New Zealand and Michoacán–Guanajuato Volcanic Field in central Mexico (e.g. Kereszturi and Németh, 2013; Silva and Lindsay, 2015). Both polygenetic (e.g. Kora Volcano, offshore Taranaki Basin; Bergman et al., 1992) and monogenetic volcanic systems (e.g. Ben Nevis Monogenetic Volcanic Field, offshore the Faroe-Shetland Basin; MacLean et al., 2017) are commonly found buried in sedimentary basins.

To understand the past geological events that control the formation and evolution of sedimentary basins, standard analysis consist of sub-divid their regional stratigraphic record according to events that mark important sedimentation shifts during their evolution (e.g. Miall, 2000; Catuneanu, 2006; Catuneanu et al., 2009; Catuneanu et al., 2010). Sedimentary basins that contain large volumes of magma are known as "volcanic basins" (e.g. Planke et al., 2017; Svensen et al., 2017). Subdivision of the stratigraphic record of these basins was first proposed in Planke et al. (2000), who recognized six main volcano-stratigraphic units[6] related to large-volume extrusive igneous provinces. Bischoff et al. (2017)[7] subdivided the record of a single buried polygenetic volcanic system into three first-order stratigraphic intervals (i.e. pre, syn and post-magmatic sequences). The pre-magmatic sequence predates magmatism and is cross-cut by the volcanic plumbing system. The syn-magmatic sequence comprises of both intrusive and extrusive parts of the volcano. The post-magmatic sequence is characterised by degradation and burial of the volcanic structures after magmatism has ceased. These first-order sequences can be sub-divided into second-order magmatic stages (i.e. emplacement, construction, degradation and burial stages), according to the dominant magmatic or sedimentary processes that control the

[5] Kereszturi and Németh (2013), explain the construction of volcanoes by the interplay of simple vs. complex edifice grown mechanisms. They conclude that typical "mono" genetic volcanoes are the final product of many interactions between internally (e.g. composition) and externally (e.g. presence of water) driven factors. These interactions can change dynamically during the active volcanic stage (including transitions from eruptive-styles), without necessarily have interruptions in the life cycle of an eruption. The product of these dynamic changes may or may not be recorded in the final architecture of a volcano, which can complicate the use of conceptual boundaries such as single vs. multiple eruptive cycles to describe the active life cycle of a volcano. In seismic data, most of these nuances are likely unresolved. Thus, definitions such as mono vs. poly genetic from seismic data have to address criteria including reconstructed volcanic morphology, areal distribution of the vents, estimation of volume of magma erupted by each vent and relationship with enclosing sedimentary strata, which can provide information about short vs. long-lived eruptive cycles.

[6] The volcano-stratigraphic units of Planke et al. (2000) for large-volume basaltic provinces are: landward flows, lava delta, inner flows, inner seaward dipping reflectors, outer high, and outer seaward dipping reflectors. It is important to remember that this classification was made for rifted margins associated with large igneous provinces, which are orders of magnitude bigger than the volcanic systems presented in this thesis.

[7] Note that Bischoff et al., 2017 is part of this thesis, and is presented in chapter 3.

basin architecture at each time. Each one of these stages is characterised by a network of genetically related fundamental building blocks (i.e. architectural elements), formed by interactions between intrusions, eruptions, and sedimentation.

Systematic distribution of architectural elements in buried volcanic systems has been proposed by Bischoff et al. (2017). Syn-intrusive architectural elements are formed by magma emplacement at sub-volcanic levels (*emplacement stage*), and include hypabyssal intrusions such as sills, dikes and small plutonic bodies, together with pre-magmatic strata deformed by magmatism. Syn-eruptive and inter-eruptive architectural elements are formed during the *constructional stage*, and include all primary eruptive, epiclastic and associated sedimentary deposits formed during active and quiescent volcanism. Post-magmatic architectural elements are formed during the passive *degradational and burial stages* of volcanism, and include sedimentary deposits impacted by the presence of volcanic structures. In addition to this temporal order (i.e. pre- syn- and post-magmatic), lateral variations of architectural elements can be observed with increasing distance from one or more eruptive centres (e.g. deposits and facies variation shown in: Cas and Wright, 1993; Orton, 1996; Single and Jerram, 2004; Pittari et al., 2008; Kereszturi et al, 2010; Planke et al, 2017; Bischoff et al., 2017; Reynolds et al, 2017; Martí et al., 2018).

As mentioned in the previous chapter, this study has two parts. In chapter 4, we introduce the study area, explain the methods and limitations in characterizing buried volcanoes from seismic and well data, and present the results from detailed petrographic analysis, seismic interpretation, seismic morphologic characterisation, and paleo-environmental reconstruction of the Maahunui Volcanic Field (MVF) area. In this part, we apply the previous results to build a comprehensive volcano-stratigraphic framework that explains the complete architecture of the Maahunui Volcanic System (MVS). The *volcanic system* concept applied in this work is an extension of the igneous boundaries of the MVF, and includes two extra parts: i) the sedimentary strata deformed by intrusions, and ii) the post-eruptive sedimentary deposits impacted by the presence of the volcanoes (Figure 63), according the definition of Bischoff et al. (2017).

Studies that characterise the morphology (i.e. the form) and architecture (i.e. the arrangement of the parts) of monogenetic volcanoes are well constrained from the interpretation of modern and ancient outcropping systems (e.g. Lorenz, 1985; Cas and Wright, 1993; Orton, 1996; Kereszturi et al., 2010; Németh, 2010; Kereszturi and Németh, 2013; Silva and Lindsay, 2015). However, complete architectural characterisation of both endogenous and exogenous parts of

monogenetic fields is only possible in rare outcrops of exhumed volcanoes (e.g. White, 1991; Muirhead et al., 2016). Because of this, significant research is required to understand the key processes that control volcanic and sub-volcanic architecture together. High-quality 2D and 3D seismic surveys can provide a valuable opportunity to observe buried volcanic systems on scales ranging from seismic to outcrop analogues (e.g. Jerram et al., 2009; Schofield et al., 2012; Planke et al., 2017; Rabbel et al., 2018). This approach can be enriched by coupling the seismic data with information from borehole samples, wireline data, and laboratory experiments (e.g. Planke et al., 1999; Millett et al., 2015). Interpretation of the "big picture" of volcanic systems can provide valuable insights into how they evolve in time and space, which can be beneficial for estimating the potential of the system to host geoenergy resources such as petroleum and geothermal power (presented in Chapter 6 of this thesis). Currently, very few studies have been conducted to characterise the architecture of monogenetic volcanic systems from their emplacement to complete burial (e.g. Reynolds et al, 2016; McLean et al., 2017). Here, we adapt the approach presented in Bischoff et al. (2017) for polygenetic volcanic systems, to characterise the architecture of a buried monogenetic volcanic field and its enclosing sedimentary strata, collectively referred in this thesis to as the MVS (Figure 63).

5.3 Concepts, Methods and Terminology

Results from chapter 4 allow us to understand the broad-scale geologic history of the MVS, including insights into its plumbing system, eruptive-styles, and impacts on the pre-, syn- and post-magmatic sequences. The data set and methods applied during the seismic interpretation and petrographic analysis are described in Chapter 4. The available information helps us to build a comprehensive volcano-stratigraphic framework (Figure 63), showing the locations of individual (or sets of) cogenetic volcanic and sedimentary architectural elements. The volcano-stratigraphy framework was built from observations of stratigraphic surfaces that represent shifts in the local architecture of the basin, marking the boundaries between the magmatic sequences and stages in the study area (e.g. Bischoff et al., 2017). Table 7 shows the characteristics of these surfaces and their correlative magmatic sequences and stages in the MVS.

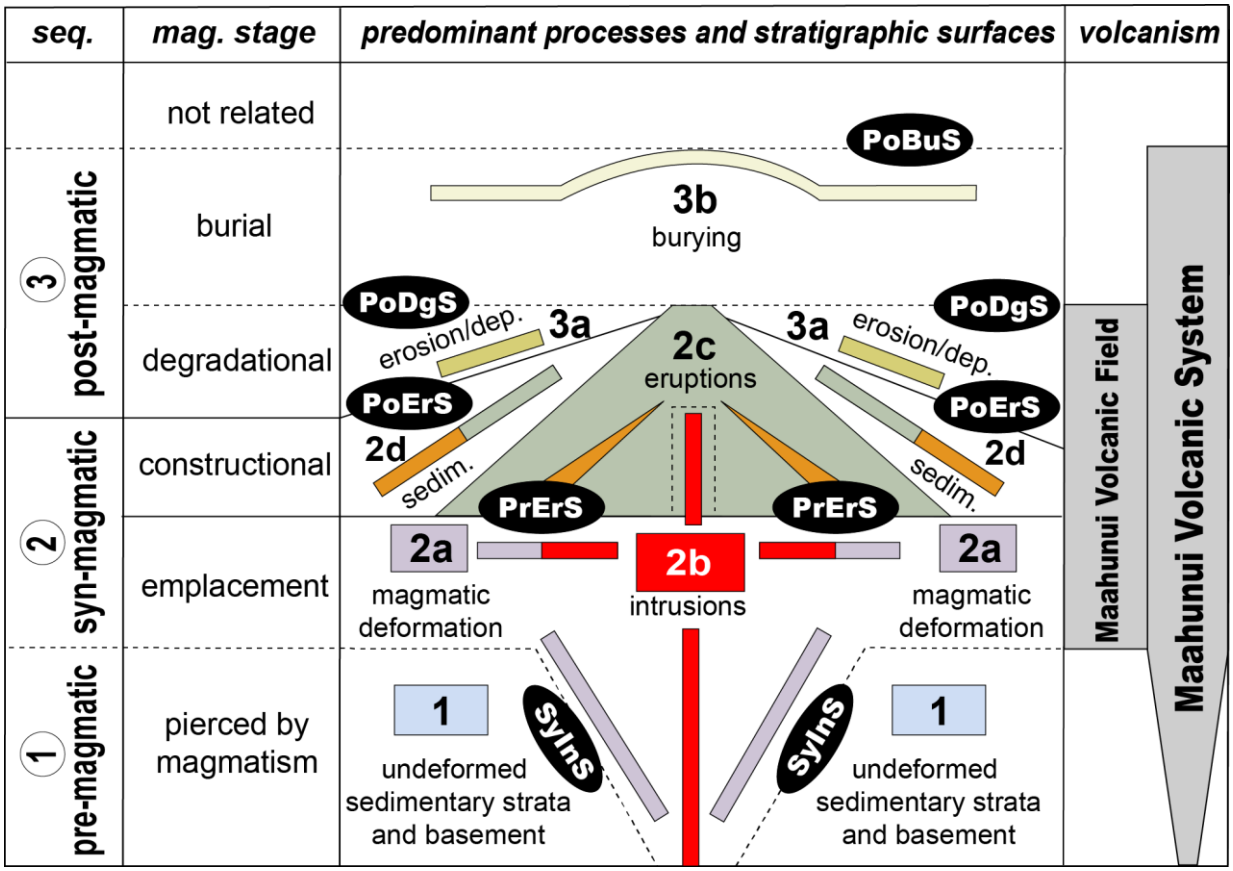

Figure 63: Conceptual representation of the magmatic sequences and stages (left), predominant geological processes, stratigraphic surfaces (centre), and boundaries of MVF and MFS (right).

Definition of the magmatic-stratigraphic surfaces follow well-established terminology such as pre-eruptive surface (PrErS) and post-eruptive surfaces (PoErS). In other cases, we introduce new terminology such as syn-intrusive surface (SyInS), post-degradational surface (PoDgS) and post-burial surface (PoBuS). The main magmatic-stratigraphic surfaces are defined as follows.

- The upper stratigraphic boundary of the pre-magmatic sequence (Figure 63) is defined by the oldest (in age) eruptive event in the volcanic field, and corresponds to the PrErS. Its lower and lateral limits are defined by the SyInS, which is an arbitrary boundary that limits the occurrence of intrusive bodies and associated deformation.
- The syn-magmatic sequence (Figure 63) is subdivided into two magmatic stages: i) the emplacement stage has its upper boundary at the PrErS, and an arbitrary lateral limit at the SyInS, ii) the constructional stage has a basal boundary defined by the PrErS, an upper boundary defined by the PoErS, which is concordant with the youngest (in age) eruptive event in the MVS, and a lateral boundary defined by the presence of eruptive and time-equivalent sedimentary deposits.

- The post-magmatic sequence (Figure 63) is subdivided into two recurrent magmatic stages: degradational and burial. The degradational stage has a lower stratigraphic boundary at the PoErS, and an upper boundary at the PoDgS, which is an arbitrary boundary relative to one or more eruption centres, and represent the time in when the rate of degradation exceeds the rate of burial in the field. The burial stage has a lower boundary at PoErS or PoDgS, and an upper boundary at the PoBuS, which is defined as an arbitrary surface that delimits the influence of the buried volcanic edifices on basinal sedimentation.

In addition to the stratigraphic surfaces, the presence of certain rock associations (i.e. architectural elements) helps to define the architecture of volcanic systems (Table 7). The concept of architectural elements was introduced by Allen (1983) and extended by Miall (1985), to describe sets of genetically related rock associations that form the fundamental building blocks of fluvial systems. The application of the architectural element concept is now widely used in most clastic systems (e.g. Mutti and Normark, 1987; Miall and Tyler, 1991; Miall, 2000; Borgui 2000; Posamentier and Kolla, 2003; Slatt, 2006; Moraes et al., 2006; Gamboa and Alves, 2015), and has also been successfully applied in carbonate systems (e.g. Kendall and Tucker, 2010; Catuneanu et al., 2011; Liu et al., 2018). To our knowledge, Bischoff et al. (2017) was the first work to apply this concept to characterise the architecture of volcanic systems.

Here, interpretation of the architectural elements of the MVS was primarily achieved by observations from seismic lines that image the volcanic field, and follows two approaches (Figure 64): one with complementary information from well data; the second without well data. In both approaches, we initially characterised the 2D aspects of seismic anomalies that represent buried igneous rocks in the study area, based on their morphology, internal, external and termination of seismic reflectors, geometry of enclosing strata, and surfaces that bound the anomaly from adjacent strata. Next, the results from 2D characterisation were compared with observations from outcropping and buried analogues elsewhere, searching for insights into possible 3D architectures expected to represent the seismic anomalies identified in 2D data. The final output interpretation can be very similar following both approaches, however, “ground-true” confirmation of the seismic images using data from drill holes can provide an accurate geological characterisation of the anomaly, while interpretation without well data remains only hypothetical (Figure 64).

Table 7: Main characteristics of the stratigraphic surfaces that bound distinctive magmatic sequences and stages in the MVS.

Stratigraphic Surface	Abbr.	Contact relationship	Defined by	Time-relative	Typical architectural elements associated
Post-burial surface	PoBuS	Conformable to both degradational and constructional stages.	Arbitrary surface that limits the relative influence of MVF basin architecture.	Can be synchronous or strongly diachronous (> 5 Ma) from diverse eruptive centres	Top of the burial dome and associated seamount-edge fans.
Post-degradational surface	PoDgS	Erosional into constructional stage. Laterally conformable within burial stage.	Arbitrary surface relative to one or more eruption centres, for which the rate of burial exceeds the rate of degradation.	Can be synchronous or diachronous from diverse eruptive centres (> 1 Ma and < 2 Ma)	Epiclastic debris deposits proximal to volcanic edifices and distal non-volcanogenic sedimentary deposits. Canyons and gullies, inter-cone plains.
Post-eruptive surface	PoErS	Overlies the constructional stage. Amalgamated or parallel with the PrErS for increasing distance from eruptive centres.	Younger (in age) eruptive event in MVF.	Minor diachronous from diverse eruptive centres (Usually < 1 Ma. Max 1.5 Ma)	Epiclastic debris deposits proximal to volcanic edifices and distal non-volcanogenic sedimentary deposits that overlay PoErS.
Pre-eruptive surface	PrErS	Overlies the pre-magmatic sequence and the emplacement stage.	Older (in age) eruptive event in MVF.	Minor diachronous from diverse eruptive centres (Usually < 1 Ma. Max 1.5 Ma)	Primary eruptive and eruption-related deposits that overlay PrErS.
Syn-intrusive surface	SyInS	Cross-cut the pre-magmatic sequence. Eventual minor cross-cutting into the constructional stage near eruptive centres or at very shallow intrusions.	Presence of intrusive bodies and strata deformed by magmatism.	Minor diachronous from diverse eruptive centres (Usually < 1 Ma. Max 1.5 Ma)	Dikes, sills, laccoliths, stocks, saucer-shaped sills, and disrupted blocks.

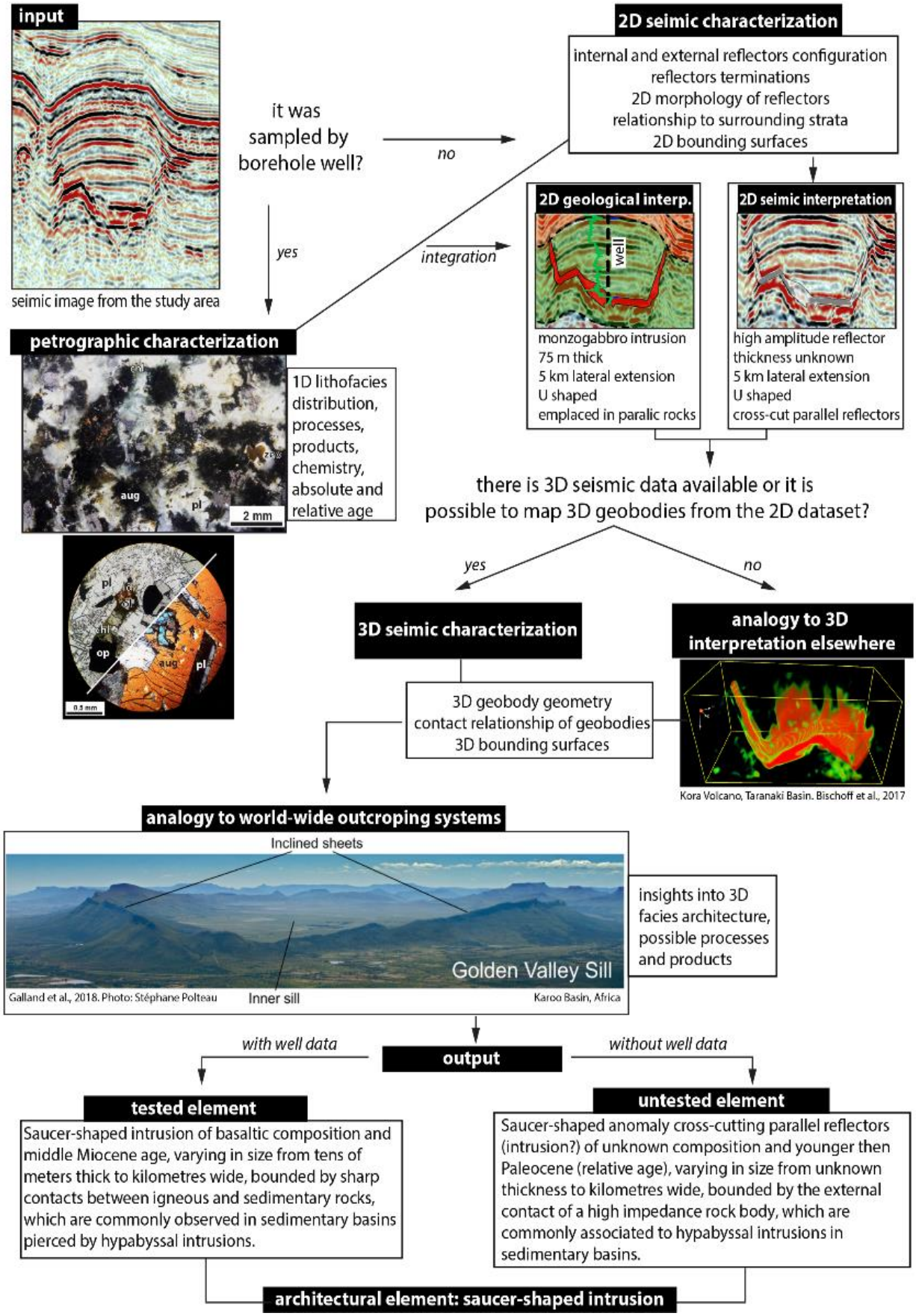

Figure 64: Methods used for the identification and interpretation of volcanic and sedimentary architectural elements in the MVS. The input 2D seismic reflection are described and compared with analogues. Elements sampled by drillholes can provide an accurate geological characterisation of the anomaly, while interpretation without physical confirmation remains only hypothetical.

5.4 Stratigraphy of Architectural Elements of Maahunui Volcanic System

We have identified 25 main individual architectural elements that together compose the architecture of MVS (Figure 65). In this section we present a detailed characterisation of each architectural element according to their stratigraphic position into the pre-, syn and post-magmatic sequences. Architectural elements formed during the pre-magmatic sequence and undeformed by magmatic processes are not described in detail further here. The syn-magmatic sequence is characterised by rock units formed during the emplacement of intrusive bodies, eruptions, and time-equivalent sedimentation, as well as by deformation of pre-magmatic strata during magmatism. Sedimentary processes such as erosion and burial of the volcanic edifice are dominant during the post-magmatic stage, after volcanism has ceased (Figure 63; Figure 65)

5.4.1 Syn-Magmatic Sequence

The MVS syn-magmatic sequence comprises the endogenous and exogenous parts of the volcanic system. The endogenous component of the MVS is characterised by the presence of syn-intrusive architectural elements, which also include their enclosing deformed strata. The exogenous component of the system is defined by the occurrence of syn-eruptive architectural elements, together with their contemporaneous non-volcanogenic sedimentary deposits.

5.4.1.1 Syn-intrusive architectural elements: plumbing system and magmatic deformation

Syn-intrusive architectural elements of MVS were formed in association with the emplacement of a shallow magmatic plumbing system (up to 3 km deep) that intruded and deformed Cretaceous to middle Miocene sedimentary strata in the study area. Typically, syn-intrusive architectural elements such as sill, dikes and strata deformed by magmatism occur below the PrErS surface, within pre-magmatic sedimentary strata, although some very shallow intrusions may cross-cut or emplace within syn-eruptive deposits. We broadly characterise the shallow plumbing system of the MVS (up to 3 km deep) into five plumbing-types (Figure 69; Figure 70), presented in the last part of this sub-chapter. Table 8 shows the main characteristics of the syn-intrusive architectural elements in the MVS.

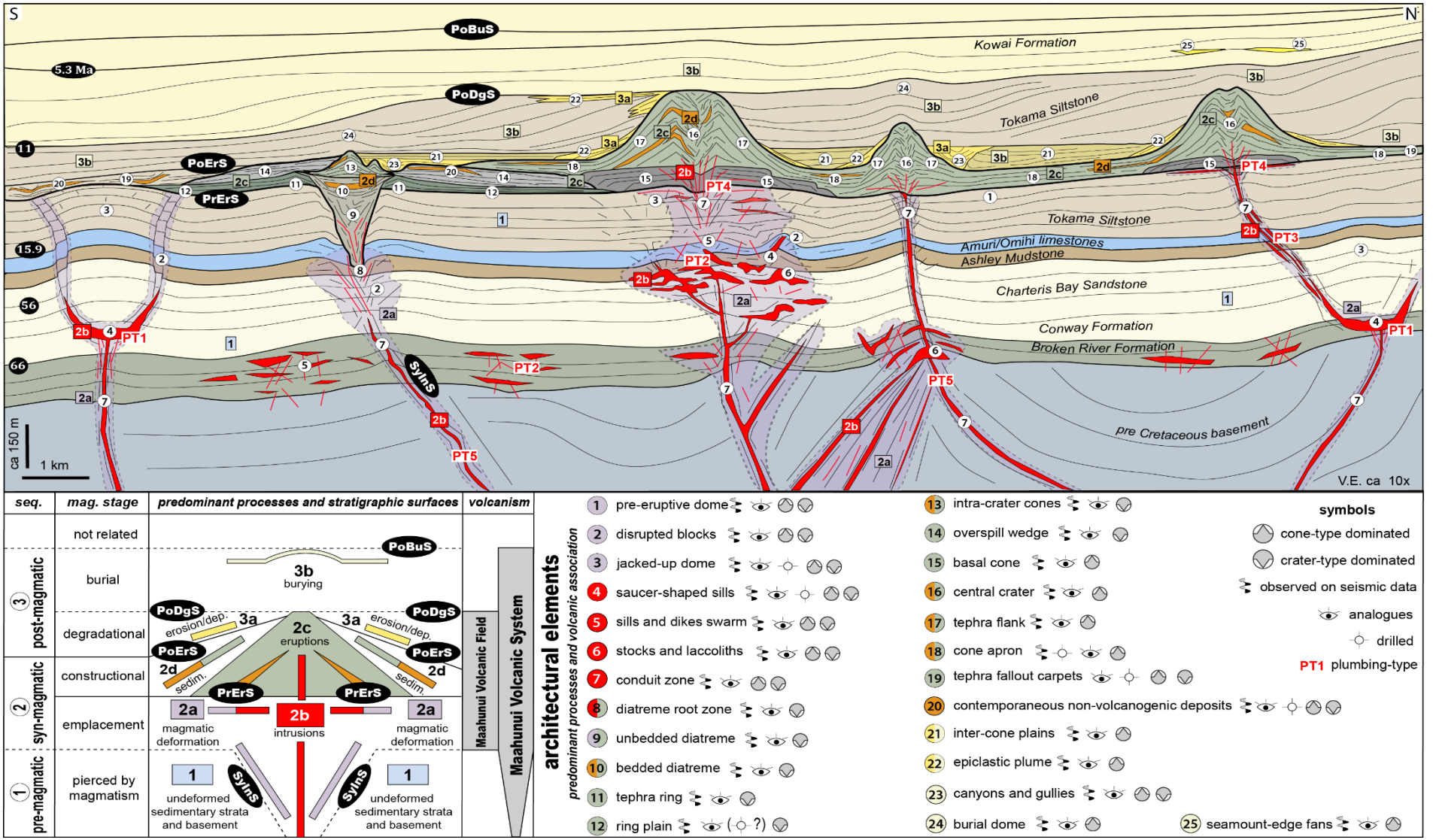

Figure 65: Schematic representation of the stratigraphic sequences and surfaces, magmatic stages, architectural elements, and predominant processes associated with MVS. Numbers in circles represent the location of the architectural elements indicated in the key. Numbers in squares indicate the predominant processes in the key. The symbols in the right hand corner illustrate the database used for interpretations. Conduit zones and dikes have lateral thicknesses exaggerated for visualization proposes. In this framework, PoDgS and PoBuS are related to the volcano in the centre of the figure, and to the 11 Ma unconformity described in chapter 4. Lateral variation of the lithostratigraphic units are not shown in the image. The pre-eruptive dome is a regional feature shown in Figure 68.

Table 8: Main characteristics of the syn-intrusive architectural elements in the MVS.

Element	Association	Seismic facies	Bounding surfaces	Geometry	Indicative process
Sill	Plumbing-types 2 and 4.	Anomalous single, high amplitude semi-continuous horizontal reflector.	Sharp contact between single high amplitude reflector and external bedded seismic facies.	Tabular horizontal to sub-horizontal.	Rock body emplaced parallel within enclosing strata.
Saucer-shaped sill	Plumbing-type 1 and 2.	Typically single high amplitude, semi-continuous, horizontal to inclined reflector.	Sharp contact between single high amplitude reflector and external bedded seismic facies.	Saucer-like.	Rock body emplaced parallel within enclosing strata. Jack-up, brittle deformation and body cross-cutting enclosing strata.
Dike	Plumbing-types 3, 4 and 5.	Single, narrow, vertical to sub-vertical transparent (i.e. reflector-free) discontinuities in bedded strata.	Sharp contact between sub-vertical transparent discontinuities and external bedded seismic facies.	Tabular vertical to sub-vertical. Typically seismically unresolved.	Rock body cross-cutting enclosing strata.
Dike and sill swarm	Plumbing-types 2, 3 and 4.	Multiple high amplitude, discontinuous, horizontal to steeply inclined reflectors in chaotic configuration.	Sharp contacts between multiple, chaotic, high amplitude reflectors and external bedded seismic facies.	Complex, chaotic.	Multiple rock bodies cross-cutting and parallel emplacing within bedded strata.
Stocks and laccoliths	Plumbing-types 2 and 3.	Single, thick, high amplitude, typically continuous, semi-circular reflector.	Sharp contacts between high amplitude reflectors and external seismic facies.	Sub-geoidal. Not always resolved in seismic data.	Rock body cross-cutting enclosing strata.
Disrupted block	Plumbing-types 1, 2, 3, 4 and 5.	Multiple narrow, vertical to sub-vertical transparent discontinuities in bedded strata.	Sharp contact between sub-vertical transparent discontinuities and external bedded seismic facies.	Chaotic.	Brittle deformation of bedded strata.
Jacked-up dome	Plumbing-types 1, 2, and 3.	Bedded strata domed above typically single high amplitude, semi-continuous, horizontal to inclined reflector.	Gradational contact between domed and parallel bedded seismic facies.	Downward-concave dome.	Strata jacked up above rock body emplaced parallel within enclosing strata.

Sills and saucer-shaped sills

Sills and saucer-shaped sills are the most common syn-intrusive architectural elements in the MVS (Figure 65; Figure 66; Figure 69; Figure 70). In the seismic data, these syn-intrusive architectural elements occur between 1.1 and 1.8 sec TWT, usually intruding paralic to marine

Cretaceous-Paleocene sedimentary strata. Individual or sets of tabular, parallel, transgressive and saucer-shaped sills vary in lateral size from a few hundred meters to 5 km in width and ca 100 m in vertical dimension (Figure 70). The presence of intrusions is often associated with disrupted and arched enclosing reflectors, demonstrating that magma transferring through (and into) the sedimentary basin can produce seismically resolvable structural deformation. This deformation can include folds, jacked-up strata, reverse and normal faults. These interpretations are supported by laboratory experiments (Montanari et al., 2017) and by observations from sedimentary basins elsewhere (e.g. Hansen and Cartwright, 2006; Holford et al., 2012; Planke et al., 2005; Blanke, 2012; Barrier et al., 2017; Jackson, 2012; Muirhead et al., 2016; McLean et al., 2017; Schmiedel et al., 2017).

Petrographic analyses of a Type-1 intrusion recovered from the Resolution-1 well provides evidence that this plumbing-type is typically emplaced and has crystalized at relatively shallow depths in the basin (ca 1000 m). Seismic images (Figure 69 and Figure 70) show a direct connection between Type-1 intrusions and many MVS eruptive vents, which in association with petrographic and geochemistry results, indicate that some of these saucer-shaped sills are likely to have fed eruptions at the middle Miocene paleo submarine seabed. This relationship between sill intrusions and eruptions is also observed in southern Australian marginn (Holford et al., 2012; Reynolds et al, 2017) and North Sea sedimentary basins (Jackson, 2012; McLean et al., 2017), and in outcrops of Hopi Buttes Volcanic Field, USA (Muirhead et al., 2016).

Dikes and magmatic conduits

Dikes and other potential magmatic conduits are syn-intrusive architectural elements characterised by vertical and sub-vertical igneous bodies emplaced beneath the pre- and post-eruptive surfaces (Figure 65; Figure 69; Figure 70). Due to their steep inclination and narrow lateral thickness, dikes and other magmatic conduits are seismically unresolvable in many cases. We recognize these bodies by narrow, steeply inclined, tabular high amplitude reflectors, and by sub-vertical discontinuities that crosscut pre-magmatic sedimentary strata (Figure 69; Figure 70). In the MVS, these intrusions typically form complex branched networks, in association with sills and stocks (plumbing-types 2, 3 and 4), similar to networks observed from 3D seismic reflection data and wells in the Ben Nevis monogenetic volcanic

field (McLean, et al., 2017). In other cases, we observe narrow sub-vertical discontinuities in host strata that can be tracked from MVS eruptive centres to depths of at least 4 km (plumbing-type 5). This plumbing style does not show branching or lateral migration, and could potentially represent simpler source-to-surface magmatic pathways from deeper magma chambers.

An analogy for dikes in the MVS is provided by a network of dikes and sills intruding poorly indurated Eocene marine strata from outcrops in the inland Canterbury Basin (Figure 66). These intrusions show distinctive outcrop patterns dependent on their emplacement depths. Deeper level intrusions mainly comprise sub-vertical dikes in sharp contact relationship with their host sandstones (Figure 66). Shallower intrusions have magma-finger terminations associated with thin sill apophysis and peperitic borders. Up-sequence (and above the intrusions), calcite veins occur in the absence of hypabyssal rocks, suggesting migration of fluids above the intrusions.

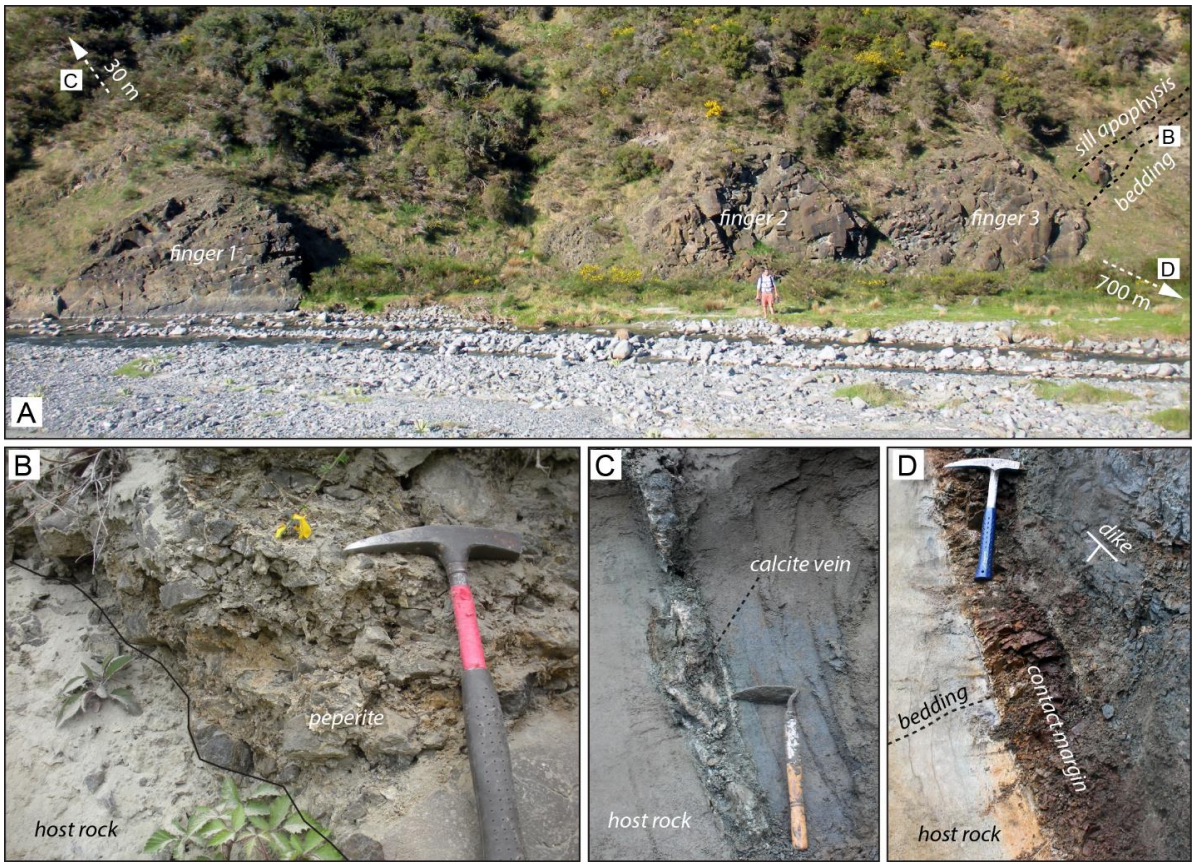

Figure 66: Photographs of potential analogue dikes outcropping in the Canterbury Basin. Intrusions have different patterns and products according to their depth of emplacement. At deeper levels, dikes show sharp contacts and little branching into enclosing sediments (D), while at shallower levels, they show magma finger terminations and several thin apophysis with peperitic borders. Thirty meters above the shallower intrusions, calcite veins (C) suggest migration of fluids up-sequence.

Disrupted blocks

Disrupted blocks are recognized in 2D seismic lines by parallel reflectors with abrupt lateral discontinuities (Figure 70; Figure 67). These seismic facies are interpreted to represent host sedimentary strata intensively deformed and cross-cut by intrusive bodies. Disrupted blocks typically occur below eruptive centres and in association with plumbing-types 3, 4 and 5, or above and lateral to intrusive bodies of plumbing-types 1 and 2 (Figure 65; Figure 69; Figure 70). These discontinuous "blocks" are likely formed due to fracturing, faulting and forced-folding of host strata, to accommodate deformation caused by the emplacement of intrusive bodies (e.g. Hansen and Cartwright, 2006; Jackson et al., 2012; Bischoff et al., 2017). Rupture and faulting of host sedimentary strata can be an important process for creating pathways for magma and/or fluid migration within the basin strata (e.g. Montanari et al., 2017).

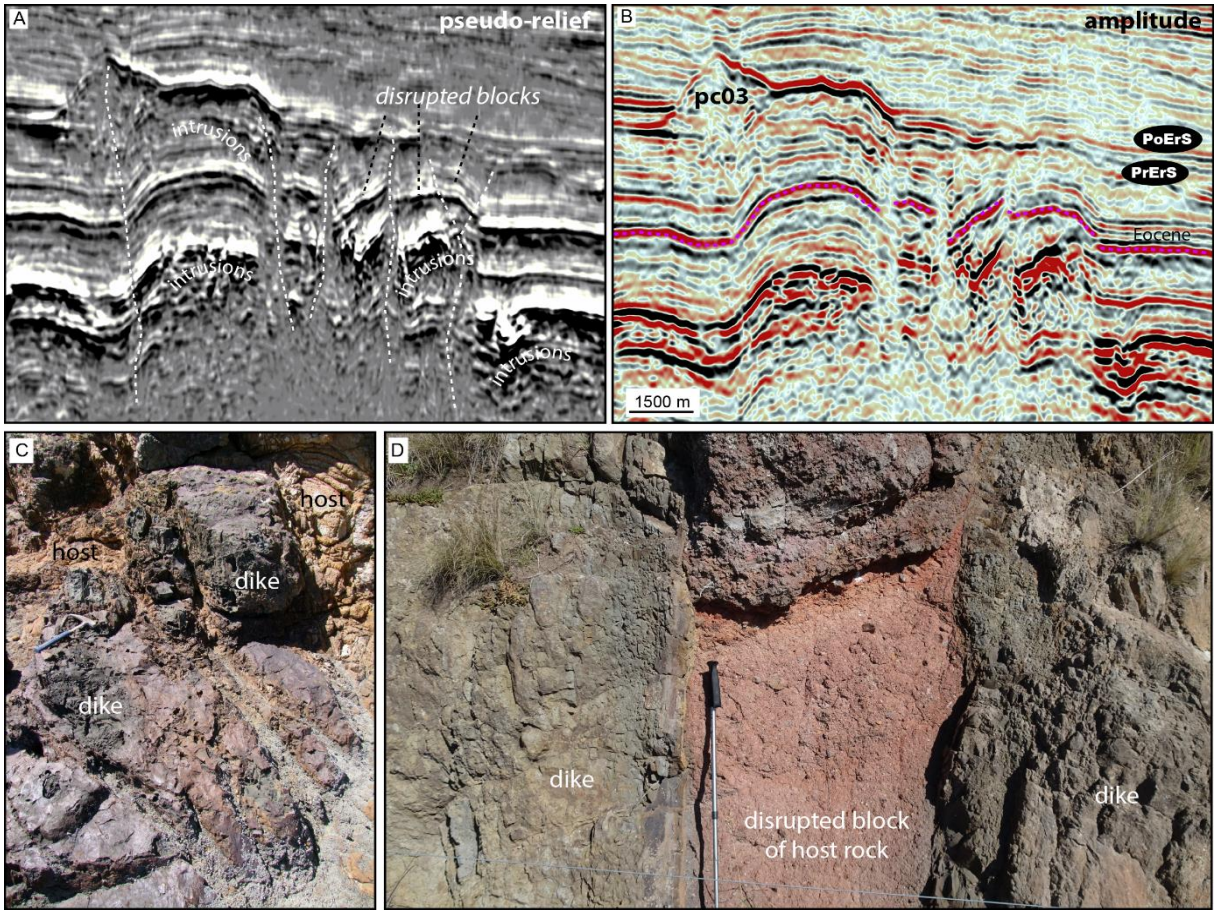

Figure 67: 2D seismic images (A and B) of disrupted blocks, and a possible outcrop scale analogue (C and D) of this architectural element in Banks Peninsula formed by host pyroclastic deposits cross-cut by multiple dike intrusions.

Jacked-up domes and pre-eruptive dome

Jacked-up domes are formed by uplift of pre-eruptive sedimentary strata above large intrusions (Figure 65; Figure 68; Figure 69; Figure 70; Figure 67).

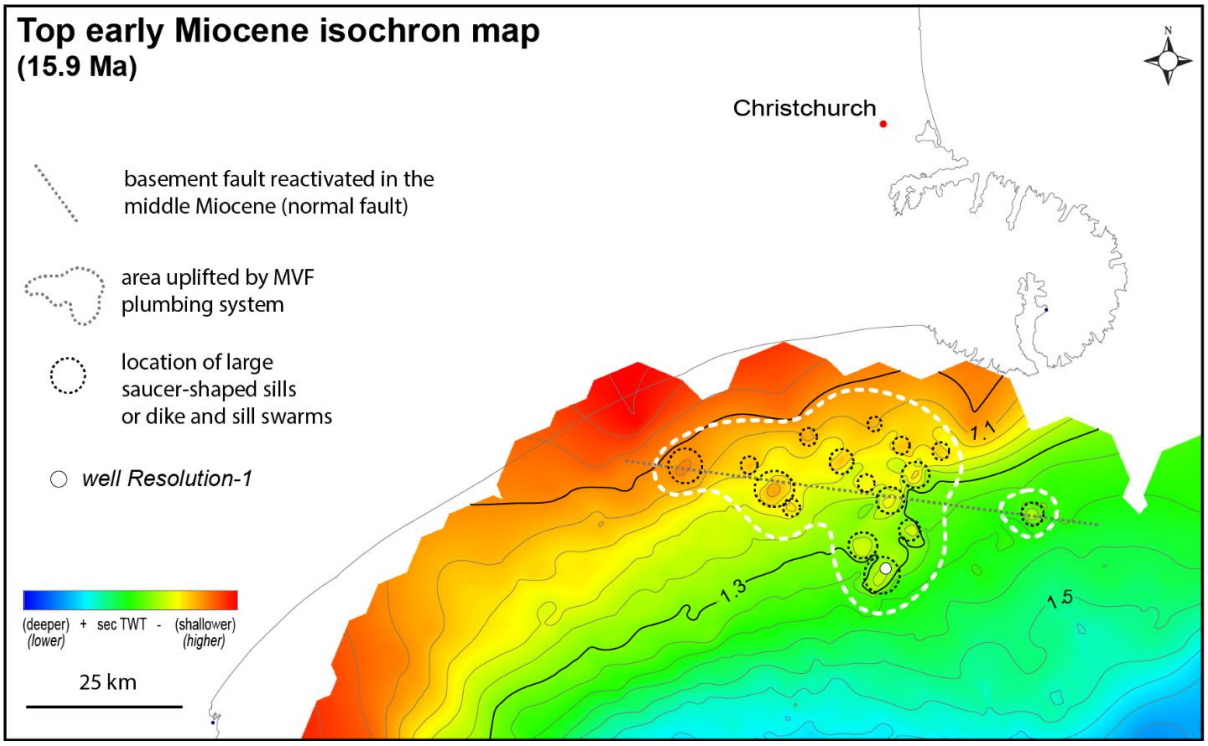

Figure 68: Top early Miocene isochron map of the northern part of Canterbury Basin. Red contours correspond to higher topography. The area inside the white dashed line shows semi-regional uplift with maximum vertical relief of ca 100 meters, coincident with the location of large sill and dike and sill swarms of the MVS plumbing system. This surface was chosen to demonstrate uplift of the sequence that predate the MVS, because in contrast to the PrErS, the top early Miocene surface is less disrupted by shallow intrusions, and reflectors can be tracked with more confidence at the sub-volcanic level.

In the study area, these dome structures are commonly associated with saucer-shaped sills (plumbing-type 1), and vary in diameter from 1 to 5 km. Complex fracture/fault networks with both normal and reverse faults are often observed along the borders of domed structures (e.g. Hansen and Cartwright, 2006; Montanari et al., 2017), providing conduits for magma and fluids as they ascend up-sequence (plumbing-type 3). In the MVS, the isochron map corresponding to the top of the early Miocene shows a semi-elliptical area of 1,137 km^2 that contains several four-way dipping structures with maximum vertical relief of ca 100 m, located above large saucer-shaped intrusions and associated dike and sill swarms (Figure 68). Possible explanations for this semi-regional uplift (pre-eruptive dome) is that the large size of swarms of intrusions emplaced within the sedimentary basin may produces inflation and ground dilatation above the MVS plumbing system, as in the pre-eruptive dome beneath Kora

volcano (e.g. Bischoff et al., 2017; Infante-Paez and Marfurt, 2017; Morley, 2018), or the uplift could be influenced by thermal uplift, representing a small scale process of the uplift that formed the Ethiopian and Kenya domes (e.g. Macdonald, 2003; Chorowicz, 2005; Ring, 2014). Further studies are necessary to characterise this uplift.

Stocks and laccoliths

Some seismic anomalies associated with plumbing-types 2 and 3 show high amplitude reflectors with irregular and concave downward shapes (Figure 70). These anomalies cross-cut enclosing strata and produce a domed configuration in enclosing strata immediately above the anomalies. These bodies have been interpreted to represent small (< 200 m) stocks that intruded pre-magmatic sedimentary sequences. Laccoliths possible occur in the plumbing-types 2 and 3, however separating them from stocks is not possible in the seismic data from the MVS.

MVS plumbing-types

We characterise typical plumbing-types of the MVS based on the geometry, size and depth of the intrusions, and on their relationship to enclosing sedimentary strata. Each plumbing-type usually contains a variety of intrusive bodies such as dikes, sills and stocks. Figure 65, Figure 69, Figure 70 show a schematic representation and seismic images of these plumbing-types.

- Type 1: large (up to 5 km in width and ca 100 m thick) sills and saucer-shaped intrusions emplaced at deeper levels within the basin (500 to 1400 m), into Cretaceous-Paleocene sedimentary strata, showing minor branching, simple intrusive network, and extensive lateral migration of magma (up to 5 km).
- Type 2: small (up to 1 km), disrupted, parallel, transgressive or saucer-shaped intrusions emplaced into Cretaceous to Oligocene strata, showing intense lateral and vertical branching, very complex intrusive networks, and moderate magma lateral migration.
- Type 3: narrow, steeply inclined and discontinuous conduit zones, located immediately above the tips of large saucer-shaped intrusions (type-1), showing intense vertical branching, complex intrusive networks, and little lateral migration of magma.

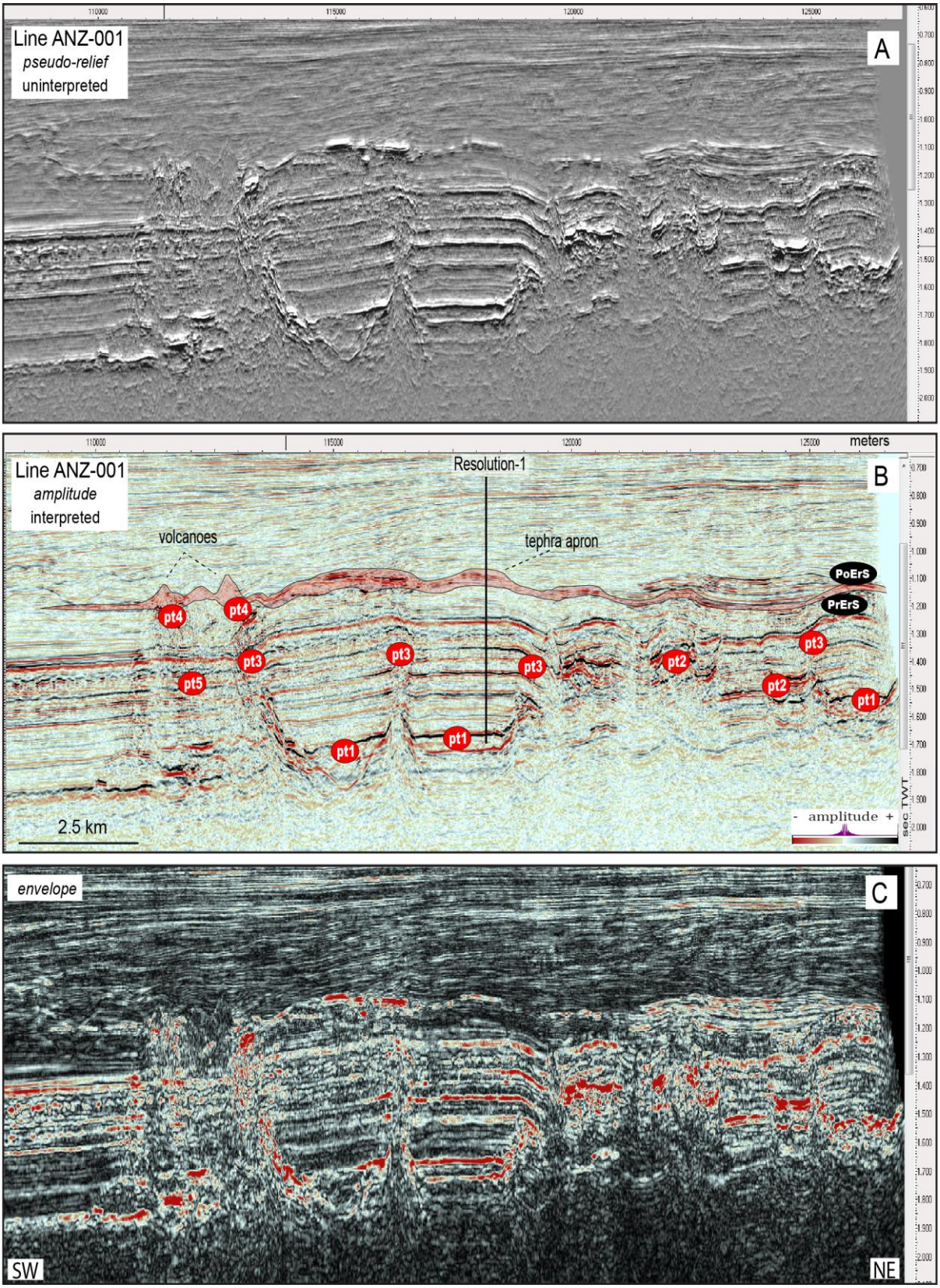

Figure 69: 2D seismic reflection lines showing the locations and geometries of the five plumbing-types observed in the MVS. Images A, B and C for the same line ANZ-001 which display the seismic attributes pseudo-relief (A), amplitude (B) and envelope (C). Note the systematic vertical distribution from type-1 (deeper) to type-4 (shallower) and their relationship. Type-5 differs from the other types in that it represents a deep source-to-surface feeder systems.

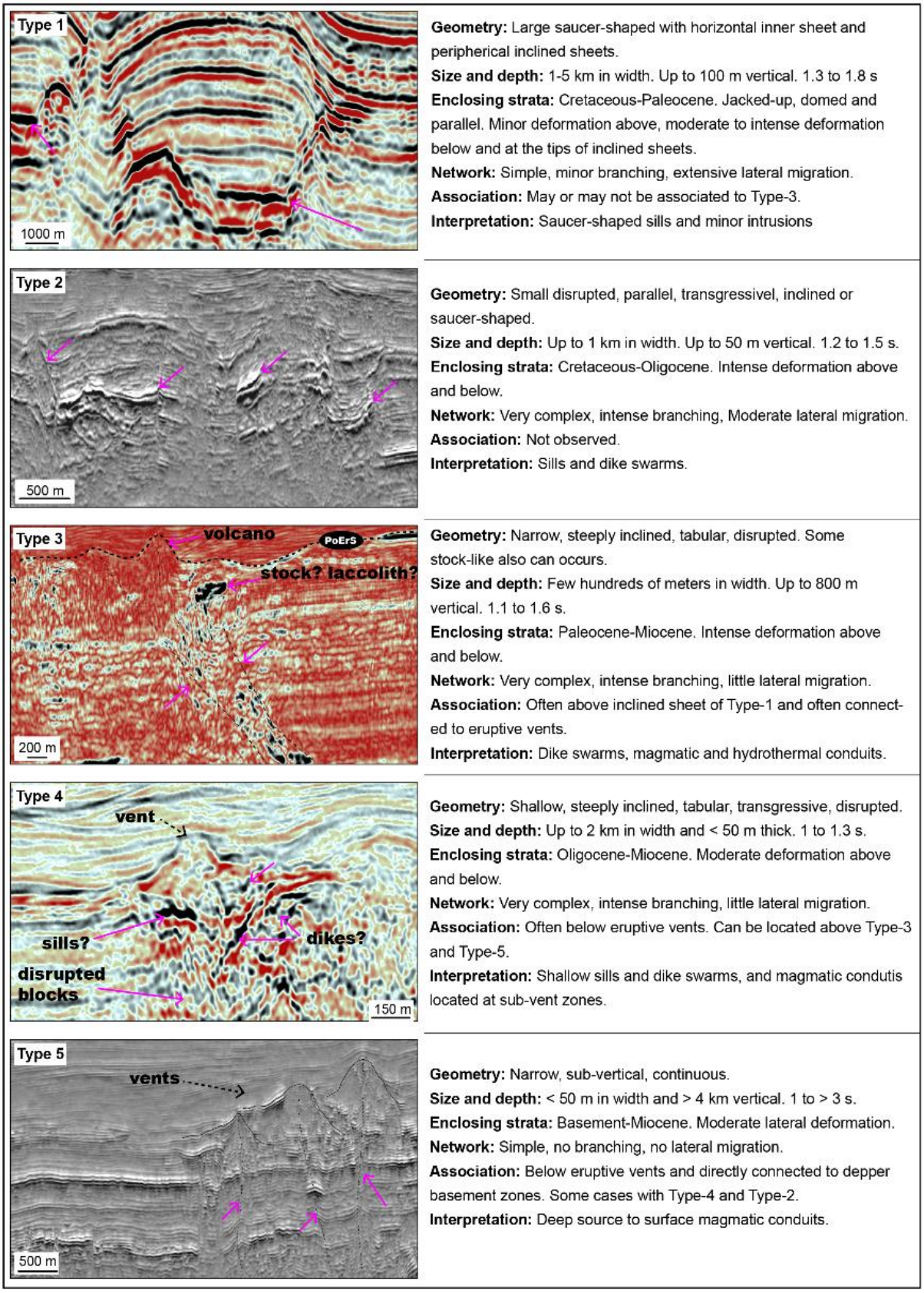

Figure 70: 2D seismic reflection images and characterisation of the five plumbing-types from the MVS. Seismic attributes of the images are: Type-1= amplitude, Type-2= pseudo-relief, Type-3= envelope, Type-4= amplitude and Type-5= pseudo-relief.

- Type 4: shallow (up to 250 m deep) swarms of narrow, steeply inclined, parallel and transgressive intrusions, located immediately below eruptive vents, showing intense branching, complex intrusive networks, and little lateral migration of magma.
- Type 5: narrow, very deep to shallow, steeply inclined conduit zones located immediately below eruptive vents, showing little branching, simple intrusive networks, and little lateral migration of magma.

In summary, the plumbing system of the MVS is characterised by a complex network of sills and dikes that deform pre-magmatic sedimentary strata. Many of these intrusions (i.e. large saucer-shaped sills of plumbing-type 1) served as stationary shallow magmatic chambers that fed eruptions at the middle Miocene seabed. In other cases, a deeper source-to-surface (plumbing-type 5) is likely to have fed some submarine volcanoes. Seismic images of the MVS plumbing system suggest that a greater volume of magma has been emplaced within the basin sedimentary strata of the basins, in contrast with a much smaller volume that reached the paleo seabed (e.g. Figure 69).

5.4.1.2 Syn-eruptive architectural elements: eruptive, eruption-related and contemporaneous non-volcanogenic sedimentary deposits

Syn-eruptive architectural elements are cogenetic sets of eruptive, eruption-related and time-equivalent non-volcanogenic sedimentary units formed during the active constructional stage of the MVS. During this stage, the architecture of the volcanoes in the MVS was mainly controlled by interactions between internally (i.e. magma composition, pressure and magma ascension rate) and externally (i.e. interaction with water, soft or hard country rock and presence of pre-existent structures) driven mechanisms of fragmentation, dispersion and edifice growth (e.g. Kereszturi and Németh, 2013). Two main volcano-morphologies are observed in the MVS: i) crater-type and ii: crater-type volcanoes. Each of these volcano-types contains distinctive combinations of cogenetic sets of syn-eruptive architectural elements at different scales, although some elements can occur in both types (e.g. tephra fallout carpets). Seismic morphology and the morphometry parameters of these buried volcanoes show similarities to subaerial and submarine monogenetic volcanoes (Figure 71; Figure 72; Figure 73) well documented in the literature (Lorenz, 1985; Cas et al., 1989; White, 1996; Lorenz and Kurszlaukis, 2007; White, 2000; Corcoran and Moore, 2009; White and Ross, 2011; Kaulfuss

et al., 2012; Kereszturi and Németh, 2013; Jones et al., 2017; Reynolds et al., 2017). These similarities assist our interpretations and provide information for the construction of a comprehensive time-space framework, showing the distribution of different sets of architectural elements for each volcano-type.

Crater-type volcanoes: subaqueous equivalent of maar-diatreme volcanoes

Crater-type volcanoes of the MVS are characterised in seismic reflection imagery by funnel and basin-like excavations into pre-magmatic sedimentary strata. Reconstructed MVS diatremes vary in diameter from 901 to 1682 m, and show 91 to 230 m in depth excavated into the PrErS. These craters were excavated into relatively soft ground, locally corresponding to the bathyal Tokama siltstone in the upper part, and to the micritic Amuri limestone and Ashley mudstone in the root zone (Figure 71). The lateral variation of these sedimentary rock units is not always possible to predict in seismic images, due to a limited number of wells in the study area to confirm they presence. Basin-like excavations are rare in the MVS and difficult to characterise due to seismic resolution limitations, thus, further descriptions consider morphological aspects of funnel-like volcanoes.

The architecture of MVS crater-type dominate volcanoes can be divided into eight distinctive fundamental architectural elements (Figure 71; Figure 72; Figure 73). Mapping of these elements was based on distinctive seismic facies, and on bounding surfaces that separate characteristic seismic morphologies. The distribution of these elements varies according to their relative distance from eruptive centres. The main aspects of the large-scale architecture of crater-type dominate volcanoes are presented in Table 9.

Based on the presence of disrupted reflectors showing minor depressions located at the base of the diatreme structures (Figure 71; Figure 72), we interpret that the bottom part of the diatremes in the MVS may contain a *root zone* (Figure 9; Figure 10; Figure 11). Studies elsewhere suggest that this zone is the locus of thermohydraulic explosions (e.g. Lorenz, 1985; Lorenz and Kurszlaukis, 2007; White and Ross, 2011; Kereszturi and Németh, 2013), and likely contains syn-intrusive architectural elements such as contact breccias, disrupted pre-magmatic blocks, and late intrusive plugs. However, we do not recognize indicative seismic facies that could support the occurrence of these elements, perhaps because they are seismically unresolved. In some cases, the location of the root zone is coherent with seismic

reflectors that correspond to the Amuri and Omihi limestones, and maybe to Charteris Bay Sandstone in its deepest part. The MVS volcaniclastic rocks sampled in Resolution-1 from 1140 to 1150 m contain numerous lithics of limestone and white very-fine sandstone, which may provide evidence that the country rocks of the root zone have experienced intense fragmentation, and were incorporated into the material ejected by explosive eruptions. In diatremes of the MVS, the depression at the centre of the funnel-like structure may indicate post-eruptive subsidence (Figure 72).

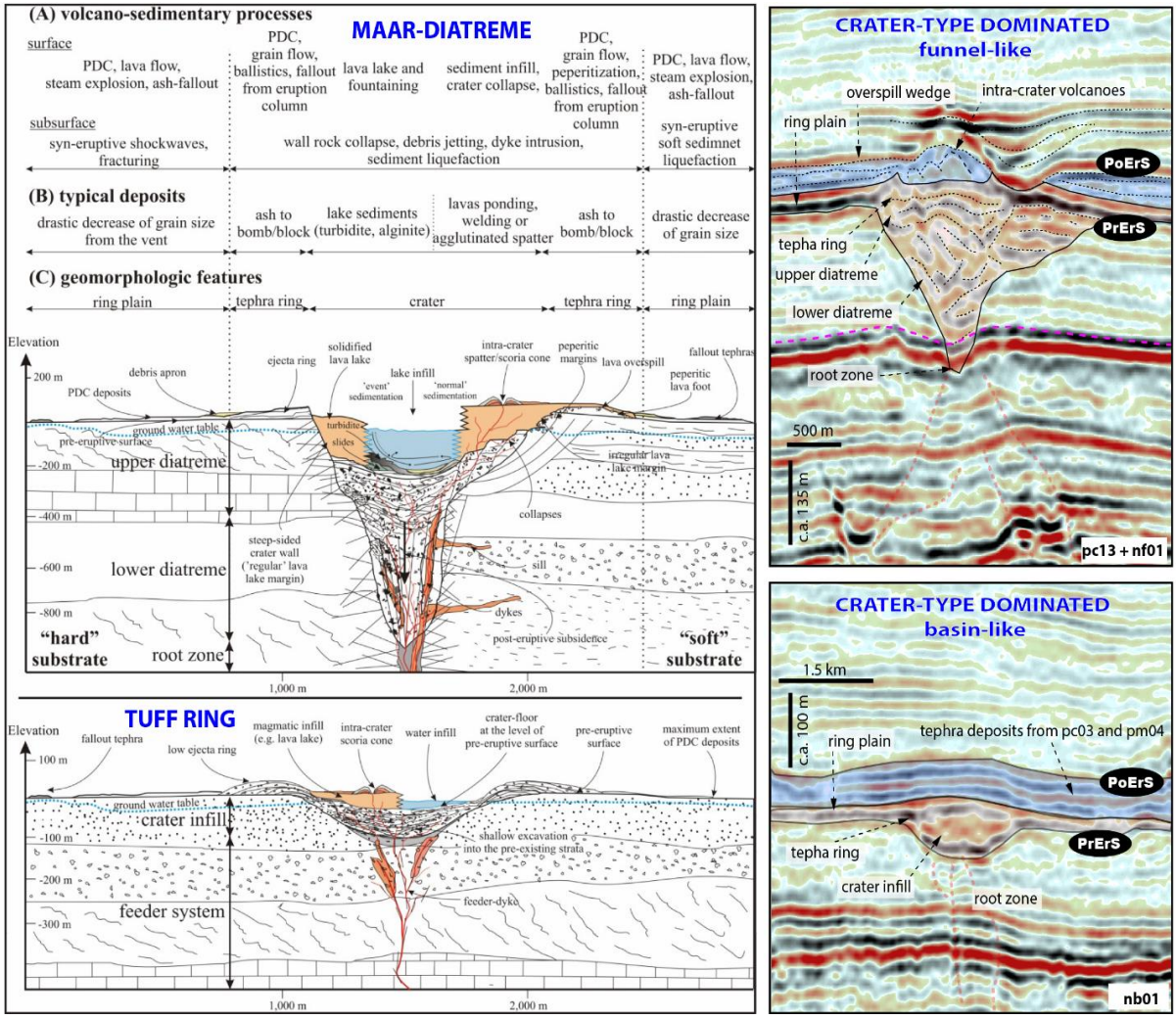

Figure 71: Images on the left hand side show schematic cross-sections through a maar-diatreme and a tuff ring, and their typical volcano-sedimentary processes, deposits and geomorphologic features (from Kereszturi and Németh, 2013). On the right-hand side are shown interpreted 2D seismic lines of the MVS crater-type volcanoes, and their main large scale architecture.

Table 9: Main characteristics of the architectural elements of the crater-type dominate volcanoes formed during the constructional magmatic stage in the MVS.

Element	Location	Seismic facies	Bounding surfaces	Geometry	Indicative processes
Root zone	Bottom of the funnel-like structure.	Moderate to high amplitude and disrupted reflectors showing depression towards the centre of the structure.	Seismically unresolved.	Unsure, probably geoidal.	Brittle deformation. Post-eruptive subsidence?
Lower diatreme	Centre of the funnel-like structure.	Moderate amplitude, discontinuous and chaotic reflectors.	Sharp contact between internal unbedded seismic facies from external bedded reflectors.	Funnel-like.	Brittle deformation. Excavation into PrErS. Intense fragmentation and dispersion of material.
Upper diatreme	Top of the funnel-like structure.	Moderate amplitude, semi-continuous, parallel and sub-horizontal reflectors.	Sharp contact between Internal bedded seismic facies from external unbedded seismic facies below, and mound-like facies above.	Funnel-like.	Deposition of layered material into an upper crater.
Tephra ring	Symmetrically lateral to the upper diatreme.	Single high amplitude, continuous and inclined reflectors in A shape.	Sharp contacts between the upper and lower limits of the high amplitude reflector. Laterally gradational to facies of the ring plain.	Ring-like.	Deposition of “hard” material in relatively steep repose angle near a vent zone.
Ring plain	Symmetrically lateral to the tephra ring.	Single high amplitude, continuous, parallel and sub-horizontal reflectors.	Sharp contacts between upper and lower limits of the high amplitude reflector. Laterally gradational to facies of the ring plain. Fade with increasing distance from the vent zone.	Circular tabular, thinner with increasing distance from the vent.	Intense fragmentation and dispersion of material ejected from the diatreme. Deposit parallel to basinal sediments immediately above PrErS.
Intra-crater cones	Above of the funnel-like structure.	Moderate amplitude reflector with mound-like shape and transparent internal seismic facies.	Sharp contacts between the upper and lower limits of the mound-like structure and external bedded facies.	Mound-like and possible small cone-like.	Deposition of material above the upper diatreme. Late eruptive events?
Overspill wedge	Symmetrically lateral to the intra-crater cones.	High-to-low amplitude, discontinuous reflectors that together show a wedge shape.	Sharp contacts between upper and lower limits of the wedge-like structure. Fade with increasing distance from the vent zone.	Circular wedge-like.	Material that overspill the tephra ring and deposit parallel to basinal sediments immediately above the ring plain.

Tephra fallout carpet	Seismically unresolved, but probably distal to the funnel-like structure.	Seismically unresolved, but probably amalgamated with reflectors that represent basinal sediments.	Seismically unresolved, but probably sharp and parallel contact between volcaniclastics and Tokama Siltstone (wire-logs of the Resolution-1)	Seismically unresolved, but probably tabular.	Probably represent thin and tabular layers of tephra interbedded with basinal sediments.

The *lower diatreme* shows an unbedded and chaotic structure (Figure 71; Figure 72) below the PrErS, which can indicate that pre-magmatic sedimentary strata were deformed by fracturing of host rocks due to shockwaves, crater wall brecciation and blocks collapsing during large explosion (e.g. Kereszturi and Németh, 2013). Elsewhere, intra-diatreme faults formed by subsidence after the eruptions are a common process in this part of the diatreme (e.g. Lorenz, 1985; White and Ross, 2011; Kereszturi and Németh, 2013; Jones et al., 2017). The presence of feeder intrusions (plumbing-type 4 and 5) are likely to occur in the lower diatreme zone, supported by observation from outcrops elsewhere (e.g. Lorenz, 1985; White and Ross, 2011; Kereszturi and Németh, 2013), and by seismic images of the MVS showing sub-vertical to sub-horizontal moderate amplitude reflectors in association with disrupted pre-magmatic blocks (Figure 71; Figure 72). The *upper diatreme* (Figure 71; Figure 72) shows bedded structure, evidence of the presence of rock bodies deposited sub-horizontally to each other. The stratigraphic character of the upper diatreme suggest that this zone is likely composed of alternating layers of tephra sourced from late stage eruptions, together with possible slumps, slides, debris deposits and blocks collapsed from the diatreme walls that infill the top part to the diatreme (Figure 71). Similar stratigraphic relationship is observed in analogue diatremes (e.g. Lorenz, 1985; White and Ross, 2011; Kereszturi and Németh, 2013).

Laterally and symmetrical to the both sides of the diatreme, a distinctive parallel and continuous high amplitude reflector located immediately above PrErS is observed (Figure 71; Figure 72). Close to the vent, these reflectors are inclined at ca 20^{o}. Distal, reflectors become progressively sub-horizontal and parallel with basin strata reflectors. With increasing distance from the vent, their high amplitude and continuous character fades to become parallel, semi-continuous and moderate-to-low amplitude (this last, is the characteristic seismic facies of Tokama siltstone). It is possible to map the lateral extension of the high amplitude reflectors for ca 5 km from both sides of the diatreme, which suggests that these reflectors represent

material dispersed from the vent zone, possibly by high energy explosive eruptions. The inclined reflectors proximal to the diatreme are interpreted to correspond with the *tephra ring* of a maar volcano, likely formed by accumulation of tephra ejected as ballistic material during submarine eruptions. At its thickest part, this tephra ring may be as thick as 20 m. The lateral continuity of the tephra ring is represented by sub-horizontal reflectors, which we interpret to correspond with the *ring plain* of a maar volcano (Figure 71; Figure 72). In plain view, the ring plain of some volcanoes shows a semi-circular geometry with ca 10 km of lateral extent (Figure 56). The bedded diatreme is typically overlain by a dome- and cone-like structure (Figure 71; Figure 72), likely to represent material that accumulated inside the negative morphology limited by the internal boundaries of the tephra ring. Based on the convex upwards seismic facies of this zone, and in association with examples described in the literature (e.g. Lorenz, 1985; Kereszturi and Németh, 2013), we interpret this architectural element to correspond to *intra-crater cones* formed by accumulation of tephra, and maybe minor hyaloclastite and pillow-lava material formed during late stage eruptions.

Lateral to the intra-crater cone and overlaying the tephra and ring plains, we observe a characteristic seismic facies composed of discontinuous moderate amplitude reflectors, here referred to as the *overspill wedge*. This wedge has a maximum lateral extension of ca 7 km, and typical vertical heights of ca 30 m. Distal reflectors of the overspill wedge merge and fade with increasing distance from the eruptive centre (Figure 72). We interpret this architectural element to represent fragmented material that overspills the tephra ring by ballistics and other dispersion mechanisms related to submarine eruptive plumes (e.g. eruption-fed density currents; White, 2000). The overspill wedge may also contain minor pillow-lavas and hyaloclastite deposits (e.g. Kereszturi and Németh, 2013), interbedded to deposits from explosive submarine eruptions. However, we did not identify seismic facies that indicate lavas deposits in the overspill wedge. The *tephra fallout carpet* is an architectural elements seismically unresolved. The presence of this element is based on thin volcaniclastic layers interbedded with the Tokama Siltstone, recovered in Resolution-1. Studies of the deposits of submarine eruptions (e.g. Fiske et al., 1998; Bonadonna et al., 2002; White, 2000; Deardoff et al., 2011; Cas and Giordano, 2014), show that submarine eruptions can eject significant amount of tephra into the water column. This material can be transported in suspension and be deposited distal to the eruptive centre as thin and tabular layers of tephra.

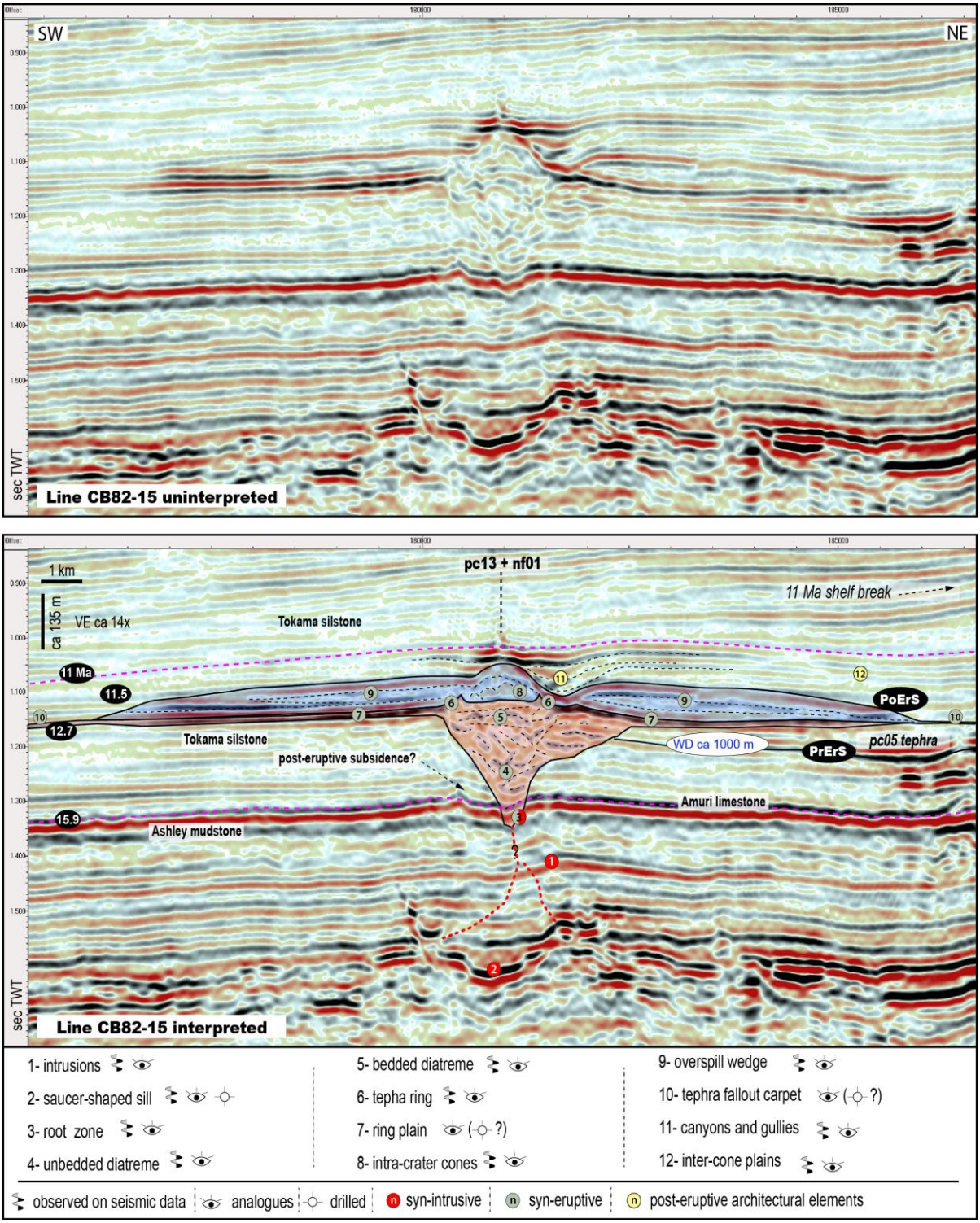

Figure 72: Uninterpreted (above) and interpreted (below) 2D seismic line showing the main architectural elements related to crater-type volcanoes in the MVS. Numbers in red circles are syn-intrusive architectural elements, in green syn-eruptive, and in yellow post-magmatic architectural elements. We observe that crater-type volcanoes present two distinctive morphologies related to at least two different eruptive-styles: lower part (in red) shows funnel-like excavation into PrErS and lateral high amplitude parallel reflectors, which we interpret to represent a submarine equivalent of a maar-diatreme volcano, and may be related to large subaqueous phreatomagmatic eruptions. Upper part (in blue) shows cone-like morphology and lateral semi-continuous reflectors in wedge-shape, which we interpreted as intra-crater volcanoes formed by late eruptive events, and associated material that overspills from the rim of the underlying maar-diatreme structure. WD is the interpreted approximate water-depth at the time of the formation of the volcanos.

Origin of the crater-type volcanoes in the MVS

Crater-type volcanoes of the MVS contain syn-eruptive architectural elements that show deep craters excavated into the PrErS horizon, and associated deposits that suggests substantial material dispersion laterally to these craters. Deep excavations into the PrErS requires significant energy and intense material fragmentation (e.g. Zimanowski et al., 1997). White and Valentine (2016) suggest that the funnel-like structure of maar-diatreme volcanoes, in association with dispersed lateral tephra deposits, may be one of the most direct evidence for dominant phreatomagmatic activity. In subaerial and shallow subaqueous environments, it is widely accepted that basaltic maar-diatremes result from phreatomagmatic eruptions (e.g. White and Valentine, 2016). Zimanowski and Büttner (2003) argue that subaqueous volcanic thermohydraulic explosions become increasingly improbable at water depths > 100 m, and practically impossible at water depths > 1000 m. However, Clague et al. (2000) inferred that phreatomagmatic eruptions at the Loihi seamount offshore Hawaii occurred at a minimum depth of 1356 m, which is approximately equivalent to the depth of the root zone of the volcanoes studied here. Some rock-types recovered from Resolution-1 well have textures that indicate intense material fragmentation (rocks composed of very-fine broken crystals and glassy shards with platy and cuspate shapes), and deposits that commonly contain limestone and sandstones lithics, potentially sourced from the root zone of the MVS diatremes (Figure 72 and Figure 48), which maybe represent of fallout material formed by submarine pyroclastic eruptions in the MVS.

Cas and Simmons (2018) suggest that subaqueous effusive eruptions can produce fallout deposits of ash size autoclastic vitric material, similar to typical deposits of subaqueous pyroclastic eruptions. This autoclastic process could explain the large (ca 5 km) seismically detected limits of our ring plain and overspill wedge architectural elements, without necessarily requiring large explosive eruptions, but cannot explain the pit craters excavated into the PrErS horizon. We consider an autoclastic explanation for the crater-type volcanos of the MVS implausible, as their morphology suggests high-energy mechanisms of fragmentation and dispersion of material (e.g. Lorenz, 1985; White, 2000; Kereszturi and Németh, 2013; White and Valentine, 2016). In addition, the ring plain and the overspill wedge elements observed in the MVS indicate that material was deposited symmetrically on both sides to the diatreme structure (Figure 9; Figure 10), with distal representative rock-types of

these architectural elements possibly recovered by the Resolution-1 well, containing textures that indicate intense material fragmentation (Figure 48). These observations together suggest that the crater-type volcanos in the MVS were likely formed by high-energy explosive eruptions, such as those triggered by phreatomagmatic processes. The geometry and spatial arrangement of the architectural elements in the crater-type volcanoes suggests they are likely to represent the submarine equivalent of maar-diatremes (funnel-like structure) and maybe tuff rings (basin-like structure), formed by high-energy explosive eruptions in a subaqueous environment around 1000 m deep.

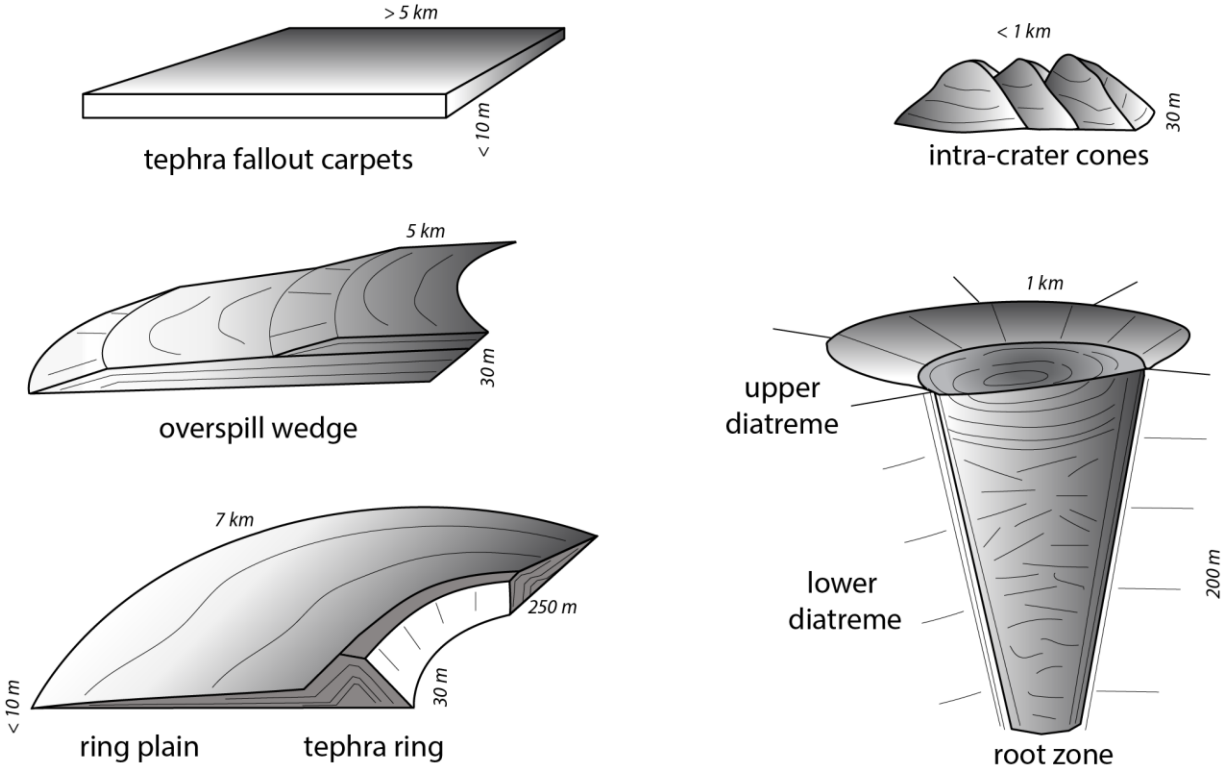

Figure 73: Three-dimensional representation of the main syn-eruptive architectural elements of crater-type volcanoes of the MFV and their average size. Each of these large-scale elements can be composed by sets of smaller-scale elements formed by the interplay of volcanism, external environments, and concomitant sedimentation.

Crater-type volcanoes: subaqueous equivalent of tuff cones.

In contrast to their counterpart crater-type volcanoes, MVS cone-type volcanoes are characterised in seismic imagery by a sequence of reflectors that pile-up close to the vent zone, forming convex upwards curvature of the PoErS above PrErS, and minor excavation into the pre-eruptive strata (Figure 74; Figure 75; Figure 76; Figure 77). This volcano-type typically occurs as isolated cones (exceptions are the overlapping edifices of pc02, pm01 and pm02;

Figure 70, type-5), ranging in average size from 1 to 3 km in diameter, and 100 to 300 m in height (oHm). Seismic data show that the sub-vent zone of this volcano-type (Figure 74) contains shallow high-amplitude reflectors that may represent intrusions related to plumbing-type 4 (Figure 70). Most MVS cone-type volcanoes appear to be fed by large sill intrusions related to plumbing-type 1 and 3. The exception is the overlapped volcanic cluster (Figure 70) that appears to be fed by plumbing-type 5, and does not show evidence that it was fed by a shallow (< 4 km) magmatic chamber.

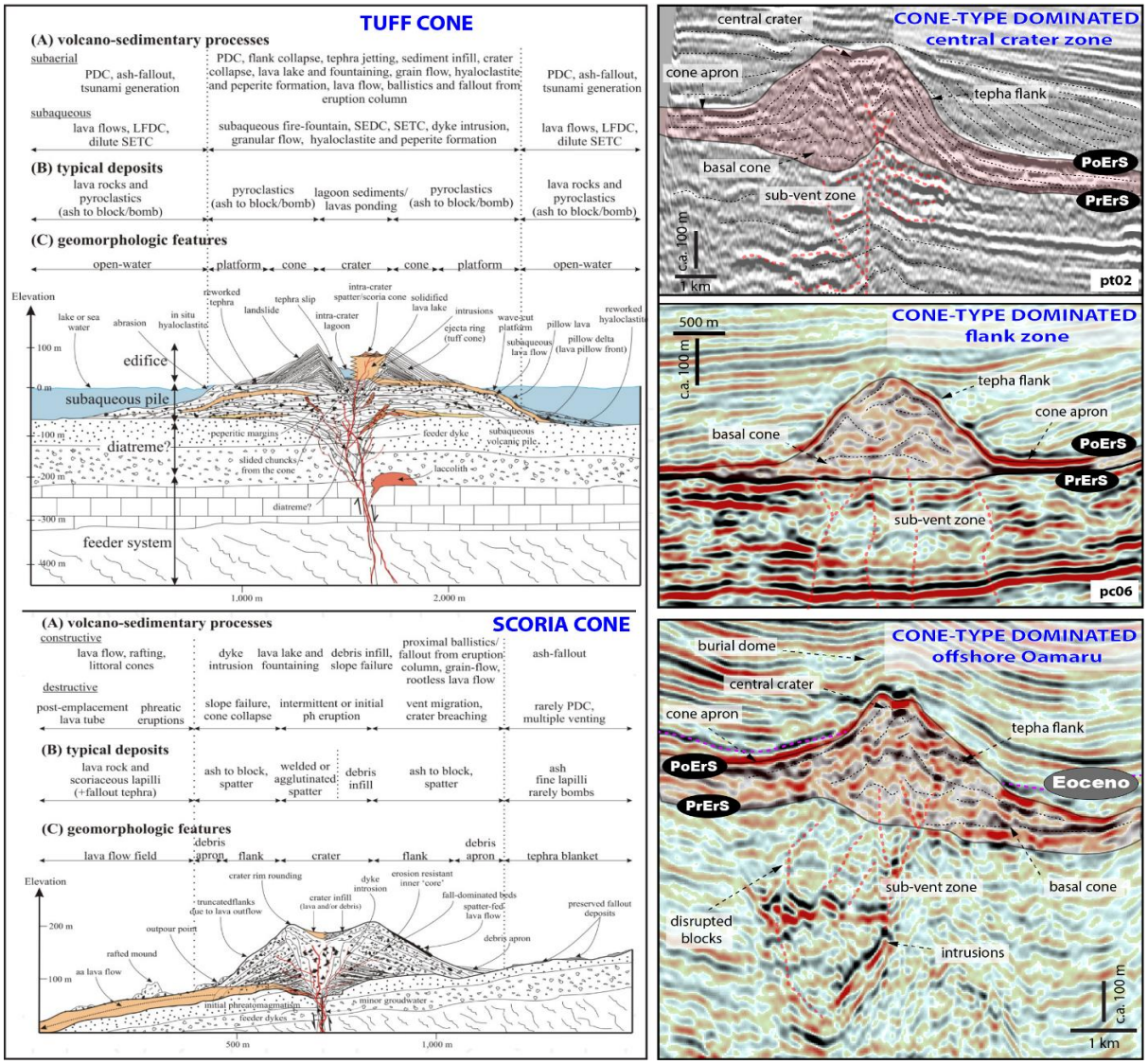

Figure 74: Images on the left-hand side show schematic cross-sections through tuff and scoria cones showing their typical volcano-sedimentary processes, deposits and morphology (from Kereszturi and Németh, 2013). Seismic images on the right-hand side show interpreted 2D lines of MVS crater-type volcanoes, and their large-scale architecture. The seismic section in the lower right-hand corner shows a buried submarine Eocene volcano 40 km offshore of Oamaru (Barrier et al., 2017), which we use as analogue for our interpretations.

The syn-eruptive architecture of the crater-type volcanoes of the MVS can be divided into five fundamental elements, based on distinctive seismic facies, and on surfaces that bound characteristic morphologies. As is the case for crater-type dominate volcanoes, each one of these five large-scale parts may contain individual or sets of cogenetic architectural elements (Figure 74; Figure 75; Figure 76; Figure 77). The main characteristics of the syn-eruptive architectural elements of this volcano-type are shown in Table 10.

Table 10: Main characteristics of the architectural elements of the cone-type dominate volcanoes formed during the constructional magmatic stage in the MVS.

Element	Location	Seismic facies	Bounding surfaces	Geometry	Indicative processes
Basal cone	Bottom of the cone-like structure.	Moderate to high amplitude sub-horizontal and parallel reflectors.	Sharp to gradational contact between internal sub-horizontal and parallel facies, from external seismic facies with inclined, disrupted or chaotic reflectors	Unsure, probably tabular.	Material piled-up near vent, sub-parallel to basinal sediments and above the PrErS.
Central crater or vent zone	Centre of the cone-like structure.	Typically transparent, but also show moderate to low amplitude, discontinuous, chaotic or parallel reflectors dipping inward the central crater.	Sharp to erosive contact between internal chaotic seismic facies from external facies typically bedded and inclined.	Probably cylindrical based in analogues.	Material disperse out of the crater zone. Chaotic deposits probably represent collapses of the crater walls, and deposition of intra-crater layers of tephra.
Tephra flank	Symmetrically lateral to the central crater.	Moderate to low amplitude, semi-continuous, parallel and inclined reflectors dipping outwards from the central crater zone.	Sharp to erosive contact between internal inclined and bedded seismic facies from external chaotic (towards the central crater) or sub-parallel seismic facies (towards the basin).	Conical.	Deposition of layered material near a vent zone and above the basal cone, or above PrErS.
Cone apron	Symmetrically lateral to the tephra flank.	Low to high amplitude, typically continuous and sub-parallel and sub-horizontal reflectors.	Sharp to gradational between bedded seismic facies that pinch with increasing distance from the eruptive centre.	Ring-like.	Deposition of material distal to a vent zone and above PrErS
Tephra fallout carpet	Seismically unresolved, but probably distal to the funnel-like structure.	Seismically unresolved, but probably amalgamated with reflectors that represent basinal sediments.	Seismically unresolved, but probably sharp and parallel contact between volcaniclastics and Tokama Siltstone (wire-logs of the Resolution-1)	Seismically unresolved, but probably tabular.	Probably represent thin and tabular layers of tephra interbedded with basinal sediments.

The *basal cone* is characterised by sub-horizontal and parallel reflectors of high to moderate amplitude that are located near the vent zone. This architectural element typically shows stacked high-amplitude reflectors, suggesting that the basal cone contains layers of relatively dense material, perhaps indicating the presence of deposits such as submarine lavas and hyaloclastites formed during the initial eruptive stages of the cone construction (Figure 70, type 5). However, it is also commonly observed that the geometries and seismic character of the basal cone is seismically similar to the tephra flank, comprising low amplitude reflectors (see further explanation for the formation of the tephra flank in this section), which may indicate deposition of layered tephra at this zone. Based on the presence of high amplitude reflectors cross cutting sub-horizontal reflectors (Figure 70; Figure 74), it is likely that the basal cone also contains minor shallow intrusions (our plumbing type-4), which are common in monogenetic volcanoes (e.g. Kereszturi and Németh, 2013).

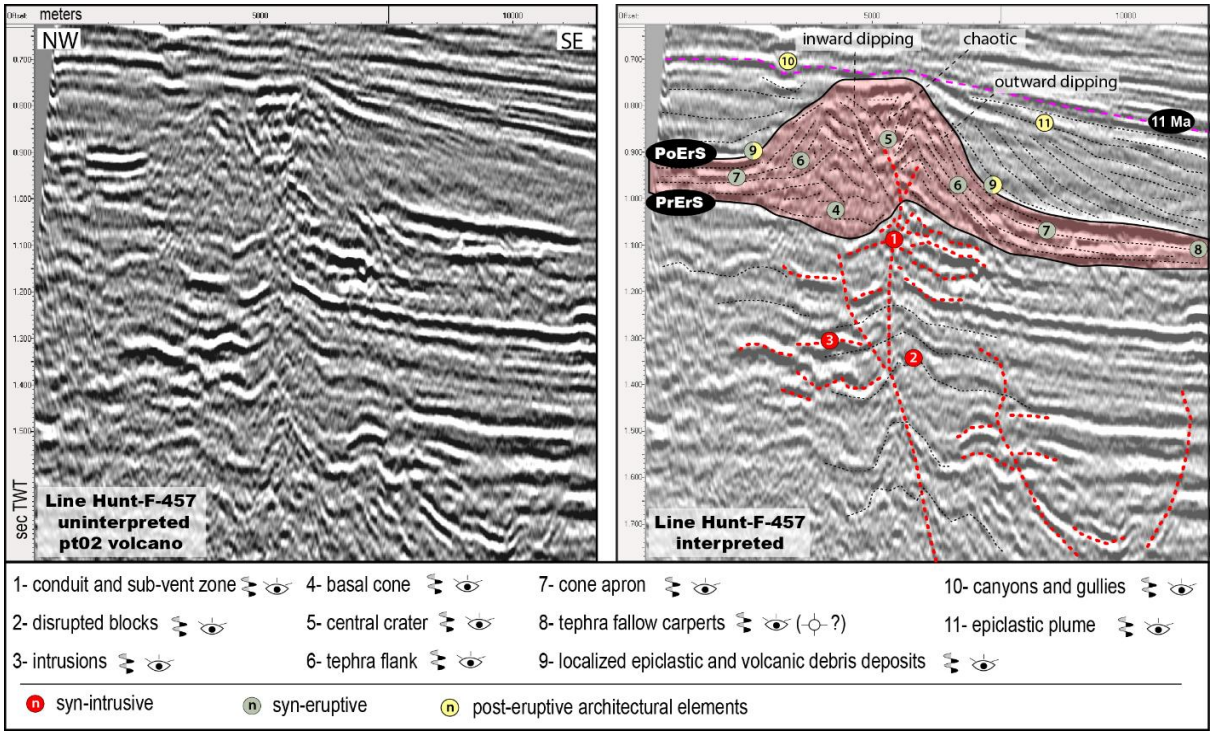

Figure 75: Uninterpreted (left) and interpreted (right) 2D seismic line showing the main architectural elements related to crater-type in the MVS. Numbers in red circles are syn-intrusive architectural elements, in green syn-eruptive, and in yellow post-magmatic architectural elements. We observe that crater-type volcanoes are mainly composed of a basal cone, a central crater, a tephra flank and a cone apron. These volcano-types produce upward convex morphologies between the PrErS and PoErS horizons, which we have interpreted to represent the submarine equivalents of tuff cones. Note that the central-crater show inward dipping reflectors while the tephra flank shows outward-dipping reflectors and minor excavation into the PrErS horizon.

The *central crater or vent zone* is characterised by disrupted, chaotic and layered reflectors dipping inward toward the centre of the cone structure (Figure 75; Figure 76; Figure 78), evidence that deposits has infilled a negative shallow depression at this location. This architectural element is typically located above seismic facies (i.e. disrupted pre-magmatic reflectors, high amplitude reflectors cross-cutting enclosing strata) that indicate the presence of magmatic conduits and intrusive bodies (e.g. McLean et al., 2017; Bischoff et al., 2017; Infante-Paez and Marfurt, 2017; Morley, 2018). The structure of the central crater shows minor excavation into the PrErS horizon, which suggest that the eruptions in cone-type volcanoes were much less damaging to the to host rocks beneath the vent, in contrast with the deep diatremes observed in the crater-type volcanoes (e.g. White and Valentine, 2016). We interpret this architectural element to be formed by explosive eruptions and associated jets of tephra, which create space for subsequence deposition of chaotic and amalgamated layers of tephra inward-dipping into the central crater. Observations in ancient outcropping submarine monogenetic volcanoes of Waiareka-Deborah offshore Oamaru, South Island of New Zealand (e.g. Cas et al., 1989; Corcoran and Moore, 2009; Moorhouse; 2015) show that the crater zone of those volcanoes typically contain massive, chaotic, to amalgamated deposits of lapilli-tuff to tuff-breccia, formed by tephra jets and ballistics during explosive eruptions, and deposits of tephra dipping inwards in the crater zone (Figure 76A, B and C). Deposits of the central crater of the Waiareka-Deborah volcanoes have ben reworked by gravitational processes (Corcoran and Moore, 2009).

The *tephra flank* of the volcanoes in the MVS is characterised by inclined, low-to-moderate amplitude reflectors dipping outward from the centre of the cone-like structure (Figure 74; Figure 75). We interpret the flanks of MVF cone-type volcanoes to predominately contain fragmented material that originated from submarine pyroclastic eruptions, rather than subaqueous lava deposits. This interpretation is supported by: i) a clear lateral relationship of the tephra flank with a crater (vent) zone that suggests explosive activity, ii) seismic facies showing low-to-moderate amplitude[8], semi-continuous, parallel and inclined reflectors, symmetrically dipping away from the vent zone[9], iii) rock-types collected in the Resolution-1

[8] Typically, lava deposits show high-amplitude continuous reflectors. Volcaniclastic material usually show moderate amplitude (e.g. Planke et al., 1999; Reynolds et al., 2017).

[9] This stratal relationships are commonly observed for deposits formed by explosive eruptions in both subaerial and submarine environments (Cas et al., 1989; White, 1996; White, 2000; Kereszturi and Németh, 2013),

well that evidence explosivity[10] (e.g. peloidal fragments enveloped by palagonite films, armoured lapilli?, broken crystals, relics of bubble walls, and high vesiculated rocks; see section 4.5.1.5 for more details) in the MVS. However, some minor lavas and hyaloclastite deposits are commonly observed in explosive monogenetic volcanoes (e.g. Kereszturi and Németh, 2013), thus, these deposits (and maybe type-4 intrusions) are expected to occur in the tephra flank, evidenced by localized and isolated high-amplitude reflectors (pm02 in Figure 38). Observations from outcrops in the Waiareka-Deborah volcanoes suggest that their flanks were constructed by multiple explosive eruptions with minor interruptions, in which dispersion of material was induced by mechanisms such as tephra jets, ballistics, grain flow, debris remobilization, and eruption-fed density currents (e.g. Cas et al., 1989; Corcoran and Moore, 2009; Kaulfuss et al., 2012; Moorhouse; 2015). Deposits on the flanks of those volcanoes are typically tabular and composed of thin-bedded layers of tephra dipping away from the vent zone (Figure 76A, C and D). Eruption-fed density currents usually form well-sorted and thinly-bedded pyroclastic deposits that show similarities to the Td and Te turbidite facies of the Bouma sequence (e.g. Cas et al., 1989; White, 1996; Corcoran and Moore, 2009; White, 2000; Di Capua and Groppelli, 2016).

The *cone apron* architectural element is characterised by sub-horizontal and parallel reflectors that pinch and amalgamate with basin reflectors with progressive distance from the cone structure (Figure 74; Figure 75). The Resolution-1 well likely penetrates the distal cone apron of pc14 at depths of 1103.5 to 1114 m (see discussion in sections 4.4.2 and 4.5.1.5 for more details). We interpreted the cone apron to contain fine-grained layers of tephra transported by subaqueous eruption plumes, likely interbedded with reworked material from cone collapses and degradation, a phenomena commonly observed in volcanoes elsewhere (e.g. White, 1996; Kereszturi and Németh, 2013; Pope et al., 2018). This architectural element likely contains minor subaqueous lavas that overspill from the crater rim (and possible pereritic material associated with invasive lavas and/or shallow type-4 intrusions; e.g. Planke et al., 2017), as indicated by the localized high-amplitude reflectors that occur in association with this element (right flank of pt01 in Figure 38). The interpretation of 3D seismic data of

[10] As explained in Chapter 4, these textures alone are not diagnose for explosivity, but could also represent submarine auto-brecciation (e.g. White and Valentine, 2016; Cas and Simmons, 2018). Because of this, our interpretations are made in association with the seismic aspects (e.g. morphology, seismic facies) of the volcano-types.

lava-flows associated with submarine monogenetic volcanism along the southern Australian margin shows that these flows could extend for more than 34 km in length (Reynolds et al., 2017).

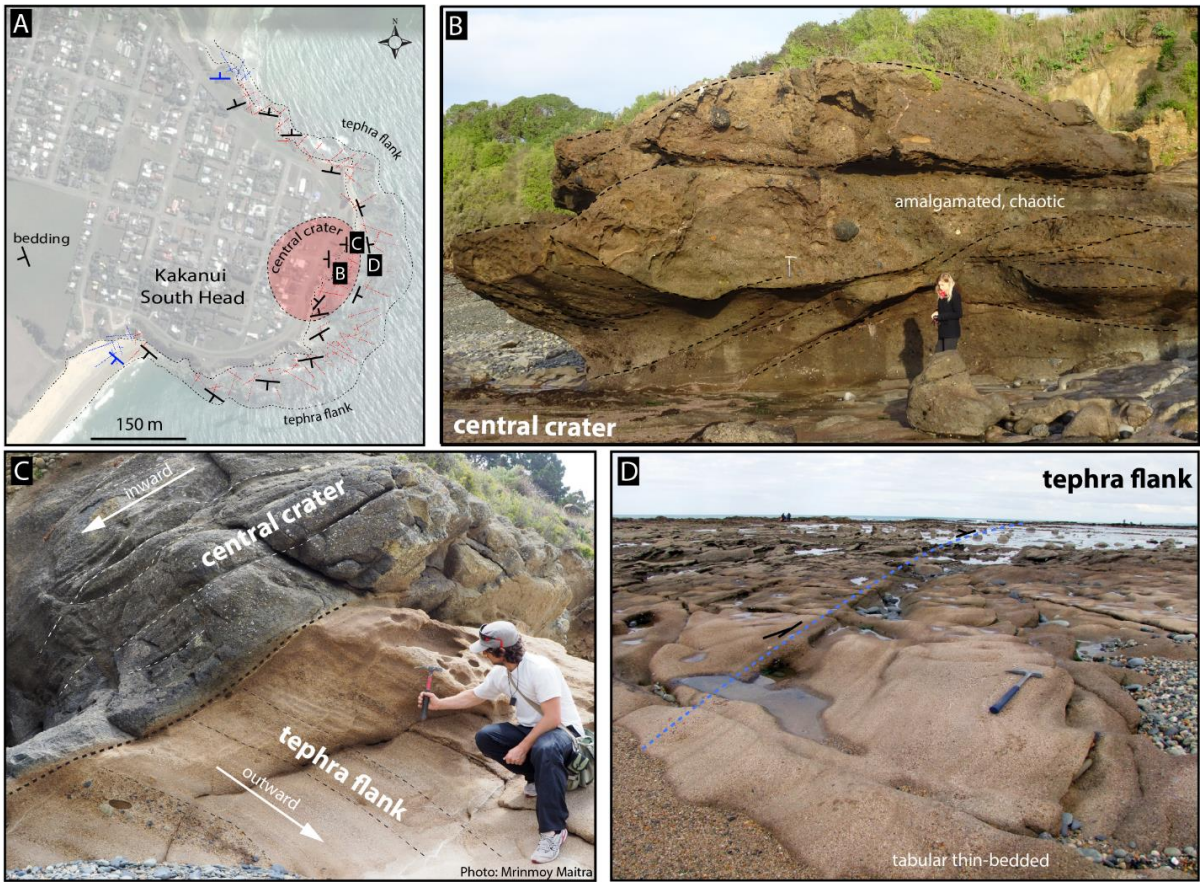

Figure 76: Photographs of potential analogue for MVS syn-eruptive architectural elements outcropping in Kakanui South Head submarine volcanic edifice, near Oamaru, South Island of New Zealand. A) Map showing the location of the vent and flanks of the cone. B) Massive, chaotic, to amalgamated intra-crater lapilli-tuff to tuff-breccia interpreted to be deposited by tephra jets, ballistic and debris flow of material remobilized into the central crater (Corcoran and Moore, 2009; Moorhouse; 2015). C) Angular contact between amalgamated beds inward dipping towards the central crater, and tabular layers of tephra outward-dipping towards the flanks of the edifice. D) Thin-bedded, tabular, semi-circular layers of lapilli-tuff formed by low-volume tephra jetting and eruption-fed density currents deposited at the flanks of the volcanic edifice (Corcoran and Moore, 2009; Kaulfuss et al., 2012).

The *tephra fallout carpet* of cone-type volcanos (like their counterpart crater-type volcanoes) is typically seismically unresolved and based on studies elsewhere (e.g. Fiske et al., 1998; Bonadonna et al., 2002; White, 2000; Deardoff et al., 2011; Cas and Giordano, 2014). Volcaniclastic rocks interbedded with the Tokama Siltstone recovered in the Resolution-1 well from 1114 to 1200 m depth may represent this element in cone-type volcanos of the MVS (see discussion in sections 4.4.2 and 4.5.1.5 for more details). Submarine eruption plumes (and also subaerial pyroclastic density currents entering the water) can introduce pyroclasts

and rock fragments into the water column, while residual buoyant material can remain suspended and be transported by oceanic currents (e.g. Fiske et al., 1998; Bonadonna et al., 2002; White, 2000; Deardoff et al., 2011; Cas and Giordano, 2014; Di Capua and Groppelli, 2016). Rafts of highly vesiculated pumice can travel long distances carried out by currents (Rotella et al., 2013; Cas and Giordano, 2014; Cas and Simmons, 2018). When saturated in water, these fragments sink and can form deposits with size varying from ash to blocks (e.g. Fiske et al., 1998).

Origin of the crater-type volcanoes in the MVS

MVS crater-type volcanoes contain syn-eruptive architectural elements that shows reflectors pilling-up above the PrErS horizon, next to an interpreted vent zone with little or no excavations into the PrErS horizon. White and Valentine (2016) state that the vent structure and associated ejecta deposits may be the best evidence that characterises past eruptive processes in monogenetic volcanoes. These authors infer that volcanoes dominated by purely magmatic volatile-driven processes have discrete explosions when compared with those dominated by phreatomagmatic activity, a process that is much less damaging to host rocks beneath the vent. In mafic systems that form cone-type volcanoes (e.g. scoria cones), explosions are typically manifested as Strombolian and Vulcanian-types (e.g. Kereszturi and Németh, 2013; White and Valentine, 2016). However, crater-type volcanoes (e.g. tuff cones) can also form by phreatomagmatic processes (e.g. Cas et al., 1989; White, 1996; White, 2000). In addition, the final morphology of a monogenetic volcano does not necessarily represent a single eruptive-style, but more commonly these morphologies result from simple or complex edifice growing mechanisms (Kereszturi and Németh, 2013), which makes their characterisation difficult based exclusively on morphological parameters. However, the vent structure of cone-type volcanoes of the MVS shows minor excavation into the PrErS horizon, which suggests that the effects of eruptions on the host rocks are minimal, when compared to those of crater-type volcanoes. Further, the predominance of inclined, low-to-moderate amplitude reflectors dipping symmetrically outward from the centre of the cone-like structure suggests that the flanks of the cone-type volcanoes are mainly comprised of fragmented material, probably (radially?) ejected by pyroclastic eruptions rather than the deposits of effusive eruptions. The predominant slope angles (< 16^{o} in inclination) of the cone-type volcanoes in MVS, in association with the textures (e.g. possible armoured lapilli and ash

aggregates) recovered in Resolution-1, and the widespread (up to 6 km) seismically detected extension of the tephra flank and cone apron together, suggests that this volcano-type is likely to represent a submarine equivalent of a tuff-cone. However, we do not discard the possibility of the occurrence of spatter cones and pillow mounds in the MVS, which could be verified with additional high quality 3D seismic data and/or wells that drill into these volcanoes proximal to their vents.

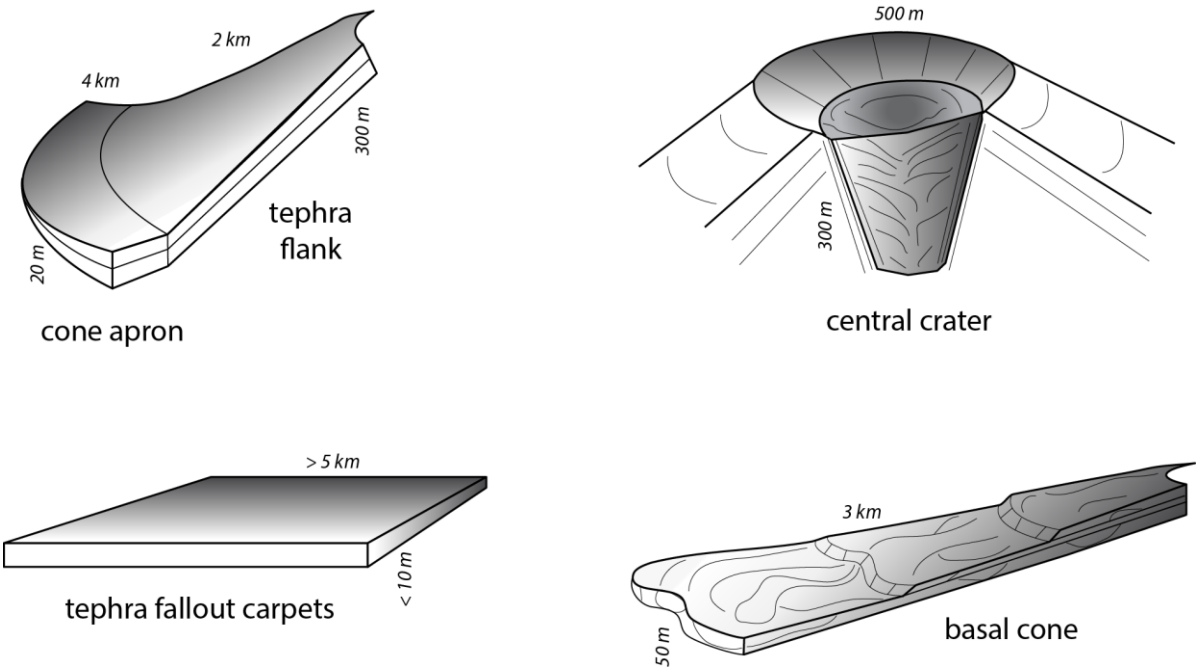

Figure 77: Three-dimensional representation of the main syn-eruptive architectural elements of crater-type volcanoes of the MFV and their average size. Each of these large scale elements can contain sets of smaller-scale architectural elements formed by the interplay of volcanism and concomitant sedimentation.

In addition, we contrast the seismic morphology and architectural elements of potential volcanoes buried in Eocene strata in the Canterbury Basin, ca 40 km offshore of Oamaru (e.g. Barrier et al., 2017) with the volcanoes of MVS (Figure 74). These buried Eocene volcanoes are likely part to the Waiareka-Deborah Volcanic Field, and show similarities with the buried volcanoes of the MVS. As in MVS, the sub-vent zone of these volcanoes contains disrupted blocks and high amplitude reflectors that cross-cut pre-eruptive strata, which likely represent intrusive rocks and magmatic conduits. Above the conduit zone, the presence of chaotic seismic facies indicates the location of the central crater. Laterally to the central crater, symmetrical inclined reflectors outward-dipping represent the tephra flank. Distal to the tephra flank, these reflectors become sub-horizontal and parallel to basin strata, and produce the seismic-equivalent expression of the cone apron. At the top of the edifice, reflectors have

a domed configuration, which is commonly interpreted as the product of differential compaction (e.g. Planke et al., 2000; Bischoff et al., 2017). The above described morphologic and spatial relationships could indicate that crater-type volcanoes of the MVF experience similar fragmentation and dispersion processes as those from the Waiareka-Deborah volcanic field, those interpreted to be formed by phreatomagmatic eruptions (e.g. Cas et al., 1989; Corcoran and Moore, 2009; White and Ross, 2011; Jackson, 2012; Kaulfuss et al., 2012).

Eruption-related sedimentary architectural elements

Sedimentological and volcanological processes observed on modern volcanoes (e.g. White, 1991; Cas and Wright, 1992; Chadweck et al., 2012; Kereszturi and Németh, 2013; Pope et al., 2018) suggest that the syn-eruptive interval of the MVS may comprise sedimentary deposits triggered by simultaneous eruptions, together with primary volcanic eruptive deposits. Processes related to the eruptions such as earthquake shockwave, explosions and magmatic inflation are potential triggers for debris flows, submarine landslides and cone-sector collapses (e.g. submarine landslides triggered by the 2009 eruption at NW Rota-1 volcano, Mariana arc; Chadweck et al., 2012). Tephra material can be reworked during or immediately after eruptions by mechanism such as submarine currents, waves and tsunamis (e.g. Kereszturi and Németh, 2013). Based on the available 2D seismic data and limited number of wells, distinguishing eruptive volcanic deposits from eruption-related sedimentary deposits, or from resedimented epiclastic deposits is not always possible. We tentatively infer five settings (Figure 65; Figure 71; Figure 74; Figure 78) in which distinctive sets of eruption-related sedimentary architectural elements can form, based on seismic facies (e.g. chaotic reflectors, sediment waves) that could indicate reworking of parts of the volcanic edifices during eruptions.

- (1 and 2) the crater zone of both volcano types;
- (3) the flanks of crater-type volcanoes;
- (4) the tephra ring of crater-type volcanoes;
- (5) the cone apron of cone-type volcanoes.

Seismic images and analogues elsewhere suggest that the crater zone of MVS volcanoes may contain sedimentary deposits controlled by gravitational flows and other types of mass transport deposits that infill the space created by explosions and by ground collapses during

(and immediately after) eruptions. Common sedimentary facies in the crater zone may include coarse-grained, massive, chaotic and amalgamated deposits formed by tephra reworking and slip into the crater (Figure 76 B and C), and by slide and slump blocks from the crater walls (e.g. White and Ross, 2011; Kereszturi and Németh, 2013; White and Valentine, 2016). On the flanks of cone-type and along the tephra ring of crater-type volcanoes, material reworking by currents and mass-wasting are important syn (and post) eruptive process (e.g. Cas et al., 1989; Fiske et al., 1998; Corcoran and Moore, 2008; Pope et al., 2018). On the cone apron of pc14 (Figure 78), seismic images show a characteristic facies that resembles sediment waves occurring between the PrErS and PoErS horizons, which may represent syn-eruptive submarine landslides such as those reported by Pope et al. (2018).

5.4.1.3 Inter-eruptive architectural elements

Monogenetic volcanic fields are characterised by a cluster of dispersed and isolated volcanoes usually formed by one eruptive cycle with minor interruptions (e.g. Kereszturi and Németh, 2013; Silva and Lindsay, 2015). Individual volcanoes are typically diachronous with one another, and have an active life of years to centuries (e.g. Silva and Lindsay, 2015), and hundreds of thousands to a few million years for the complete volcanic field (e.g. Connor and Hill, 1995; Hintz, 2008; Condit, 2010; Kiyosugi et al., 2010 apud Kiyosugi, 2012).

In our volcano-stratigraphic model (Figure 63; Figure 65), inter-eruptive architectural elements can be formed in association with volcanoes that have finished their eruptive cycle, but may start to degrade and interact with basin sedimentation while volcanism is still active in the MVS. In contrast to polygenetic volcanoes, for where syn-and inter-eruptive deposits are piled-up and interbedded close to a single eruptive centre, in monogenetic fields, these inter-eruptive sedimentary deposits can by identified by the presence of sedimentary deposits (epiclastic or non-volcanogenic) interbedded with primary volcanic deposits erupted from different vents. In MVS, these inter-eruptive architectural elements are represented by sedimentary rocks of the Tokama siltstone interbedded with volcaniclastics that likely were erupted from different vents (e.g. Figure 78). Other inter-eruptive deposits related to mass transport and erosion of inactive volcanoes are likely to occur in MVS, however, as mentioned in the previous sub-chapter, we cannot separate these rock units from syn-eruptive sedimentary deposits, due to limitations in the seismic resolution of our dataset.

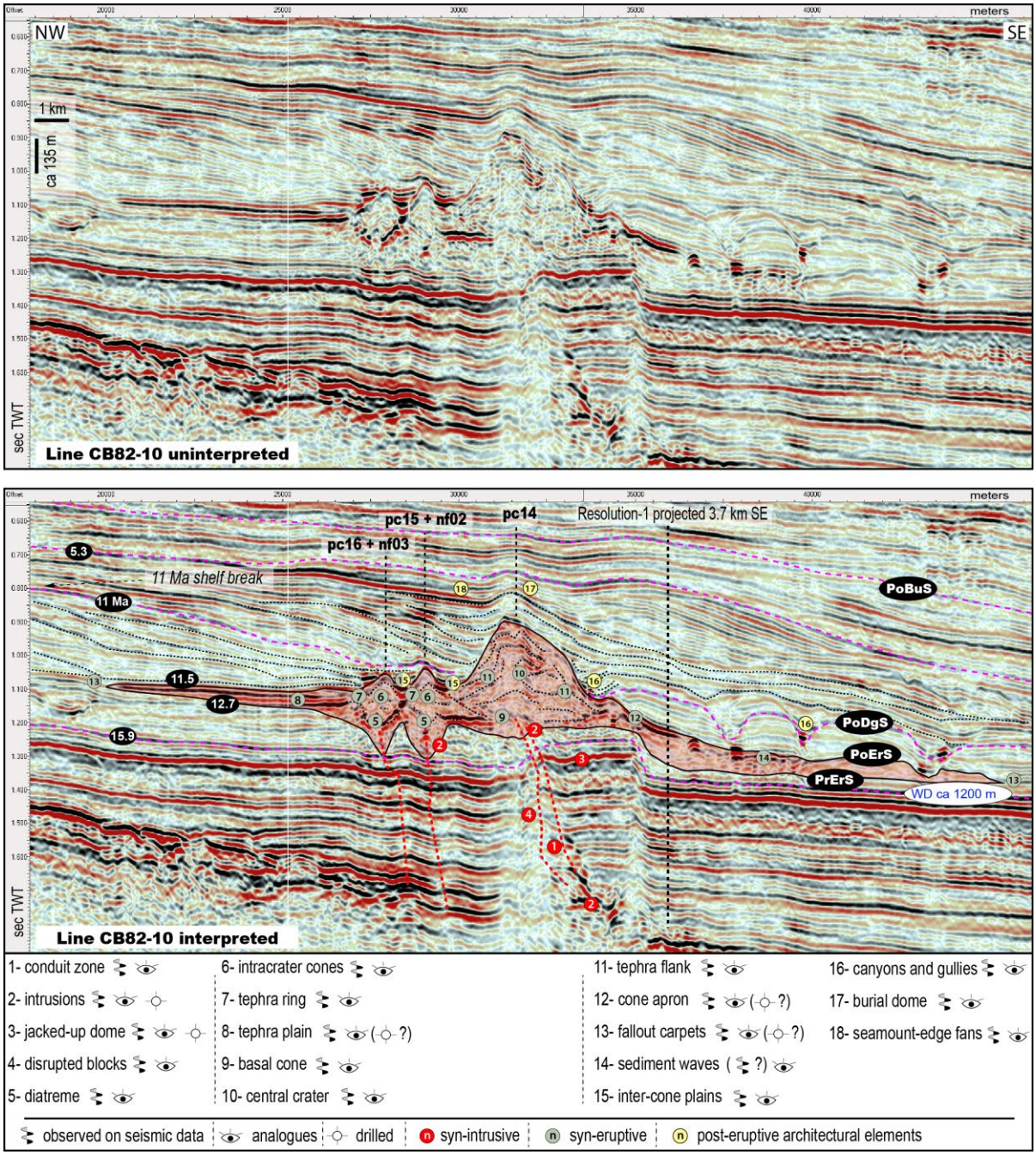

Figure 78: Uninterpreted (above) and interpreted (below) 2D seismic line showing the main architectural elements related to cone-type volcanoes in the MVS volcanoes. Numbers in red dots are syn-intrusive architectural elements, in green syn-eruptive, and in yellow post-magmatic architectural elements. Based on seismic stratigraphic interpretation, the lower sequence of volcaniclastics recovered in Resolution-1 was probably sourced from volcanoes NW or W of the well (likely nf02 and nf03). Tuffs from -1103 to -1110 m depth were likely vented from pc14. WD is the interpreted approximate water depth at the time of the formation of these volcanoes.

5.4.2 Post-Magmatic Sequence

After the magmatic activity in the MVS had ceased at ca 11.5 Ma, the submarine volcanic morphology had a strong impact on the sedimentation patterns of the study area. We divide

the post-magmatic sequence into degradational and burial stages. Each stage is marked by different processes of erosion and burial of the volcanic edifices, which control the formation and distribution of MVS post-magmatic architectural elements.

5.4.2.1 Degradational stage: rate of erosion > rate of burial

The degradational stage is marked by high rates of erosion of the volcanic edifices. In the MVS, we place the PoDgS coincident with the lM unconformity (Figure 65), because this surface represents the last significant event that eroded the volcanic edifices (see section 4.6.2 for more details). The architectural elements of this stage include canyons, gullies, localized epiclastic deposits and contemporaneous non-volcanogenic sedimentary deposits impacted by the presence of the volcanoes. Canyons and gullies are usually associated with the lM unconformity, varying in size from < 100 m to 1100 m wide and present internal channelized deposits up to ca 175 m thick (Figure 78; Figure 79). Channels are narrow towards shallow waters and wider and more deeply incised at the slope/abyssal interface, sometimes occurring stacked at the base of the tephra flank and cone apron of crater-type volcanoes (Figure 78; Figure 79). Canyon erosion can removes material from the volcano flanks, which may cause instability and collapse of parts of the cone, forming localized small size debris deposits (Figure 65). However, if these deposits occur in the MVS they are seismically unresolved with the available data. Between the cones, a characteristic seismic facies is observed, comprising of horizontal and parallel continuous reflectors, here referred to as inter-cone plains (Figure 78; Figure 79). The seismic facies of the inter-cone plains are similar (moderate amplitude, semi-continuous and parallel reflectors) to those where the well Resolution-1 recovered fine-grained sedimentary rocks of the Tokama siltstone. This seismic character suggests that the inter-cone plains were mostly formed by non-volcanogenic sedimentary strata confined between volcanic edifices, however, minor epiclastic deposits may occur next to the flanks of the volcanoes.

Volcanoes with flattened tops concordant with the lM unconformity typically show reflectors downlapping from the edifice onto the basin floor, which suggests that these volcanoes provide a local source of epiclastic sediments (Figure 65). Seismic attribute analysis shows that these deposits likely contain material eroded from the volcanoes (Figure 79). This degradational seismic facies only occurs in association with volcanoes > 200 oHm located

proximal to the 11 Ma shelf-break position. We interpret this facies to represent a plume of epiclastic sediments eroded from volcanoes that were emergent and/or eroded in a shallow submarine environment by the action of waves and shallow currents. The epiclastic plume is deposited parallel to the direction of the prograding clinoforms, with maximum seismically detected horizontal and vertical dimensions of up to 3 km and 70 m respectively, and probably represent sediments deposited next to extinct volcanic islands. Similar seismic facies are evident in the Vulcan-3D, located in the offshore Taranaki Basin (Bischoff, unpublished data 2018).

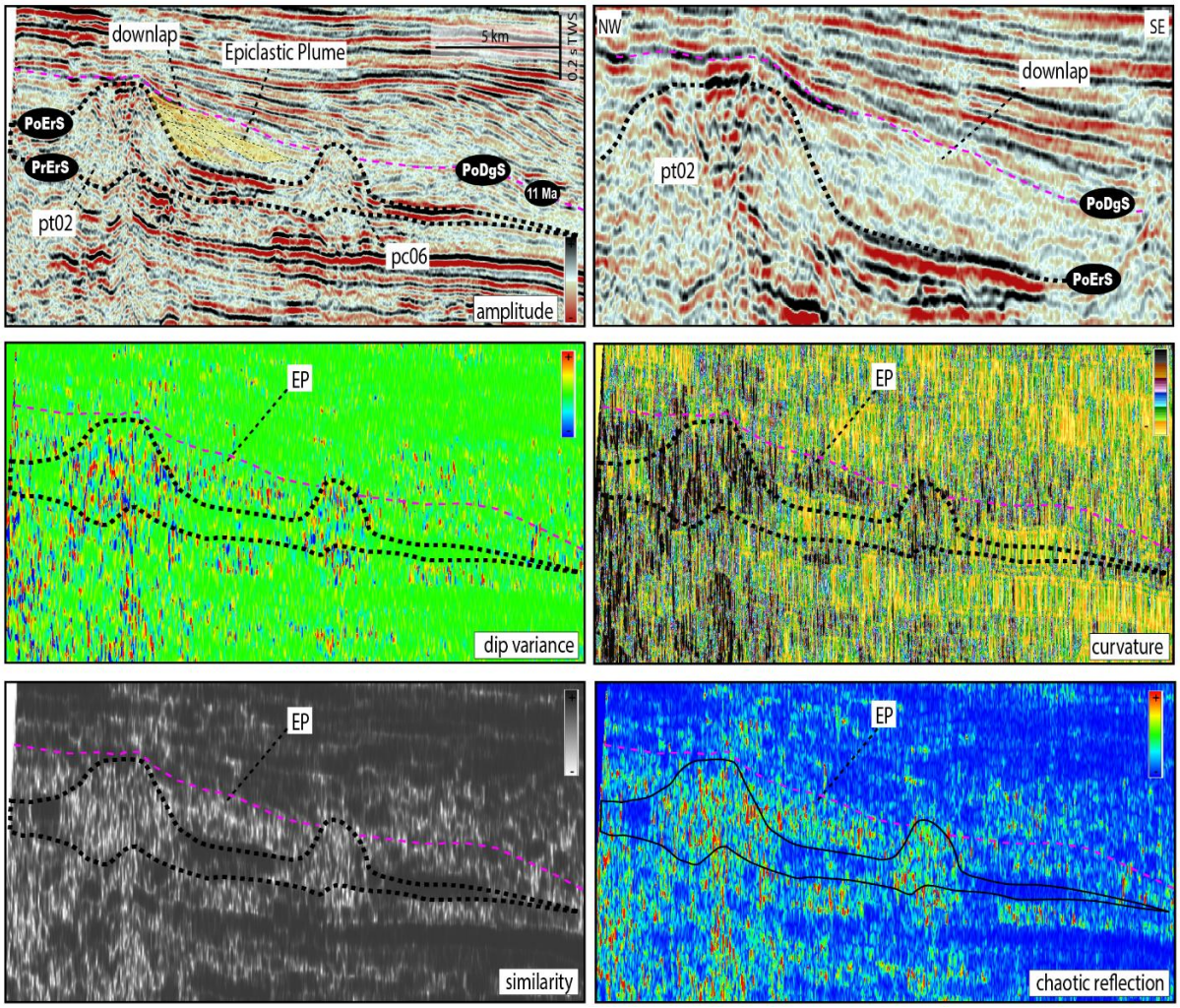

Figure 79: Seismic attribute analysis of pt02 and pc06 volcanoes. Note that the attributes show similarity between the internal and external parts of pt02, which we interpreted as a plume of sediments deposited after erosion of extinct volcanic islands during the degradational stage.

5.4.2.2 *Burial stage: rate of erosion < rate of burial*

In seismic imagery, the burial stage is characterised by facies showing evidence that the volcanic edifies impacted local sedimentation for a long time after these structures were buried. The burial stage is marked by high rates of burial and little or non-degradation of the volcanic edifices that remained unburied after the lM unconformity (i.e. PoDgS). Seismic reflectors above 11 cone-dominated volcanoes display a domal structure, here referred to as burial dome, suggesting the presence of a persistent bathymetric high after these volcanoes were buried. The processes that resulted in the production of the burial dome likely include differential compaction (e.g. Planke et al, 2005; Bischoff et al., 2017; Holford et al., 2017). Because the impact of buried volcanoes in the basin architecture varies from one volcano to another, we place the PoBuS according to observations from pc14, which shows that the edifice impacted basin sedimentation until at least the Opoitian (5.3 to 3.7 Ma), at least ca 6 Ma after volcanism in the MVS has ceased, and ca 1 Ma after pc14 was completely buried at ca 5 Ma. This is evidenced by the canyons scars located on the edges of the burial dome above pc14 (Figure 78). Seismic images of the MVS show that the presence of peripheral canyons (i.e. around the margins of the burial domes) are likely to be associated with the deposition of fans up to 2 km wide, which we refer to as seamount-edge fans (Figure 78). Fans such as these are well imaged from 3D seismic data over the buried Kora Volcano, offshore of Taranaki Basin (Bischoff et al., 2017). The processes that control the deposition of these fans remains poorly understood, but are likely either to involve erosion around the burial dome due to local formation of a hard seafloor substrate associated with the dome structure, or could be related to carbonate deposits at the top of the domes.

5.5 Conclusions

Reconstruction of the architecture of the Maahunui Volcanic System enables us to understand how igneous and sedimentary architectural elements interact and are distributed in time and space, due to the emplacement of magma, construction of a volcanic sub-sea morphology, degradation and burial of a monogenetic volcanic field in a sedimentary basin. The MVS plumbing system comprises mainly saucer-shaped sills, sills and dike swarms and minor laccoliths, distributed systematically into five plumbing-types, which have been characterised according to their level of emplacement and spatial relationship to each other,

and to host sedimentary strata. Saucer-sills emplaced at ca 1000 m depth in paralic to marine sedimentary strata are likely to have fed many MVS eruptive vents. The extrusive part of the volcanic field was erupted entirely in a deep marine setting (ca 1000 m water depth) and contains at least 31 submarine equivalents to crater-type (i.e. maar-diatreme volcanoes), as well as crater-type volcanoes (i.e. tuff cones). Crater-type volcanoes have 8 main syn-eruptive architectural elements: root zone, lower and upper diatreme, tephra ring and tephra plain, intra-crater cones, overspill wedge and tephra fallow carpets. Crater-type volcanoes have five main syn-eruptive architectural elements: basal cone, central crater, tephra flank, cone apron and tephra fallout carpets. Each of these elements have been formed by a combination of eruptive and associated sedimentary deposits, with minor and localized intrusions. After volcanism ceased, processes of degradation and burial of the volcanic edifies strongly impacted local sedimentation for at least ca 6 Ma after the volcanoes ceased to erupt, and ca 1 Ma after they were completely buried. Degradation and burial of the volcanic edifices of MVS produced five main sedimentary architectural elements (i.e. inter-cone plains, epiclastic plumes, canyons and gullies, burial domes and seamount-edge fans). Understanding the relationship of these diverse architectural elements is important to assess the risks, and to improve the likelihood of finding commercially viable geoenergy resources in association with buried and active monogenetic volcanic systems (which is presented in the Chapter 6).

5.6 References

Allen, J. R. L., 1983, Studies in Fluviatile Sedimentation: Bars, Bar-Complexes and Sandstone Sheets (Low-Sinuosity Braided Streams) in the Brownstones (L. Devonian), Welsh Borders: Sedimentary Geology, 33 (4): 237–93. doi:10.1016/0037-0738(83)90076-3.

Barrier, A., A. Nicol, A. P. Bischoff., 2017, Volcanism Occurrences in the Canterbury Basin, New Zealand and Implication for Petroleum Exploration. In AAPG GTW Influence of Volcanism and Associated Magmatic Processes on Petroleum Systems. Conference, Oamaru New Zealand.

Bischoff, A. P., A. Nicol, M. Beggs., 2017, Stratigraphy of architectural elements in a buried volcanic system and implications for hydrocarbon exploration: Interpretation, doi:10.1190/INT-2016-0201.1.

Blanke, S. J., 2010, “Saucer Sills” of the Offshore Canterbury Basin: GNS Publication, doi:10.1177/0094306114545742f.

Bonadonna, C., G. C. Mayberry, E. S. Calder, R. S. J. Sparks, C. Choux, P. Jackson, A. M. Lejeune, S. C. Loughlin, G. E. Norton, W. I. Rose, G. Ryan, S. R. Young., 2002, Tephra fallout in the eruption of Soufrière Hills Volcano, Montserrat: Geological Society, London, Memoirs, doi:10.1144/GSL.MEM.2002.021.01.22.

Borghi, L., 2000, Visão geral da análise de fácies do ponto de vista da arquitetura deposicional. Boletim do Museu Nacional. Nova Série Geologia, Rio de Janeiro, v. 53, n.58, p. 1-26.

Clague, D., R. Batiza., J.W. Head., A. Davis.,2000, Pyroclastic and Hydroclastic Deposits on Loihi Seamount, Hawaii, in Explosive Subaqueous Volcanism, edited by J.D.L. White, J.L. Smellie, and D.A. Clague, American Geophysical Union, Washington D.C., 200. Bulletin of Volcanology. doi.org/10.1029/140GM05.

Cas, R. A. F., G. Giordano., 2014, Submarine volcanism: A review of the constraints, processes and products, and relevance to the Cabo de Gata volcanic succession: doi:10.3301/IJG.2014.46.

Cas, R. A. F., J. V. Wright., 1993, Volcanic Successions: Modern and Ancient - A Geological Approach to Processes, Products and Successions. Chapman and Hall, UK. doi:10.1007/978-0-412-44640-5.

Cas, R. A. F., Landis, C. A., and Fordyce, R. E., 1989, A monogenetic, Surtla-type, Surtseyan volcano from the Eocene-Oligocene Waiareka-Deborah volcanics, Otago, New Zealand: A model: Bulletin of Volcanology, v. 51, no. 4, p. 281-298.

Cas, R. A. F., J. M. Simmons., 2018, Why Deep-Water Eruptions Are So Different From Subaerial Eruptions: Frontiers in Earth Science, v. 6, p. 198, doi:10.3389/feart.2018.00198.

Catuneanu, O., 2006, Principles of Sequence Stratigraphy. Changes, 375. doi:10.5860/Choice.44-4462.

Catuneanu, O., Abreu, V., Bhattacharya, J.P., Blum, M.D., Dalrymple, R.W., Eriksson, P.G.,Fielding, C.R., Fisher, W.L., Galloway, W.E., Gibling, M.R., Giles, K.A., Holbrook, J.M.,Jordan, R., Kendall, C.G.St.C., Macurda, B., Martinsen, O.J., Miall, A.D., Neal, J.E.,Nummedal, D., Pomar, L., Posamentier, H.W., Pratt, B.R., Sarg, J.F., Shanley, K.W.,Steel, R.J., Strasser, A., Tucker, M.E., Winker, C., 2009, Towards the standardization of sequence stratigraphy. Earth-Science Reviews 92, 1–33. Elsevier B.V.: 1–33. doi:10.1016/j.earscirev.2008.10.003.

Catuneanu, O., W. E. Galloway, C.G. St. C. Kendall, A. D. Miall, H. W. Posamentier, A. Strasser., M. E. Tucker., 2011, Sequence Stratigraphy: Methodology and Nomenclature. Newsletters on Stratigraphy. doi:10.1127/0078-0421/2011/0011.

Catuneanu, O., J. P. Bhattacharya, M. D. Blum, R. W. Dalrymple, P. G. Eriksson, C. R. Fielding, W. L. Fisher, et al., 2010, Sequence Stratigraphy: Common Ground after Three Decades of Development. First Break. doi:10.3997/1365-2397.2010002.

Chadwick, W. W., R. P. Dziak, J. H. Haxel, R. W. Embley, H. Matsumoto., 2012, Submarine landslide triggered by volcanic eruption recorded by in situ hydrophone: Geology, v. 40, no. 1, p. 51–54, doi:10.1130/G32495.1

Chorowicz, J., 2005, The East African rift system: Journal of African Earth Sciences, v. 43, no. 1, p. 379–410, doi:https://doi.org/10.1016/j.jafrearsci.2005.07.019.

Corcoran, P. L., L. N. Moore., 2008, Subaqueous eruption and shallow-water reworking of a small-volume Surtseyan edifice at Kakanui, New Zealand: Canadian Journal of Earth Sciences, v. 45, no. 12, p. 1469-1485.

Deardorff, N. D., K. V. Cashman., W. W. Chadwick., 2011, Observations of eruptive plume dynamics and pyroclastic deposits from submarine explosive eruptions at NW Rota-1, Mariana arc: Journal of Volcanology and Geothermal Research, doi:10.1016/j.jvolgeores.2011.01.003.

Di Capua, A., G. Groppelli., 2016, Emplacement of pyroclastic density currents (PDCs) in a deep-sea environment: The Val d'Aveto Formation case (Northern Apennines, Italy): Journal of Volcanology and Geothermal Research, doi:10.1016/j.jvolgeores.2016.08.003.

Fiske, R.S., Cashman, K.V., Shibata, A., Watanabe, K., 1998, Tephra dispersal from Myojinsho, Japan, during its shallow submarine eruption of 1952–1953: Bulletin of Volcanology , v. 59, p. 262–275, doi:10.1007/s004450050190.

Gamboa, D., T. M. Alves., 2015, Spatial and Dimensional Relationships of Submarine Slope Architectural Elements: A Seismic-Scale Analysis from the Espírito Santo Basin (SE Brazil). Marine and Petroleum Geology. doi:10.1016/j.marpetgeo.2015.02.035.

Hansen, D. M., J. Cartwright., 2006, Saucer-Shaped Sill with Lobate Morphology Revealed by 3D Seismic Data: Implications for Resolving a Shallow-Level Sill Emplacement Mechanism. Journal of the Geological Society 163 (3): 509–23. doi:10.1144/0016-764905-073.

Holford, S. P., N. Schofield, J. D. MacDonald, I. R. Duddy, P. F. Green., 2012, Seismic Analysis of Igneous Systems in Sedimentary Basins and Their Impacts on Hydrocarbon Prospectivity: Examples from the Southern Australian Margin. APPEA Journal, 52, 229–52.

Infante-Paez, L., and K. J. Marfurt, 2017, Seismic expression and geomorphology of igneous bodies: A Taranaki Basin, New Zealand, case study: Interpretation, v. 5, no. 3, p. SK121-SK140, doi:10.1190/INT-2016-0244.1.

Jackson, C. A.-L., 2012, Seismic reflection imaging and controls on the preservation of ancient sill-fed magmatic vents: Journal of the Geological Society, doi:10.1144/0016-76492011-147.

Jerram, D. A., R. T. Single., R. W. Hobbs., C. E. Nelson., 2009, Understanding the offshore flood basalt sequence using onshore volcanic facies analogues: An example from the Faroe-Shetland basin: Geological Magazine, doi:10.1017/S0016756809005974.

Jones, A., D., G. Wilson., A. Gorman., B. Fox., D. Lee., U. Kaulfuss., 2017, A drill-hole calibrated geophysical characterisation of the 23 Ma Foulden Maar stratigraphic sequence, Otago, New Zealand: 1-13 p., doi:10.1080/00288306.2017.1369130.

Kaulfuss, U., K. Németh, and J. White., 2012, Field Guide Miocene subaerial to subaqueous monogenetic volcanism in Otago, New Zealand.

Kendall, C. G. C., Tucker, M. E., 2010, SEPM STRATA website. http://www.sepmstrata.org/page.aspx?pageid=410.

Kereszturi, G., K. Németh., 2013, Monogenetic Basaltic Volcanoes: Genetic Classification, Growth, Geomorphology and Degradation: Updates in Volcanology - New Advances in Understanding Volcanic Systems, doi:http://dx.doi.org/10.5772/51387.

Kereszturi, G., G. Csillag., K. Németh., K. Sebe., K. Balogh., and V. Jáger., 2010, Volcanic architecture, eruption mechanism and landform evolution of a Plio/Pleistocene intracontinental basaltic polycyclic monogenetic volcano from the Bakony-Balaton Highland Volcanic Field, Hungary: Central European Journal of Geosciences, doi:10.2478/v10085-010-0019-2.

Kereszturi, G., K. Németh., G. Csillag., K. Balogh., J. Kovács., 2011, The role of external environmental factors in changing eruption styles of monogenetic volcanoes in a Mio/Pleistocene continental volcanic field in western Hungary: 227-240 p., doi:10.1016/j.jvolgeores.2010.08.018.

Kiyosugi, K., 2012. Temporal and Spatial Analysis of Monogenetic Volcanic Fields. PhD theses. https://scholarcommons.usf.edu/etd/4101.

LaFemina, P. C., 2015, Chapter 3 - Plate Tectonics and Volcanism, in The Encyclopedia of Volcanoes. Sigurdsson, ed.: Amsterdam, Academic Press, p. 65–92, doi:https://doi.org/10.1016/B978-0-12-385938-9.00003-1.

Liu, J. Hou, Y. Li, Y. Dong, X. Ma, X. Wang., 2018, Characterisation of architectural elements of Ordovician fractured-cavernous carbonate reservoirs, Tahe Oilfield, China J. Geol. Soc. India, 91 (3) (2018), pp. 315-322

Lorenz, V., 1985. Maars and diatremes of phreatomagmatic origin, a review. Transactions of the Geological Society of South Africa, 88: 459-470.: 459-470 p.

Lorenz, V. and Kurszlaukis, S., 2007, Root Zone Processes in the Phreatomagmatic Pipe Emplacement Model and Consequences for the Evolution of Maar-Diatreme Volcanoes. Journal of Volcanology and Geothermal Research, 159, 4-32.

Macdonald, R., 2003, Magmatism of the Kenya Rift Valley: A review. Transactions of the Royal Society of Edinburgh: Earth Sciences, 239-253 p., doi:10.1017/S0263593300000420.

Magee, C., E. Hunt-Stewart., C. A. L. Jackson., 2013, Volcano growth mechanisms and the role of sub-volcanic intrusions: Insights from 2D seismic reflection data: Earth and Planetary Science Letters, doi:10.1016/j.epsl.2013.04.041.

McLean, C. E., N. Schofield., D. J. Brown., D. W. Jolley., and A. Reid, 2017, 3D seismic imaging of the shallow plumbing system beneath the Ben Nevis Monogenetic Volcanic Field: Faroe–Shetland Basin: Journal of the Geological Society, doi:10.1144/jgs2016-118.

Marti, J., G. Groppelli., A. B. Silveira., 2018, Volcanic stratigraphy: A review. Journal of Volcanology and Geothermal Research. Vol 357. doi:10.1016/j.jvolgeores.2018.04.006.

Miall, A. D., 1985, Architectural-Element Analysis: A New Method of Facies Analysis Applied to Fluvial Deposits. Earth-Science Reviews Elsevier Science Publishers B.V 22: 261–308. doi:10.1016/0012-8252(85)90001-7.

Miall, A. D., Tyler, N., 1991, Three-Dimensional Facies Architecture of Terrigenous Clastic Sediments and Its Implications for Hydrocarbon Discovery and Recovery. 1–5. SEPM (Society for Sedimentary Geology). doi:10.2110/csp.91.03.0001.

Miall, A. D., 2000, Principles of Sedimentary Basin Analysis; Springer-Verlag, New York, 616p.

Millett, J., A. Wilkins., E. Campbell., M. Hole., R. Taylor., D. Healy., D. Jerram., D. Jolley., S. Planke., S. Archer., A. Blischke., 2016, The geology of offshore drilling through basalt sequences: Understanding operational complications to improve efficiency: doi:10.1016/j.marpetgeo.2016.08.010.

Montanari, D., M. Bonini,, G. Corti,, A. Agostini,, C. Ventisette., 2017, Forced folding above shallow magma intrusions: Insights on supercritical fluid flow from analogue modelling: doi:10.1016/j.jvolgeores.2017.07.022.

Moorhouse, B. L., J. D. L. White, and J. M. Scott, 2015, Cape Wanbrow: A stack of Surtseyan-style volcanoes built over millions of years in the Waiareka-Deborah volcanic field, New Zealand: Journal of Volcanology and Geothermal Research, doi:10.1016/j.jvolgeores.2015.03.019.

Moraes, M. A. S., P. R. Blaskovski., P. L. B. Paraizo., 2005, Arquitetura de Reservatórios de Águas Profundas. Boletim de Geociencias Da Petrobras.

Morley, C., 2018, 3D seismic imaging of the plumbing system of the Kora volcano, Taranaki Basin, New Zealand: The influences of syn-rift structure on shallow igneous intrusion architecture: Geosphere, 2018. doi.org/10.1130/GES01645.1.

Muirhead, J. D., A. R. Van Eaton., G. Re, J. D. L. White., and M. H. Ort., 2016, Monogenetic volcanoes fed by interconnected dikes and sills in the Hopi Buttes volcanic field, Navajo Nation, USA: Bulletin of Volcanology, doi:10.1007/s00445-016-1005-8.

Mutti, E., W. R. Normark., 1987, Comparing Examples of Modern and Ancient Turbidite Systems: Problems and Concepts. In Marine Clastic Sedimentology. doi:10.1007/978-94-009-3241-8_1.

Németh, K., 2010. Monogenetic Volcanic Fields; Origin, Sedimentary Record, and Relationship with Polygenetic Volcanism. Special Paper Geological Society of America. doi:http://dx.doi.org/10.1130/2010.2470(04).

Orton, G.J, 1996, Volcanic Environments. I n Reading, H. G., 1996, Sedimentary Environments: Processes, Facies and Stratigraphy: 688 p.

Pittari, A., Cas, R. A. F., Lefebvre, N., Robey, J., Kurszlaukis, S., Webb, K., 2008. Eruption processes and facies architecture of the Orion Central kimberlite volcanic complex, Fort à la Corne, Saskatchewan; kimberlite mass flow deposits in a sedimentary basin. Journal of Volcanology and Geothermal Research, 174(1), 152–170. https://doi.org/https://doi.org/10.1016/j.jvolgeores.2007.12.019

Planke, S., P. A. Symonds, E. Alvestad, J. Skogseid., 2000, Seismic Volcanostratigraphy of Large-Volume Basaltic Extrusive Complexes on Rifted Margins. Journal of Geophysical Research 105 (B8): 19335. doi:10.1029/1999JB900005.

Planke, S., E. Alvestad, O. Eldholm., 1999, Seismic Characteristics of Basaltic Extrusive and Intrusive Rocks. The Leading Edge 18 (3): 342. doi:10.1190/1.1438289.

Planke, S., T. Rasmussen, S. S. Rey, and R. Myklebust, 2005, Seismic characteristics and distribution of volcanic intrusions and hydrothermal vent complexes in the Vøring and Møre basins, in Petroleum Geology: North-West Europe and Global Perspectives – Proceedings of the 6th Petroleum Geology Conference: doi:10.1144/0060833.

Planke, S., J. M. Millett., D. Maharjan., D. A. Jerram., M. M. Abdelmalak., A. Groth., J. Hoffmann., C. Berndt., and R. Myklebust., 2017, Igneous seismic geomorphology of buried lava fields and coastal escarpments on the Vøring volcanic rifted margin: Interpretation, doi:10.1190/INT-2016-0164.1.

Pope, E. L., M. Jutzeler., M. J. B. Cartigny., J. Shreeve., P. J. Talling., I. C. Wright., and R. J. Wysoczanski., 2018, Origin of spectacular fields of submarine sediment waves around volcanic islands: Earth and Planetary Science Letters, doi:10.1016/j.epsl.2018.04.020.

Posamentier, H. W., V. Kolla, 2003, Seismic Geomorphology and Stratigraphy of Depositional Elements in Deep-Water Settings. Journal of Sedimentary Research 73 (3): 367–88. doi:10.1306/111302730367.

Rabbel, O., O. Galland., K. Mair., I. Lecomte., K. Senger., J. B. Spacapan., R. Manceda., 2018, From field analogues to realistic seismic modelling: a case study of an oil-producing andesitic sill complex in the Neuquén Basin, Argentina: Journal of the Geological Society, doi:10.1144/jgs2017-116.

Reynolds, P., N. Schofield., R. J. Brown., S. P. Holford., 2016, The architecture of submarine monogenetic volcanoes - insights from 3D seismic data: Basin Research, v. 30, p. 437–451, doi:10.1111/bre.12230.

Reynolds, P., S., Holford, N. Schofield., A. Ross., 2017, Three-Dimensional Seismic Imaging of Ancient Submarine Lava Flows: An Example From the Southern Australian Margin: Geochemistry, Geophysics, Geosystems, doi:10.1002/2017GC007178.

Ring, U., 2014, The East African rift system: Austrian Journal of Earth Sciences, doi:10.1016/j.jafrearsci.2005.07.019.

Rogers, N., 2015, Chapter 4 – The Composition and Origin of Magmas, in The Encyclopedia of Volcanoes: doi:10.1016/B978-0-12-385938-9.00004-3.

Rotella, M. D., C. J. N. Wilson, S. J. Barker, I. C. Wright, 2013., Highly vesicular pumice generated by buoyant detachment of magma in subaqueous volcanism: Nature Geoscience, doi:10.1038/ngeo1709.

Schofield, N., L. Heaton, S. P. Holford., S. G. Archer., C. A.-L. Jackson., and D. W. Jolley., 2012, Seismic imaging of “broken bridges”: linking seismic to outcrop-scale investigations of intrusive magma lobes: Journal of the Geological Society, doi:10.1144/0016-76492011-150.

Schofield, N., D. A. Jerram., S. Holford., A. Stuart., M. Niall., A. Hartley., J. Howell., M. David., P. Green., D. Hutton., C. Stevenson, 2016, Sills in sedimentary basin and petroleum systems, in K. Németh, ed., The Series Advances in Volcanology, 1–22.

Schmiedel, T., S. Kjoberg., S. Planke., C. Magee., O. Galland., N. Schofield., C. A.-L. Jackson., and D. A. Jerram., 2017., Mechanisms of overburden deformation associated with the emplacement of the Tulipan sill, mid-Norwegian margin: Interpretation, doi:10.1190/INT-2016-0155.1.

Silva, S. D., J. M. Lindsay., 2015, Primary Volcanic Landforms. The Encyclopedia of Volcanoes. doi:10.1016/B978-0-12-385938-9.00015-8.

Single, R.T., Jerram, D.A., 2004. The 3-D facies architecture of flood basalt provinces and their internal heterogeneity: examples from the Palaeogene Skye Lava Field. Journal of the Geological Society 161, 911-926

Slatt, R. M., 2013, Stratigraphic Reservoir Characterization for Petroleum Geologists. Developments in Petroleum Science. doi:10.1016/B978-0-444-56365-1.00013-4.

Svensen, H. H., T. H. Torsvik., S. Callegaro., L. Augland., T. H. Heimdal., D. A. Jerram., S. Planke., and E. Pereira., 2017, Gondwana Large Igneous Provinces: plate reconstructions, volcanic basins and sill volumes: Geological Society, London, Special Publications, doi:10.1144/SP463.7.

White, J. D. L., 1991, The depositional record of small, monogenetic volcanoes within terrestrial basins, in Sedimentation in volcanic settings. In: Sedimentation in Volcanic Settings (Eds R.V. Fisher and G.A. Smith), SEPM Spec. Publ., 45, 155–171.

White, J.D.L., 1996. Pre-emergent construction of a lacustrine basaltic volcano, Pahvant Butte, Utah (USA). Bull. Volcanol. 58, 249-262.

White, J. D. L., 2000, Subaqueous eruption-fed density currents and their deposits: Precambrian Research 101 (2000) 87–109. doi:10.1016/S0301-9268(99)00096-0.

White, J. D. L., P. S. Ross., 2011, Maar-diatreme volcanoes: A review: doi:10.1016/j.jvolgeores.2011.01.010.

Zimanowski, B., R. Büttner., V. Lorenz., H.-G. Häfele., 1997, Fragmentation of basaltic melt in the course of explosive volcanism: Journal of Geophysical Research: Solid Earth, doi:10.1029/96JB02935.

Zimanowski, B., R. Büttner., 2003, Phreatomagmatic explosions in subaqueous volcanism, in Geophysical Monograph Series: doi:10.1029/140GM03.

Chapter 6

Models for Exploration of Geoenergy Resources in Monogenetic Volcanic Fields within Sedimentary Basins

6 Models for Exploration of Geoenergy Resources in Monogenetic Volcanic Fields within Sedimentary Basins

6.1 Implications for Geoenergy Resources

In this section, we show how insights from the analysis of architectural elements of the MVS (chapters 4 and 5) can be applied to the exploration of geoenergy resources such as hydrocarbons and geothermal energy. In both cases, subsurface fluid-dynamics are strongly influenced by the presence of architectural elements that can store, conduct or entrap fluids such as water, oil and gas. Here we present two models to illustrate possible combinations of architectural elements that favour the formation of petroleum accumulations and geothermal fields in association with monogenetic volcanism. It is important to remember that these models are a simplified representation of a great number of variables with associated uncertainties. These models were built to provide guidelines for the potential of buried and active monogenetic systems to contain geoenergy resources within different stratigraphic parts of the volcanic system, and to illustrate how the architectural elements can possibly influence the subsurface dynamic fluid-flow of these systems. The conditions that determine if certain architectural elements have the ability to transmit or obstruct fluids are some of the key unknowns in any prospect evaluation. To assess the risks and improve the likelihood of finding commercially important geoenergy resources, in association with volcanic systems it is import to understand how these architectural elements are combined, to quantify their petrophysical properties, and to determine how post-formational events can change their original characteristics. Given the large number of variables, the fluid-flow properties of volcanic systems will likely need to be considered on a case-by-case basis.

6.2 Petroleum Plays in Buried Monogenetic Volcanic Fields

To illustrate the great range of possible petroleum plays associated with buried monogenetic volcanic fields (Figure 80), we use the concept of a “petroleum system” from Magoon and Dow (1994). Here, this concept is applied to describe possible combinations of architectural elements and processes that are necessary to form hydrocarbon accumulations in different parts of buried monogenetic volcanic systems.

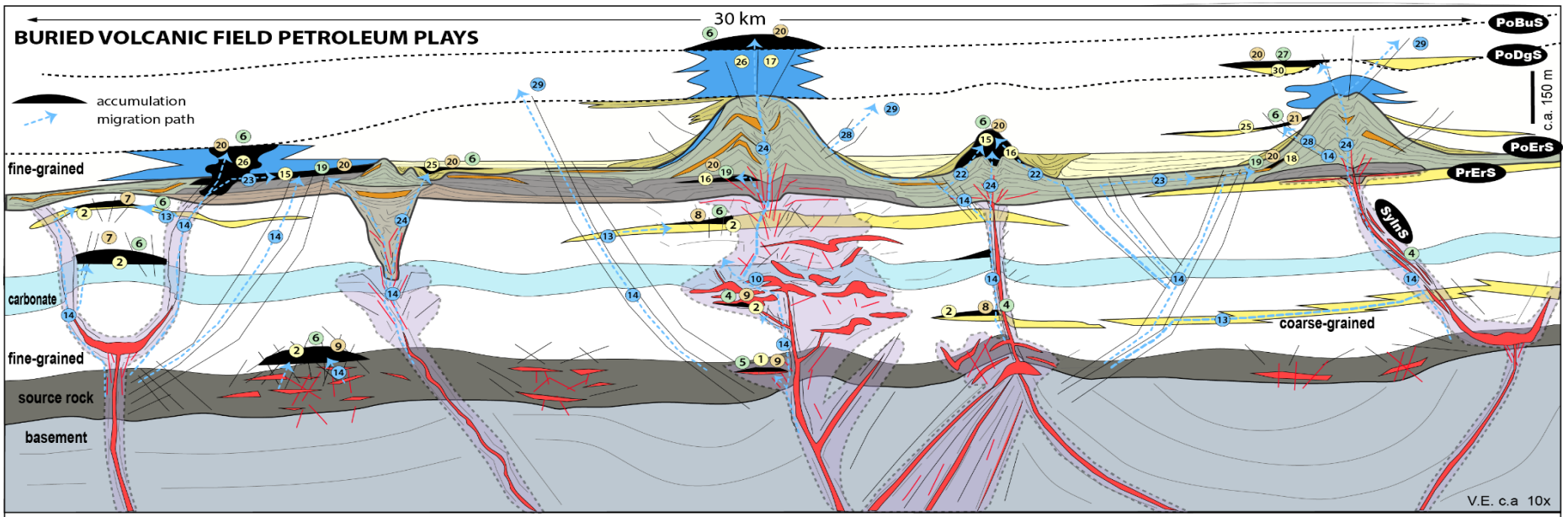

	emplacement (below PrErS and between SyInS)	**constructional** (between PrErS and PoErS)	**degradational** (between PoErS and PoDgS)	**burial** (between PoDgS and PoBuS)
reservoirs	(1) fractured intrusive rocks (2) fractured and porous host rocks (3) hydrothermally induced secondary porosity	(15) fractured and/or vesicular effusive and pyroclastic rocks (16) porous pillow-lavas, hyaloclastites, peperites (17) carbonates associated to volcanoes (18) volcanic debris (3) hydrothermally induced secondary porosity	(25) volcanic debris, epiclastic and siliciclastic deposits (17) carbonates associated to volcanoes (26) tardi hydrothermalism (secondary porosity)	(17) carbonates associated to volcanoes (30) siliciclastic deposits impacted by burial (26) tardi hydrothermalism (secondary porosity)
seals	(4) massive intrusions (5) hydrothermally induced cementation (6) fine-grained sedimentary deposits	(19) massive intrusions, lavas and pyroclastic deposits (5) hydrothermally induced cementation (6) fine-grained sedimentary deposits	(6) fine-grained sedimentary deposits (27) tardi hydrothermalism (cementation)	(6) fine-grained sedimentary deposits (27) tardi hydrothermalism (cementation)
traps	(7) jacked-up domes (8) drag folds and puncturing (9) stratigraphic/structural	(20) paleogeomorphic and stratigraphic (21) upturned pinchouts	(20) paleogeomorphic and stratigraphic (21) upturned pinchouts	(20) paleogeomorphic and stratigraphic
migration	(10) broken-bridge structures (11) reservoir compartmentalization (12) pressure cages (13) sub-horizontal and inclined porous deposits (14) igneous and tectonic fractures/faults	(22) inclined bedded deposits (23) sub-horizontal bedded deposits (24) cylindrical chaotic deposits (14) igneous and tectonic fractures/faults	(28) post-volcanic fractures and faults (29) leakage to atmosfere	(28) post-volcanic fractures and faults (29) leakage to atmosfere

Figure 80: Schematic representation of the possible petroleum plays associated with buried monogenetic volcanic systems, based on the observation of the MVS architectural elements. Distinctive sets of architectural elements can create prospective plays according to the magmatic stages of emplacement, construction, degradation, and burial of the volcanoes (following volcano-stratigraphic models proposed in Bischoff et al. (2017) and chapter 5 of this thesis). Sandstones below the PrErS (yellow), limestones above the PoErS (blue) and faults were added to this model to illustrate possible plays formed by the interaction of these lithologies with volcanism.

6.2.1 Petroleum Elements of the Emplacement Stage

In the endogenous part of the system (emplacement stage), potential reservoirs can occur in both porous and non-porous host sedimentary rocks, with increasing permeability related to fracturing caused by the emplacement of magma (i.e. formation of the architectural element disrupted blocks), and in fractured intrusive bodies formed by thermal contraction during cooling. An example of such a reservoir occurs in the Wichian Buri field in Thailand, where 30 Mbbl of oil and gas is contained in dolerite intrusions and associated sandstones (Remus et al., 1993; apud Schutter, 2003). Seals can be formed by fine-grained host sedimentary deposits and massive intrusions (e.g. Jurua field, Solimões Basin, Brazil; Barata and Caputo, 2007). Hydrothermal fluids can induce secondary porosity by mineral dissolution (e.g. Vieira de Luca et al., 2017), or can clog potential reservoirs by precipitation of cements (e.g. Schutter, 2003).

Intrusive bodies are likely to form many isolated or combined four-way closures such as jacked-up domes above intrusions with sizes up to 30 km^2, mainly associated with the emplacement of saucer-shaped sills and dike-sill swarms (Figure 80), such as those from plumbing-types 1 and 2 of the MVS. A combination of stratigraphic and structural traps can occur above sill intrusions or fractured rocks in contact with fine-grained sedimentary rocks, or in coarse-grained sedimentary rocks in contact with massive sills. In the state of Montana (USA), many oil and gas fields with tens of millions of barrels were found in sandstones trapped by intrusions (Lopez, 1995; apud Schutter, 2003).

Fluids can migrate upwards through inclined porous host strata, fractured dikes (Holford et al., 2017), tectonic and magmatic induced fractures and faults (especially associated with disrupted blocks and above inclined sheets of saucer-shaped intrusions such as those of plumbing-type 3 in the MVF), and at broken-bridge structures (i.e. elongate and discontinuous magma lobes located at the extremities of sill intrusions; e.g. Schofield et al., 2012). Lateral migration of hydrocarbons is possible in sub-horizontal coarse-grained host rocks, and/or below sills with fractured edges, and along the contact of permeable rocks with strata cemented by metasomatism or contact metamorphism (Figure 80). Intrusions emplaced in organic-rich sedimentary rocks have the potential to elevate the geothermal gradient to ideal conditions and generate thermogenic gas (e.g. Aarnes et al., 2015). For example, heating by

intrusions produced hydrocarbon accumulations with > 33 billion m^3 of gas in the Urucu province, Solimões Basin, Brazil (Barata and Caputo, 2007). Intrusions emplaced in organic-rich rocks can release high amounts of CO_2 and CH_4 (e.g. Delmelle et al., 2015; Svensen et al., 2017), and may release sulfidic acids (e.g. H_2S) if the host rocks, or the original magma was enriched in sulphur (e.g. Iacono-Marziano et al., 2013; Stimac et al., 2015; Robertson et al., 2015; Arnórsson et al., 2015). Magma emplaced in carbonate rocks can release CO_2 (e.g. Deegan et al., 2010; Blythe et al., 2015), which may be one possible explanation for the high content of this acid gas flooding some reservoirs in the Mero field, in the offshore of Brazil.

In summary, intrusions and associated deformation of host strata can impact the fluid dynamic of the emplacement stage with potential to host commercial hydrocarbon accumulations in fractured igneous rocks, and in porous and fractured host sedimentary rocks. Intrusions can degrade the quality of hydrocarbons by adding gases such as CO_2 and H_2S into the system.

6.2.2 Petroleum Elements of the Constructional Stage

Potential reservoirs of the constructional stage comprise many of eruptive and sedimentary deposits. Porous and fractured reservoirs can occur in lava deposits with vesiculated and brecciated margins and coherent cores with columnar joints formed due to cooling. In northwest Java, Indonesia, the Jatibarang field has produced 1.2 Gbbl of oil and 2.7 TCF of gas from andesitic rocks (Kartanegara et al., 1996; apud Schutter, 2003). Seismic images from the MVF suggest that lava deposits may occur at the basal cone and cone apron of crater-type volcanoes, and can extend as far as 3 km from the vent (Figure 80). Pyroclastic rocks usually present very high primary intergranular porosity due to fragmentation, which can be rapidly lost due to compaction during burial, or could also increase permeability by development of micro-fractures that connect pores (Heap and Kennedy, 2016; Heap et al., 2017). Observations in the Songliao Basin show that pyroclastic rocks have the potential to maintain high porosity and permeability at greater depths (up to 20% and 33 mD at depths of 1500 to 3500 m; Wang et al., 2018). Hyaloclastites, peperites, and pillow-lavas (Figure 80) show primary and secondary porosity and have potential to form hydrocarbon reservoirs, as demonstrated from pillow-lava deposits of the Pão de Açúcar field. This field contains oil in primary volcanic vesiculated rocks, inter-pillow megapores, and pillow breccias (Vieira de

Luca et al., 2017). Fine-grained contemporaneous sedimentary deposits, massive lavas, welded coarse-grained pyroclastic rocks, and ash deposits can form seals (e.g. Schutter, 2003). As well as in the emplacement stage, hydrothermal activity can induce secondary porosity, or cement reservoirs (e.g. Schutter, 2003). Possible paleogeomorphic and stratigraphic traps can form at unconformities due to burial of volcanic edifices, valley infill and contacts between reservoirs and seals deposited on the tephra flanks, with reservoirs pinching-out towards the central crater (e.g. Bergman et al., 1992; Bischoff et al., 2017). Sub-vertical fluid migration can be controlled by igneous and tectonics fractures/faults (including intrusions of type-4 that cross-cut the base of syn-eruptive deposits, such as in the MVS), or by cooling fractures, by inclined tabular permeable deposits located on the tephra flank and tephra ring, and by cylindrical chaotic deposits of the central crater and diatremes (Figure 80). In summary, eruptive rocks can form world-class hydrocarbon fields. Reservoirs in these fields can have high fluid deliverability towards four-way closures, due to the inclined flanks of volcanic cones that often contain interbedded permeable and non-permeable rocks as part of the same structure. The geometries and interconnectivity of these reservoir rocks are complex and may be difficult to predict.

6.2.3 Petroleum Elements of the Degradational Stage

Potential reservoirs formed during the degradational stage can be composed of debris deposits eroded from the volcanic edifices, which can include volcanic breccias and conglomerates, reworked carbonates, and non-volcanogenic siliciclastic coarse-grained deposits transported by submarine channels in association with the volcanic edifices (Figure 80). Based on examples of the MVS, these deposits are most likely to be located in the central crater, tephra flank, and cone apron of crater-type volcanoes. Seals are mainly formed by fine-grained sedimentary deposits that drape the volcanoes. Late hydrothermalism can induce both secondary porosity and cementation. Post-volcanic faults associated with differential compaction and subsidence can transport hydrocarbons to paleo-geomorphic and stratigraphic traps, and to permeable sedimentary deposits that dip away from and pinch-out against the volcanic edifice (Figure 80). In summary, there is some potential for accumulation in the degradational stage, however, reservoirs are likely small, disconnected and localized.

6.2.4 Petroleum Elements of the Burial Stage

During the burial stage, sedimentary reservoirs can be impacted by the location of the volcanic structures. Sandstone reservoirs with 2.5 Mbbl of oil are reported to drape buried volcanoes in the Torch field, USA (Rives, 1968; apud Schutter, 2003). High-quality carbonate reservoirs can form on volcanic highs, with the potential to trap very large hydrocarbon volumes in four-way closures associated with the volcanic structures during progressive burial (Figure 80). Discoveries in Indonesia demonstrate that tropical carbonates located on volcanic structures have been a proven petroleum play since the 1970's. In offshore Sumatra, Krishna and Rama fields together produced 198 Mbbl from reefs and lagoon facies on the rim of volcanic islands. During lowstand cycles and exposure to freshwater conditions, original tight facies developed high secondary porosity due to leaching of aragonitic material (Wight and Hardian, 1982). In offshore Myanmar, the Yadana field is formed by shallow-water carbonate rocks build-up on a paleo volcanic high, and contains an estimated 7 TCF of gas (Paumard et al., 2017)

More recently, world-class accumulations discovered in offshore Brazil suggest that this play works in the pre-salt sequence of both South Atlantic conjugate margins. For example, the Pão de Açúcar field contains estimated values of 700 Mbbl of oil and 3 TCF of gas in carbonates and pillow-basalts located on the top of a volcanic edifice. Reservoirs of this field present abundant vugs, fractures, caverns, and patches of microporosity developed due to intense late hydrothermal alteration (Vieira de Luca et al., 2017). The Lula and Mero fields together have a reserve estimated at > 10 Gbbl. Reservoirs are composed of carbonates deposited on volcanic-siliciclastic rift sequences associated with structural highs (e.g. Mohriak, 2008; Carlotto et al., 2017). The role of the syn-rift volcanic structures on the formation of carbonate reservoirs remains unclear and will need to be unravelled by future work. In South Island, New Zealand, outcrop observations from the Waiareka-Deborah monogenetic volcanic field suggest that these clusters of volcanoes can create localized highs of >225 km^2. Above these structures, high energy currents winnow micrite and cause fragmentation of cool-water bioclasts (Thompson et al., 2014). Aragonitic components underwent dissolution at the seafloor and the lack of cements/matrix produces a clean bryozoan grainstone ca 50 m thick, and porosity above 50% before deep burial (Thompson et al., 2014). Offshore seismic surveys and wells indicate that there are many Meso-Cenozoic monogenetic fields and large

polygenetic volcanic complexes in the Canterbury and Taranaki basins, potentially associated with overlaying carbonates and commonly forming four-way closures (Figure 80) due to burial doming (Barrier et al., 2017; Bischoff et al., 2018). In summary, very large hydrocarbon accumulations can form on the top of buried volcanoes (Figure 80). Volcanic structures can provide ideal conditions for the deposition of sedimentary rocks (mainly carbonates) with high quality reservoir properties. These rocks are likely entrapped in large four-way closures due to progressive burial and differential compaction across the volcanic edifice.

6.3 Intrusion-Related Hydrothermal Systems

In this section we explore the analysis of architectural elements of the MVS to identify potential impacts on hydrothermal systems related to shallow intrusions in sedimentary basins. In Chapter 4, we show how different plumbing-types of the MVS can vary in relation to geometries of intrusions, their size, architecture, and emplacement in different host rocks. These variations create situations that can impact hydrothermal systems, mostly related to fluid migration pathways within the system, the location of potential prospective zones, and changes in the composition of fluids due to interaction with host rocks (Figure 81). Petroleum and geothermal systems share many similarities. Both systems rely on the presence of fundamental elements and processes to form a working system. Key elements for geothermal systems are a source of heat (e.g. magma or igneous rocks that remain hot), a reservoir rock (which can be fractured or porous), water (vapour or liquid), and a permeable network to transfer fluids and heat through the system (e.g. Goff and Janik, 1999; Stimac et al., 2015). The heat content of intrusions is related to their body volume and temperature. Intrusion-related hydrothermal systems are formed when a shallow magmatic intrusion interacts with a permeable water network. These systems are considered the hottest (220^{o} to 350^{o} C) and most prolific producers for geothermal energy (Stimac et al., 2015). Basaltic intrusions in sedimentary basins (e.g. MVS) usually have very high temperatures, in which melts are estimated to be > 1100^{o} C (e.g. Grove and Till, 2015; Aarnes et al., 2015).

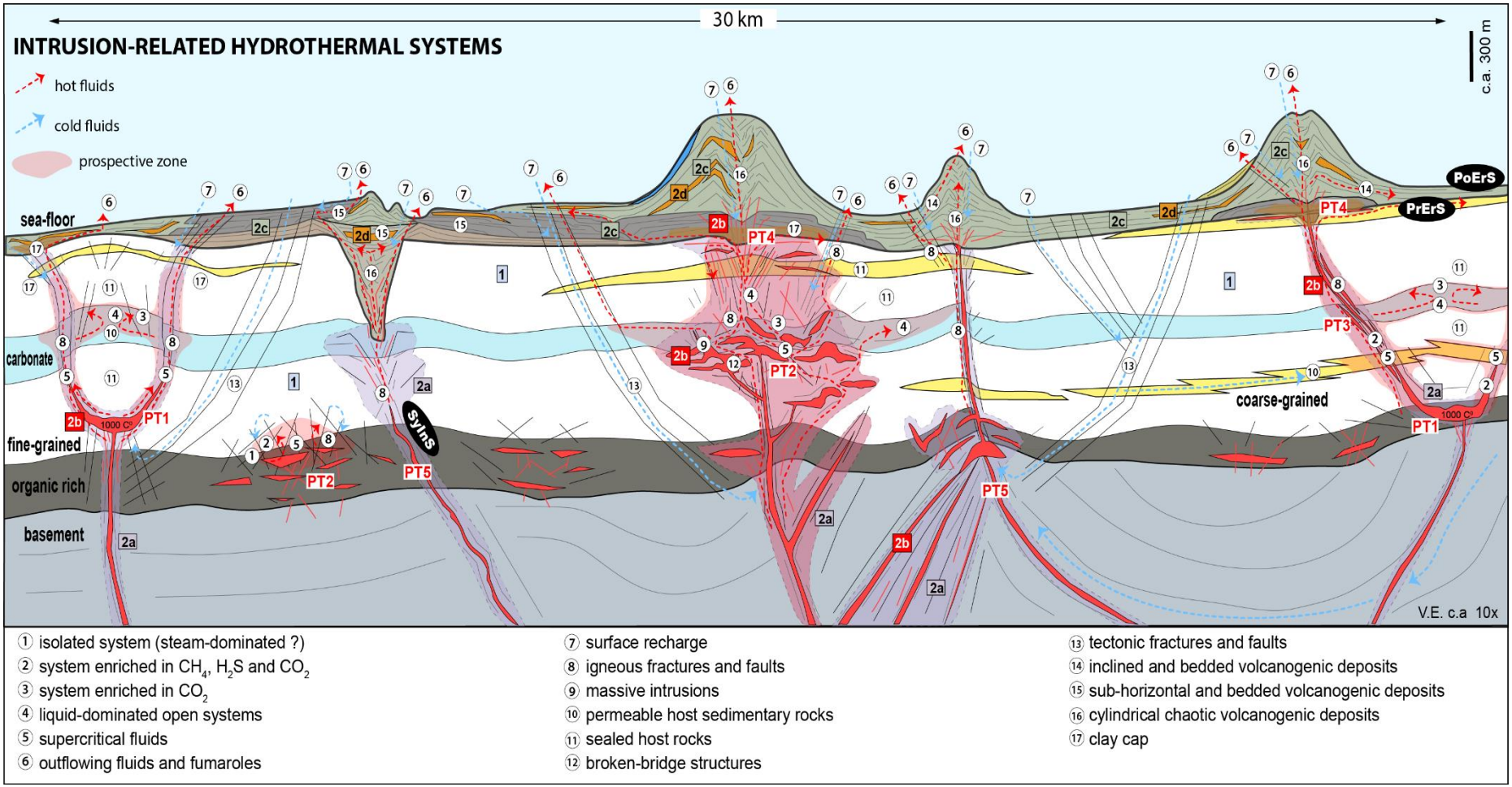

Figure 81: Schematic representation of the possible intrusion-related hydrothermal systems associated with buried monogenetic volcanic systems, based on the observation of MVS architectural elements. Distinctive sets of architectural elements can create prospective plays according to the magmatic stages of emplacement, construction, degradation and burial of the volcanoes. Sandstones below the PrErS (yellow) and faults were added to this model to illustrate possible plays formed by the interaction of this lithology with volcanism.

Saucer-shaped sills (plumbing-type 1) are the most prolific type of intrusion in the MVS (Figure 81), with rock volumes estimated to be up to 2.5 km^3 for individual sills. The emplacement of these intrusions is associated with a ring-shaped network of faults and fractures in the overburden strata that accommodate deformation (e.g. Hansen and Cartwright, 2006). Flow models presented in Iyer et al. (2013) show that the merging of fluids from near saucer-intrusions could result in hydrothermal plumes located at the lateral edges of the sills. Based on laboratory experiments, Montanari et al. (2017) argue that these fracture and fault networks could influence the formation of potential prospects for supercritical geothermal fluids. In the MVS, the tips of the inclined sheets of saucer-intrusions (Figure 81) correspond to the transition between plumbing-type 1 and 3. This transition is characterised by a strong sub-vertical network of faults and fractures, where fractures and faults could be a prospective zone for directly tapping into magmatic heat by drilling into or near shallow intrusive bodies (e.g. Stimac et al., 2015). These sub vertical fracture networks can conduct magma upwards and feed eruptions at the surface, or facilitate outflowing of fluids to hydrothermal vents and fumaroles (e.g. Holford et al., 2012; Planke et al., 2005; Blanke, 2012; Jackson, 2012; McLean et al., 2017). Faults and fractures may create pathways for surface water to recharge the system, which can favour the formation of hydrothermal convection cells (Figure 81).

Plumbing-type 2 intrusions are usually shallow (< 500 m deep) and individual intrusions that have smaller volumes (up to 0.05 km^3) than saucer-sills, however, they are typically characterised by a complex intrusive network with dozens (maybe hundreds) of intrusions. Their association with fractures and disrupted blocks may favour contact with surface water and development of a liquid-dominated open system (Figure 81). In rare cases they may form a system isolated from groundwater, in which steam-dominated conditions may prevail (Stimac et al., 2015). Plumbing-types 4 and 5 show small and isolated intrusions and have little potential to form economic intrusion-fed geothermal systems (Figure 81).

As a rule-of-thumb for all plumbing types, geothermal systems hosting intrusions and reservoirs in carbonates are likely to be enriched in CO_2, while systems hosted in organic-rich rocks are potentially enriched in CO_2, CH_4, and H_2S (e.g. Goff and Janik, 1999; Deegan et al., 2010; Iacono-Marziano et al., 2013; Aarnes et al., 2015; Robertson et al., 2015; Arnórsson et al., 2015). Clay caps are more likely to form at shallow levels due to alteration of volcanic rocks with high glass and plagioclase content, rather than in siliciclastic and carbonate pre-magmatic sequences, which could maintain the life spans of these systems (e.g. Stimac et al., 2015).

6.4 Conclusions

The complete characterisation of the architecture of the MVS allows us to understand how certain combinations of volcanic and sedimentary architectural elements can form hydrocarbon leads and possible geothermal systems in association with volcanoes buried in sedimentary basins. At the endogenous level, intrusions and magmatic deformation can create fractured reservoirs, seals, structural traps, and pathways to fluid percolation. Large saucer-sills and intrusion swarms have the potential to host significant oil and gas accumulations, and can produce high-temperature intrusion-related geothermal systems. Both petroleum and geothermal systems are likely to be enriched in CO_2 if the intrusions are emplaced in carbonate rocks, or are likely to be enriched in CO_2, CH_4, and H_2S if the intrusions interact with organic-rich host rocks. At the exogenous level, a complex network of eruptive and sedimentary deposits can form substantial hydrocarbon fields due to high fluid deliverability towards four-way closures, which can be sealed if the volcanic structures are buried in fine-grained marine sediments or evaporitic rocks. Progressive burial of the volcanoes can create ideal conditions for the formation of high-quality carbonate reservoirs located above buried volcanic structures. Differential compaction between the volcanic structures and enclosing sedimentary rocks can entrap these carbonate reservoirs in large four-way closures, with potential to host world-class (> 1Gbbl) hydrocarbon fields. Understanding the relationship of diverse architectural elements, their petrophysical properties, and post-formational events that can change their original characteristics is important to assess the risks and to improve the likelihood of finding commercially viable geoenergy resources in association with buried and active monogenetic volcanic systems.

6.5 References

Aarnes, I., Planke, S., Trulsvik, M., Svensen, H., 2015. Contact metamorphism and thermogenic gas generation in the Vøring and Møre basins, offshore Norway, during the Paleocene-Eocene thermal maximum. Journal of the Geological Society, 172(5), 588-598

Arnórsson, S., S. Thórhallsson., A. Stefánsson., 2015, Utilization of Geothermal Resources, in The Encyclopedia of Volcanoes: doi:10.1016/B978-0-12-385938-9.00071-7.

Barata, C. F., M. V. Caputo,. 2007. Geologia Do Petróleo Da Bacia Do Solimões. O “Estado Da Arte”. In 4o Pdpetro.

Barrier, A., A. Nicol, A. P. Bischoff., 2017, Volcanism Occurrences in the Canterbury Basin, New Zealand and Implication for Petroleum Exploration. In AAPG GTW Influence of Volcanism and Associated Magmatic Processes on Petroleum Systems. Conference, Oamaru New Zealand.

Bergman, S.C., J.P. Talbot, and P.R. Thompson., 1992, The Kora Miocene Submarine Andesite Stratovolcano Hydrocarbon Reservoir, Northern Taranaki Basin, New Zealand. In 1991 New Zealand Oil Exploration Conference, 178–206.

Bischoff, A. P., A. Nicol, M. Beggs., 2017, Stratigraphy of architectural elements in a buried volcanic system and implications for hydrocarbon exploration: Interpretation, doi:10.1190/INT-2016-0201.1.

Bischoff, A.P., A. Barrier., A. Nicol., W. Mohriak., 2018, Carbonate Build-up on Volcanic Highs - Global Petroleum Plays and Analogues from New Zealand Sedimentary Basins. In 2018 Brazilian Petroleum Conference, Rio de Janeiro, Brazil, Abstract.

Blanke, S. J., 2010, "Saucer Sills" of the Offshore Canterbury Basin: GNS Publication, doi:10.1177/0094306114545742f.

Carlotto, M. A., R. C. B. Silva., A. A. Yamato., W. L. Trindade., J. L. P. Moreira., R. A. R. Fernandes, O. J. S. Ribeiro., et al. 2017. Libra: A Newborn Giant in the Brazilian Presalt Province. In Gialnt Fields of the Decade 2000-2010. doi:10.1306/13572006M1133685.

Deegan, F. M., V. R. Troll., C. Freda., V. Misiti., J. P. Chadwick., C. L. McLeod., J. P. Davidson., 2010, Magma–Carbonate Interaction Processes and Associated CO2 Release at Merapi Volcano, Indonesia: Insights from Experimental Petrology. Journal of Petrology 51 (5): 1027–51. http://dx.doi.org/10.1093/petrology/egq010.

Delmelle, P., E. Maters., C. Oppenheimer., 2015, Volcanic Influences on the Carbon, Sulfur, and Halogen Biogeochemical Cycles, in The Encyclopedia of Volcanoes: doi:10.1016/B978-0-12-385938-9.00050-X.

Goff, F., Janik, C.J., 2000, Geothermal Systems, Encyclopedia of Volcanoes, Academic Press, Chapter-49, pp. 817 – 834.

Grove, T. L., C. B. Till, 2015, Melting the Earth's Upper Mantle, in The Encyclopedia of Volcanoes: doi:10.1016/B978-0-12-385938-9.00001-8.

Hansen, D. M., J. Cartwright., 2006, Saucer-Shaped Sill with Lobate Morphology Revealed by 3D Seismic Data: Implications for Resolving a Shallow-Level Sill Emplacement Mechanism. Journal of the Geological Society 163 (3): 509–23. doi:10.1144/0016-764905-073.

Heap, M. J., B. M. Kennedy., 2016, Exploring the scale-dependent permeability of fractured andesite: Earth and Planetary Science Letters, doi:10.1016/j.epsl.2016.05.004.

Heap, M. J., B. M. Kennedy., J. I. Farquharson., J. Ashworth., K. Mayer., M. Letham-Brake., T. Reuschlé., H. A. Gilg., B. Scheu., Y. Lavallée., P. Siratovich., J. Cole., A. D. Jolly., P. Baud., D. B. Dingwell., 2017, A multidisciplinary approach to quantify the permeability of the Whakaari/White Island volcanic hydrothermal system (Taupo Volcanic Zone, New Zealand): Journal of Volcanology and Geothermal Research, doi:10.1016/j.jvolgeores.2016.12.004.

Holford, S. P., N. Schofield, J. D. MacDonald, I. R. Duddy, P. F. Green., 2012, Seismic Analysis of Igneous Systems in Sedimentary Basins and Their Impacts on Hydrocarbon Prospectivity: Examples from the Southern Australian Margin. APPEA Journal, 52, 229–52.

Holford, S., N. Schofield, and P. Reynolds., 2017, Subsurface fluid flow focused by buried volcanoes in sedimentary basins: Evidence from 3D seismic data, Bass Basin, offshore southeastern Australia: 39-50 p., doi:10.1190/INT-2016-0205.1.

Iacono-Marziano, G., Morizet, Y., Le Trong, E., Gaillard, F., 2013, New experimental data and semi-empirical parameterization of H2O-CO2 solubility in mafic melts. Geochimica Et Cosmochimica Acta 97. 145-157.

Iyer, K., L. Ruepke., C. Galerne., 2013, Modeling fluid flow in sedimentary basins with sill intrusions: Implications for hydrothermal venting and climate change: doi:10.1002/2013GC005012.

Jackson, C. A.-L., 2012, Seismic reflection imaging and controls on the preservation of ancient sill-fed magmatic vents: Journal of the Geological Society, doi:10.1144/0016-76492011-147.

Magoon, L. B., and W. G. Dow, 1994, The Petroleum System: AAPG Memoir, doi:10.1126/science.51.1323.468.

McLean, C. E., N. Schofield., D. J. Brown., D. W. Jolley., and A. Reid, 2017, 3D seismic imaging of the shallow plumbing system beneath the Ben Nevis Monogenetic Volcanic Field: Faroe–Shetland Basin: Journal of the Geological Society, doi:10.1144/jgs2016-118.

Mohriak, W.U., M. Nemcok., G. Enciso., 2008. South Atlantic divergent margin evolution: rift-border uplift and salt tectonics in the basins of SE Brazil. In: Pankhurst, R.J., Trouw, R.A.J., Brito Neves, B.B. & de Wit, M.J. (eds.), West Gondwana pre-Cenozoic correlations across the South Atlantic region. Geological Society of London, Special Publication 294, p.365-398.

Paumard, V., E. Zuckmeyer., R. Boichard., S. Jorry., J. Bourget., J. Borgomano., T. Maurin., J.-N. Ferry, 2017, Evolution of Late Oligocene - Early Miocene attached and isolated carbonate platforms in a volcanic ridge context (Maldives type), Yadana field, offshore Myanmar: 361-387 p., doi:10.1016/j.marpetgeo.2016.12.012.

Planke, S., T. Rasmussen, S. S. Rey, and R. Myklebust, 2005, Seismic characteristics and distribution of volcanic intrusions and hydrothermal vent complexes in the Vøring and Møre basins, in Petroleum Geology: North-West Europe and Global Perspectives – Proceedings of the 6th Petroleum Geology Conference: doi:10.1144/0060833.

Robertson, J., E. M. Ripley., S. J. Barnes., C. Li, 2015., Sulfur liberation from country rocks and incorporation in mafic magmas: Economic Geology, doi:10.2113/econgeo.110.4.1111.

Schofield, N., L. Heaton, S. P. Holford., S. G. Archer., C. A.-L. Jackson., and D. W. Jolley., 2012, Seismic imaging of “broken bridges”: linking seismic to outcrop-scale investigations of intrusive magma lobes: Journal of the Geological Society, doi:10.1144/0016-76492011-150.

Schutter, S. R., 2003, Hydrocarbon Occurrence and Exploration in and around Igneous Rocks. Geological Society, London, Special Publications 214 (1): 7–33. doi:10.1144/GSL.SP.2003.214.01.02.

Stimac, J., F. Goff, and C. J. Goff., 2015, Intrusion-Related Geothermal Systems, in The Encyclopedia of Volcanoes: doi:10.1016/B978-0-12-385938-9.00046-8.

Svensen, H. H., T. H. Torsvik., S. Callegaro., L. Augland., T. H. Heimdal., D. A. Jerram., S. Planke., and E. Pereira., 2017, Gondwana Large Igneous Provinces: plate reconstructions, volcanic basins and sill volumes: Geological Society, London, Special Publications, doi:10.1144/SP463.7.

Thompson, N. K., K. N. Bassett., C. M. Reid., 2014, The effect of volcanism on cool-water carbonate facies during maximum inundation of Zealandia in the Waitaki–Oamaru region: New Zealand Journal of Geology and Geophysics, v. 57, no. 2, p. 149-169.

Luca, P., H. Matias., J. Carballo., D. Sineva., G. Pimentel., J. Tritlla., M. Cerdà., R. Loma., R. P. Jiménez., M. Pontet., P. B. Martinez., V. Veja., 2017, Breaking Barriers and Paradigms in Presalt Exploration: the Pao de Açúcar Discovery (Offshore Brazil). In book: Giant Fields of the Decade 2000-2010, AAPG Memoir 113.

Wang., H. Bischoff, A.P., A. Nicol., Rossetti, M., 2018, Fluid-flow Properties of Pyroclastic Rocks – Insights from Songliao Basin, China. In 2018 Geoscience Society of New Zealand Conference, Napier, Abstract.

Wight, A.W.R., Hardian, D., 1982, Importance of diagenesis in carbonate exploration and production, Lower Batu Raja Carbonates, Krisna Field, Java Sea: Indonesian Petroleum Association, 11th Annual Convention, Proceedings, p. 211–236.

Chapter 7

Conclusion and Further Work

7 Conclusions

Interpretation of volcanoes in the subsurface requires a multidisciplinary approach that combines insights from sedimentology, stratigraphy, tectonics and volcanology into a unified model. In this PhD thesis, we successfully apply concepts traditionally used to analyse sedimentary basins (i.e. architectural elements and stratigraphic sequences), to characterise the architecture of sedimentary basins impacted by volcanism. Here we demonstrate that these "volcanic basins" can be divided into three first-order magmatic sequences (i.e. pre-, syn- and post-magmatic), which can be further divided into second-order magmatic stages related with the emplacement, construction, degradation and burial of the volcanoes. Each one of these sequences and stages are characterised by a network of genetically related fundamental building blocks (i.e. architectural elements), formed by interactions between intrusions, eruptions, and sedimentation. Reconstruction of the architecture of the Kora Volcanic System (KVS) and Maahunui Volcanic System (MVS) allows us to understand how igneous and sedimentary architectural elements interact, and are distributed in space and time relative to buried volcanic systems. In both polygenetic and monogenetic case-studies, the lateral and vertical relationships between architectural elements vary systematically and in a predictable volcano-stratigraphic order. Syn-intrusive architectural elements typically cross-cut and deform pre-magmatic sequences, but minor intrusions can cross-cut into the constructional stage near eruptive centres. Syn-and inter-eruptive architectural elements generally overlay pre-magmatic sequences and are controlled by their distance from the eruptive centres. Post-magmatic architectural elements usually overlay the syn-magmatic sequence and are formed by the interaction of local volcanic degradation and regional basin sedimentation, which buries the volcanic edifices.

Remarks for the KVS

The orientation and location of the KVS plumbing system is directly related to the simultaneous rift faulting that prevailed in the northern Taranaki Basin during the Miocene and early Pliocene. KVS syn-intrusive architectural elements such as sills and dikes are typically formed along, or branching from, Miocene rift faults. Explosive submarine volcanism in Kora formed a large-volume (ca 95 km^3) basaltic-andesitic compound volcano erupted from a fixed central conduit, with associated scattered multi cone-sectors, parasitic and satellite vents. Degradation of the volcanic edifice created localized debris deposits that interfinger with hemipalagic sediments and

with enclosing deposits from deep-water channels. Kora volcano influenced basin sedimentation for at least six million years after volcanism had ceased and around two million years after the volcanic edifice was completely buried. Following complete burial, a dome structure formed on the seafloor above the buried cone. This dome influenced the deposition of submarine fans with geometries not observed elsewhere.

Remarks for the MVS

The MVS plumbing system created distinctive geometric relationships between the intrusions and the enclosing strata, which were mainly controlled by their depth of emplacement. The plumbing system of the MVS typically distributes magma to dispersed eruptive centres, which formed small-volume (< 6 km^3) basaltic submarine volcanoes equivalent of maar-diatreme and tuff cones. Degradation in the MVS was primarily controlled by a late Miocene base-level fall, which produced differential erosion in volcanoes that were emergent at the paleo sea-surface. Volcanoes within the MVS that remained below wave base and in deep water (e.g. >200 m) were not subject to erosion and are well preserved buried beneath bathyal sediments. In similar fashion to the KVS, burial in the MVS created dome structures in the strata overlaying the volcanic edifices. These domes and their impacts on basin sedimentation can be observed for at least 6 million years after the volcanoes ceased to erupt and around 1 million year after they were completely buried.

Implications for geoenergy exploration

The interactions between magmatism and sedimentation create a range of geological conditions that favour or decrease the potential of occurrences of geoenergy resources in volcanic systems. These conditions are influenced by a diverse array of volcanic and sedimentary architectural elements. At the endogenous level, intrusions and magmatic deformation can create architectural elements associated with fractured reservoirs, seals, and structural traps, which typically provide pathways for fluid percolation in the subsurface. Large saucer-sills and intrusion swarms have the potential to form four-way closures and reservoirs that can host significant oil and gas accumulations. These intrusions can also produce high-temperature intrusion-related geothermal systems. If the intrusions are emplaced in carbonate or organic-rich host rocks both petroleum and geothermal systems are likely to be enriched in CO_2, CH_4, and H_2S. At the exogenous level, a complex network of eruptive and sedimentary architectural elements can

form substantial hydrocarbon fields if fluids are delivered to syn-eruptive reservoirs located on the flanks and tops of the volcanoes. These reservoirs can be entrapped in paleogeomorphic structures formed by changes in lithologies and by the presence of stratigraphic discontinuities between the volcano and enclosing strata. Syn-eruptive reservoirs can be sealed, if volcanic structures are buried by fine-grained marine sediments or evaporitic rocks. Progressive burial of the volcanoes can create ideal conditions for deposition of high-quality carbonate reservoirs located above buried volcanic structures. Differential compaction between the volcanoes and enclosing sedimentary rocks can entrap these carbonate reservoirs in large four-way closures, with potential to host world-class hydrocarbon fields.

The analysis of architectural elements is proven useful to characterise volcanic systems buried in sedimentary basins. This analysis helps the construction of volcano-stratigraphic frameworks that represent the complete architecture of buried volcanoes, which can be used to build models for the exploration of geoenergy resources such as hydrocarbons and geothermal energy. Understanding the relationships between diverse architectural elements, their petrophysical properties, and the events that can change their original characteristics have to be assessed on a case-by-case basis. The characterisation of volcanic and sedimentary architectural elements is important for de-risking prospects and improving the likelihood of finding commercially viable geoenergy resources in association with buried and active volcanic systems.

Further work

In this PhD thesis, we propose models based on a buried composite volcano, and a buried monogenetic volcanic field. Both volcanic systems have basaltic-andesitic composition. Further efforts will be necessary to understand how the architectural elements (and their associated geoenergy systems) can occur for a range of volcanic, sedimentological and tectonic settings such as caldera volcanoes and other silicic systems. The work developed in this PhD study is proposed to continue as a post-doctoral research project funded by the 2017 Endeavour Fund - Smart Ideas from the Ministry of Business, Innovation and Employment of New Zealand. Following, we list some of the main questions that we aim to study in the post-doctoral research project as listed below:

- How can the analysis of architectural elements improve the interpretation of buried and outcropping volcanic systems in other locations?
- What are the main architectural elements of silicic systems?

- What are the main mechanisms that control the formation and evolution of the pre-eruptive and burial dome?
- How do permeability and porosity vary systematically for the diverse array of architectural elements associated with buried volcanoes?
- How do architectural elements influence the subsurface flow of fluids?
- Can we quantify the number and geometries of architectural elements, to help improve the chances of finding geoenergy resources in the future?
- Under what geological conditions can we expect potential petroleum systems to occur in buried volcanic systems in the New Zealand sedimentary basins?
- Can we recognize these architectural elements in active and buried volcanoes of the Taupo Volcanic Zone using onshore seismic reflection and well data?
- What are the typical volumes of saucer-shaped sills in the New Zealand sedimentary basins? What volumes are expected to form prolific intrusion-related geothermal systems?
- Can we image active intrusive-related geothermal systems using seismic reflection?
- Can volcanic reservoirs in the New Zealand sedimentary basins be used for CO_2 sequestration?

Appendix I

Complementary Information of the Methods Used to Calculate the Height and Volume of Buried Volcanoes from Seismic Reflection Data

8 Appendix 1: Complementary Information of the Methods Used to Calculate the Height and Volume of Buried Volcanoes from Seismic Reflection Data

This section aims to provide complementary information of the methods used to calculate the height and volume of buried volcanoes from seismic reflection data. Calculations and Statistical analysis was made in conjunct with Hanfei Wang (UC PhD candidate in fluid-dynamics of volcanic rocks).

Estimation of acoustic velocities of buried volcanoes

This section provides complementary information for the estimation of acoustic velocities of buried volcanoes in Maahunui Volcanic Field (section 4.4.3.1). Statistical analysis suggests that the application of the RII method produces a population of height values that are more stable compared to methods that use pre-defined maximum and minimum (or average) values (Figure 82).

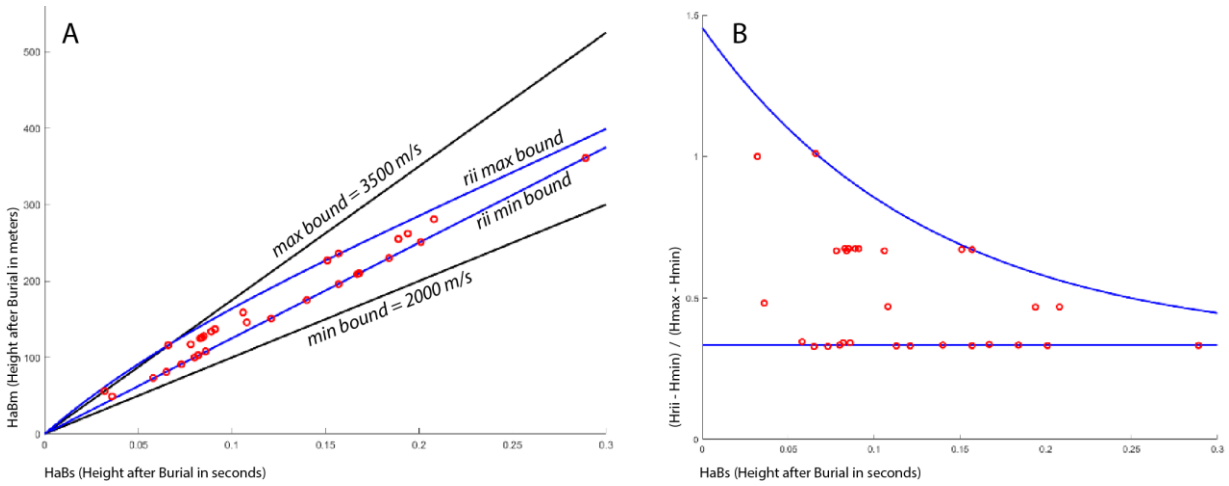

Figure 82: Graphs showing the population of HaBm (Height after burial in meters) for MVF volcanoes using the Relative Impedance Index method (RII) to estimate the acoustic velocities of buried volcanoes. A) Black lines show expected bounds in HaBm calculated from maximum and minimum velocities of tuffaceous rocks compiled from laboratory and drill-hole measurements elsewhere. Blue lines define the bounds in HaBm using estimations of velocities from the RII method. Note that blue lines (RII approach) show a property of convergence between maximum and minimum ranges with increasing calculated height, while black lines show divergence.

The maximum and minimum estimated values of RII (Figure 82A) were derived from the graph in Figure 82B. B) shows the HaBs (height after burial in seconds) calculated by applying the RII method vs. the relative upper and lower bound estimated by both methods, that can be defined as: $Hr = \frac{HRRI - Hmin}{Hmax - Hmin}$ in which Hr is the relative height. As we can see in (B), the variability of Hr decreases as HaBs increases, and the Hr minimum (Hrmin) can be described by a horizontal line

that corresponds to Hr=0.333 (lower blue line in B). Thus, we can describe the Hr maximum (Hrmax) using a line with decreasing high above the horizontal line Hrmin from left to right on the graph. In this case, we can fit the Hrmax as $Hr_{max} = a \times e^{-b \times Ht} + c, c > 0.3333$. The fitted result is $Hr_{max} = 1.121 \times e^{-7.643 \times Ht} + 0.334$. Then, we can derive the HaBm max and min estimated by RII height according to:

$$RII = Hr_{max} \times (Hmax - Hmin) + Hmin$$

$$= 840.8 \times Ht \times e^{-7.643 \times Ht} + 1250 \times Ht$$

and

$$RII_{min} = Hr_{min} \times (Hmax - Hmin) + Hmin$$

$$= 1250Ht.$$

Constant used in the equations are e= Euler number ~ 2.71828; c is the theoretical minimum of Hrmax; a+c are the theoretical maximum of Hrmax, and b represent the decreasing trend of Hrmax.

The stability of the RII analysis could arise because it is based exclusively on data from within the study area and because RII constrains errors for a range of anomaly heights, while conventional methods have uniform errors (Figure 82). The benefit of the RII method is that it enables an *in situ* evaluation of the acoustic velocities of MVF volcanoes in the absence of a very large number of wells. Figure 38 shows 2D images of some MVF volcanoes and morphometric parameters calculated using RII velocities estimations.

Calculating the volume of buried volcanoes from seismic reflection data

We calculate an approximate volume of two volcanoes in the Maahunui Volcanic Field, and the volume of the Kora Volcano. To calculate the volume of these volcanoes, we first mapped the area of the volcanoes in 2D seismic images, using lines that approximately correspond to their "summits" (Figure 85; Figure 84). The width of these volcanoes were measured directly in meters from the seismic lines, and their height was converted to meters using the RII method described in the Chapter 4. Then, we slice the volcanoes in delta (*d*) number of depth intervals, in which (*l'*) correspond to the length of each interval and (h') is the height of the interval (Figure 83). We assume that the volume of the volcanoes could be approximate to a series of superimposed

cylinders with different lengths ((Figure 83). The final volume of the volcanoes was calculated by the integration of the volumes of each cylinder using the equation:

$$V = \int \frac{\pi}{4} l^2 dh$$

Volcano pc17 was sliced in 137 cylinders of 2.6 m in height, and have a volume estimated in 1.6 km^3. Volcano pc14 was sliced in 230 cylinders of 2.6 m in height, and have a volume estimated in 5.7 km^3. Kora volcano have a more complex morphology due to the presence of a local pre-eruptive dome. Kora was sliced in 512 cylinders of 5.1 m in height. We first calculate the total volume of the volcano, including its pre-eruptive dome, and then calculate the volume of the pre-eruptive dome separately. The volume of Kora volcano was calculated by subtracting the total volume minus the volume of the pre-eruptive dome (Figure 85).

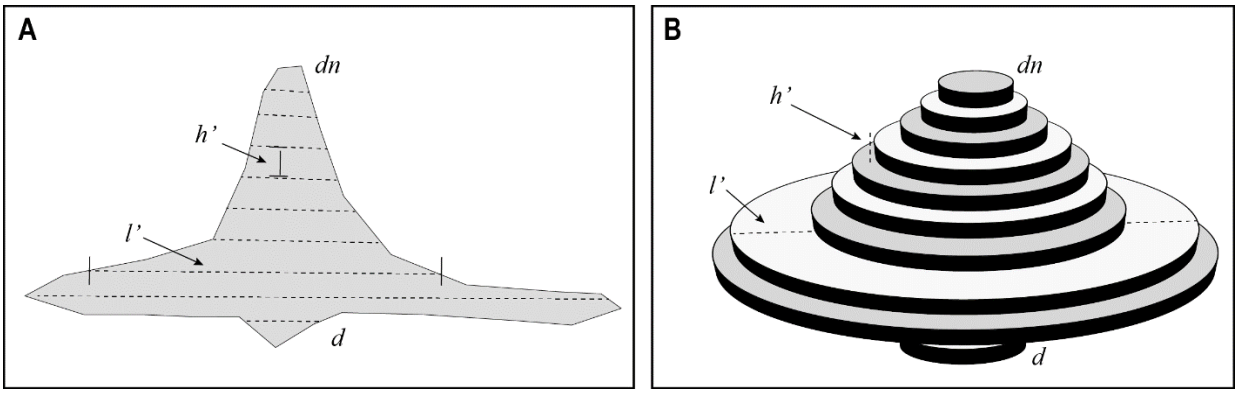

Figure 83: Method to calculate the volumes of volcanoes from 2D seismic images.

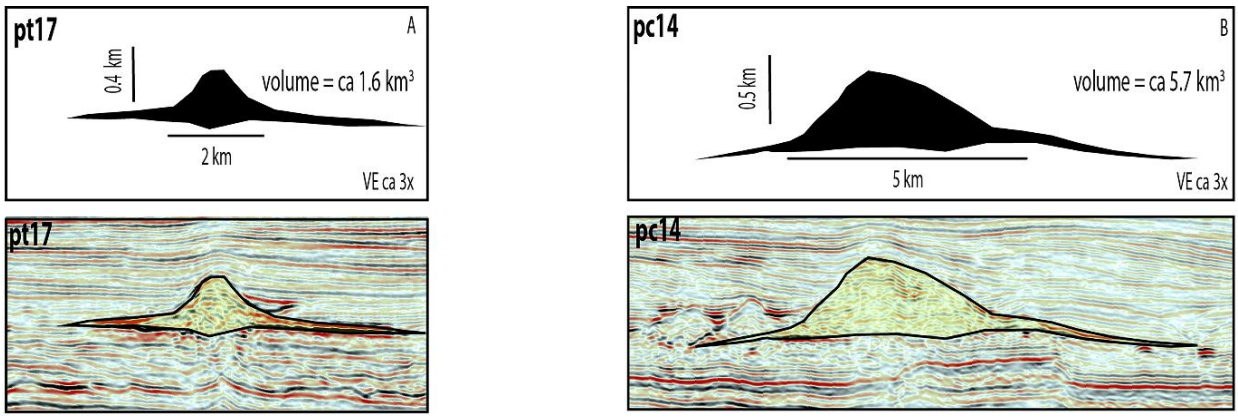

Figure 84: Reconstructed morphology of volcanoes imaged by 2D seismic lines in Maahunui Volcanic Field. Seismic lines correspond to the height of the "summit" of the volcanoes.

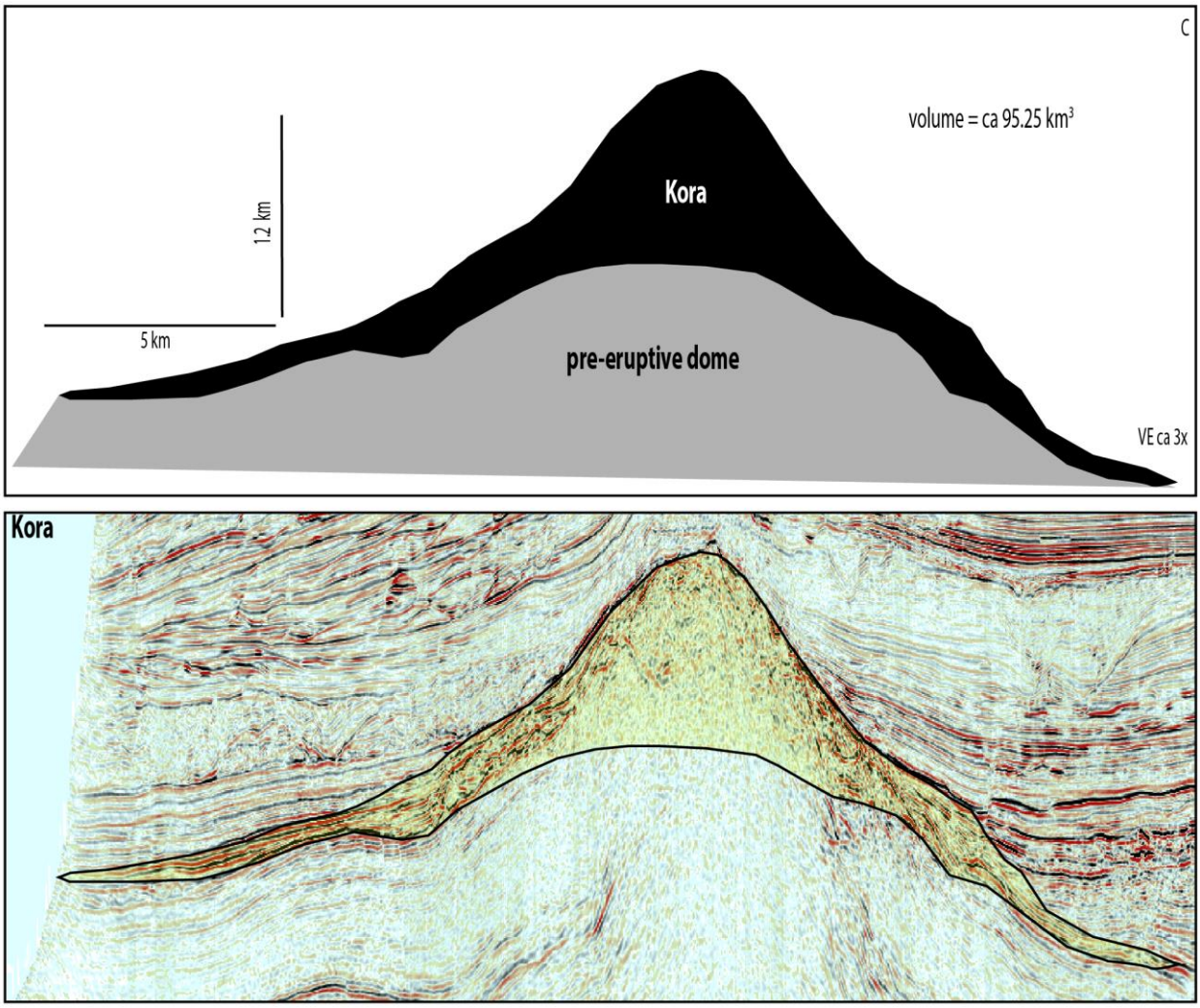

Figure 85: Reconstructed morphology of volcanoes imaged by 2D seismic lines in Kora Volcano. Seismic lines correspond to the height of the “summit” of the volcano.